THE UNIVERSITY *of* EDINBURGH

This thesis has been submitted in fulfilment of the requirements for a postgraduate degree (e.g. PhD, MPhil, DClinPsychol) at the University of Edinburgh. Please note the following terms and conditions of use:

This work is protected by copyright and other intellectual property rights, which are retained by the thesis author, unless otherwise stated.
A copy can be downloaded for personal non-commercial research or study, without prior permission or charge.
This thesis cannot be reproduced or quoted extensively from without first obtaining permission in writing from the author.
The content must not be changed in any way or sold commercially in any format or medium without the formal permission of the author.
When referring to this work, full bibliographic details including the author, title, awarding institution and date of the thesis must be given.

Development of the Deepwater Turbine Installation-Floating concept

Jordi Serret i Magaz

A thesis submitted in partial fulfilment of the requirements for the award of an Engineering Doctorate

UNIVERSITY OF STRATHCLYDE

2019

This thesis is submitted in partial fulfilment of the requirements for the award of an Engineering Doctorate, jointly awarded by the University of Edinburgh, the University of Exeter and the University of Strathclyde. The work presented has been conducted under the industrial supervision of Floating Wind Turbines Ltd. as a project within the Industrial Doctoral Centre for Offshore Renewable Energy (IDCORE).

Signed: Jordi Serret i Magaz

Date: 01/11/19

Abstract

Floating offshore wind turbine technology is progressing from the research stages to commercial projects. It will be an increasing source of renewable energy over the next few years. The better quality of the wind resource and environmental considerations will encourage developers further offshore, if commercially viable. This research work presents the initial development of the Deep Turbine Installation-Floating (DTI-F) concept. The DTI-F concept is a hybrid spar buoy-based floating offshore substructure capable of supporting a 7 MW wind turbine with the uniqueness of being able to raise and lower the tower and nacelle, which simplifies construction, installation, maintenance, and decommissioning. The research proceeds in three parts; the first part is a compilation of the background of floating wind turbines and the DTI-F concept. A novel construction method and the installation and assembly processes are outlined, as well as the parametric approach used to perform the preliminary design of the floater. The second part presents both the aerodynamic and hydrodynamic modelling techniques applied during this research. It covers the aeroelastic analysis of the Levenmouth wind turbine (WT) and the experimental and numerical hydrodynamic analysis of the DTI-F concept holding the Levenmouth WT. The Levenmouth (Samsung Heavy Industries - S7.0-171) offshore wind turbine owned by the Offshore Renewable Energy Catapult (ORE Catapult) is a real, operating demonstration wind turbine. The aeroelastic model of the Levenmouth WT has provided the load-matrix of a real, operating seven megawatts WT. The results of the aeroelastic analysis have been integrated parametrically into the design of the DTI-F floater. The hydrodynamic analysis of the floating system undertaken for this research is based on experimental and numerical modelling work. A 1:45 Froude scale model of the DTI-F wind concept was tested using three different mooring configurations: i) three mooring lines, ii) four mooring lines, and iii) three mooring lines with a delta connection. Free decay and stiffness decay tests were carried out together with regular and irregular

wave tests. The numerical study comprises diffraction analysis (ANSYS AQWA) and time-domain modelling (OrcaFlex) of the system, and it has been validated against the aforementioned experimental results. The outcome of this research has demonstrated the good practice of the DTI-F concept and has increased the Technology Readiness Level of the studied concept from 1 to 3 while proving that the DTI-F concept has a high degree of technical feasibility. The concluding part of the research provides a discussion of the overall work along with conclusions, recommendations, and future work suggestions.

Lay Summary

Human society has progressed in parallel with energy consumption. The bigger and more refined our society becomes, bigger amounts of energy are needed to fulfil our requirements. Due to the increasing demand, new sources of energy must be sought. Humans started unlocking energy by burning wood and then, during the industrial revolution, evolved to burn fossil fuels which provided more energy. Nowadays, as we are aware of the harmful effects on the environment caused by the burning of fossil fuels, the global economy is transiting to renewable sources of energy. One of the most promising technologies regarding sustainable energy production is wind energy. We have developed wind turbines to harvest the energy inside the wind and make it useful. It has been demonstrated that offshore wind turbines are more efficient than onshore due to the better quality of the wind offshore. Moreover, floating wind gives the possibility of expanding wind energy into new deep-water areas, unlocking a vast amount of new energy resource. However, the challenges associated with floating offshore wind are huge. The static stability of a tall floating structure holding a massive wind turbine on the top is complex. Considering the dynamic conditions, where the floating system is subjected to loads of wind, waves, and currents increase the level of complexity even more. The present research aims to de-risk floating offshore wind by conducting several simulations of the different subsystems conforming a floating offshore wind turbine. The mechanical behaviour of a large wind turbine is studied, and the results are used as a basis for a subsequent floater design. The complete floating system has been built to scale, tested, and the results were fed to the simulations to make them more accurate. It is expected that the outcomes of this research will support floating wind development.

Authorship Declaration

I hereby declare that all the developments included in this dissertation can be attributed to the author except where is clearly stated. Furthermore, the work contained in this document has not been submitted for any other degree or professional qualification.

Acknowledgements

I acknowledge gratefully the funding from Floating Wind Turbines Limited (FWT Ltd), the Energy Technologies Institute (ETI), and the Research Councils UK (RCUK) Energy Programme for the Industrial Doctorate Centre for Offshore Renewable Energy (IDCORE) through the grant EP/J500847/1. The release of the technical features of the Levenmouth Wind Turbine owned by Offshore Renewables Catapults under the licence agreement O0699.36 56584179 2 JBT is acknowledged. Regarding that, special thanks go to Carlos Rodriguez senior Aeroelasticity engineer at ORE Catapult. Funding from the Energy Technology Partnership-Knowledge Exchange Network (ETP-KEN) through the contract Ref PJ02000-M, and MaRINET2 through the grant 731084 are gratefully acknowledged. I would like to thank Orcina Ltd. for kindly providing a research licence of their software OrcaFlex under a loan agreement. I am grateful to my supervisory team including Tahsin Tezdogan, Tim Stratford, Philipp Thies, and Vengatesan Venugopal. My gratitude extends to Lir National Ocean Test Facility and FloWave Ocean Energy Research Facility teams. Regarding that, I would link to thank Donald Noble, Tom Davey, and Edd Nixon for their guidance during the testing camping. Also, special thanks to Jim Hutcheson for helping in the structure's laboratory of the University of Edinburgh. I am most grateful to my industrial supervisor Rodger Taylor for his contribution and inspiration on my project, and my IDCORE and industrial colleague, Mohammad Yousef for sharing such an interesting and endless philosophical chats. Finally, I want to dedicate this work to my family, especially my mom and dad, my partner Ana, and my beloved son Xurxo for their love and for being my driving force.

Contents

List of Figures

List of Tables

Part I.

Background

1. Introduction

1.1. Background

In recent years, as driven by globalisation and population growth, the world energy demand has been increasing [1]. Emerging countries where the economy is blooming increase significantly their energy demand as well as developed countries at a modest level. However, although the global energy mix relies primarily on fossil fuel, the energy consumption by fuel projections shows how renewable energy, nuclear power and natural gas are the fastest-growing energy sources (Figure 1.1.1).

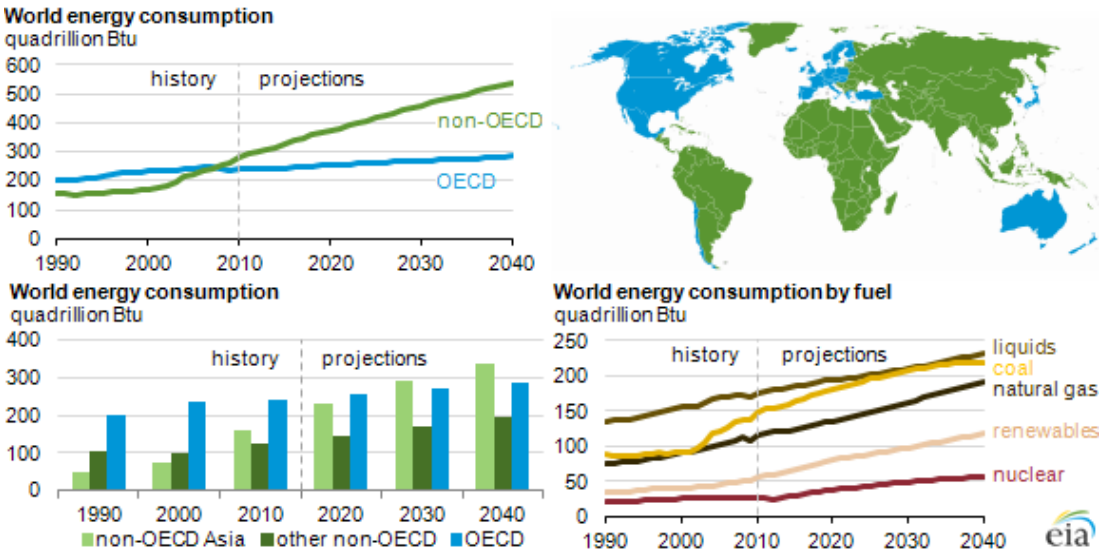

Figure 1.1.1.: World energy demand [1].

The ability to decarbonise a country's energy mix to mitigate the risk to the envi-

ronment and use its indigenous renewable resources to reduce the risk to its energy supply will determine the future economic and social wellness of the society. Without reliable, sustainable, and reasonably priced energy there can be no long-term sustainable growth. These three goals are the so-called energy 'trilemma' (Figure 1.1.2) connecting public and private actors, governments and regulators, economic and social factors, natural resources, environmental concerns, and individual behaviours [2]. In philosophy, a trilemma is a difficult choice between three options which appear contradicting each other. It is also known as 'impossible trinity'. The reason for the existence of a trilemma is the conflict of interest between the different actors involved. While affordability and decarbonisation are the dominant issues for the public, energy security is paramount for governments stability. The world energy trilemma has pushed policymakers to develop and deliver policies addressing security, sustainability, and equity in the energy supply simultaneously.

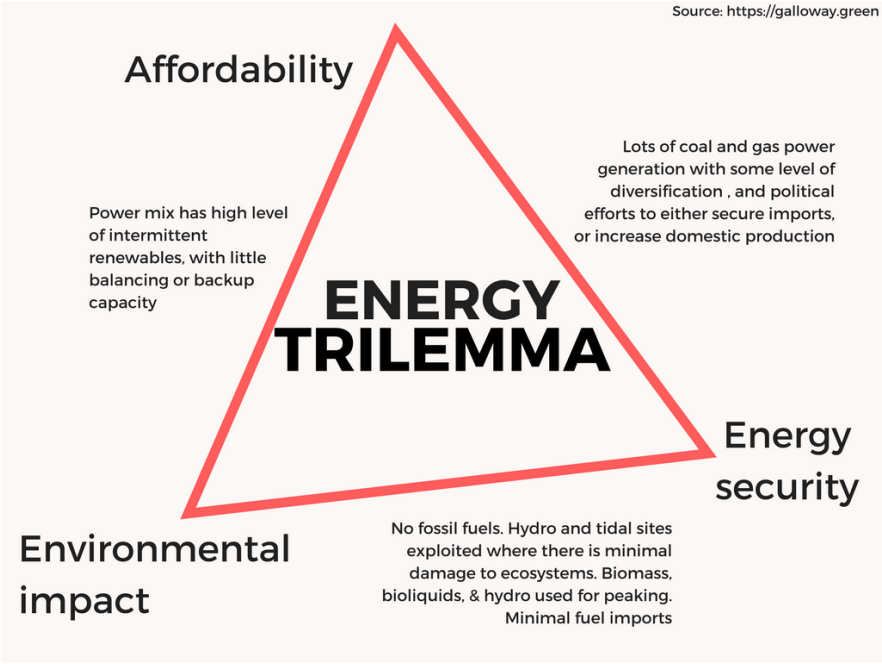

Figure 1.1.2.: Energy 'trilemma' [3].

In the European Union (EU), the share of energy from renewable sources in gross final of energy in 2018 [4] reached 17.5%, up from 8.5% in 2004. This increase in renewable energy consumption has been boosted by EU policies like the target of 20% energy in gross final consumption of energy from renewable sources by 2020. In parallel, the UK, which is the flagship of renewable energy development in the world has set ambitious objectives like bring all greenhouse gas emissions to net zero by 2050.

The combination of a market eager for energy and a thriving renewable industry, along with the proper policy alignment and international agreements, e.g. Kyoto Protocol, Paris agreement, or the European Renewable Energy Directive, are the main drivers behind the development of electrical wind power.

1.2. Wind Energy

Humans have used wind energy in sailing ships since the sixth-fifth millennia BC [5]. During the last two millennia, wind-powered machines have converted wind energy into rotational energy using vanes. The produced rotational energy can be transformed into heat, potential and linear kinetic energy, and more recently wind turbines transforms it into electrical power. Professor James Blyth built the world's first electricity-generating wind-powered machine, i.e. wind turbine, in Scotland in the late 1880s. Although Professor Blyth published a paper in 1891 [6] supporting the benefits of renewable energy sources like wind, it was not until 1973 when the oil price crisis pushed forward the investigation regarding non-petroleum energy sources. In 1978, the world's first multi-megawatt wind turbine was built in Denmark, and since then the wind industry has continued growing and developing edge technology to produce cost-effective wind power. WindEurope has presented a set of estimates for the wind development in Europe by 2030 with installed cumulative wind energy capacity ranging from 256 GW to over 397 GW [7]. Figure 1.2.1 shows a comparative summary of the expected macroeconomic

benefits linked to eventual wind energy development for the three possible scenarios.

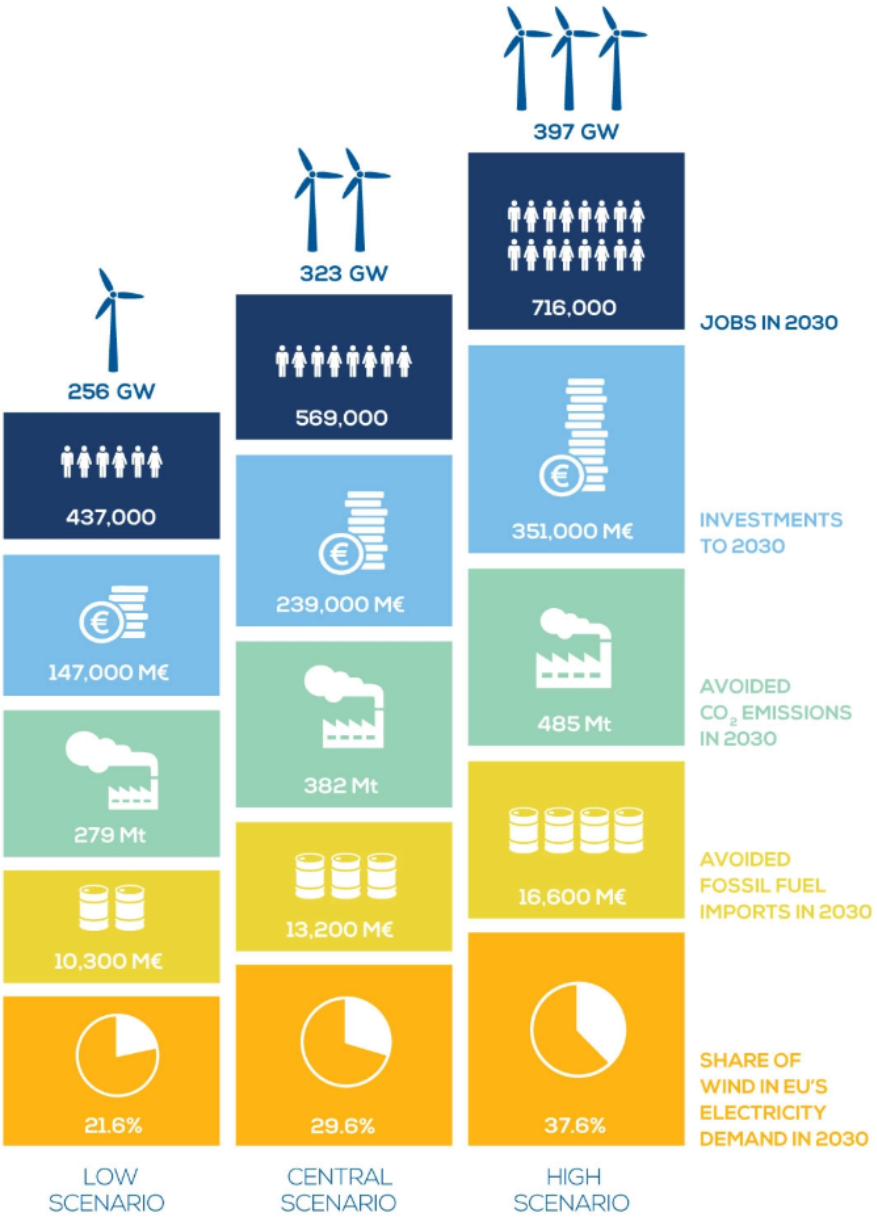

Figure 1.2.1.: Wind development in Europe by 2030[7].

1.3. Offshore Wind Energy

In 1991 the wind industry led by DONG (Dansk Olie og Naturgas A/S), a Danish power company, began its offshore expansion starting with the North Sea continental shelf. Thereafter, the wind industry has been gradually moving further and deeper offshore. In 2016, Vattenfall won an auction for Denmark's 600MW Kriegers Flak offshore wind project at €49.9/MWh, and in 2018 Ørsted won a subsidy-free project in Germany to develop the 420 MW Borkum Riffgrund West 1 wind farm [8]. At the end of 2018, Europe's cumulative offshore wind capacity reached 18,499 MW (Figure 1.3.1). The United Kingdom represented 49% of Europe's gross capacity, followed by Germany (36%), Belgium (12%), and Denmark, Spain, France and Sweden.

Offshore wind in deeper water will be an increasing source of renewable energy over the next years. The better quality of the wind resource will encourage developers further offshore, making floating solutions increasingly commercially viable. However, moving into deep marine environment will increase the cost and complexity of some operations, such as maintenance and decommissioning, over land-based or shallow water-based works. Deepwater challenges are mainly related to the lack of a fixed and stable operating surface, but also due to the constant motion of the water-free surface through waves and currents, the corrosive environment, the increasing distance to the shore, the harshest weather conditions, a higher loading, and fatigue-related problems among others. However, first and foremost, cost reduction is the main challenge for the industry, and much work is being done to address it.

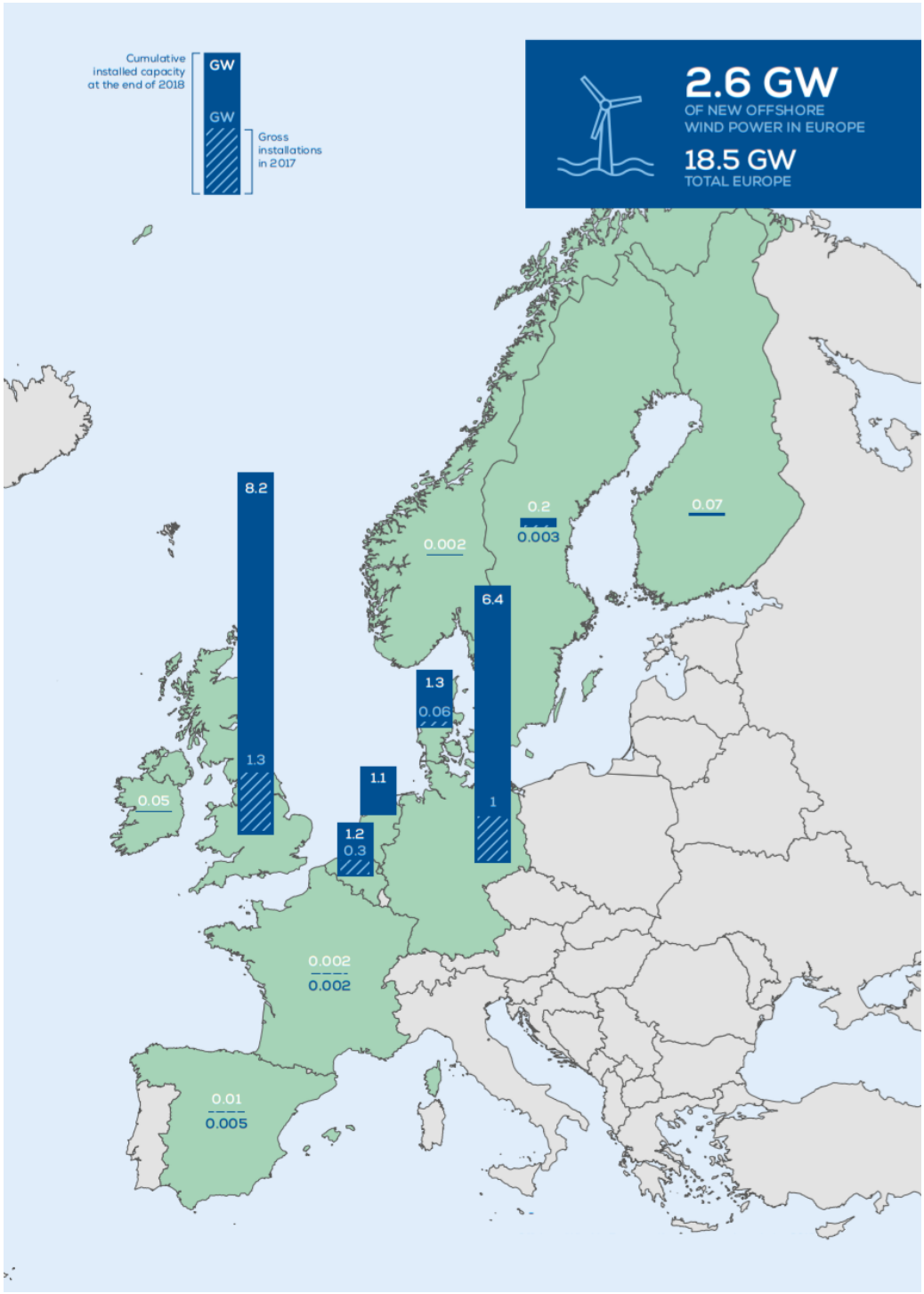

Figure 1.3.1.: 2018 Europe's cumulative offshore wind capacity[9].

1.4. Floating Offshore Wind

Over the last few years, experience has been gained with floating wind technology. It has evolved from being an academic topic to start delivering sustainable, reliable energy supply to the grid. The Equinor's Hywind project [10] installed their first full-scale spar buoy floating offshore wind turbine (FOWT) back in 2009 in the North Sea close to the Norwegian coast. The project continued in Scotland, and in 2018 became the world's first floating wind farm producing electricity to the grid [11]. In order to have a standard and systematised framework to assess the level of development of a technology, the National Aeronautics and Space Administration (NASA) agency of the United Stated government introduced back in the seventies the Technology Readiness Level (TRL) scheme [12]. Regarding the TRL scheme, the first full-scale spar buoy FOWT installed in 2009 has a level 6-7, whereas the floating wind farm inaugurated in 2018 achieved the TRL 9. Full description of the TRL schemes is provided in Appendix I.

Hitherto, different floating foundations have been proposed [13, 14]. Semi-submersibles [15, 16], barges [17], and tension leg platforms [18, 19] have been developed along with spar buoy-based [20] developments (Figure 1.4.1). Figure 1.4.2 displays the different stability mechanisms used by the above-mentioned floating foundations.

The barge-type FOWT have a large pontoon structure holding the tower and nacelle set. Distributed buoyancy and a large waterplane area give the stability required to the pontoon, which may be moored by conventional catenary chains and anchored by drag anchors or suction caissons. Due to its susceptibility to the roll and pitch motions and its limited draft, it may only be installed in calm and shallow waters.

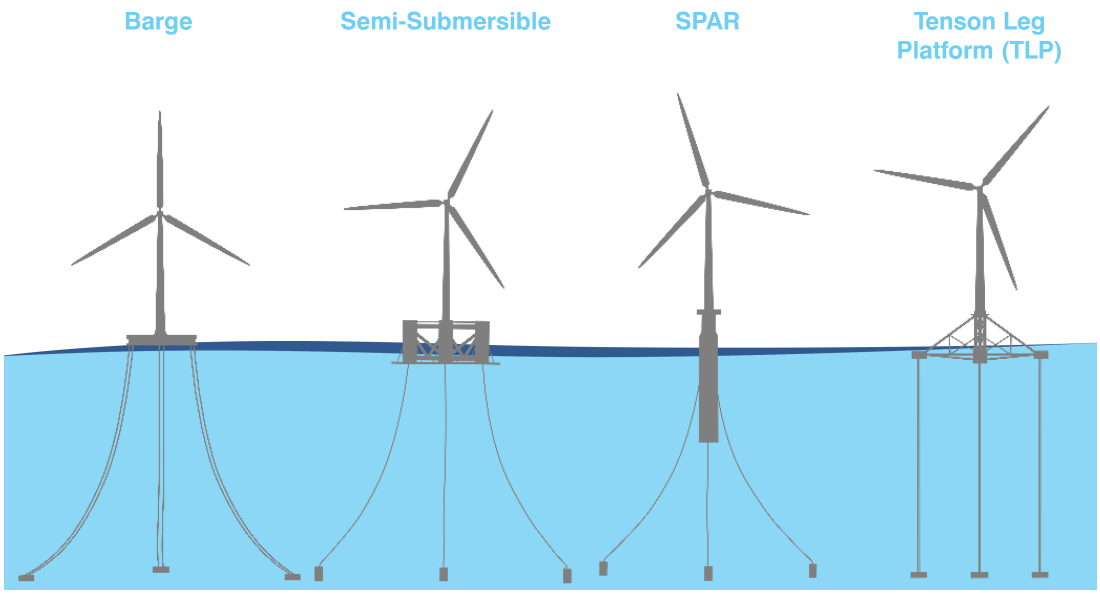

Figure 1.4.1.: Different types of floating wind foundations. Modified from [21].

Semi-submersible concepts consist of several flotation columns connected by bracing members and kept in position by mooring lines. The wind turbine may be sitting on one of these flotation columns or in the geometric centre of the structure. The flotation columns provide ballast and the needed water-plane area for stabilisation purposes. Its relatively shallow draft allows for site flexibility.

A spar buoy-based FOWT system comprises the floating foundation also known as floater, the tower and the rotor-nacelle assembly (RNA). The floater may be towed in the horizontal position, upended, ballasted, and finally, tower sections and the RNA are assembled and installed by a derrick crane barge. Then, the structure is towed in the vertical position to the deployment site and connected to the mooring system. The large draft of the floating foundation ensures excellent ballast stability and stays upright thanks to the sizeable righting moment arm and high inertial resistance to pitch and roll motions. Therefore, deep-water sites are required for deploying a spar-type FOWT, and adequate keel to sea-bed vertical clearance is also necessary to ensure mooring system effectivity. Conventional catenary chains moor the spar system which is anchored to the

seabed by drag anchors or suction caissons.

The TLP-type concept comprises a floating platform held in position by vertical tendons (also known as tethers) anchored by a gravity base foundation, suction caissons or by pile-driven anchors. TLP-type FOWT has a low dynamic response but is subject to 'pull down' phenomena which relate to the increase in the draft when the platform offsets from its equilibrium position. TLP wind turbine may be assembled and commissioned onshore and then towed to the deployment site reducing expensive heavy-lift vessels or derrick crane barges for offshore construction.

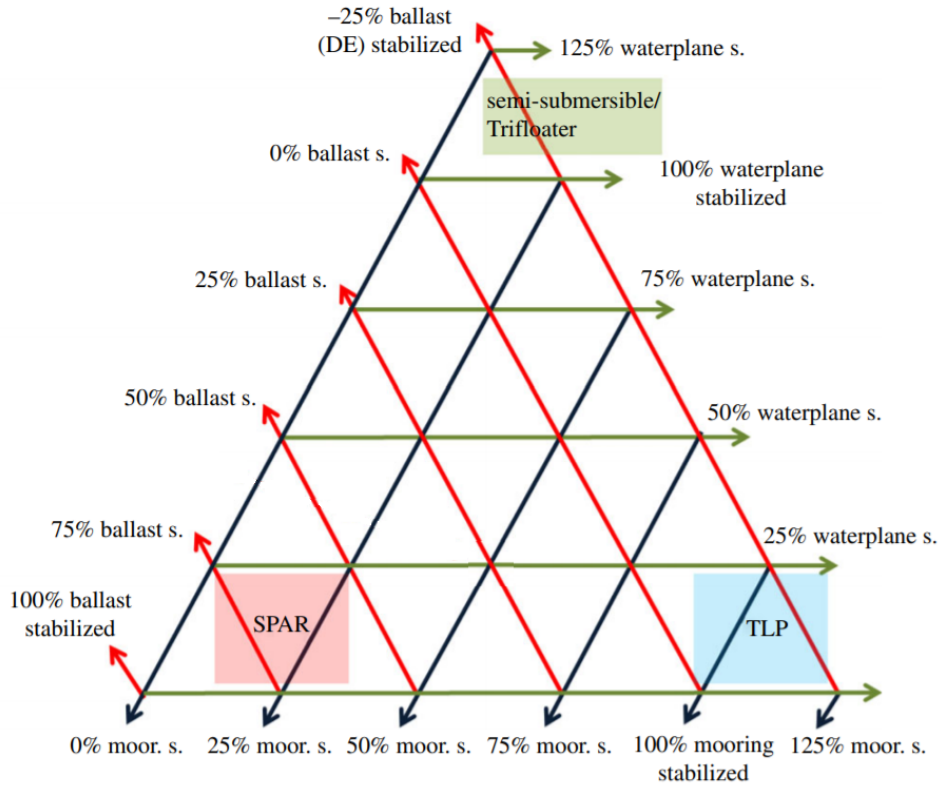

Figure 1.4.2.: Stability mechanisms used by the above-mentioned floating foundations [22].

It should be remarked that there are hybrid types of floating wind turbines. Thus, there are spar-buoy concepts moored by a single vertical tendon held at the base by a swivel connection, or adding heave plates, or truss structures connected to the bottom of

the floater. The present work focusses on a utility-scale, single-turbine hybrid spar buoy-based floating design called Deepwater Turbine Installation-Floating (DTI-F) concept.

1.5. Deepwater Turbine Installation-Floating concept

Back in 2013, Concrete Marine Solutions (CMS) Ltd [23] developed an offshore wind gravity-based concrete foundation called DTI-50 which stands for Deepwater Turbine Installation – 50 metres draft (Figure 1.5.1). The idea was also applied to met-mast foundations [22] since the modular design was flexible enough to fulfil requirements for heavier and lighter structures compared with an offshore wind turbine. As shown in Figure 1.5.1, the DTI-50 has the uniqueness of being able to raise and lower the tower and nacelle, which simplifies construction, installation, maintenance, and decommissioning.

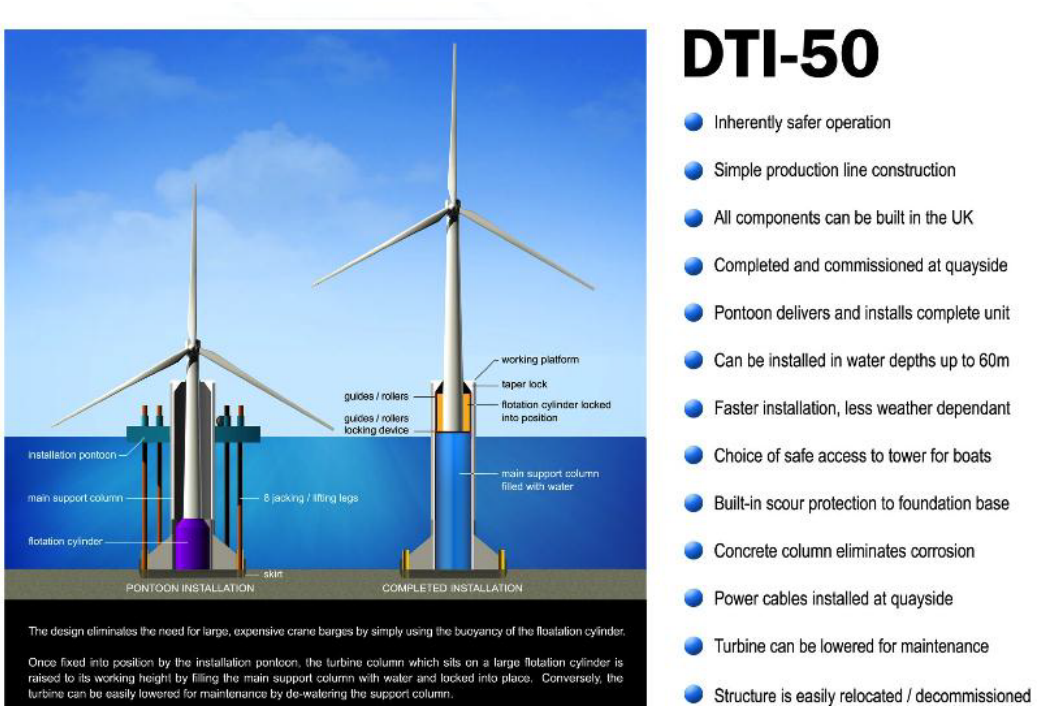

Figure 1.5.1.: Promotional leaflet of the DTI-50 with a list of the main advantages of the technology [22].

In 2014, Statoil launched its 'Hywind Challenge' [24, 25] inviting any interested com-

pany to help to improve the Hywind turbines assembly and installation sequence. CMS responded to the challenge presenting a modification of the DTI-50, the DTI-80F which stands for Deepwater Turbine Installation-80 metres draft Floating concept (Figure 1.5.2). The DTI-80F was strongly inspired in the DTI-50, but in this case, it was a hybrid steel-concrete substructure, i.e. the frustum base was designed on steel following naval architecture basis and the main support column was designed as a modular concrete structure. One of the requirements of the 'Hywind Challenge' was participating with ideas with no intellectual property rights. Since the DTI-80F had an intellectual property (IP) in place [26], the idea was not further considered for the challenge.

In 2016, CMS decided to apply for an Industrial Centre for Doctoral Training for Offshore Renewable Energy (IDCORE) student to further develop the DTI-80F concept by:

1. Developing funding applications to ensure the long-term viability of the project.

2. Reducing the draft of the floating substructure to fill the gap left between the DTI-50 and the current floating concept.

3. Redesigning the substructure using concrete and allowing the use of novel multi-megawatt sized wind turbines.

By the time of starting the research project, the focus of the research and the main objectives changed to conform what is explained in the following Sections.

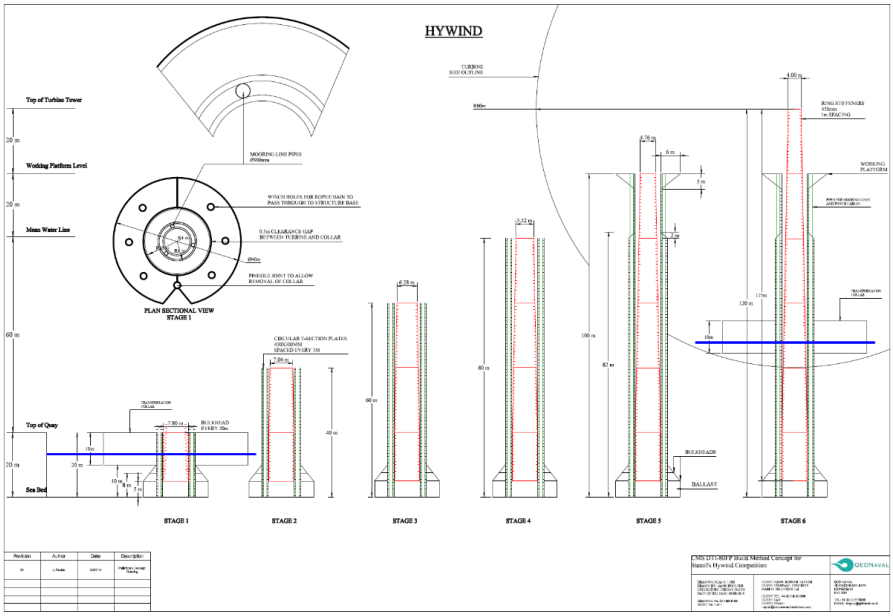

Figure 1.5.2.: Technical sketch of the DTI-80F showing the construction and installation method.

1.6. Motivation

FOWTs are a recurrent topic nowadays. Technical research projects range from designing new concepts, optimising existing ones or further developing any of the subsystems, e.g. blades, controllers, floaters, moorings among others. However, the common motivation behind them is to reduce the costs of the cleanest and most secure indigenous energy resource. The economics of the FOWTs is determined by the additional expenditure of the floating structure, the power distribution system, the operations and maintenance, and decommissioning. Therefore, the aim of this research is to bring to the market an economically viable floating foundation able to reduce capital, operations and maintenance (O&M), and decommission costs, i.e. CAPEX, OPEX, and DECEX; while reducing global dependence on fossil fuels and fulfilling customer requirements. Despite the Equinor's Hywind project technical achievements, the published Levelised Cost of Energy (LCoE) was 156 EUR/MWh [24]. LCoE for onshore wind developments

ranged between 40 and 82 EUR/MWh in 2018, and the range rises between 75 and 138 EUR/MWh for 'conventional' offshore wind developments [27]. The goal is to achieve an LCOE between 40 to 60 EUR/MWh by 2030 [28]. Hitherto, a substantial amount of research work is being carried out to identify the optimal floating configuration. The optimal floating system must deliver sustainable energy while reducing capital and O&M expenditure and decommission costs. Therefore, there is room in the market for novel floating systems if they can significantly address the challenges stated before. This work aims to perform the initial design of a novel concrete floater able to raise up and lower down the tower and nacelle set.

1.7. Scope

As stated before, the design of a FOWT is complex and involves several engineering disciplines. The wind field interacts with the blades through bending and rotation. Regardless of the gearing system used, the rotation of the rotor is transmitted to the shafts where the elasticity plays an important role. This rotatory motion is then transmitted to the generator which is also affected by the electric network. This set of loads are then communicated from the nacelle to the tower by the yaw system which will introduce a new stiffness to the system on top of the blades and shaft. The tower will receive the loads coming from the nacelle and the load from the wind field directly impacting the tower (which will be affected by the pass-through of the blades while spinning). Again, the elasticity/bending of the tower will notably affect the transmission of the loads to the substructure. Usually, the substructure is modelled as a flexible body with a global response, which will be finally transmitted to the anchoring system through the mooring lines. It is worth highlighting that all these systems have complex dynamics on their own. Therefore, the level of complexity reached, once all the systems are fully-coupled is elevated. Moreover, the control system and the transmission piece effects

should also be considered, and in order to increase the fidelity of the simulations, the hydrodynamic interactions between the substructure, the moorings, and power cables with waves and currents, e.g. ringing, vortex-induced vibrations (VIV) and the complicated soil-anchoring system interaction, should be investigated. Therefore, only a few topics regarding the design will be treated in this thesis.

Blades, rotor, shaft system, gearbox, generator, and nacelle namely wind turbine system, are discussed and numerically modelled. This part of the study is subjected to a confidentiality agreement with Offshore Renewable Energy Catapults which prevents the disclosure of the Levenmouth WT data as well as the generated results except for the interface loads. The interactions of the WT system with the tower and yaw system are also covered. However, the setup of a suitable controller is specifically out of the scope of this work. As a result, an aeroelastic model of the Levenmouth WT in addition to its load-matrix were provided allowing both, the development of a structural analysis of the floater and a fully-coupled simulation once the hydrodynamic model was also developed.

Once the WT, yaw system and tower are defined by the aeroelastic model, the next logical step within the initial design is the foundation definition. An initial parametric design of a novel concrete floating foundation is presented in addition to a number of stability requirements that are controlled within the parametric design. Finally, the mooring layout an the construction and installation methods are outlined.

At this stage, the floating system is completely defined, apart from the control system strategy. Therefore, a scale model was designed and tested twice to get the needed information to set up, calibrate and eventually validate hydrodynamic numerical simulations of the mentioned experimental campaigns. Numerical models were developed only for the scale model. Even tough full-scale results can be provided by the numerical models, performing the full-scale calculations or scaling up the results is out of the scope except for the natural periods of oscillation results that have been scale-up to facilitate the comparison with standards.

1.8. Aims and objectives

The general aim of this work is to advance the development of the DTI-F concept, a floating substructure able to raise and lower the tower and nacelle set for effective cost reduction during construction, installation, maintenance and decommissioning stages. Specifically, the main aim is to increase the TRL level of the DTI-F concept from 1 to 3.

In the following, the specific objectives for each Chapter are given and the actions taken in order to achieve these objectives are summarised.

1.8.1. Chapter 3: Numerical methods for aeroelastic analysis of wind turbines.

In order to perform the first dimensioning of the floater, the WT to be installed must be chosen. Defining the WT will set the tip weight of the floating system and will allow forecasting the external forces acting on the structure. Excluding wave driven load cases, the main contribution regarding loads in a FOWT is generated by the WT itself. Therefore, the objective of this Chapter is the characterisation of the aero-servo-elastic response of a real large WT: the Levenmouth WT. This involves numerical modelling aiming to:

(i) Understand the coupled behaviour of the Levenmouth WT components

(ii) Build an aero-servo-elastic model of the Levenmouth WT

(iii) Estimate the Levenmouth WT load matrix and compare it with the commissioning results.

The following tasks must be performed, to accomplish the above-mentioned objectives:

(1) Establish the research methodology for building an aero-servo-elastic model based on the design of WTs.

(2) A review of aero-servo-elastic theory, numerical modelling methods and tools for floating wind turbines.

(3) Gather, classify, and process the technical data and parameters of the Levenmouth WT system to produce the required inputs for an aeroelastic simulation.

(4) Set up and run aeroelastic simulations of the critical design load cases previously identified by Offshore Renewable Energy Catapult staff.

1.8.2. Chapter 4: Baseline design.

The primary objective of this Chapter is to establish the new design of the floating substructure by using a parametric approach. It is proposed that the original design would improve by:

(i) reducing the draft of the substructure from 80 metres to approximately 60 metres,

(ii) investigating the feasibility of a 100% concrete substructure.

To achieve the above-mentioned objectives, the next tasks have been identified as below:

(1) Establish the research methodology for designing parametrically a floater for a FOWT.

(2) Build a tool to parametrically design the dimensions of the floater while fulfilling static stability and simple dynamic stability requirements.

(3) Include all the specific requirements of the DTI-F concept into the parametric design tool.

(4) Iterate the initial design to reduce the draft of the original steel floater while increasing the weight due to the new construction material by changing the wall thickness of the concrete substructure.

(5) Outline a novel construction method as well as the installation and assembly processes.

Since the initial dimensions of the floater are already established, the first estimation of the natural periods of the floater and maximum pitch angle can be performed. Keeping those natural periods away from wave excitation and the maximum pitch angle within operational conditions is extremely important.

1.8.3. Chapter 5: Experimental methods and analysis techniques for FOWT

The main objective of this Chapter is to characterise the hydrodynamic response of the DTI-F concept by using experimental methods. This part of the investigation aims to:

(i) Establish the guidelines to design, build, test and validate a scale model including the mooring lines.

(ii) Characterise the static, quasi-static, and dynamic response of the floater.

(iii) Identify the optimal mooring-line configuration.

(iv) Establish the performance of the DTI-F concept in regular and irregular seas.

(v) Produce the required data to validate the numerical models of the DTI-F concept with the chosen mooring configuration.

To accomplish the objectives above, hydrodynamic testing of a scale model of a floating wind turbine was performed along with the following tasks:

(1) Establish the research methodology for building and testing a physical model of the DTI-F concept.

(2) Build a physical model of the DTI-F system carrying the Levenmouth WT.

(3) Determine the mass properties of the scale model by carrying out inclination and swing tests.

(4) Determine the axial stiffness of the chain used to scale the mooring lines by performing tensile testing.

(5) Determine the draft, trim and heel values of the free-floating system by carrying out static experiments.

(6) Identify the stiffness of the floating system by performing quai-static tests over the moored system.

(7) Characterise the unmoored DTI-F substructure hydrodynamically i.e. no mooring lines and 'soft' mooring lines, by calculating natural periods, damping ratios and response amplitude operators (RAOs).

(8) Evaluate the advantages and disadvantages of different catenary mooring configurations, i.e. three lines, four lines, and three lines with a delta connection, by comparing natural periods, damping ratios. Use the produced results as a basis for mooring system selection.

(9) Characterise the DTI-F substructure hydrodynamically with the chosen mooring configurations by calculating its RAOs in multi-directional regular seas and the non-dimensional displacements for random seas.

(10) Measure and quantify the hydrodynamic response and evaluate the loading on mooring lines.

(11) Produce the required data to validate the numerical models of the DTI-F concept with the chosen mooring configuration.

(12) Compare the obtained results with previous research and international standards.

1.8.4. Chapter 6: Numerical methods for the FOWT

The primary objective of this Chapter is to develop the numerical hydrodynamic models of the DTI-F and to validate them using the experimental results obtained in Chapter 5. In addition, an accurate 3D computer-aided design (CAD) model and a mass model will be developed in order to characterise the mass properties and stability features of the system. This part of the investigation aims to:

(i) Understand the coupled behaviour of the DTI floater and mooring lines.

(ii) Build numerical models matching the experimental response of the floater.

(iii) Simulate the performance of the DTI-F concept in realistic seas.

(iv) Produce a hydrodynamic model able to be coupled with the aeroelastic model developed in Chapter 3 in order to simulate fully-coupled dynamic conditions.

Given the aims stated before, the following tasks have been identified:

(1) Establish numerical models to simulate the coupled hydrodynamic behaviour of the DTI-F system as tested.

(2) Calibrate and validate the numerical model with results from the experiments conducted in the previous Chapter.

1.9. Outline of this thesis

The present work is divided in seven Chapters, each of which deals with a different aspect of FOWTs. After the preamble presented in this Chapter, introducing the increase of energy demand, the wind energy, and how this novel technology has been shifted from onshore sites to deeper locations, the Deepwater Turbine Installation-Floating concept has been presented along with the motivation, scope and objectives of this dissertation.

Chapter 2 provides a review of the literature used in this dissertation to guide, justify and backup the main methodologies employed, and conclusions made.

Chapter 3 deals with aerodynamic analysis. It covers an introduction to wind turbine design, the available simulation tools, a review of some basic concepts regarding aeroelasticity, and the aero-servo-elastic analysis of the Levenmouth wind turbine.

Chapter 4 introduces the key design considerations adopted when developing a FOWT and presents the initial parametric dimensioning of the DTI floater. Construction and deployments strategies are also outlined.

Chapter 5 and 6 develop the hydrodynamic analysis of the DTI-F concept using both, numerical and experimental methods. Chapter 5 gives an insight of the facilities used for the hydrodynamic testing, the scale model design and construction, and the instrumentation employed to record the responses and environmental conditions. It covers all the experimental tests performed over the scale model, the analysis from the raw data to generate the results, and their discussion and conclusions.

In Chapter 6, the numerical developments performed to simulate the scale model of the DTI-F concept are explained along with some notes on wave forces acting on floating bodies. The numerical models are calibrated and validated against the experimental results shown in Chapter 5, and the results are discussed within the context of FOWTs.

Chapter 7 provides a summary of the most important findings and the implications that can be derived from them, and the suggested recommendations for future research respectively.

The overall structure of this engineering doctorate (EngD) dissertation is presented in Figure 1.9.1.

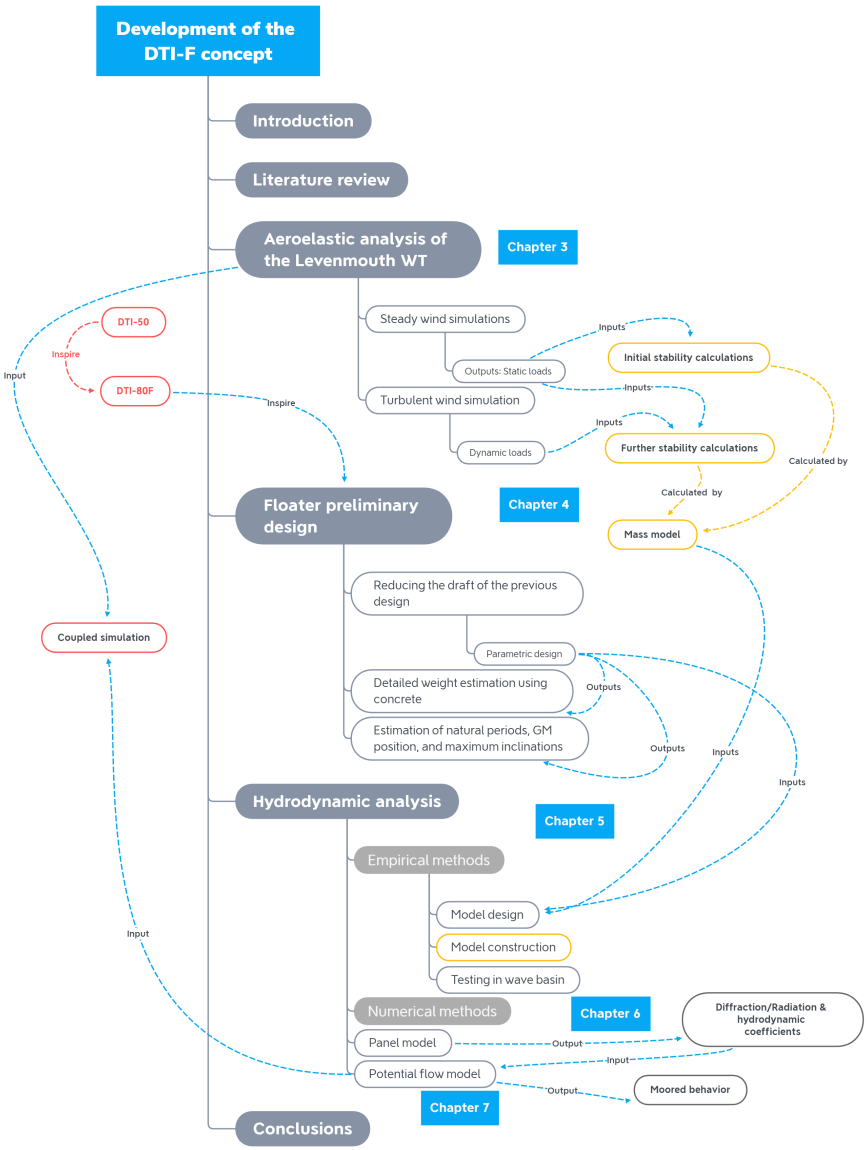

Figure 1.9.1.: Research structure.

1.10. Merits

The following merits have been achieved during the doctoral investigation:

- Offshore Renewable Energy Catapult agreement to have the royalty-free, fully paid-up, non-exclusive license to use its Levenmouth Wind Turbine data for the purpose

of developing an aeroelastic numerical model. Moreover, a royalty-free right to use the results for academic and research purposes was granted.

- Serret, J., Rodriguez, C., Tezdogan, T., Stratford, T., Thies, P.R. (2018). Code comparison of a NREL-FAST model of the Levenmouth wind turbine with the GH Bladed commissioning results. Proceedings of the ASME 2018 37th International Conference on Ocean, Offshore and Arctic Engineering. DOI: 10.1115/OMAE2018-77495. [online] Available at:

- Energy Technology Partnership-Knowledge Exchange Network grant secured to build the scale model

- One week of hydrodynamic testing granted in Lir National Ocean Test Facility through the MaRINET2 transnational access.

- One week of hydrodynamic testing granted in Ocean Energy Research Facility through the 'PhD Test Access' competitive application.

- Serret, J., Tezdogan, T., Stratford, T., Thies, P.R. and Venugopal, V. (2018). Model test of the DTI-Floating wind concept. Proceedings of the 3rd International Conference on Offshore Renewable Energy.

- Serret, J., Tezdogan, T., Stratford, T., Thies, P.R. and Venugopal, V. (2019). Baseline design of the deep turbine installation-floating, a new floating wind concept. Proceedings of the ASME 2019 38th International Conference on Ocean, Offshore and Arctic Engineering.

- Serret, J., Tezdogan, T., Stratford, T., Thies, P.R. and Venugopal, V. (2019). Hydrodynamic response of the deep turbine installation-floating concept. Proceedings of the ASME 2019 99th International Power Conference.

2. Literature Review

As a result of the wind industry moving further offshore, floating wind turbines have become a flourishing technology that has abruptly evolved from being an academic topic to deliver power to the grid. Similarities with the offshore oil industry have boosted the development of such a complex technology, but given that the dimensions, the possible locations, and the profit margins differ so much, specific developments are mandatory for floating offshore wind turbines (FOWT). Besides, the lack of previous long-term experience, the extreme conditions faced by this kind of energy systems, in addition to the necessity of decrease the cost of energy while improving reliability, create the ideal scenario to set up research programs, e.g. MSc, PhD, or EngD dissertations, facing and trying to solve as far as possible each of these issues. The previous Chapter identified the key research problems regarding the immediate development of the DTI-F concept, i.e. aeroelastic characterisation of real large wind turbines (WT), establishing the initial design of the floater, and characterising the new design holding the previously studied WT hydrodynamically from both experimental and numerical modelling approaches.

This chapter gives an overview of the key findings, concepts and developments concerning FOWTs relevant for the present research. By comparing methods and conclusions, it presents how this thesis sits in the background of other work performed in the same field. As stated before, the novelty of the present work lies in the fact that all the calculations consider a new FOWT concept. Therefore, most of the methodologies employed are sourced from international standards and there is no possibility of adopting another

approach unless the specifics of the particular research demand it. However, some developments within the present study are still research topics. In these cases, the discussion will be focussed to demonstrate that the approach adopted is the most suitable for the present work.

2.1. General

In order to understand the necessity for developing floating wind and the constantly increasing rate of energy consumption in the world, a detailed review of international energy outlooks gives the required insight. Organisations like the U.S Energy Information Administration [1], the World Energy Council [2] or Wind Europe [4] among others provide with regular reports analysing the energy consumption and more importantly, breaking down this information in terms of different sources of energy, spatial variation on consumption, and beneficial side effects produced as a consequence of the developments of new technologies, i.e. created jobs, avoided CO2 emissions among several others. These references in addition to others more focussed in the policies allowing the expansion of renewable energies [2, 3], and the ones forecasting possible scenarios [7, 8, 9, 29] provide the researchers with the appropriate framework to start the design of a suitable FOWT, narrowing the uncertainties linked to markets that are increasingly competitive.

FOWTs are complex energy systems including elements as the wind turbine, the foundations, the seakeeping arrangements, the substation connection, the substation, and the transmission to shore and the connection to the grid. Such a system should be studied in a coupled fashion due to the strong interaction between subsystems. Though as stated before, the high levels of complexity is reached when the whole system is coupled, preventing us to perform this kind of studies during the early stages of development. Regarding that, it is easy to find literature explaining the wind energy [30], covering the design of wind turbines [32, 33], and focusing exclusively in FOWTs from a holistic point

of view [30, 31], i.e. as a whole, even though this is a relatively novel research topic. Moreover, abundant literature covers specific topics from a general point of view, but the former will be tackled in its respective Sections.

A relevant metric to assess the level of maturity of a technology is the Technology Readiness Level (TRL) scheme [12]. The concept was first introduced by the National Aeronautics and Space Administration (NASA) agency of the United Stated government and subsequently modified by Lloyd's Register into more convenient floating offshore wind TRL (see Appendix II). TRL metric was employed to define the general aim of this research since the use of TRL gives a standard idea of the current level of development and the level expected to be achieved. It has been found that many of the developments regarding the technical advance of FOWTs does not mention initial and expected TRL levels. Only, large-scale well-stablished public-funded research projects, e.g. LIFES50+, The Carbon Trust, MaRINET2, use regularly the TRL metric and force their beneficiaries to report such levels since it is a requirement when applying to public/research grants. Additionally, there is a debated question as to how to calculate the TRL of a system that has parts at different TRLs. In the present research, the TRL concept has been used from a conservative point of view, i.e. the global TRL of the technology has been calculated as the minimum TRL presented by any of the different parts even though it has multiple TRLs concurrently.

2.2. Aeroelastic modelling of WT

The literature regarding the aeroelasticity is extensive. In the early stages of the wind industry development, concepts from aeronautic or civil engineering were adopted since they gather useful information that can be applied to WT developments. However, the requirements of WTs and specifically of FOWTs, in addition to the fast growth of the wind industry provided the required resources to further develop aeroelasticity methodologies

for the wind and subsequently the floating wind industries.

2.2.1. Basic concepts

The existing literature on generic topics like wind energy, wind turbine design or floating wind [30, 31, 32, 33, 34, 36, 45] links directly with aeroelasticity up to a certain level of detail. The focus of these studies is not the aeroelasticity itself; however, the effects of the aeroelastic phenomena influence some of the subsystems to such an extent that it is not possible to introduce the wind energy topic avoiding basic concepts regarding aeroelasticity such the ones presented in Chapter 3.

Moving a step forward and leaving general aeroelasticity theory, deeper studies regarding different aerodynamic models [38, 39, 41, 42, 43] applied to WT aeroelasticity, e.g. blade element momentum (BEM) theory can be found. [41] presents a comprehensive study on the BEM theory applied to blades analysis, settling down methodologies that have been subsequently adopted by other researchers in their studies, e.g. [39] presents simulation results coupling aeroelasticity based in BEM theory with hydrodynamics, [42] used BEM principles to investigate noise and vibrations at wind farm level, or [43] giving insight on the aerodynamic performance of blades using BEM approach. These methodologies have been successfully calibrated against experimental developments in [38] among others. Therefore, BEM theory is widely accepted and it is the state of art in the industry.

However, BEM theory has some limitations. [48] postulated the generalised dynamic wake (GDW) in order to avoid dynamic wake effects, and [40] extends the research to unsteady conditions and introduces a free vortex wake (FREWK) model while presenting a comparison between BEM, GWD, and FREWK results against experimental data. The results highlight the robustness of BEM techniques consolidating them as industry state-of-art. Other limitations of BEM theory have been investigated [44, 45, 46, 47] to provide with corrections to the BEM theory such as Prandt's tip loss, Glauert, dynamic stall and

tower shadow corrections to name the most relevant and accepted ones.

2.2.2. Numerical modelling of WT

Since FOWTs are a contemporary research topic, there are numerous codes able to deal with the numerical simulation of a WT. In [36, 37], two of the flagships on the development of FOWTs, i.e. National Renewable Energy Laboratory (NREL) and the Technical University of Denmark (DTU), survey the different design tools and numerical models available to design and further develop WTs.

In [36], the authors summarise the existing design tools in terms of the software available. Since the authors belong to NREL, special attention has been paid in enumerate every single possibility of coupling between their FAST code and other numerical models. NREL FAST is a very powerful and flexible glue code capable of simulating many of the possible situations and conditions that a WT system can experiment. However, its maximum strength is the simulation of the aeroelasticity of the WT itself. It is not surprising, that many efforts have been allocated to be able to couple these results with as many different hydrodynamic simulation tools as possible. The last part of the paper lists different projects relating them to the tools used and the validation process they followed to certify the result.

[36] indicates the importance of using potential flow-based solutions that include wave radiation damping when analysing the floater of a FOWT and therefore this approach has been adopted for the present study. It also states the lack of available measured data form FOWTs pointing to the conclusion that more testing and code to code comparison is needed to increase the level of confidence of the numerical models used to simulate FOWT's behaviour.

Reference [37] is a deliverable of the LIFES50+ project. It covers the available hydrodynamic, mooring, structural, and aerodynamic models relevant for the development of the project. This document has been developed by DTU researches with contributions of

the other partners of the LIFES50+ project, therefore it represents a high-quality update of the information compiled in [36]. It analyses the available hydrodynamic, mooring, structural, and aerodynamic models relevant to the development of FOWT development projects as the present research. Regarding that, the paper states how BEM is still the chosen aerodynamic model implemented in most of the integrated tools and how the FEM approach is becoming predominant in the time-domain state-of-the-art integrated tools. Like in [36], the last part of the report is dedicated to the comparison of results, and it also includes an very useful Section on the initial 'pre-design' methodologies.

Both references, in addition of [65, 67], which are considered as standard-like documents regarding verification and comparison between aeroelastic codes, set the master lines followed in Chapter 3 for the analysis, verification and subsequent comparison of the obtained simulations with the Levenmouth WT commissioning results.

Reference [65, 67] constitute the most relevant studies for this work since they set the basis for establishing a standard method to perform comparisons between codes. Especially in [65], the authors perform an analysis involving simulations of a spar buoy concept. Therefore, the major trends considered to accept or refuse simulated results are extracted from this source. These references are going to be further discussed in the next section.

Another relevant element to consider when simulating aeroelasticity is the design load cases. This is part of the main topic developed in the International Electronic Commission (IEC) standards [61, 62]. [61] refers to land-based WTs whereas [62] extends its recommendations to all the aspects regarding offshore WTs. These references define the different load cases, and when and how must be used to produce results that can be easily compared leading to straight forward conclusions. Depending on the nature of a study, other approaches can be chosen but since the objective of this work is to advance systematically in the TRL of the DTI-F, it has been concluded that following accepted standards is the most appropriate. Regarding that, the IEC is a widely recognised or-

ganisation in charge of publishing standards regarding electrical, electronic and related technologies. Therefore, their recommendations have been adopted as the methodology to define the DLCs tested over the course of this research.

Other significant aspects regarding the aeroelastic modelling are the number and the length of the simulations. Reference [60] from NREL, discusses both topics trying to fill the gap of knowledge regarding operational loads focussing. The results indicate that adequate initial simulation time must be allocated to eliminate start-up transients and recommends a minimum of 60 seconds. The results of the research showed that the length of the wind files did not affect the aerodynamic loads produced in the turbine, as long as the total simulation time is produced by repeating periodically a shorter (ten minutes at the shortest) simulated wind and the total simulation time is kept constant, i.e. a larger number of shorter simulations led to same loads than longer simulation. Although many other studies tackled the topic after [60], no relevant differences regarding the results have been reported. Therefore, and based on the fact that all the conclusions shed in [60] match the recommendations made in the standards, the initial simulation time and the total simulation length were selected based on the results provided in [60].

To perform the aeroelastic analysis of the Levenmouth WT presented in Chapter 3, an extensive amount of non-disclosable data was employed. These parameters were used to build an NREL FAST aeroelastic model. NREL FAST code is extremely powerful in terms of capabilities. However, the lack of visual interface complicates the use of the tool, making the industry opts towards commercial tools like GH Bladed which are user-friendly. Essential references to build an NREL FAST aeroelastic model include [50, 51, 52, 53, 54, 55, 56, 57, 58] covering every single pre-processor or simulator. These documents are published by NREL and define the capabilities and limitations of each module used by NREL FAST to produce final results. These documents present a considerable lack of homogeneity and are not systematic. Few of the mentioned references give a proper theoretical basis on the methods proposed and are limited to a 'how to

use' manual of the specific module. It is noted that the documents are needed to build an NREL FAST model but are insufficient to completely set up a model and there is no other way to solve certain issues than contacting NREL directly or looking for further information in the public forums.

2.2.3. Code comparison

Once a numerical model is built, its results should be compared and validated against other sets of results or experiments.

There is still controversy regarding the use of comparison and validation terms. While some researchers and academics used both terms as a synonym, others argue about the differences between them. Henceforth, the term comparison is going to be used to refer the work developed in Chapter 3, i.e. compare results from two different codes that are verified but there is no evidence of one being more accurate than the other, and validation will be the comparison of results obtained from a verified code against data obtained from field measurements, i.e. the real records of the quantity that the numerical model tries to predict also known as Supervisory Control And Data Acquisition (SCADA) data.

For the reasons explained above, the paramount task that must be performed is to establish the functional framework to compare the results of the numerical model developed with the commissioning results.

The definition of commissioning covers all activities after all components of the wind turbine are installed. Hence, it comprises all the testing leading to the operational stage. It is the most reliable information on the operation of the wind turbine, besides SCADA data. GH Bladed, the industry aero-elastic standard modelling tool, was used during the commissioning of the Levenmouth turbine.

As mentioned in the previous Section, references [65, 67] provide an accepted functional framework to compare the results from different verified numerical model results.

Both are publications lead by NREL although [67] compiles the results of a consortium

including several universities and industrial partners and are considered as standards regarding code to code results comparison.

[65] presents the comparison of the results produced using different numerical models for monopiles with both, rigid and flexible foundations as well as for a tripod support-foundation and a floating spar-buoy WT within the frame of the Offshore Code Comparison Collaboration (OC3) project. In these references, it is shown how irrespective of the type of foundation tackled, comparing two numerical models means comparing the dynamic and steady-state behaviours. Therefore, the eigenvalues from different subsystems, the steady power curves, the deflections in static equilibrium and the power coefficient versus tip-speed-ratio curves should be compared before the dynamic behaviour of the models.

The conclusions of the study present a factual comparison between the different relevant results obtained from the simulation of the different systems studied. However, the most remarkable common conclusion, i.e. irrespective of the type of foundation considered, states that the observations regarding the comparison of different numerical models for monopile concepts are also applicable to the observations made for the tripod support-foundation and a floating spar-buoy WT. Therefore, it must be concluded that the methodology applied during the comparison is satisfactory.

Reference [67] describes the activities performed during the Offshore Code Comparison Collaboration Continuation (OC4) project. As stated before, the research is similar to the one performed in reference

[65] however, the results are not so relevant for the present study since the floater considered is a semi-submersible FOWT.

The references presented above validate both, the choice of NREL FAST as a modelling tool and the approach followed within the present research since it is based on a standard procedure allowing to direct comparison with the majority of the FOWT developments that are also following them.

2.3. Experimental hydrodynamics

Building scale models to test their hydrodynamic responses under a controlled environment as a wave basin or a towing tank is a common practice within several engineering disciplines. The shipbuilding industry tests scale ship models since 1868 when William Froude developed the formula known as the Froude number. The Froude number allows using the results of a small-scale prototype to forecast the behaviour of the full-size maintaining certain quantities as the ratio of water particle to wave velocity, the Keulegan-Carpenter number, and the aerodynamic Lock number.

2.3.1. Tank testing methodology

The experimental developments regarding FOWTs have several similitudes with ship models and oil and gas floating structures. However, the range of scales is so different that specific rules and methodologies must be conducted.

In reference [71], an exhaustive summary of tank testing and data analysis techniques for the assessment of sailboat hydrodynamic characteristic can be found. The focus of the article is not FOWTs, but it gives an overall overview of the process of performing experimental development in hydrodynamics. The paper explains from the pre-testing planning, i.e. model-scale, model construction, and test matrix to the post-test analysis, i.e. model to prototype extrapolation and hydrodynamic modelling, passing through testing setups and tank/basin typical issues. An important part of this work gives the insight to scale effects and typical issues faced when experimental programs must be run, i.e. waiting time, tank turbulence among others. The main advantage of using information from other related industries is that some aspects that normally are not the focus when investigating FOWTs can be relevant for these industries and helps us to consider them properly.

Specific methodologies regarding different experiments can be gathered from [78, 79,

80]. [78, 79] are a Der Norske Veritas-Germanischer Lloyd (DNV-GL) summary on rules and standards and a paper respectively. In [78], there is an exhaustive description of how to perform the lightweight survey and the subsequent inclining tests to obtain lightship displacements, longitudinal and transversal centres of gravity (CoG), and [79] explains the details of a set swing tests performed to calculate the moments of inertia (MoI) of an aircraft. Both documents inspired the solutions and methodologies adopted to test the transversal CoG, height of the CoG from now on, and the MoI of the scale model. No explicit references regarding the realisation of inclining or swing tests for FOWTs have been found apart from references to the fact that the tests were performed. This is due to the fact that these tests are normally conducted by the builder of the model which usually is the same body running the testing capability. Therefore, these activities have been performed in advance to the hydrodynamic testing and the researchers only mentioned that were performed without providing further information on the methodology employed or the results of the testing.

2.3.2. Analysis of experimental data

In order to evaluate the obtained results, e.g. natural frequencies of oscillation, different Der Norske Veritas-Germanischer Lloyd (DNV-GL) standards [68, 87] were employed in addition to papers like [82, 84]. Reference [82] deserve special mention since it is a state of the art paper dealing with the hydrodynamics of mooring systems under static, quasi-static, decay, regular wave, and random wave testing. The paper develops the theory to split the damping into its linear and quadratic components, which is going to be used in the subsequent numerical modelling of the experiments. It is worth mentioning that [82] gives a superb insight into procedures regarding random wave experiments. Reference [84] is also relevant for the analysis of the data obtained during the testing campaign. It presents the results of the regular and random wave tests in terms of RAO. Computing the RAOs from regular wave tests is a common practice. However, the computation of RAOs

from irregular waves and their analysis is still a research topic. In [84], the measured wave and response spectrums were used to compute the response amplitude operator for irregular waves in the frequency domain. The authors believe that response quantified as RAO computed from irregular wave tests is better since testing in more realistic irregular waves helps to identify irregularities in response, e.g. coupled excitation introduced by non-linear forces at periods other than the wave periods.

2.4. Numerical hydrodynamics

The main purpose of numerical simulations is to reduce the number of trial-and-error prototypes by using Computer-Aided Engineering processes. Using Computer-Aided Engineering (CAE) tools, e.g. finite element analysis (FEA), multibody simulations (MBS), the designers may substantially trim prototyping costing in addition to decrease time to market and improve performance and reliability while reducing material costs. This Section will provide an assessment of the state-of-art regarding numerical simulation of FOWTs. It focusses on the simulation of the free-floating wind energy system and the subsequent modelling of the mooring lines.

2.4.1. Hydrodynamic response of a free floater

The hydrodynamic response of a free FOWT can be calculated from different theoretical models.

Published research in [89] shows how solving the Navier-Stokes equations would be the right choice if accuracy is the goal, although linearising such equations is a more reasonable approach for an early analysis of the hydrodynamic response of floating bodies. However, to understand the limitations of the linear method compared with computational fluid dynamic (CFD) calculations, deep insight on the different results obtained with reduced order hydrodynamic models and CFD is mandatory.

Reference [88] investigate these differences for the OC4-DeepCwind semi-submersible concept using the reduced-order hydrodynamic model NREL FAST+WAMIT and Open FOAM CFD. When analysing current interaction results, OpenFOAM properly captures the time-varying nature of the forces acting on the floating body while the reduced-order hydrodynamic model forecasts overestimate the results due to the disregard of the vortex shedding, the shadowing effects, and the difference in drag coefficients between NREL FAST+WAMIT and OpenFOAM. However, when analysing regular wave results the reduced-order hydrodynamic model shows excellent agreement with CFD results since the load contributions from drag are negligible compared to contributions from diffraction.

Reference [84], as mentioned above, has influenced the present research since it presents model testing on a spar-buoy FOWT. The research focuses on the hydrodynamic characterisation of a stepped-spar FOWT and was performed at the University of Edinburgh. Even though the scaling was 1:100, the results obtained during the testing campaign were used as accepted patterns for spar-buoy FOWTs and have been compared with the results of the present investigation.

Another study influencing the present research is reported in [18]. In this case, researchers from the University of Strathclyde performed scale testing of a TLP-concept, i.e. Iberdrola TLP WIND. The scale of choice was close to the one used in this research. Therefore, convergences were expected and subsequently checked. The paper also describes the practicalities of using a software-in-the-loop (SiL) solution to replicate realistic loads in the nacelle by means of a ducted fan fed by the results of an aeroelastic code, e.g. NREL FAST. Since this is the methodology accepted to validate fully-coupled simulations, it is relevant to configure the future work regarding the development of the DTI-F concept.

Reference [82] provides an excellent overview of available calibration techniques. The suggested calibration scheme has been applied to the ANSYS AQWA simulation to get

maximum accuracy matching the testing results.

Reference [82] presents a numerical model validation study using the methodology explained before. The authors retrieve RAOs, added masses, stiffness, radiation damping and quadratic transfer functions (QTFs) from the Hydrostar radiation/diffraction potential code to feed OrcaFlex. The results obtained are comparable with the results of the present research, but the different scheme used by Hydrostar and ANSYS AQWA to calculate the mean wave drift load QTFs, i.e. ANSYS AQWA uses the Pinkster's approximation whereas Hydrostar uses full second-order results, in addition to the fact that [82] studies the response of a wave energy converter justifies the differences.

2.4.2. Modelling and analysis of the mooring line dynamics

Modelling the coupled response of a floating body with the mooring lines attached is a key issue since the response of the floating body is hugely influenced by the seakeeping system. The primary purpose of a mooring line is to restrain the motion of a floating body to avoid damage of the energy export cable and to maintain the desired position. When modelling FOWTs, different mooring types can be considered, e.g. catenary, taut tendons among others. In addition to the type of mooring, the type of floating body interacting with waves also influences the responses obtained. Therefore, using the proper tool that includes the needed models to consider all the characteristics of the floating body to be analysed is paramount.

OrcaFlex is a hydrodynamic software package which enables to perform the analysis of a moored system. The code is accompanied with an exhaustive amount of documentation and it can answer any questions regarding the software functionalities. This documentation is relevant since it tackles some of the procedures that must be followed when performing advanced simulations, e.g. [99, 100, 101, 103].

In the present study, a novel modelling approach has been employed: a hybrid buoy-vessel model. Reference [101] provides the theoretical base and methodology to properly

build hybrid models since they are a relatively new development in OrcaFlex that has suffered from changes since it was firstly released in 2015.

Once the numerical model is built, it must be calibrated to match stiffness decay results. As mentioned before, reference [82] provides an excellent overview of calibration techniques. Specifically, the methodology explained to apply the additional linear and quadratic damping has been also used in the present study with satisfactory results. As mentioned before, [82] presents results regarding a wave energy converter. Therefore, the results cannot be directly compared. However, both the present study and [82] show modelling and response similitudes, and many trends found in [82] have served as a verification for the present results. As expected, the results shown in [82] present a remarkable matching with testing results for decay and regular experiments whereas the level of accuracy decrease for irregular wave experiments. Regarding random waves, the authors presented only short-length time series, e.g. 12 seconds of duration, showing an acceptable fit between simulated and experimental responses. It is worth noting that the authors chose a vessel object to model the floater.

Another relevant work regarding the analysis of the mooring lines dynamics is reference [84]. As mentioned before, the research focusses on the response analysis of a spar-buoy based FOWT. However, the results of the present study must be compared with care since the scale considered, i.e. 1:100 sets a different hydrodynamic regime than the one considered in the present study; therefore the authors chose a buoy object to model the floater. Regardless of the different scale and hydrodynamic regime, the modelling approach is also different than the one used in the present study. The authors used a superimposed motion based on the displacement RAOs plus a harmonic motion, meaning that the motions due to waves are being imposed on the vessel. Using that approach the vessel will affect the motion of the mooring lines but not vice versa. Therefore, the floating structure's motion will follow a steady, repeatable pattern of motions in regular waves as shown in [82].

2.5. Summary

This Chapter discussed the relevant literature used during the execution of the present research to ensure that the approach presented is the most suitable for the present work.

From the above-mentioned literature, it has been extracted procedures and methods to successfully perform the needed tasks to accomplish the aims and objectives listed in Section 1.8. Some of the references give insight into the key findings regarding aeroelastic and hydrodynamic modelling, and a few of them are useful when comparing trends found in the results.

Another important outcome of the Literature Review is the identification of several gaps in the literature that have been addressed in the thesis.

As stated before, the literature concerning the NREL FAST code is necessary but not sufficient to successfully set up an aeroelastic model. Many procedures have to be extracted from the NREL Forum, and in the present case, some of them have been inquired directly to NREL staff. These procedures have been detailed in an attempt to fill the previous gap.

Dimensions, parameters, and results from aeroelastic modelling of real wind turbines are restricted to small and relatively old WTs technology. This thesis has tried to solve this issue as far as possible. However, many of the most relevant information has been kept as ORE Catapult proprietary information due to legal constraints.

In particular, there is a lack of loading matrices from both real and reference WTs. The loading matrix of a WT is the initial information used to perform the subsequent structural analysis of the floater and the optimisation of the tower design. This thesis has investigated into load matrices and even released the load matrix of the Levenmouth WT which will be an extraordinary starting point for many future studies. Another important literature gap identified during the development of the research work was regarding the inclination and swing tests needed to validate a scale model. Only a few studies regarding

FOWTs mention such testing and no mention to procedures employed have been found apart from ship standards. This situation has been addressed by extracting and compiling information from studies from other industries, e.g. aeronautic, that also use these methods within the present study.

Part II.

Modelling Floating Wind Turbines

3. Numerical methods for aeroelastic analysis of wind turbines

3.1. Introduction

This Chapter presents the characterisation of the aero-servo-elastic response of a real large WT: The Levenmouth WT. Since the general objective of this study is to further develop the DTI-F concept, ensuring initial stability of the floater, enabling fully coupled simulations of the FOWT, and providing enough strength to the substructure are paramount. In order to conduct a initial stability analysis for a FOWT, the international standards require to check on the behaviour of the floating structure when it is under steady loads of the wind thrust at rated wind speed. These loads can be obtained with simpler methodologies than an aeroelastic analysis; however, it is worth to highlight that the results obtained with these simpler methodologies turned out 25% lower than the ones obtained with the analysis presented in this Chapter and the difference in loads leads to remarkable differences in the following design, e.g. wall thickness, weight, draft. Besides, the response of the FOWT due to the wind heeling moments in severe storm conditions, and in severe storm conditions during a fault of the yaw system must be investigated. Furthermore, one of the requirements to perform a fully-coupled simulation is to have both aeroelastic and hydrodynamic models ready to be coupled. Therefore, the development of an aeroelastic model of a WT is imperative within the development of the DTI-F concept. It is worth to mention that there was no attempt to perform fully coupled

simulations within the aero-servo-elastic environment since the hydrodynamic database required (WAMIT outputs) was not available. Finally, to perform the structural analysis of the floater, the dynamic load matrix of the wind turbine is needed. Therefore, the procedure used to calculate the dynamic load matrix is going to be explained.

3.2. Wind turbine design analysis

The design of a wind turbine (WT) is subjected to multiple constraints and considerations, e.g. climatic, site-specific, and environmental factors. However, the economic viability is the determining factor in evaluating the success of a new design. A successful wind turbine design should be able to generate electric power at a lower cost than previous designs and its competitors.

The main capital cost associated with FOWT is the turbine itself [29]. Hence, reducing the cost of energy depends largely on minimising the cost of the WT. WT designers explore different solutions to reduce the cost of the individual components of a WT, which eventually will reduce the overall cost of the WT. However, the design must fulfil other constraints in terms of weight, extreme loads resistance, and withstanding cyclic loading, which eventually leads to fatigue damage. In summary, a balance between the costs control and material quality is fundamental during the design process.

The analysis of a WT can be performed following the design steps. Figure 3.2.1 presents a systematic framework establishing the critical design steps for analysing a WT [30, 31].

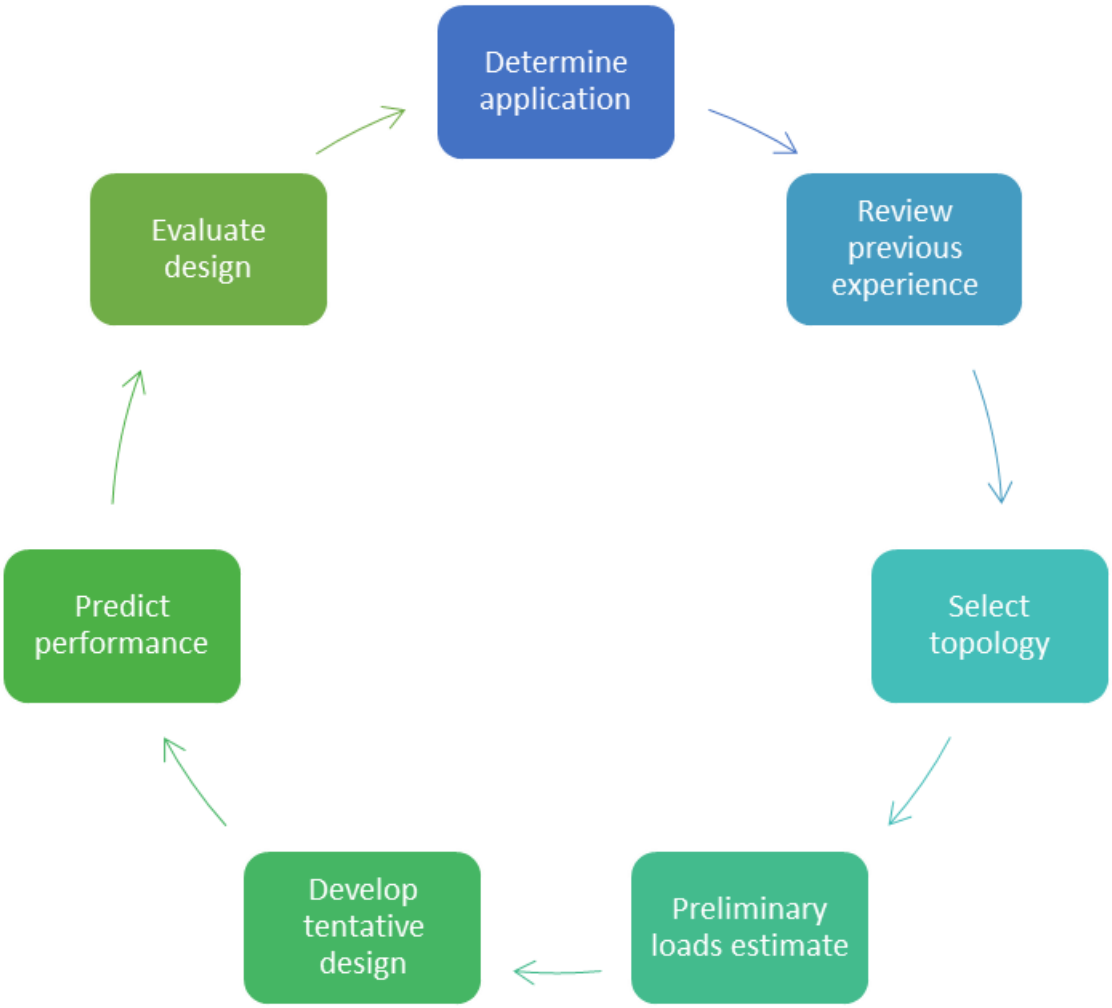

Figure 3.2.1.: Wind turbine critical design steps.

Establishing the function of a new WT is the first design step. Its application will determine the size of the WT, like so, the type of generator, control strategy and so, e.g. large multi-MW WT with rotor diameters up to 200 m are adequate to produce bulk power for supply large utility networks, whereas WTs in the range of few hundreds of kW are better suited to supply remote communities. After determining the application, the next step implies a review of the available literature regarding WTs that has been built for similar applications. There are several concepts already developed, and some of them have extensive testing already performed. A holistic approach considering operation,

maintenance, and servicing is the standard practice for successful developments.

The next step is related to the topology of the WT. The most relevant topologic characteristics of a WT are:

- Rotor axis orientation
- Power control
- Rotor position
- Yaw control
- Rotor speed
- Design tip speed ratio and solidity
- Type of hub
- Number of blades

The most fundamental topological characteristic of a WT is the rotor axis orientation. Although some developments are using vertical axis WT (VAWT), most of the developers choose horizontal axis WT. VAWTs do not need yaw control, and their blades can have a constant chord and no twist. Thus, they can be cheaply built, compared to VAWT. However, they suffer from fatigue-related problems since the angle of attack varies rapidly during each rotation producing abrupt changes in the forces applied on the airfoil and dynamic stall of the blades. The power control strategy is another essential choice. It includes stall, pitch and yaw control, among others, and influences the overall performance of the WT in many ways. The rotor position determines the yaw strategy since downwind rotors allow free yaw strategy. The rotor speed may be constant or variable, and depending on the choice, it will determine the selection of generator, gearbox and transmission system. The tip speed ratio also influences the overall performance of the WT since it is related to the power coefficient, but also with the chord, thickness, and

solidity of the blade which eventually will determine the number of blades. Given a configuration with a constant number of blades, the thickness (and the chord) will decrease as the solidity decreases. Since there is a lower limit for the thickness of the blades (due to structural limitations), the designers reduce the number the blades as the solidity decreases. It is worth mentioning that reducing the number of blades will reduce torques (for a constant power level) and weight while reducing costs. However, by reducing the number of blades, the WT will produce less power, more noise, and a variable polar moments of inertia (MoI) for the yaw mode of motion, so the designer must balance between the advantageous and disadvantages of reducing the number of blades. The number of blades also influence the type of hub. Two-bladed WTs are usually teetering or they use hinges in the hub, whereas three-bladed ones generally employ a rigid hub with variable pitch blades.

Before developing an initial design, an estimation of the loads that the wind turbine must withstand is necessary. The loads acting on a WT can be categorised as steady, cyclic, stochastic, transient or resonance-induced loads. Similarly, the WT components are designed to withstand ultimate and fatigue loads.

With the WT general layout defined along with the load's estimation, a tentative design may be considered. Now the focus moves from the WT itself to the different subsystems and components definition. Once rotor and generator subsystems are defined, the power curve can be envisaged, and with all the components in place, an integrated analysis may be performed in order to evaluate the design. Further description of the different subsystems and components of a WT is beyond the scope of this work since there is an extensive literature [32, 33, 34, 35] covering this fundamental topic.

3.3. Simulation tools

There are several computational techniques available to simulate the behaviour of a WT [36]. It is known that WTs exhibit strong coupling between their subsystems and components.

A wind field interacts with the blades bending them and making them spin. Regardless of the gearing system used, the rotational energy of the rotor is transmitted through the shaft where the elasticity plays an important role. The rotatory motion of the shaft system feeds the generator which interacts with the electric network. This set of loads are then transmitted from the nacelle frame to the tower through the yaw system, which will introduce a new stiffness to the system in addition to the blades and shaft ones.

The tower will receive the resulting loads coming from the nacelle and the loads from the wind field hitting the tower. These loads are strongly affected by the pass-through of the blades while spinning, and again the elasticity/bending of the tower will notably affect the transmission of the loads to the transmission piece, substructure, mooring lines and eventually to the anchoring system for the case of a FOWT.

Moreover, the WT control system manages and oversees the overall operation of a WT. The WT control system consists of a number of computers which continuously monitor the condition of the WT and switches between operational strategies, i.e. standby, start-up, power production, shut-down, shut-down with a fault; to minimise drive-train and structural loads while maximising the energy capture and the power quality.

To simulate the strongly coupled aero-servo-elastic problem explained before, specific simulation tools have been developed [36, 37] such as NREL FAST, GH Bladed, 3DFloat, Flex5, HAWC2, SIMA, and Simpack among others. However, uncoupled simulations are still needed for early developments, and the simulation and validation of the disconnected phenomena are required to get successful coupled results eventually.

Blade Element Momentum (BEM) theory is the most widely used method to calculate

aerodynamic loads. BEM methods are accurate enough and computationally efficient [38, 39]. However, the dynamic inflow models like the Generalized Dynamic Wake (GDW) predict blade loads far better than BEM for specific operations, e.g. yawed operations [40].

The structural analysis must be performed from static and dynamic points of view. Both strategies may be implemented using finite element (FE) or modal analysis. However, the most common approach uses both types of analysis, e.g. NREL FAST uses FE to calculate the dynamic coupled modes (BModes pre-processor) of blades and tower, i.e. cantilever beams, but henceforth it works with the mode shapes, so it becomes a modal analysis. Usually, global and local independent analysis are required, and depending on the nature of the studied phenomena, solid-rigid or flexible motions along with linear or non-linear analysis may be performed.

3.4. Basic aeroelasticity

Full development of the theory behind the aeroelastic phenomena is beyond the scope of this work. However, a summary of the primary aspects concerning BEM theory is introduced below.

As name suggests, BEM theory combines the momentum balance on a rotating annular streamtube passing through a turbine, with the lift and drag forces generated by the different aerofoil sections composing the blade.

3.4.1. Momentum theory

The air flow considered in Figure 3.4.1 always remains within the streamtube boundaries shown in blue. Therefore, two different control volumes are considered: between stations 1 and 2, i.e. before the rotor plane, and between stations 3 and 4, i.e. after the rotor plane.

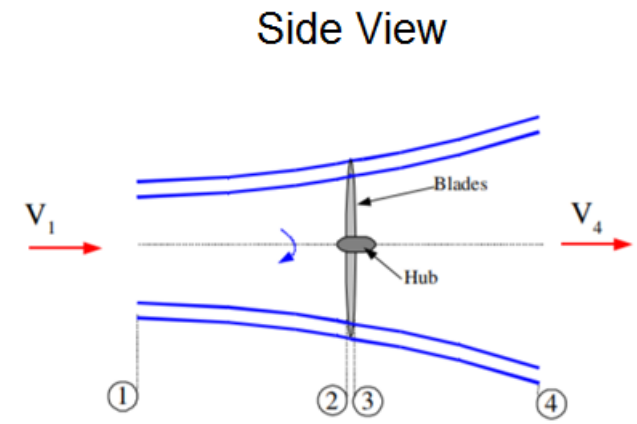

(a) Axial view of the streamtube surrounding a WT.

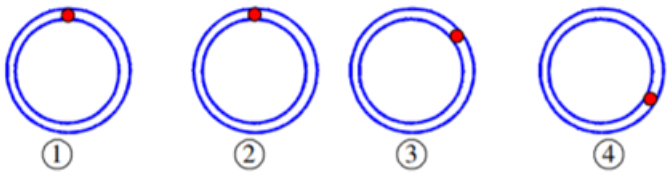

(b) Frontal view of the rotating annular streamtube.

Figure 3.4.1.: Control volumes considered in BEM theory [41].

Establishing the inlet-outlet conservation of momentum and mass conservation through the control volumes, in addition to the assumptions listed below, it can be concluded that the velocity at the rotor disk is the average of the upstream and downstream velocity.

$$a = \frac{v_1 - v_2}{v_1} \tag{3.4.1}$$

- The flow is incompressible and remains in steady-state regime,
- The pressure is equal to ambient pressure far from the disk, i.e. $P_1 = P_4$,
- Exists a pressure jump at the rotor disk with continuous velocity across the rotor disk, i.e. $v_2 = v_3$,

- The flow is frictionless between 1 and 2 and 3 and 4, i.e. Bernoulli's equation is applicable.

By using the axial induction factor (1) defined before, the thrust and power coefficients (2, 3), as well as the Betz's limit (4), can be easily defined as follows:

$$C_T = 4a(1-a) \tag{3.4.2}$$

$$C_P = 4a(1-a)^2 \tag{3.4.3}$$

$$Bentz's\ limit \equiv C_{P,max} = \frac{16}{27} = 0.593 \rightarrow 59.3\% \tag{3.4.4}$$

The axial induction factor (a in Eq. 3.4.1) is the fractional decrease in wind speed observed between the free stream and the energy extraction device. The thrust coefficient (C_T as given in Eq. 3.4.2) is the ratio between thrust and dynamic forces, and the power coefficient (C_P as given in Eq. 3.4.3) is an expression of the power performance. The Betz's limit defines the theoretical maximum power coefficient and it is determined by taking the derivative of Equation 3.4.3. The power extracted by a wind turbine is under the Betz's limit because of the wake, the inexistence of frictionless flow, both mechanical and electrical losses, and the fact that the theory explained above also assume an infinite number of blades.

Considering the rotation of the streamtube control volumes (Figure 3.4.2), the angular induction factor (a') can be defined as it was done previously with the axial induction factor (Eq. 3.4.5):

$$a' = \frac{w}{2\Omega} \tag{3.4.5}$$

Where w and Ω are the wake and rotor angular velocities respectively.

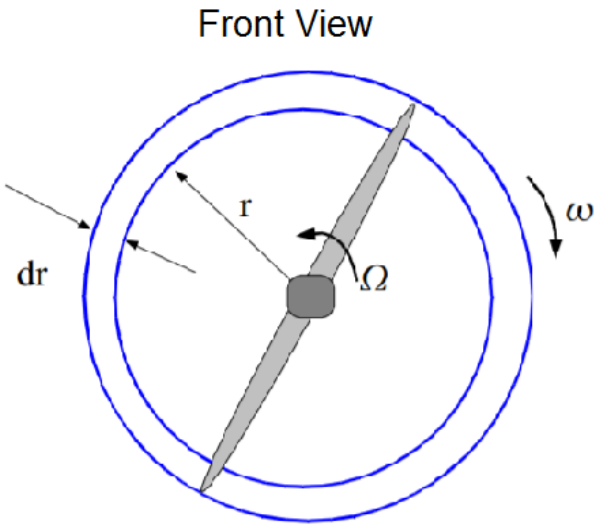

Figure 3.4.2.: Rotating annular streamtube [41].

Therefore, momentum theory yields equations for the axial (dT) and tangential (dM) force on an annular element of fluid, as shown below.

$$dT = 4\rho\pi r V_0^2 a(1-a)dr \tag{3.4.6}$$

$$dM = 4\pi r^3 w V_0 a'(1-a)dr \tag{3.4.7}$$

Where V_0refers to the wind speed.

3.4.2. Blade Element Theory

The Blade Element Theory (BET) considers the flow passing through the blade divided into a finite number of blade elements. Each blade element (Figure 3.4.3) will have slightly different geometry and aerodynamic features, i.e. rotational speed (Ωr), chord length (c), and twist angle (γ') . Therefore, the flow is curved as it passes over the

aerofoil.

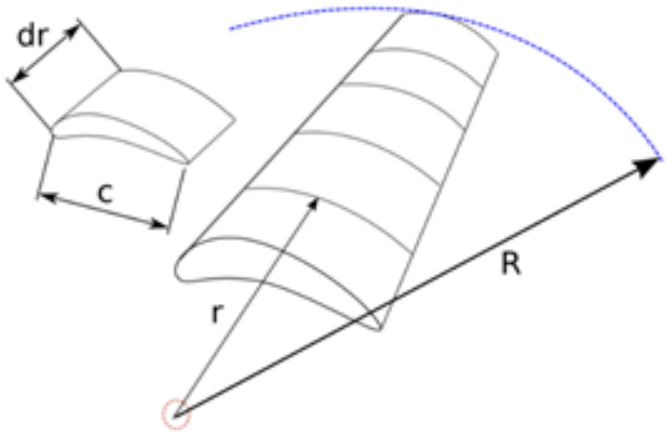

(a) Blade element model.

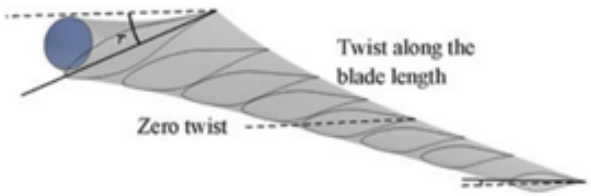

(b) Twist angle along the blade.

Figure 3.4.3.: Blade element model and twist angle along the blade, adapted from [41, 42].

Figure 3.4.4 shows the forces acting on each blade element, where dL and dD are the lift and drag forces. Lift and drag forces are calculated using the lift and drag coefficients (C_L and C_D) which are experimentally obtained for each different airfoil. It is worth mentioning that lift and drag forces are strongly dependent on Reynolds number and the lift provided by the rotational flow. Integrating the axial (Eq. 3.4.8) and tangential (Eq. 3.4.9) forces of all the blade elements along the blade span will lead to the calculation of the overall blade performance.

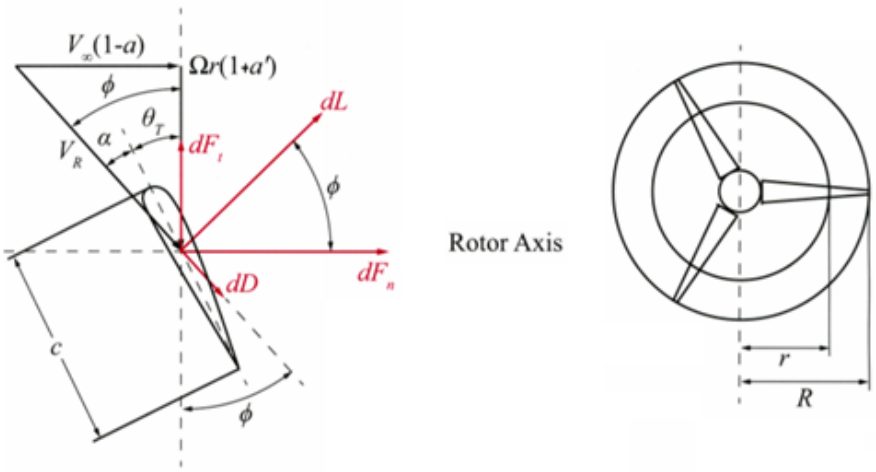

Figure 3.4.4.: Forces acting on each blade element [43].

$$dF_n = dLcos\phi + dDsin\phi \tag{3.4.8}$$

$$dFt = dLsin\phi + dDcos\phi \tag{3.4.9}$$

Multiplying the result of Equations 3.4.8 and 3.4.9 by the number of blades (B), a set of equations for the local axial and tangential forces are obtained. Rearranging them with Equations 3.4.6 and 3.4.7 will allow users to calculate the angle of attack.

Further information regarding the blade design procedure can be consulted in [41], and

the full development of the BEM equations along with the iterative procedure to obtain the angle of attack and subsequently solving the equations can be reviewed in [43].

BEM theory does have many limitations. The BEM method described before requires necessary corrections. The most important ones are:

(1) Prandtl's tip loss effect: This correction accounts for the fact that the tip experiments less aerodynamic load that the rest of the blade since the airflow tends to flow around the tip of the blade from the lower to the upper side (Figure 3.4.5).

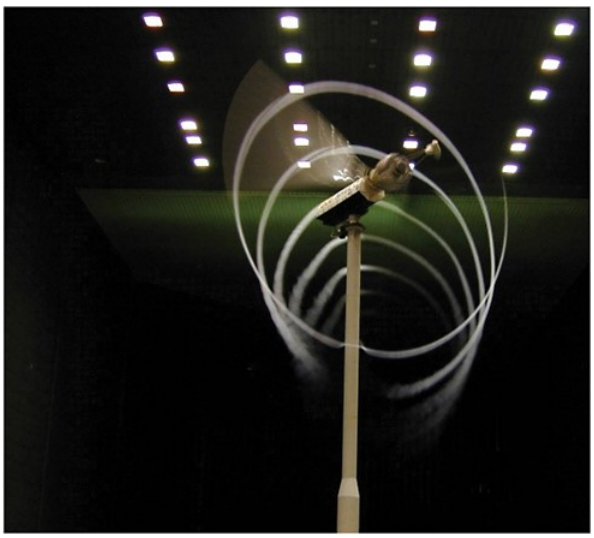

Figure 3.4.5.: Blade-tip vortices showing the swirling wake that trails downwind from an operating wind turbine [44].

(2) The Glauert correction (Figure 3.4.6): It extends the validity of BEM theory to induction factors greater than 0.4.

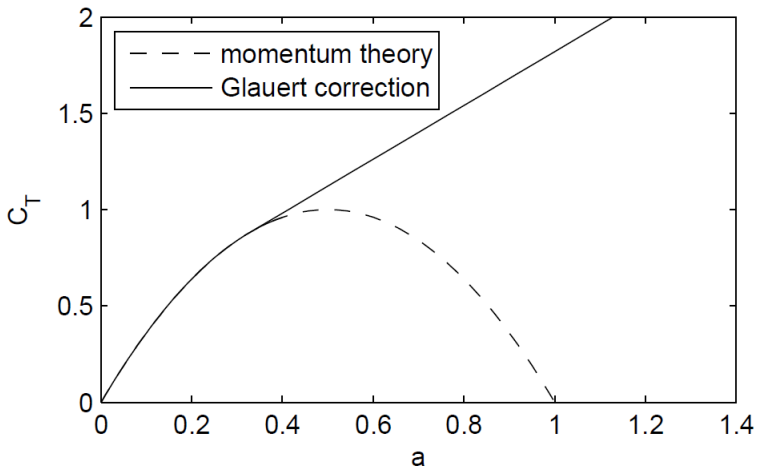

Figure 3.4.6.: Glauert correction [45].

(3) Dynamic wake effect: It comprises adding the required time lag to allow variation of the induction factor when there is a change in wind velocity, rotor speed, or blade pitch. It is related to the shedding and downstream convection of vorticity.

(4) Dynamic stall (Figure 3.4.7): Due to the dynamic wind field, the flow may be suddenly attached, detached, and reattached to the blade changing the value of the drag and lift coefficients experienced by the blades. The dynamic stall correction takes into account a lift coefficient significantly higher than the maximum in steady-state conditions.

Figure 3.4.7.: Dynamic stall of an aerofoil while varying the angle of attack [46].

(5) Tower shadow effect (Figure 3.4.8): It is the consequence of the wind flow travelling around the tower.

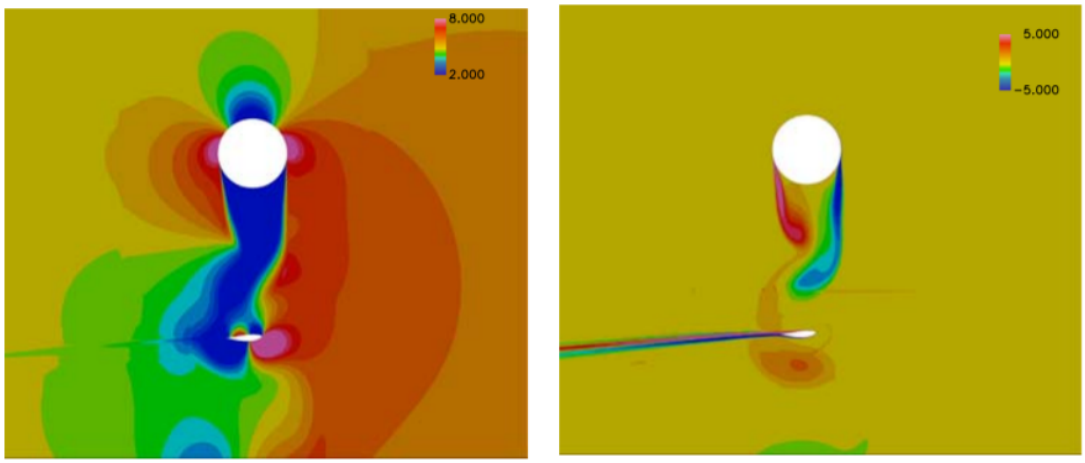

(a) Axial velocity. (b) Vorticity.

Figure 3.4.8.: Snapshot of the axial velocity and vorticity for a tubular tower configuration and the 80% radius blade section showing the shadow effect [47].

There are many other aerodynamic aspects to consider when designing a WT, e.g. during extreme wind velocity events, the drag exerted by the wind on the tower can be significant.

The Generalised Dynamic Wake (GDM) is an alternative method to overcome the issue explained in point 3 above (see Figure3.4.2). It is an acceleration potential method, based on a potential flow solution to Laplace equations. This method improves BEM since includes inherent calculation of the wake.

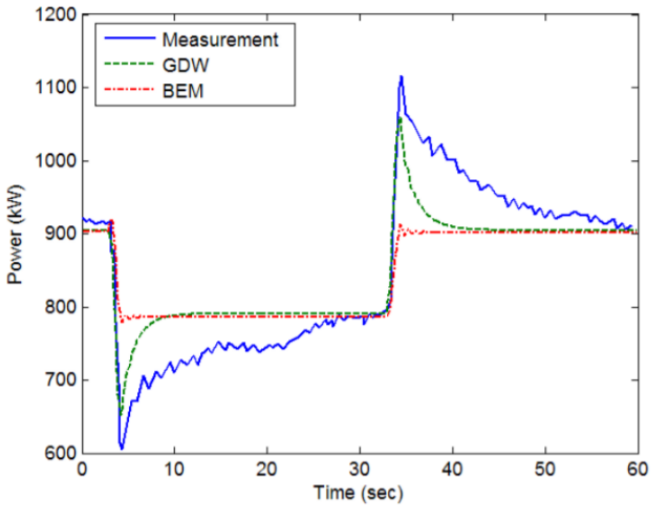

Figure 3.4.9.: Generator power output response versus GDW and BEM models [48].

3.5. Integrated analysis (aero-servo-elastic) of the Levenmouth WT

The ORE Catapult's 7MW foreshore wind turbine is a demonstration wind turbine dedicated to research. It enables testing, verification and validation of future technologies that will help to improve reliability and performance for the next generation of offshore wind turbines. ORE Catapult is working on a project to virtualise their Levenmouth wind turbine. The project's objective is to create a digital 'Clone of the Levenmouth Wind Turbine' (CLOWT) following the recommendations of the IEC 61400-1 and 61400-3 standards. It involves setting up and validating aero-hydro-servo-elastic numerical models for enhanced use of monitoring instrumentation.

The overall aim is to advance the industry's understanding of how large megawatt turbines behave and to identify cost reduction opportunities through design optimisation [49]. This Section is the starting point of this more comprehensive turbine virtualisation project. The aim is to set up an aeroelastic model of the Levenmouth wind turbine and

calculating the Levenmouth wind turbine interface loads using open-source code. The controller set up is out of the scope.

The analysis conducted with NREL FAST v8.16.00a-bjj is verified with the turbine technical specifications and the available Original Equipment Manufacturer (OEM) physical testing. The analysis is also compared to the commissioning results.

The definition of commissioning covers all activities after all components of the wind turbine are installed. Hence, it comprises all the testing leading to the operational stage. It is the most reliable information on the operation of the wind turbine, besides Supervisory Control And Data Acquisition (SCADA) data. GH Bladed, the industry aero-elastic standard modelling tool, was used during the commissioning of the Levenmouth turbine.

It should be noted that a considerable part of the data presented in this Section is either normalised or given without magnitudes to protect proprietary information.

3.6. The NREL FAST simulation tool

NREL FAST [50] is a glue code that uses the results of several pre-processors (e.g. BModes, IECWind, TurbSim and ModeShapePolyFitting), and combines them within several simulations (e.g., ElastoDyn, BeamDyn, InflowWind, AeroDyn, ServoDyn, and SubDyn).

The pre-processors are tools designed for helping to create aero-elastic models. They produce relevant information needed to feed the simulation tools. BModes is a finite-element code that provides coupled modes for a turbine blade or a tower [51]. IECWind is a utility program used to create wind files that model the extreme conditions outlined in IEC 61400-1 and IEC 61400-3 for AeroDyn-based programs [52]. TurbSim is a stochastic, full-field, turbulent-wind simulator using a statistical model to generate time series of three-component wind speed for AeroDyn-based codes such as NREL FAST [53]. Finally, ModeShapePolyFitting is a spreadsheet capable of producing polynomial coefficients for

mode shapes given BModes results.

NREL FAST couples results from different simulations. ElastoDyn is a dynamic structural model able to model the rotor, drivetrain, nacelle, tower, and platform. It computes displacement, velocities, accelerations and reactions from the acting loads taking into account the controller and the substructure reactions. In this research work, ElastoDyn is used to model the blades until the BeamDyn simulator is implemented. BeamDyn is an improved time-domain structural-dynamics module to analyse beams that are made of composite materials, initially curved and twisted, and subject to large displacement and rotation deformations [54]. InflowWind is a module for processing wind-inflow data coming from IECWind or TurbSim pre-processors. AeroDyn is a time-domain module that computes aerodynamic loads of horizontal axis wind turbines [55]. ServoDyn is a control and electrical drive model for blade pitch, generator torque, nacelle yaw, high-speed shaft brake and blade tip brake [56]. HydroDyn deals with the hydrodynamic loading. However, if FAST-OrcaFlex Interface is used, all hydrodynamic and mooring loads will be computed using OrcaFlex [57]. SubDyn is a structural dynamics module for simulating multi-member substructures [58].

3.7. Numerical model description

The system modelled includes three blades, hub, drivetrain, gearbox, generator, nacelle, tower and a jacket substructure. The numerical model accounts for the flexibility of the blades, drivetrain, tower and jacket substructure. Meanwhile, the hub, gearbox, generator, and nacelle are assumed to be rigid bodies. The main undistributed properties of the Levenmouth turbine are given in Figure 3.7.1.

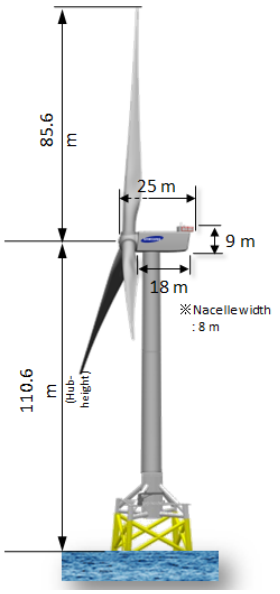

Wind Class	IEC Class 1A
Rotor diameter	171.2 m
Capacity	7 MW
Hub height	110.6 m
Blade length	83.5 m
Generator	Medium (3.3kV), PMG
Converter	Full power conversion
Drivetrain	400 rpm
Rated frequency	50 Hz
Rotor speed	5.9 – 10.6 rpm
Wind speed	3.5 – 25 ms^{-1}
Rated wind speed	10.9 ms^{-1}
Design life	25 years
Certification	DNV
Control System • Independent and collective pitch control modes • Active drive train damping • Active load control • Blade load monitoring	

Figure 3.7.1.: Main undistributed properties of the Levenmouth turbine [59].

The workflow to set up an NREL FAST model is shown in Figure 3.7.2. It consists of the generation of several input files that are going to be called sequentially by FAST. The input files may contain distributed and/or undistributed properties, section properties files (for tower, blades and airfoils), airfoil coordinate records and a controller parameter.

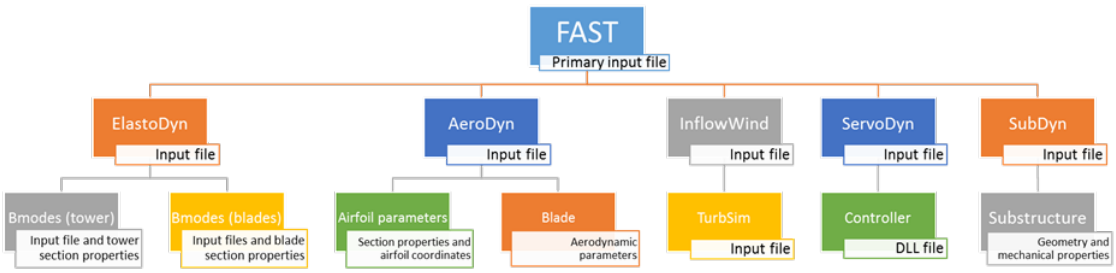

Figure 3.7.2.: NREL FAST simulation workflow.

As stated before, the input parameters and properties are not going to be disclosed to protect proprietary information. However, normalised graphics or graphics without magnitude are shown in Figure 3.7.3, illustrating the most characteristic distributed

properties of blades and tower.

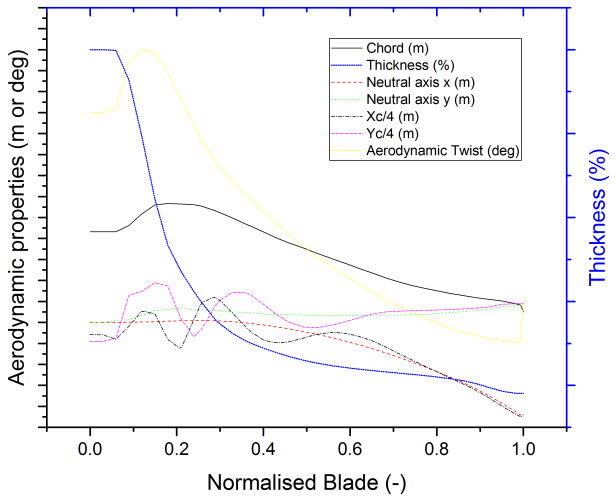

(a) Aerodynamic properties of the blade.

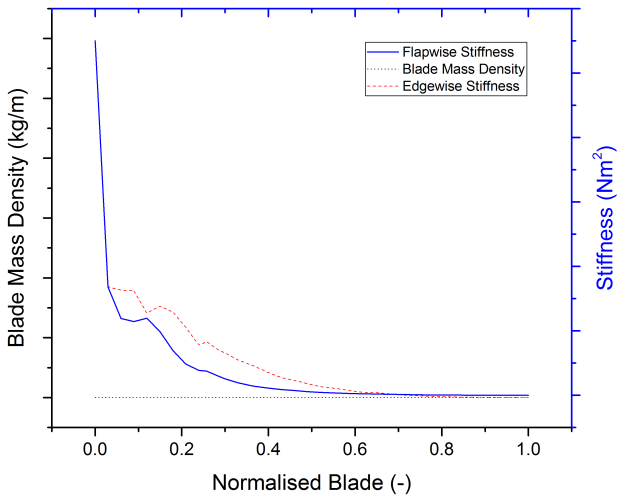

(b) Mechanical properties of the blades.

Figure 3.7.3.: Distributed properties of the Levenmouth WT.

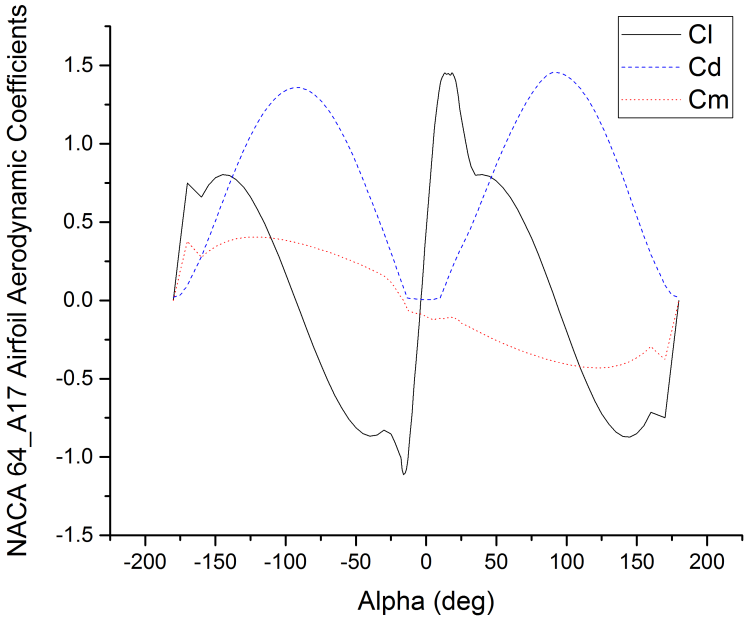

(c) Aerodynamic coefficients of the NACA 64_A17 airfoil.

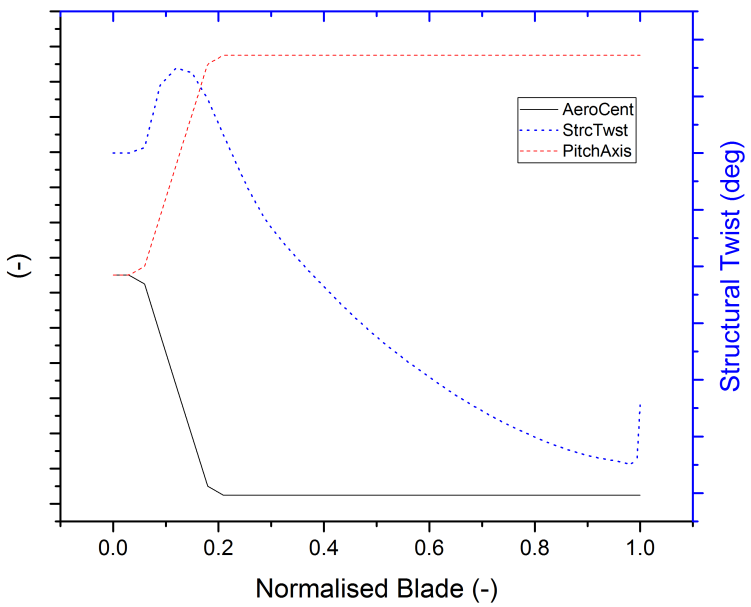

(d) Structural properties of the blades.

Figure 3.7.3.: Distributed properties of the Levenmouth WT.

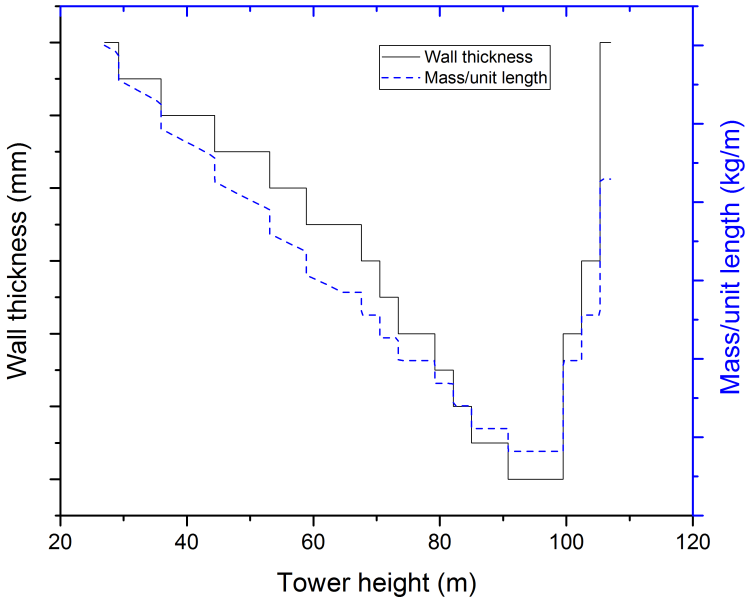

(e) Properties of the tower.

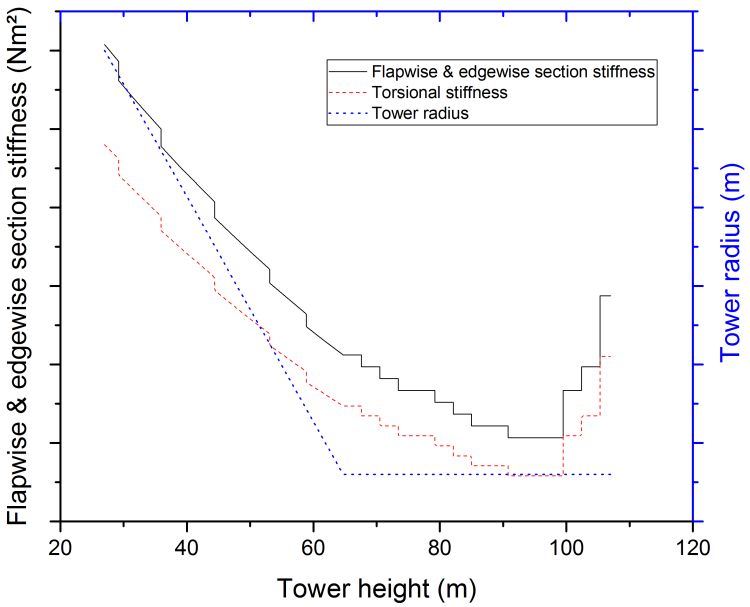

(f) More properties of the tower.

Figure 3.7.3.: Distributed properties of the Levenmouth WT.

3.7.1. Wind

InflowWind manages IECWind and TurbSim wind files to be used by NREL FAST. IECWind and TurbSim simulate non-turbulent and turbulent wind files depending on the design load case (DLC) to be simulated. IECWind and TurbSim meet the conditions outlined in IEC 61400-1 and IEC 61400-3 standards. Steady winds ranging from V_{in} to V_{out} and severe storm wind conditions with and without yaw error were simulated to produce the required inputs for the initial stability analysis. The DLCs considered to perform the aeroelastic analysis of the dynamic loads of the Levenmouth WT are listed in Table 3.1.

The study consists of ninety simulations distributed among the DLCs presented in Table 3.1. Regarding simulation-length requirements, it is important to allow enough initial simulation time to eliminate start-up transients, e.g. 50-100 s. However, it has been demonstrated that the length of the wind file does not affect the loads predicted if the total simulation time remains constant (10 minutes at the shortest). Thus, a larger number of shorter simulations lead to similar results as fewer number of longer simulations, provided that the total simulation time is comparable [60].

Further explanation of the different DLCs considered in this study, will be provided in the results section while analysing the outputs. The most sensitive parameters to set up in TurbSim are the ones related to the wind grid. Table 2 shows the selected parameters for the present study. Complete information regarding the wind conditions, faults and grid loss conditions can be found in the IEC 61400-1 [61] and IEC 61400-3 [62] standards.

Table 3.1.: DLCs considered in this study.

	DLC	Wind Condition	Wind Speed	Grid loss
Power production	1.1a	NTM	$V_{rated+2}$	No
	1.1b		V_{rated}	
	1.1c		$V_{rated-2}$	
	1.3a	ETM	$V_{rated+2}$	
	1.3b		V_{rated}	
	1.3c		$V_{rated-2}$	
PP + Fault	2.2a	NTM	$V_{rated+2}$	Yes
	2.2b		V_{rated}	
	2.2c		$V_{rated-2}$	
	2.3a	EOG	$V_{rated+2}$	
	2.3b		V_{rated}	
	2.3c		$V_{rated-2}$	
Normal shut down	4.2a	EOG	$V_{rated+2}$	
	4.2b		V_{rated}	
	4.2c		$V_{rated-2}$	
Parked	6.1	EWM	$V_{10min,50-yr}$	
	6.2			
	6.3		$V_{10min,1-yr}$	

Table 3.2.: Grid parameters used in TurbSim to generate the turbulent wind files.

NumGrid_Z (-)	41
NumGrid_Y (-)	41
GridHeight (m)	181
GridWidth (m)	181

3.7.2. Aerodynamics

AeroDyn v15.03.00 is the aerodynamics simulator used in NREL FAST. The aerodynamics is the most significant model uncertainty, and it is based on the Blade Element Momentum (BEM) theory. The AeroDyn module requires information regarding the aerofoils, the aerodynamic properties of the blades and the aerodynamic influence of the tower. The aerofoils must be defined in terms of aerodynamic constants and coordinates of the aerofoil shape.

3.7.3. Blades/tower

Within the NREL FAST environment, both blades and tower are considered as cantilever beams. The BModes pre-processor is used to calculate the rotating blade frequencies and the flap (fore-aft) and lag (side-to-side) blades (and tower) mode shapes. The calculated mode shapes are fitted into the ElastoDyn structural simulator by using a sixth-order polynomial. The ModeShapePolyFitting spreadsheet fits BModes mode shapes given deflection data along a flexible non-cantilevered beam. ModeShapePolyFitting offers three different methods to calculate the polynomial. The Projection method has been chosen among the 'Direct' and the 'Improved Direct' methods because a broader range of factors can be specified (i.e. slope and deflection at the bottom of the beam, and a y-scaling factor) to perform the calculation. BModes provides the slope and deflection at the bottom of the beam, and the suggested y-scaling factors were used so that the ratio of the deflection to the beam length corresponds to the exact ratio for a deflected beam [63].

3.7.4. Controller

ServoDyn deals with the control of the machine. The Levenmouth NREL FAST model employs an open-source Bladed-style Dynamic-Link Library (DLL) controller developed at Danmarks Tekniske Universitet (DTU). The DTU controller benefits from a user-

friendly input file allowing the adequate configuration of the controller [64]. The data used in the controller input file is subjected to confidentiality and hence, is not going to be disclosed in this thesis.

3.7.5. Substructure

The jacket substructure has been defined as a multimember structure from the bottom of the transition piece to the top of the pin piles. Therefore, joint positions, members' connectivity, and physical properties of the members must be introduced in SubDyn. The thickness and physical properties of the cylindrical members, which make up the substructure are confidential information and are not disclosed in this study. However, the top and side view of the joint position distribution is presented in Figure 3.7.4.

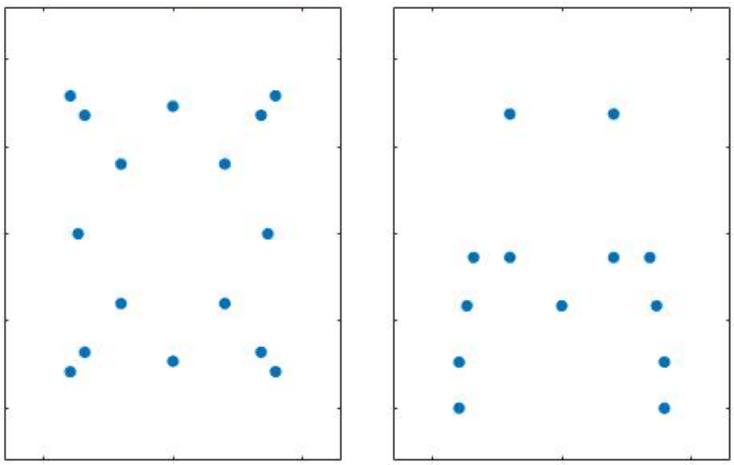

(a) Top view. (b) Side view.

Figure 3.7.4.: Views of the joint position in the jacket substructure.

3.7.6. Known model differences

Although an attempt was made to replicate the conditions used in the commissioning model accurately, there are significant differences regarding both the aero-elastic code and the simulation itself:

(1) The structural analysis method used in GH Bladed is a combined modal and FEM approach, whereas NREL FAST uses a combined modal and MBS formulation.

(2) Aero-elastic theories used by NREL FAST and GH Bladed are different. Therefore, differences are expected between the codes' outputs, e.g. FAST calculates aerodynamic forces orthogonal to the deflected blade, whereas GH Bladed calculates aerodynamic forces orthogonal to the undeflected blade regardless of deflection [65].

(3) Differing model aerodynamic loads discretisation's lead to differences among the code predictions [65].

(4) Due to IP issues, the controller used in the NREL FAST model is not the one used by the commissioning model.

(5) The substructure modelled in this study presents several differences with the substructure modelled in the commissioning ressults. It is 150 tons lighter (Figure 3.7.5), presents a third of the heigth, and the members are thicker when compared with the commisioning setup. As a consequence of these differnces a mismatch between forces and moments forecasted for both systems is expected. Accepted the possible differences in terms of responses, the comparison between the results of this study and the commisioning results allows as to to undestand how this differences are translated into system responses.

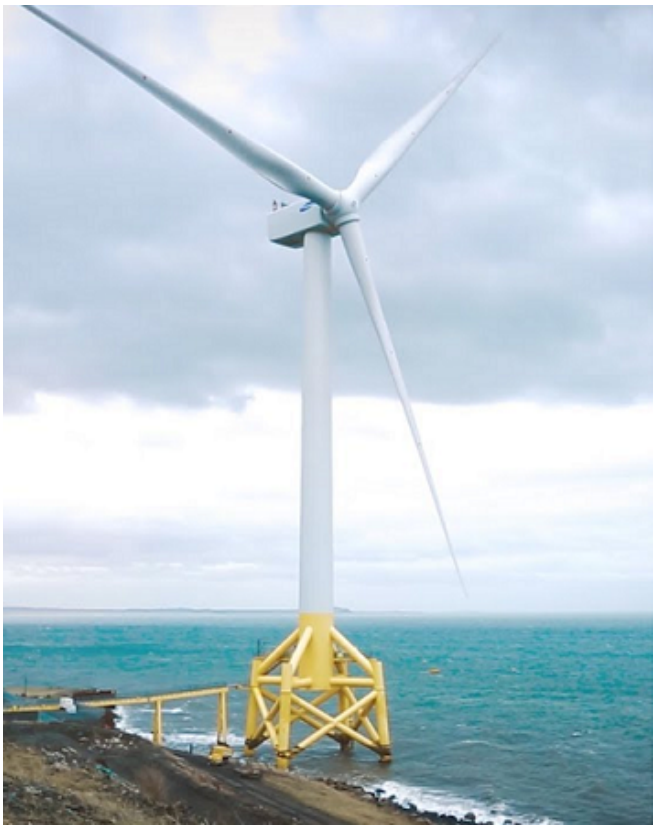

(a) Levenmouth WT.

(b) Commissioning model.

Figure 3.7.5.: Different substructures.

(6) The coordinate axes are different in both aero-elastic codes. The X-direction in NREL FAST corresponds to Y in GH Bladed, the Y to Z, and the Z to X (Figure 3.7.6).

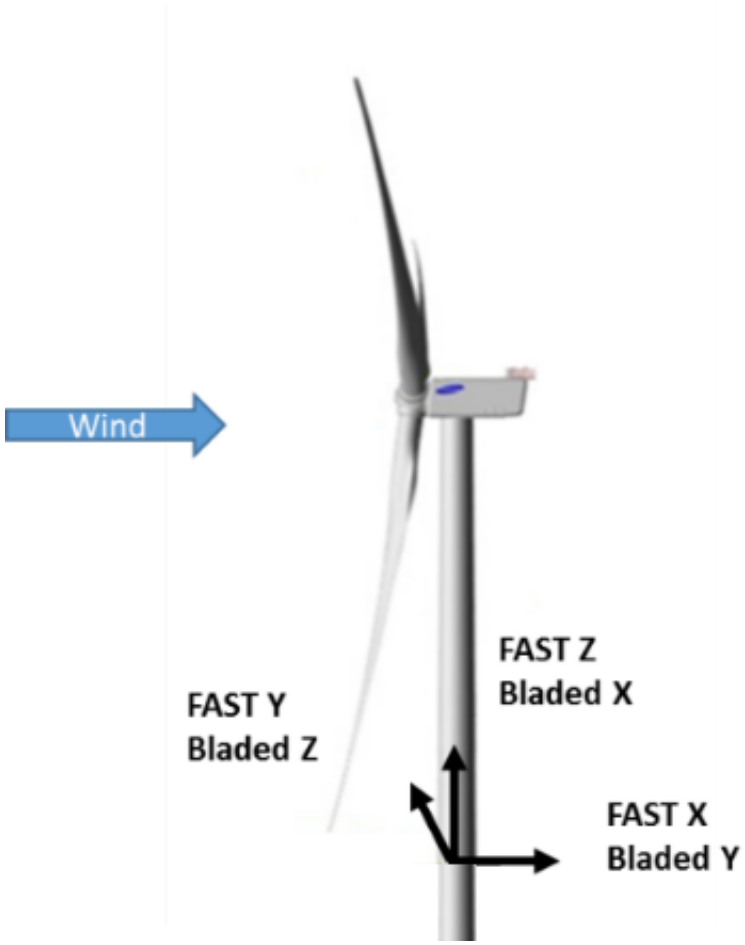

Figure 3.7.6.: Coordinate systems for NREL FAST and GH Bladed.

Existing literature has carried out FAST studies predominantly using reference turbines (e.g. NREL-5MW, DTU-10MW) instead of real prototype or commercial turbines. This Chapter presents the results for the Levenmouth wind turbine, a real, operating demonstration wind turbine. The study reported in this Chapter explores and simulates the critical loads for the turbine, which will be very valuable validation case for industrial and academic use. Moreover, the Levenmouth wind turbine exhibits a new generation of extremely flexible blades that conflict with the previous approaches used by most common aero-elastic codes and makes this simulation a challenge.

3.8. Results

The coupled eigenfrequencies of the tower and the substructure subsystems, and the blade and tower mode shapes calculated by BModes pre-processor are presented in Table 3.3 and Figure 3.8.1, respectively.

Table 3.3.: Coupled tower and substructure eigenfrequencies for the Levenmouth wind turbine.

Mode number	Tower (Hz)	Substructure (Hz)
1st	0.3675	0.7896
2nd	0.3918	0.7896
3rd	1.6466	0.8166

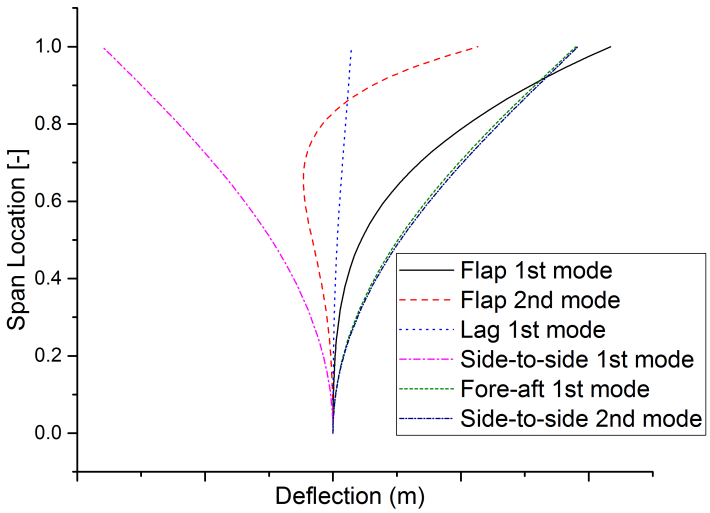

Figure 3.8.1.: Blade and tower mode shapes calculated by BModes pre-processor.

Next subsections present selected results of the DLCs shown in Table 3.1. To build summary and comparison tables, the results of the simulations were averaged over five different realisations corresponding to different seeds.

3.8.1. DLC1.1b

The first DLC considered to check the dynamic behaviour is a regular power production DLC1. DLC1.1b presents the dynamic behaviour of the WT during power production using a Normal Turbulence Model (NTM) at rated velocity and active turbine control. DLC1.1 shows the genuine behaviour of the pitch control, increasing pitch angle when the wind speed is higher and reducing it when the wind moderates. As stated before, further information regarding the DLC conditions can be found in the IEC 61400-1 [61] and IEC 61400-3 [62] standards. Figure 3.8.2 shows the results of the simulation for DLC 1.1b.

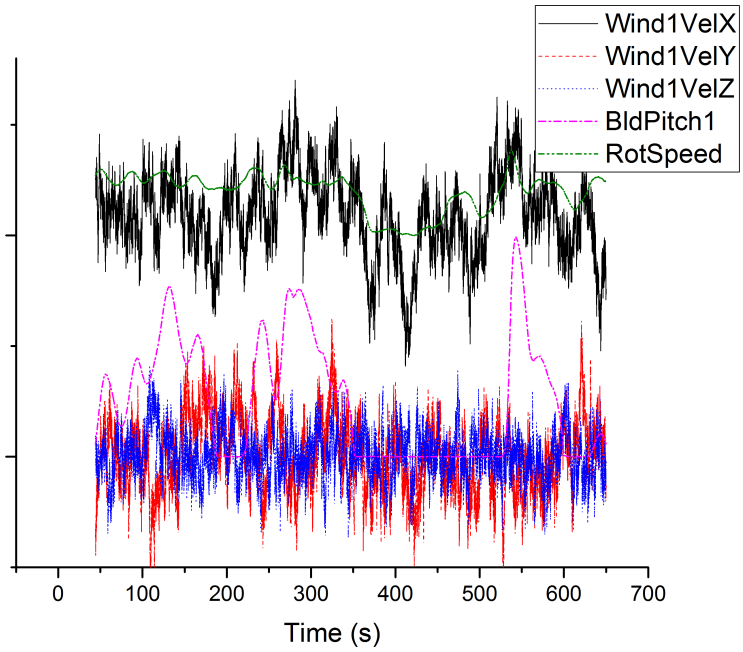

(a) Wind speed (m/s), blade pitch (deg), and rotor speed (rpm).

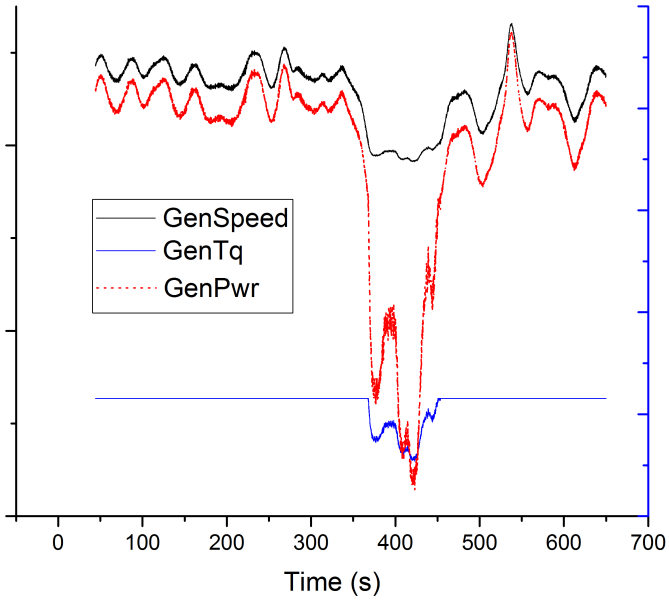

(b) Generator speed (rpm) and torque (kN), and generated power (kW).

Figure 3.8.2.: DLC1.1b results.

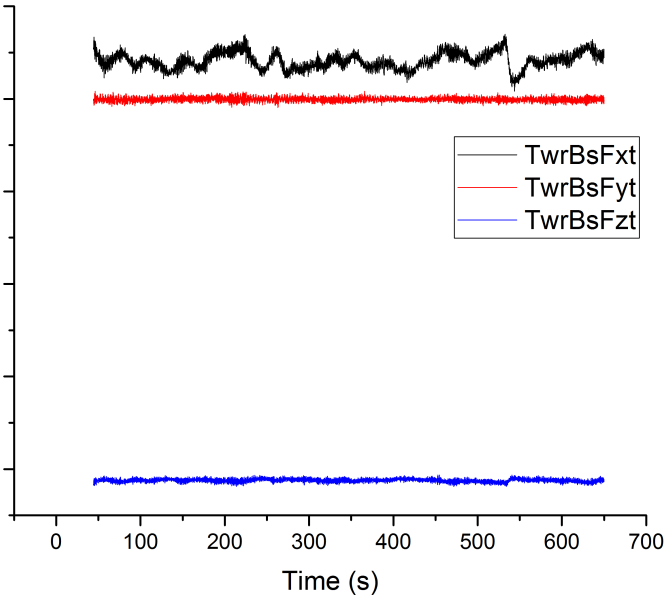

(c) Tower base forces (kN).

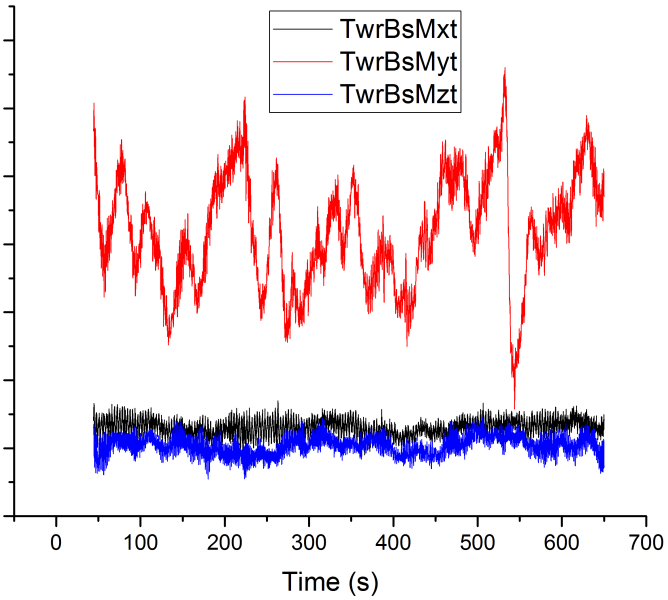

(d) Tower base moments (kNm).

Figure 3.8.2.: DLC1.1b results.

As expected, the rotor speed (RotSpeed) is strongly linked to the wind speed as shown in Figure 3.8.2a. Both are also linked the generator speed (GenSpeed), the generator torque (GenTq) and the generated power (GenPwr) depicted in Figure 3.8.2b. Figure 3.8.2c shows the forces and Figure 3.8.2d presents the moments for the DLC1.1b. The tower base force in the X-direction (TwrBsFxt) shown in Figure 3.8.2c is the primary effect of the wind over the structure, and the force in the Y-direction (TwrBsFyt) is residual since the wind speed in the X-direction (Wind1VelX) is larger than in Y-direction (Wind1VelY). The tower base force in the Z-direction (TwrBsFzt) is the larger in magnitude because it is strongly influenced by the mass of the system. Tower base moments (Figure 3.8.2d) exhibit the same behaviour shown in Figure 3.8.2c, although in the Figure the larger magnitude corresponds to the Y-direction (TwrBsMyt) since this is the moment related to tower base force in the X-direction.

3.8.2. DLC2.3b

Another characteristic structural response is shown in DLC2.3b, which is a power production design situation. It implies non-turbulent wind at rated speed, with the worst extreme operating gust (EOG) transient event expected in a 50-year recurrence period combined with the occurrence of a fault in the electrical system, e.g. grid loss. The timing of these two events was chosen to achieve the worst loading, i.e. $t_{\text{Grid Loss}} = t_{\text{EOG}} + 2.45\text{s}$. The EOG wind condition is a sharp increase, i.e. 6.4 times the wind speed standard deviation, and subsequent decrease of the wind speed occurring over a short time, i.e. assumed to rise and fall over 14 seconds, while the turbine is in operation. In this situation, the turbine pitches the blades to feather, trying to reduce the loads. However, due nature to the nature of the gust loads the control system may not be able to pitch the blades quickly enough to avoid the extreme loading. Figure 3.8.3 presents the results of the simulation.

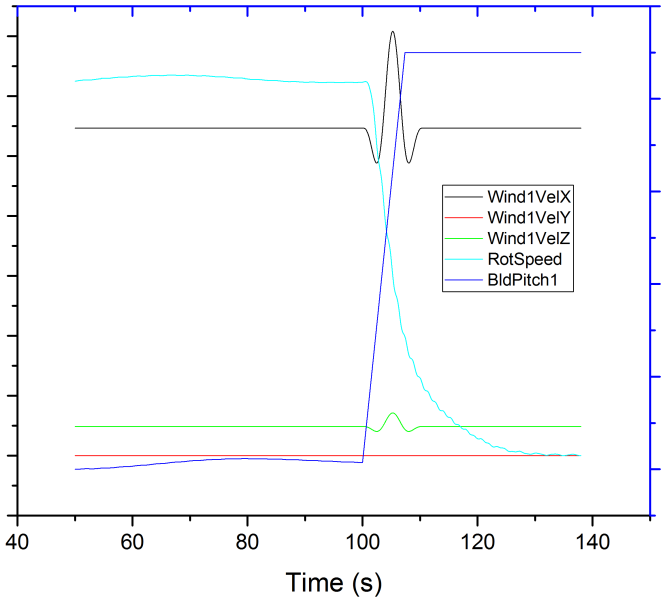

(a) Wind speed (m/s), blade pitch (deg), and rotor speed (rpm).

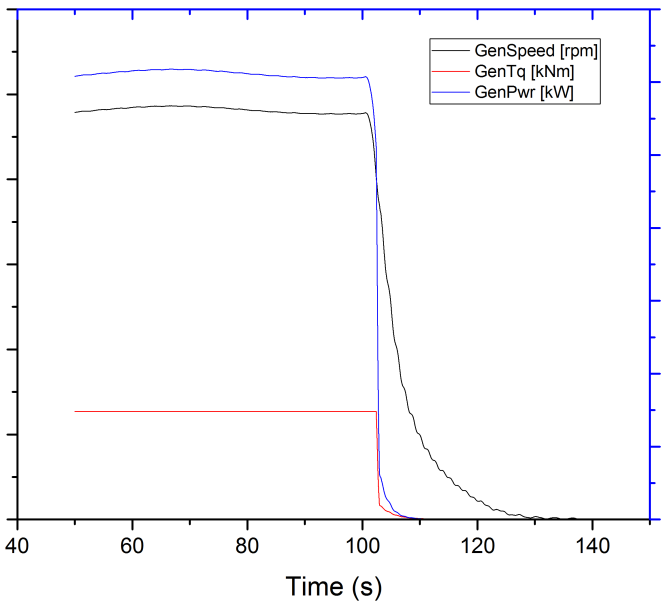

(b) Generator speed (rpm) and torque (kN), and generated power (kW).

Figure 3.8.3.: DLC2.3b results.

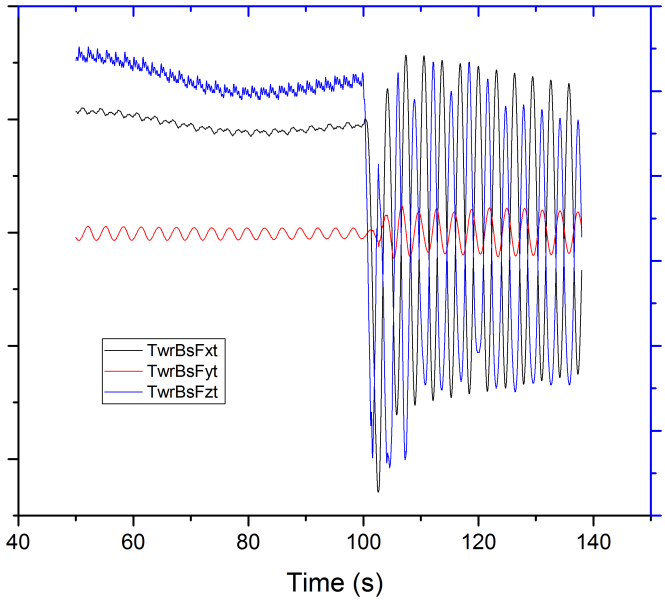

(c) Tower base forces (kN).

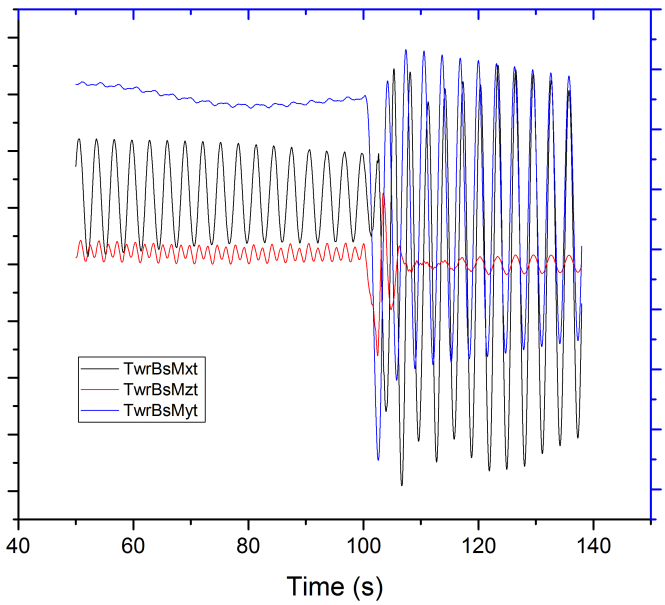

(d) Tower base moments (kNm).

Figure 3.8.3.: DLC2.3b results.

As depicted in Figure 3.8.3a, DLC 2.3 starts with regular power production under non-turbulent wind until the EOG and grid loss events arise. Automatically, the blades pitch to feather, i.e. pitch angle = 90 °, and the RotSpeed and the GenSpeed decrease along with the GenTq and the GenPwr, as depicted in Figures 3.8.3a and 3.8.3b. The wind speed in the three components and the RotSpeed are shown on the black axes, whereas the blade pitch angle (BldPitch1) is shown on the blue one.

Figures3.8.3c and 3.8.3d present the forces and moments at the base of the tower, respectively. TwrBsFxt, TwrBsFyt, and TwrBsFzt are the tower base fore-aft, side-to-side, and axial force along the X, Y and Z-axes, whereas TwrBsMxt, TwrBsMyt, and TwrBsMzt are the tower base roll, pitching, and yaw moment about the X, Y, and Z-axes.

Figure 3.8.3c shows TwrBsFxt and TwrBsFyt on the black axis and TwrBsFzt on the blue axis. Again, TwrBsFxt is the primary effect of the wind over the structure, and TwrBsFyt is residual. The simulation shows a quasi-static behaviour until the events arise. After the events, the structure starts to oscillate freely without the restriction imposed by the grid. It continues oscillating around the origin, i.e. 0kN, whereas the other two components do not. The oscillation presents damped behaviour strongly related to the dynamic characteristics of the system.

Figure 3.8.3d shows TwrBsMxt and TwrBsMzt on the black axis and TwrBsMyt on the blue axis. The behaviour exhibited is similar to the one presented in Figure 3.8.3c, although here the larger magnitude corresponds to TwrBsMyt since this is the moment related to TwrBsFxt. Again, the oscillation pattern is the same shown for the forces, but in this case, the moment oscillating around the origin is TwrBsMzt since it is related to TwrBsFyt.

3.8.3. DLC6.2

To check the dynamic behaviour in extreme winds, the DLC6.2 condition has been chosen. The parked standing still rotor design situation uses a 50-year return period turbulent

EWM extreme wind model (EWM) combined with the loss of electrical network. The DLC6.2 has a $V_{10min,50\text{-}yr} \approx 40\%$ higher than the reference wind corresponding to $50ms^{-1}$ [61, 62] for a Class I wind turbine. Figure 3.8.4 shows the results of the simulation for DLC6.2.

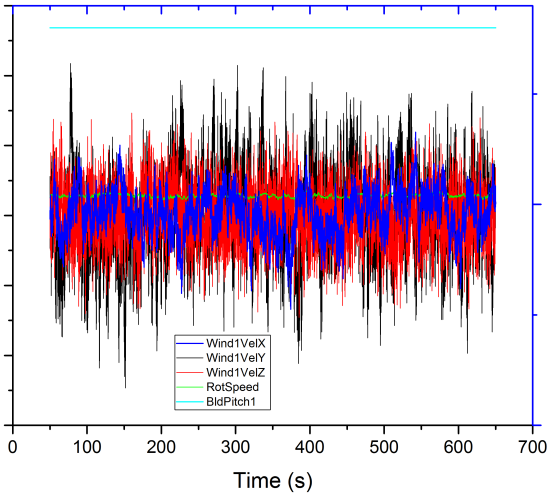

(a) Wind speed (m/s), blade pitch (deg), and rotor speed (rpm).

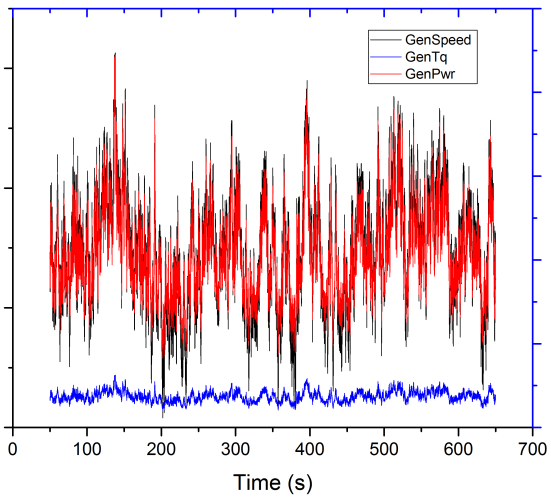

(b) Generator speed (rpm) and torque (kN), and generated power (kW).

Figure 3.8.4.: DLC6.2 results.

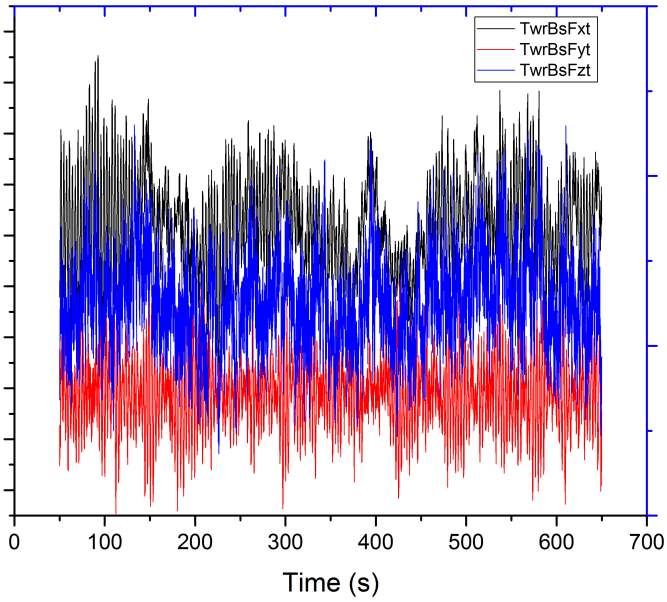

(c) Tower base forces (kN).

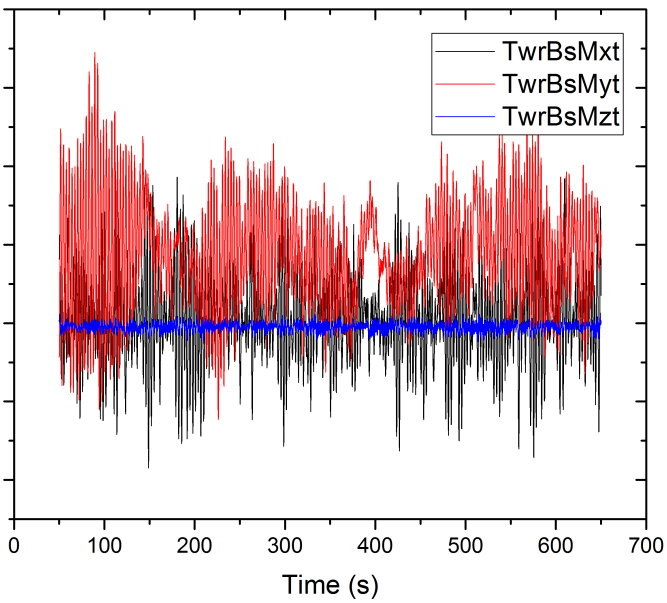

(d) Tower base moments (kNm).

Figure 3.8.4.: DLC6.2 results.

Figure 3.8.4c presents the three wind speeds, the RotSpeed, and the blade pitch angle. Wind1VelY, Wind1VelZ, and RotSpeed are projected on the black axis, whereas Wind1VelX and BldPitch1 on the blue one. Again, the magnitude of Wind1VelX is larger than Wind1VelY and Wind1VelZ, which will determine forces (Figure 3.8.4c) and moments (Figure 3.8.4d) as explained before. It is worth stating that the whole simulation elapses with the blades pitched to feather (Figure 3.8.4a) because of the high-speed wind and the action of the control system. Consequently, RotSpeed (Figure 3.8.4a, GenSpeed and GenPwr (Figure 3.8.4b) remain with low values. Figure 3.8.4b shows GenSpeed on the black axis, whereas GenTq and GenPwr to the blue axis. Figures 3.8.4c and 3.8.4d show the tower base forces and moments. The behaviour of forces and moments is the same as in DLC2.3b. Again, TwrBsMzt is the moment oscillating around the origin since it is related to TwrBsFyt. Forces and moments are high, but not as much as could be inferred from the wind speed since the control system is acting by pitching blades to feather which reduces the loads noticeably.

3.8.4. Summary of loads

Table 3.4 shows the ultimate limit state load-matrix summarising the maximum forces and moments from all the simulations listed in Table 3.1. The elements on the diagonal of the matrix represent the worse situation possible regarding loading, even though the actual combination of loads never occur in a single simulation. Each of the elements on the diagonal is maximum or minimum coming from a simulation based on one of the DLCs shown in Table 1, e.g. 42,625 kNm is the maximum moment in the X-direction, and it occurs under DLC6.2. It is important to note that the values shown in Table 6 are already factorised using the suggested Safety Factor (SF) in [61, 62]. The values accompanying a maximum or a minimum in the same row are the contemporary load results coming from the same simulation, e.g. 15,345 kNm is the moment in the Y-direction contemporary to the simulation DLC6.2 that has produced the maximum located in the diagonal.

On the other hand, the values accompanying a maximum or a minimum in the same column are moments or forces in the same direction but coming from different simulations, e.g. 23573kNm is a moment in the X-direction, but it comes from DLC2.2c.

Table 3.4.: Load-matrix for the Levenmouth wind turbine.

		DLC (-)	SF (-)	Mx (kNm)	My (kNm)	Mz (kNm)	Fx (kN)	Fy (kN)	Fz (kN)
Mx	Max	DLC6.2	1.10	**42625**	15345	-226	653	-543	-8689
Mx	Min	DLC6.2	1.10	**-40689**	34122	-3832	985	518	-8701
My	Max	DLC2.2c	1.10	23573	**149050**	1166	1745	-275	-9050
My	Min	DLC2.3b	1.10	10315	**-248270**	-8159	-2522	-103	-9022
Mz	Max	DLC1.3b	1.35	14540	79582	**19062**	1033	59	-11155
Mz	Min	DLC1.3b	1.35	10500	77125	**-19346**	1018	-153	-11069
Fx	Max	DLC1.3c	1.35	-5107	177795	11883	**2430**	191	-11356
Fx	Min	DLC2.3b	1.10	10315	-248270	-8159	**-2522**	-103	-9022
Fy	Max	DLC6.2	1.10	-40678	34738	-4039	996	**527**	-8686
Fy	Min	DLC6.2	1.10	42625	15345	-226	653	**-543**	-8689
Fz	Max	DLC6.2	1.10	-599	33319	-619	852	20	**-8514**
Fz	Min	DLC1.3c	1.35	341	146610	3237	1898	135	**-11421**

3.9. Verification

The NREL FAST code has been verified in the IEA Wind tasks 23 [66] and 30 [67], but case-by-case verification is needed here. Table 3.5 shows a comparison between the GH Bladed reference values and the eigenfrequencies resulting from BModes to model the mode shape of the blades. The first and second calculated flapwise modes of the blades agree with the referenced values to within 2.1% and 1.7% respectively. The first and second calculated edgewise modes were off by 1.4% and 1.1% respectively. The modes were not tuned.

Table 3.5.: Normalised blade eigenfrequencies comparison.

	NREL FAST	GH Bladed Reference
First Flapwise	0.979	1
Second Flapwise	0.983	1
First Edgewise	0.986	1
Second Edgewise	0.989	1

Since NREL FAST and GH Bladed use a different methodology to calculate tower eigenfrequencies, no further comparison regarding them is presented in this study. Table 3.6 shows a comparison of the mass and dimensional properties calculated by NREL FAST versus the turbine technical specifications.

Table 3.6.: Comparison of the calculated and reference normalised mass and dimensional properties.

	NREL FAST Calculated	GH Bladed Reference
Hub-Height	1.004	1
Flexible Tower Length	0.916	1
Flexible Blade Length	0.997	1
Rotor Mass	0.985	1
Rotor Inertia	1.037	1
Blade Mass	0.973	1
Blade First Mass Moment	1.040	1
Blade Second Mass Moment	1.038	1
Blade Centre of Mass	1.034	1
Tower-top Mass	0.994	1
Tower Mass	1.009	1

The calculated values have shown an acceptable agreement with the commissioning results. The most substantial deviation is found in the calculated flexible tower length, which is off by 8.4%. This disagreement is due to a different definition of the transition

piece in both codes.

3.10. Comparison with commissioning results

3.10.1. Steady-state

A comparison of the steady-state behaviour has been performed by running several simulations with different constant wind speeds ranging from 3 to 25 m/s.

Figure 3.10.1 shows the power curve and the thrust force. The power curve is in good agreement until rated speed, but from there to cut-off speed NREL FAST underestimates the electrical power by 10% when compared with GH Bladed results. NREL FAST thrust force forecast is slightly overestimated on Region 2, getting better in Region $2\frac{1}{2}$, and slightly underestimating on Region 3.

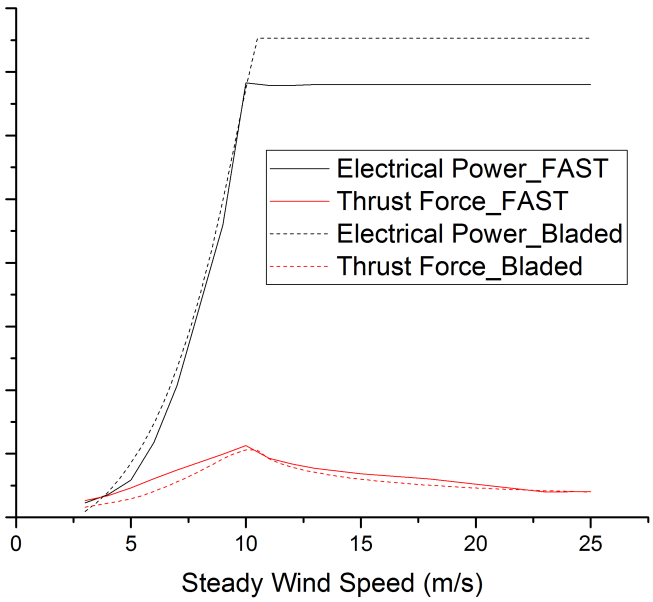

Figure 3.10.1.: Steady-state comparison, generated power and thrust force.

Figure 3.10.2 shows the pitch angle and the rotor speed steady-state behaviour.

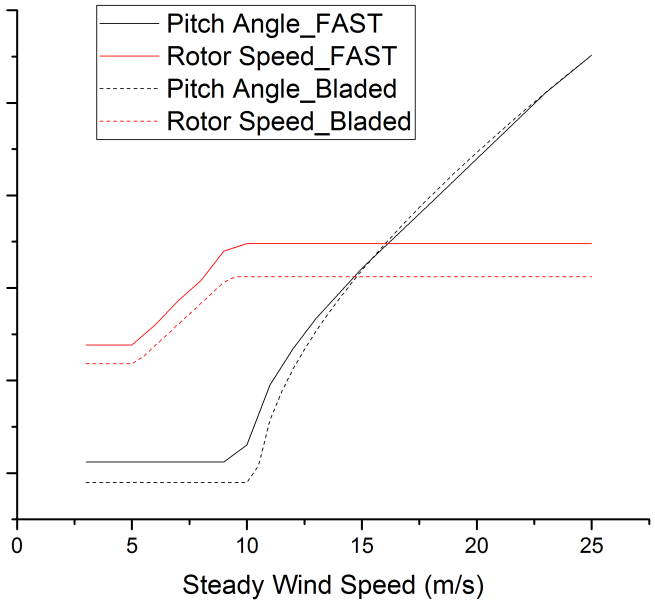

Figure 3.10.2.: Steady-state comparison, pitch angle and rotor speed.

The pitch angle curve fits well when compared with the GH Bladed results. It starts slightly off until Region $2\frac{1}{2}$. Once the rated speed has been reached, the results begin to be closer to the commissioning ones. Rotor speed results are overestimated by NREL FAST. The discrepancy increases as soon as the rated speed is reached, i.e. after Region $2\frac{1}{2}$.

Figure 3.10.3 shows the power coefficient versus the tip speed ratio comparison. NREL FAST and GH Bladed match this curve satisfactorily, although the discrepancy is more substantial at the beginning of Region 3. This behaviour changing between the regions indicates that the inaccurate tuning of the filters of the controller is the primary cause of the discrepancies.

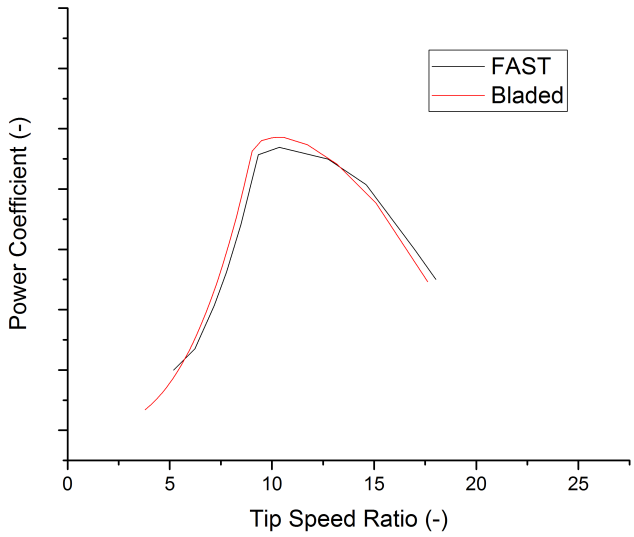

Figure 3.10.3.: Steady-state comparison, power coefficient vs tip speed ratio.

3.10.2. Dynamic behaviour: DLC1.1b

The DLC1.1b shows a good agreement with the commissioning results. Even though it is a complex DLC, the power production simulation reasonably matches the commissioning results.

Figure 3.10.4a shows good agreement between the wind produced by NREL FAST and the GH Bladed simulations. As stated previously, the controller used in the NREL FAST simulation is not the same as that used by the commissioning simulation. Therefore, it is expected that differences would be observed within the controller feature, i.e. pitch angle, rotor speed, generator speed, generator torque, and generated electrical power. The behaviour of the pitch and rotor speed (Figure 3.10.4b) shows acceptable conformity regarding the commissioning results.

It is worth noting that the NREL-FAST overestimates the rotor speed. However, the pitch angle results follow the same general trend than commissioning results. The envelope of the blade pitch angle fits well with the commissioning results, but the in-

herent differences regarding the calculation method and the controller lead to significant statistical differences.

Figures 3.10.4c and 3.10.4d present the rest of the controller results. As expected, the NREL-FAST simulation overestimates the generator speed since this is strongly linked with the rotor speed. On the contrary, the generator torque and the generated power are underestimated by the NREL-FAST simulation.

Since the model has been successfully verified and the wind field matches satisfactorily, the more significant discrepancies regarding forces and moments must be related to the differences in the substructure and transition piece definition, along with the differences in calculation method and control.

Figures 3.10.5a and 3.10.5b show an acceptable matching regarding X and Y-axis forces in the tower base. The discrepancy in the Z-axis (Figure3.10.5c) has its origin in the different definition of the substructure, i.e. the NREL FAST substructure model is 150 tonnes less than the commissioning model.

The same observations made for the forces can be applied to the moments (Figures 3.10.5d, 3.10.5e and 3.10.5f). However, it must be noted that the tower base force in the X-direction relates to the tower base moment in the Y-direction, the tower base force in the Y-direction relates to the tower base moment in the X-direction, and only the tower base force in the Z-direction relates directly to the tower base moment in the Z-direction.

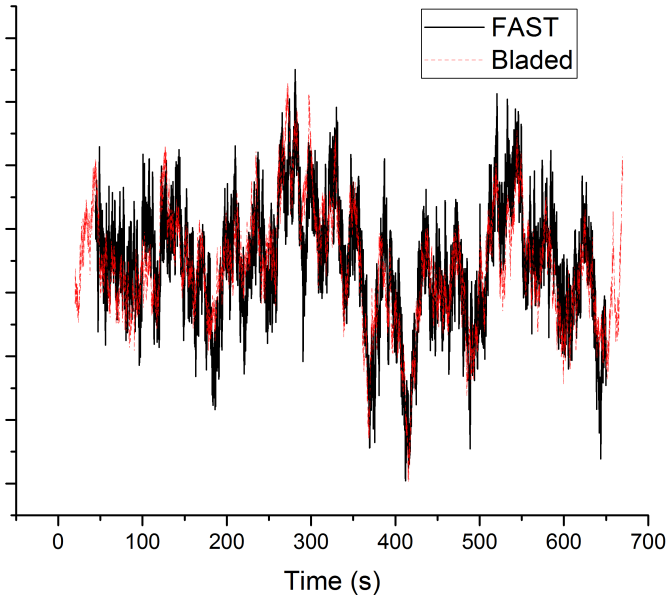

(a) Wind speed (m/s).

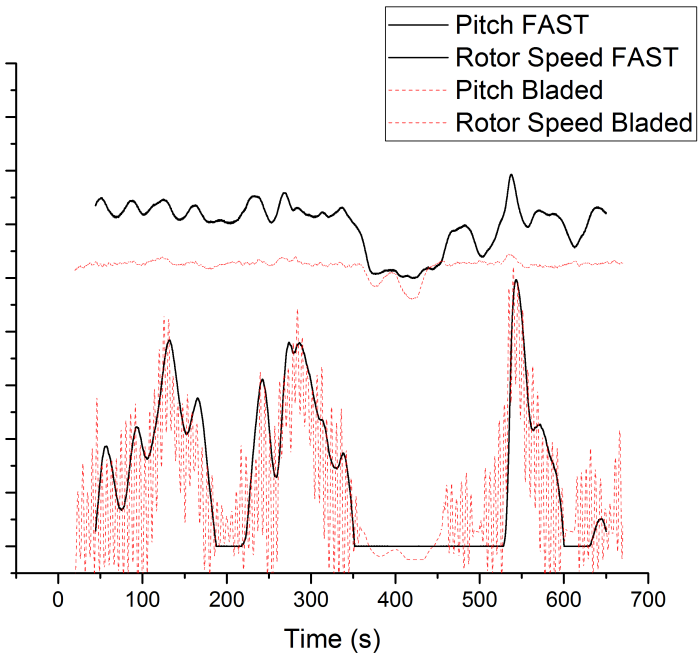

(b) Blade pitch (deg) and rotor speed (rpm).

Figure 3.10.4.: DLC1.1b results comparison.

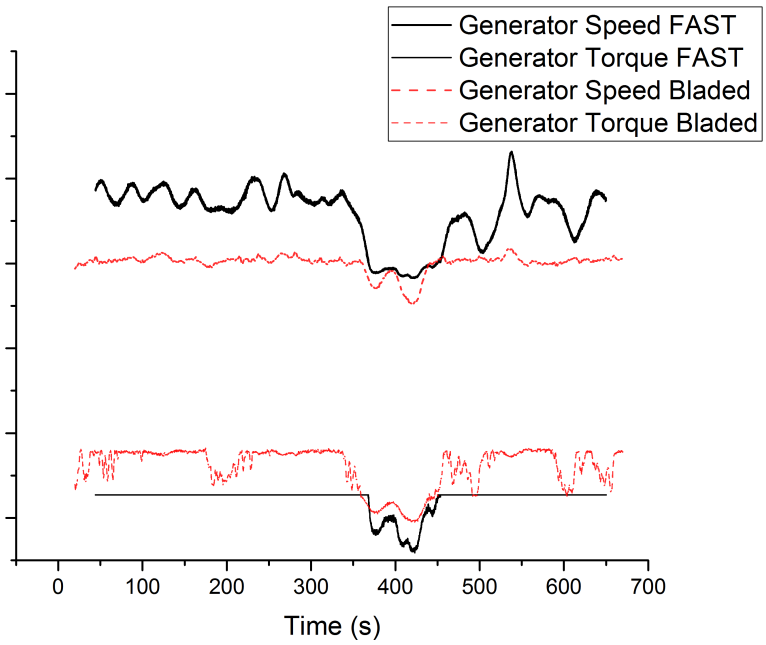

(c) Generator speed (rpm) and torque (kN).

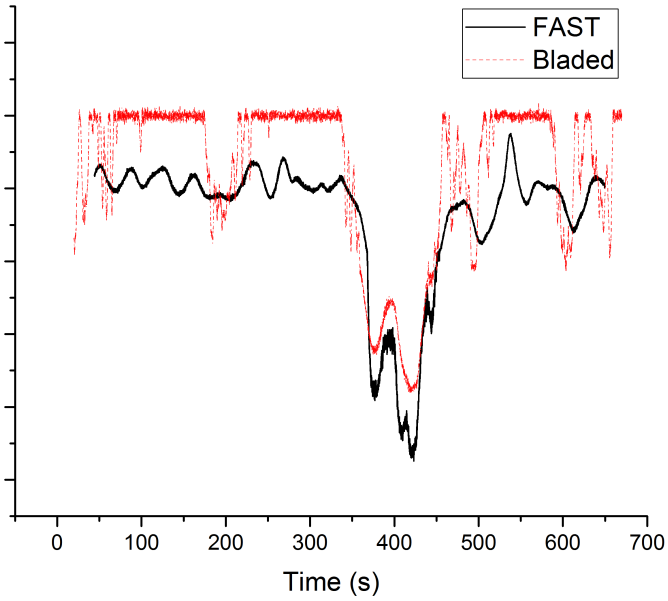

(d) Generated power (kW).

Figure 3.10.4.: DLC1.1b results comparison.

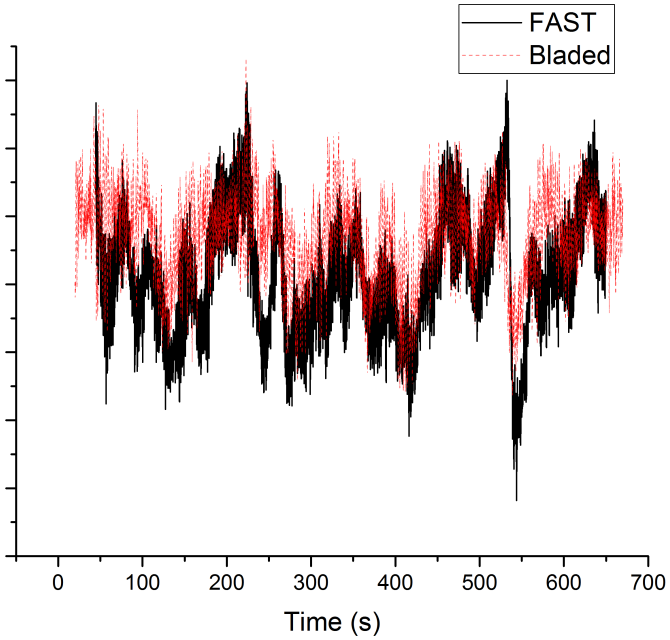

(a) Force in X-direction (kN).

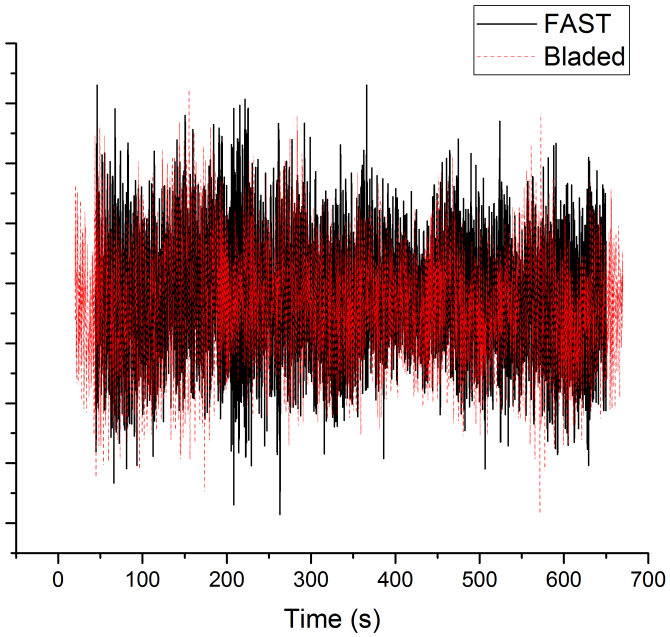

(b) Force in Y-direction (kN).

Figure 3.10.5.: Comparison of tower base forces and moments based in NREL FAST coordinate system.

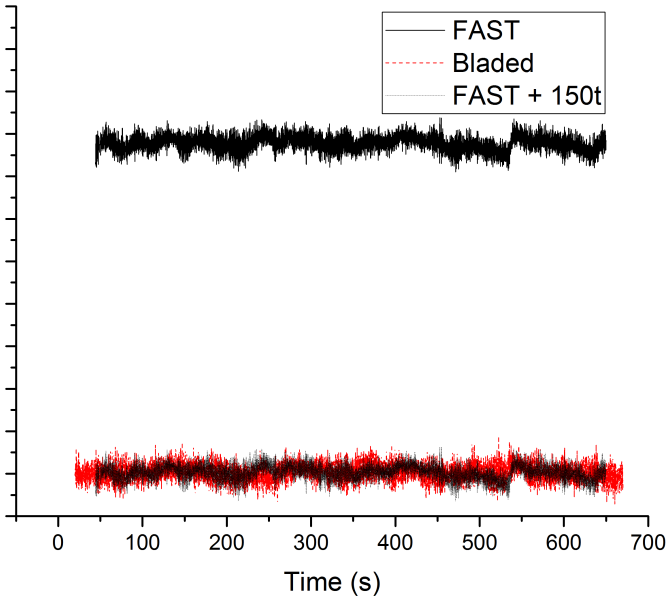

(c) Force in Z-direction (kN).

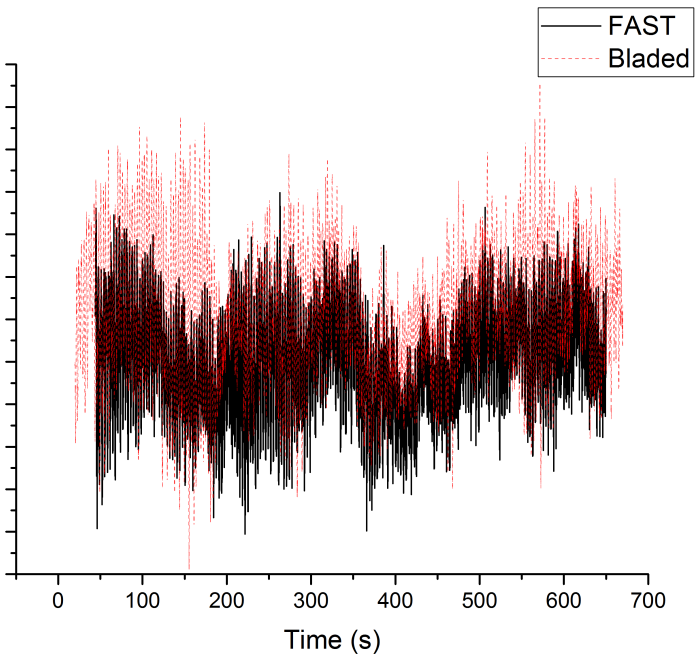

(d) Moment in X-direction (kNm).

Figure 3.10.5.: Comparison of tower base forces and moments based in NREL FAST coordinate system.

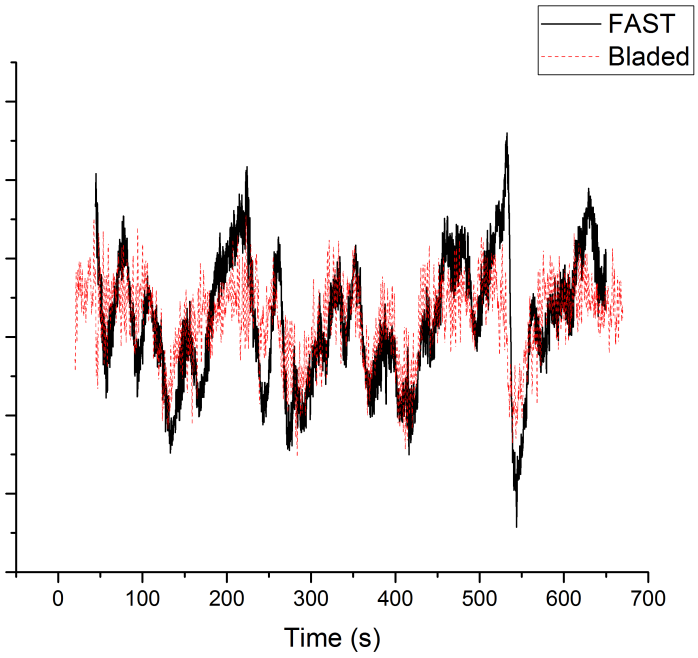

(e) Moment in Y-direction (kNm).

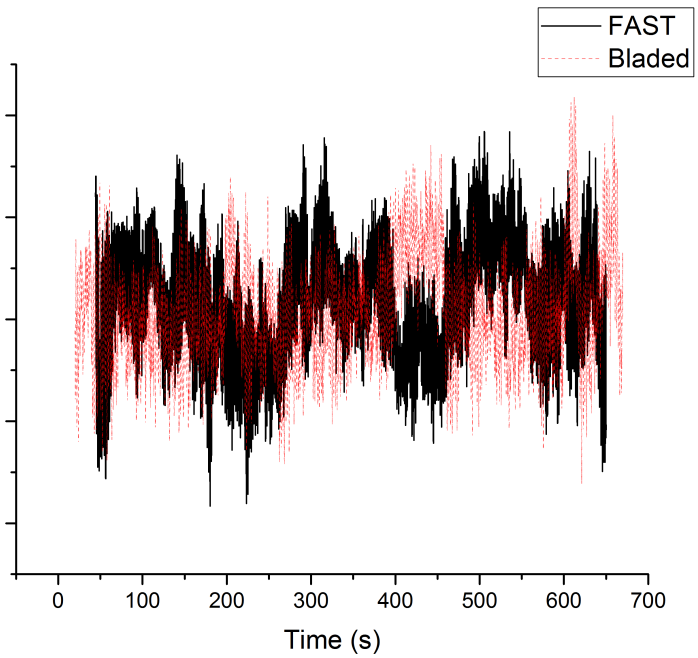

(f) Moment in Z-direction (kNm).

Figure 3.10.5.: Comparison of tower base forces and moments based in NREL FAST coordinate system.

Table 3.7 presents the statistical differences between the NREL FAST results and the GH Bladed commissioning results for the DLC 1.1b.

Table 3.7.: Percentage differences between the NREL FAST results and the GH Bladed commissioning results for the DLC1.1B.

	Mean	SD	Minimum	Maximum
Wind1VelX (ms^{-1})	1.20	4.89	7.73	4.55
BldPitch1 ($^\circ$)	21.57	10.50	0.00	4.62
RotSpeed (rpm)	14.59	24.66	8.50	27.12
GenSpeed (rpm)	14.60	24.70	8.48	27.29
TwrBsFxt (kN)	10.27	44.38	122.57	30.33
TwrBsFyt (kN)	40.09	1.26	43.80	74.55
TwrBsFzt (kN)	15.80	9.52	15.08	17.99
TwrBsMxt (kNm)	26.08	18.42	95.32	6.19
TwrBsMyt (kNm)	1.40	71.62	107.40	71.19
TwrBsMzt (kNm)	86.52	5.40	30.53	12.13
GenPwr (MW)	9.71	14.84	29.80	5.77

There are small differences regarding the calculation method, i.e. TwrBsFxt, TwrBsMyt, acceptable differences regarding the functionality of the controller, i.e. BldPitch1, and the differences regarding the different definition of the substructure. The differences regarding the maximum and minimum values are the result of the combination of the three factors explained before, along with the reduced number of simulations performed for this study.

3.10.3. Dynamic behaviour: DLC2.3b

Figure 3.10.6 shows the comparison of the wind and control features, i.e. pitch angle, rotor speed, generator speed, generator torque, and generated electrical power, between the NREL FAST and the GH Bladed simulations for the DLC2.3b. Figure 3.10.6a shows a good agreement between the wind speeds produced by both codes. The differences

in the obtained data may stem from the differences within the controller feature, as mentioned before. The behaviour of the pitch (Figure 3.10.6b) and rotor speed (Figure 3.10.6c) shows acceptable conformity regarding the commissioning results.

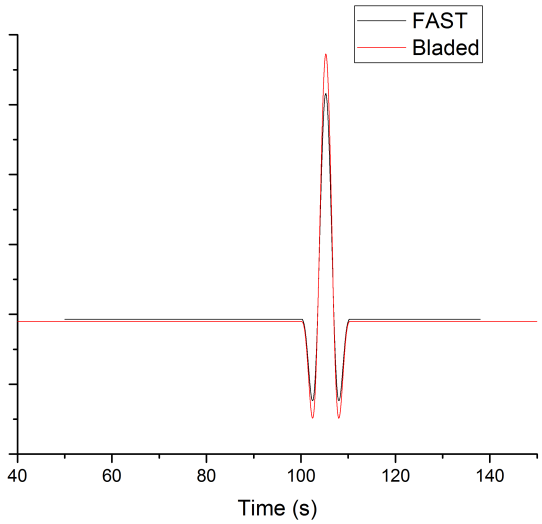

(a) Wind speed (m/s).

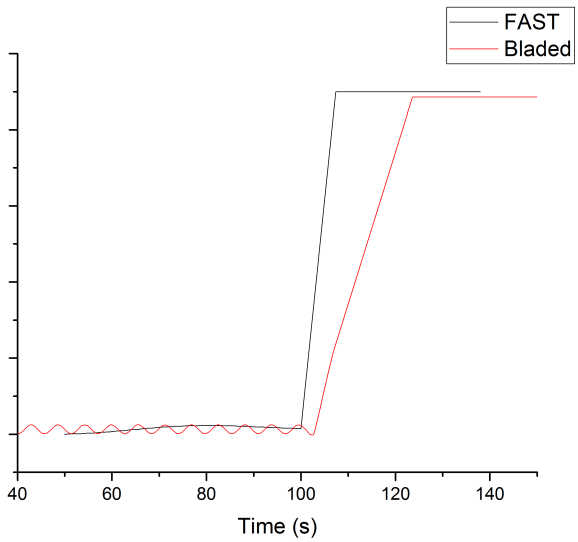

(b) Blade pitch (deg).

Figure 3.10.6.: DLC2.3b results comparison based in NREL FAST coordinate system.

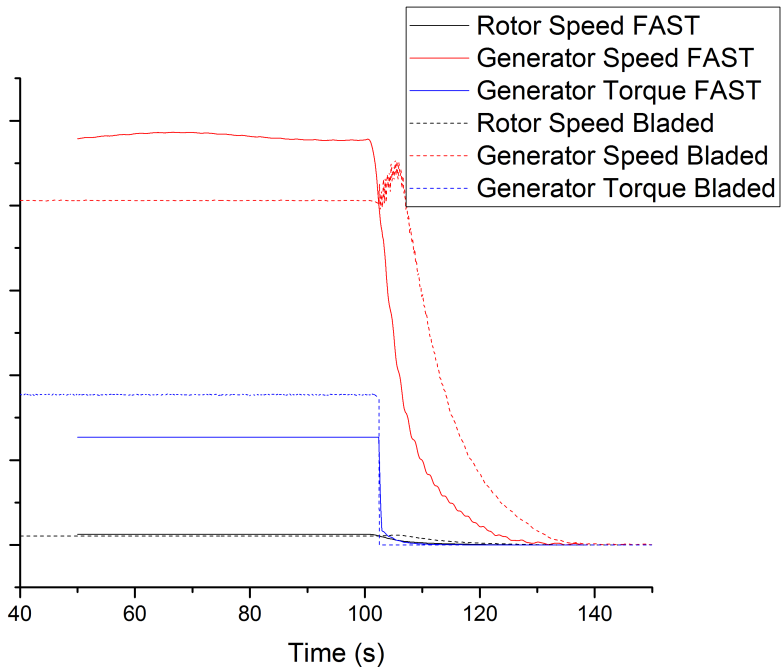

(c) Rotor speed (rpm), generator speed (rpm), and torque (kN).

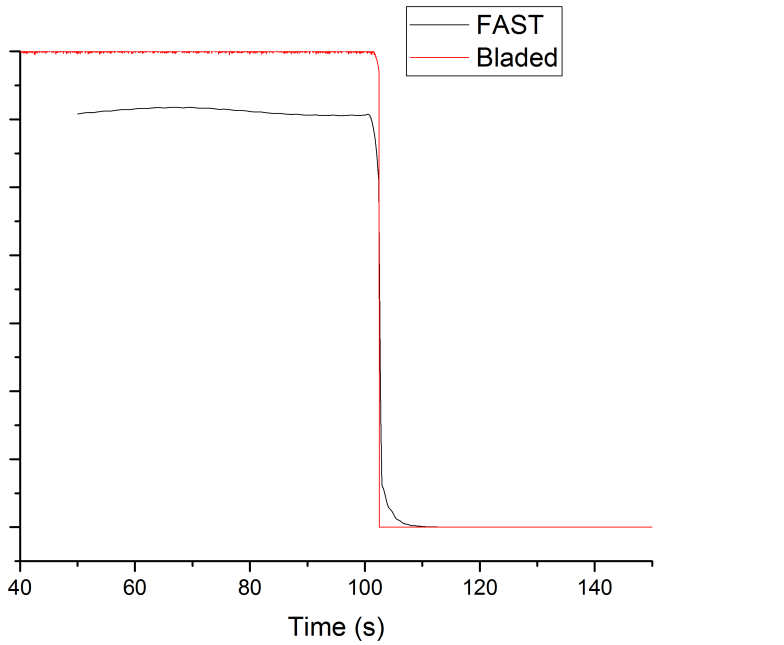

(d) Generated power (kW).

Figure 3.10.6.: DLC2.3b results comparison based in NREL FAST coordinate system.

Although the ramp-up pitch rate and the maximum pitch angle are not equal, the overall pitch operation is a close approximation to the commissioning data. On the contrary, generator speed and generator torque (Figure 3.10.6c) exhibit significant differences regarding the commissioning results, leading to generated electrical power differences, as illustrated in Figure 3.10.6d.

The same comments made for the DLC1.1b regarding forces and moments can also be applied in Figure 3.10.7. Therefore, the more significant discrepancies between the models may be related to the differences in the substructure and transition piece definition, along with the differences in calculation method and control.

The differences regarding the start of the oscillations in both simulations are related to the different pitch rate (Figure 3.10.6b). The differences in the amplitude of the oscillations (Figure 3.10.7a and 3.10.7b) are related to the different structural analysis method. The discrepancy between TwrBsFzt and Tower Fx (Figure 3.10.7c) has its origin in the different definition of the substructure, i.e. the NREL FAST substructure model is 150 tonnes less than the commissioning model.

Table 3.8 presents the statistical differences between the NREL FAST results and the GH Bladed commissioning results for the DLC2.3b.

Table 3.8.: Percentage differences between the NREL FAST results and the GH bladed commissioning results for the DLC2.3b.

	Mean	SD	Minimum	Maximum
Wind1VelX (ms^{-1})	0.29	5.71	2.64	3.84
BldPitch1 ($^\circ$)	16.96	9.47	0.00	1.52
TwrBsFxt (kN)	9.51	44.59	51.87	42.54
TwrBsFyt (kN)	40.00	32.70	37.12	16.55
TwrBsFzt (kN)	15.87	24.42	15.76	16.54
TwrBsMxt (kNm)	24.89	24.82	13.26	5.60
TwrBsMyt (kNm)	7.64	55.08	57.56	56.41
TwrBsMzt (kNm)	242.18	25.14	52.14	124.74

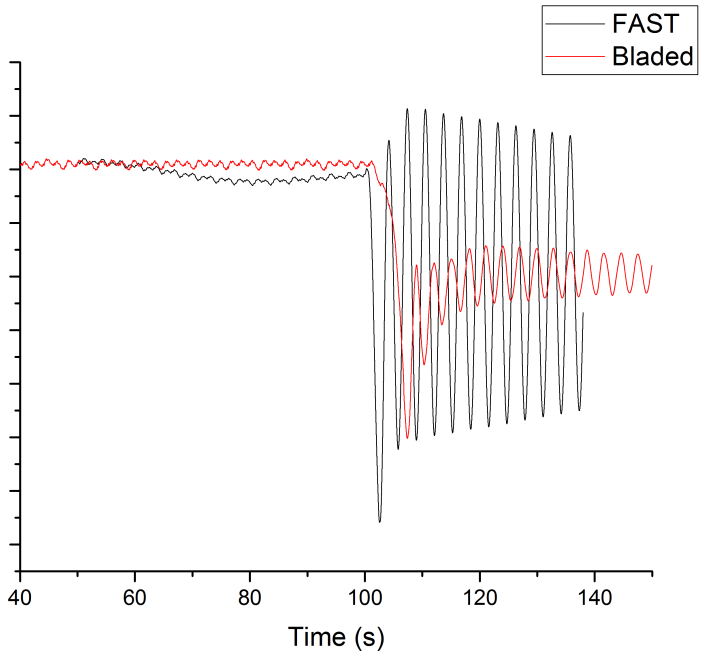

(a) Force in X-direction.

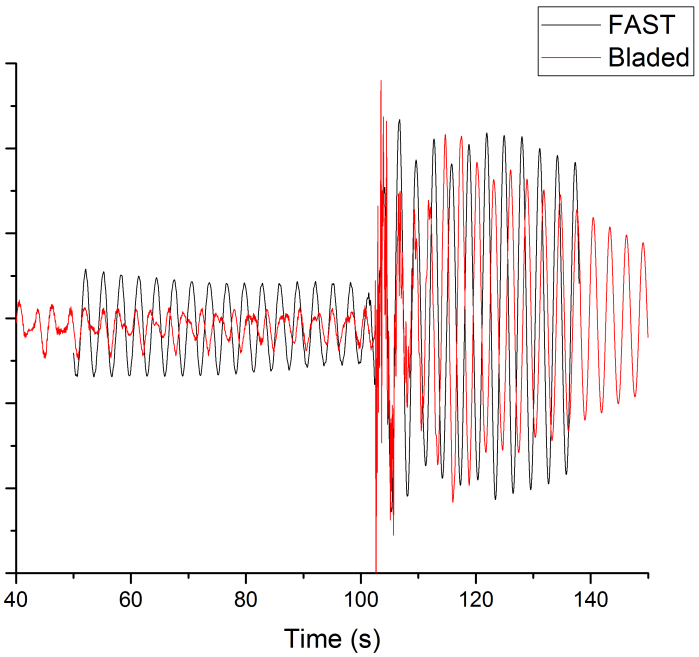

(b) Force in Y-direction.

Figure 3.10.7.: DLC2.3b tower base force (kN) and moment (kNm) results comparison based in NREL FAST coordinate system.

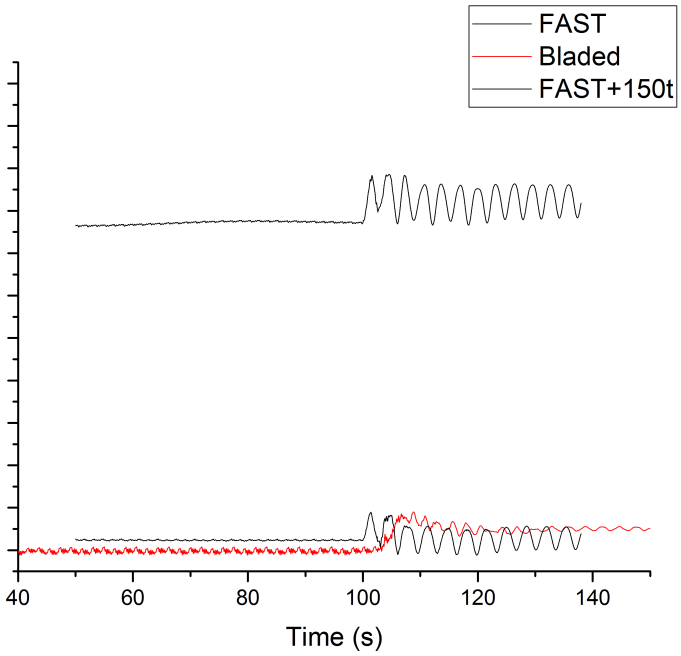

(c) Force in Z-direction.

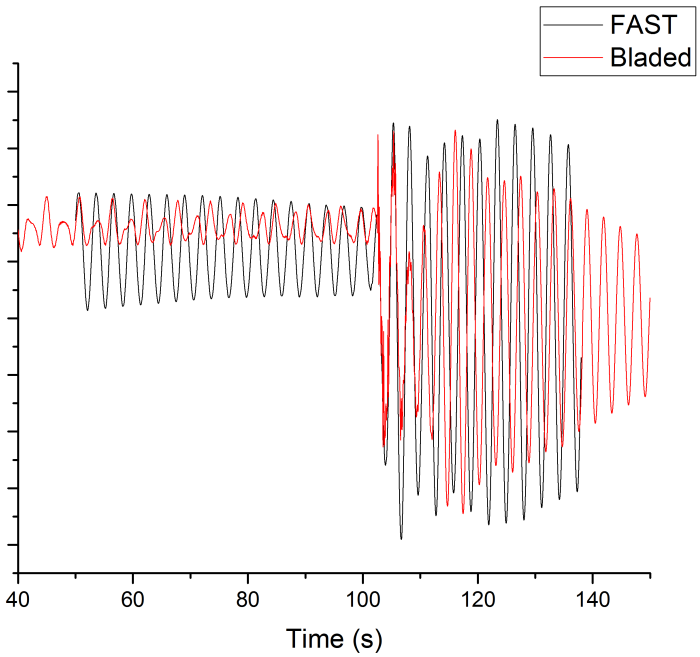

(d) Moment in X-direction.

Figure 3.10.7.: DLC2.3b tower base force (kN) and moment (kNm) results comparison based in NREL FAST coordinate system.

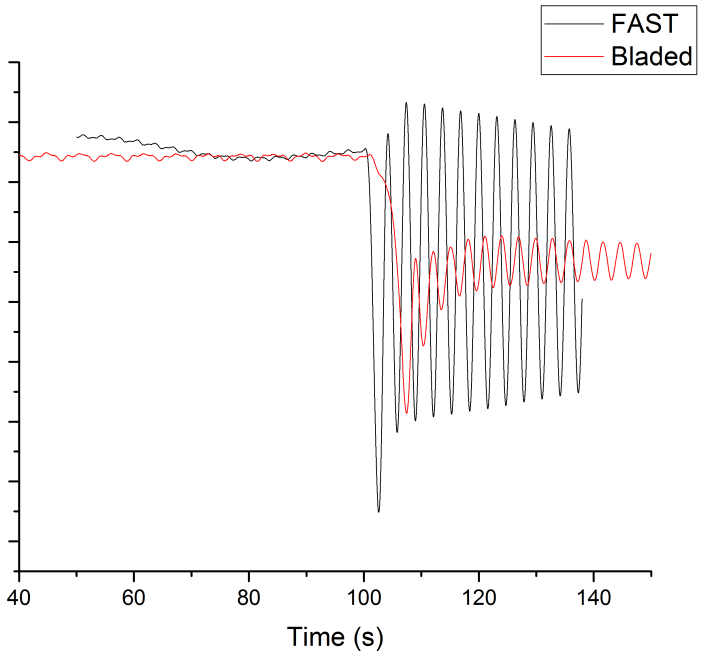

(e) Moment in Y-direction.

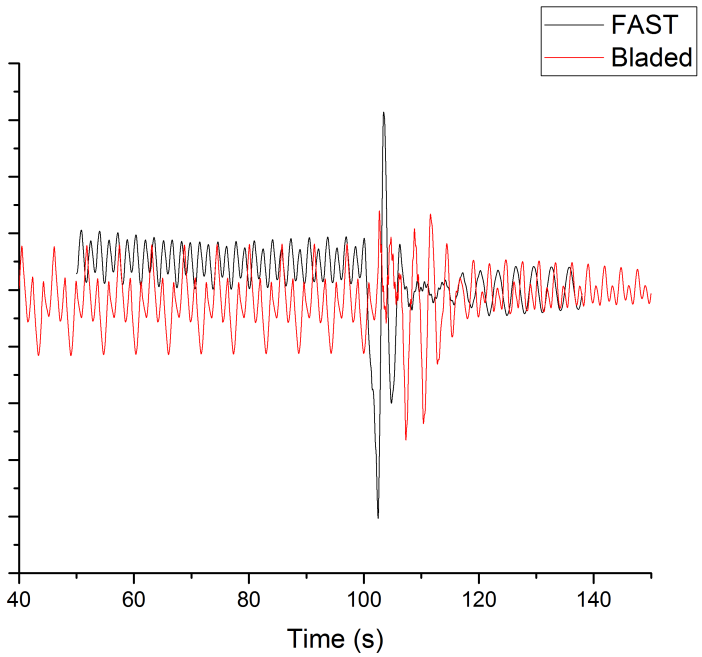

(f) Moment in Z-direction.

Figure 3.10.7.: DLC2.3b tower base force (kN) and moment (kNm) results comparison based in NREL FAST coordinate system.

3.10.4. Dynamic behaviour: DLC6.2

Regarding DLC6.2, Figures 3.10.8 and 3.10.9 show functional agreement on winds, pitch angle, and tower base force on the X-axis (always referring to the NREL FAST coordinate system).

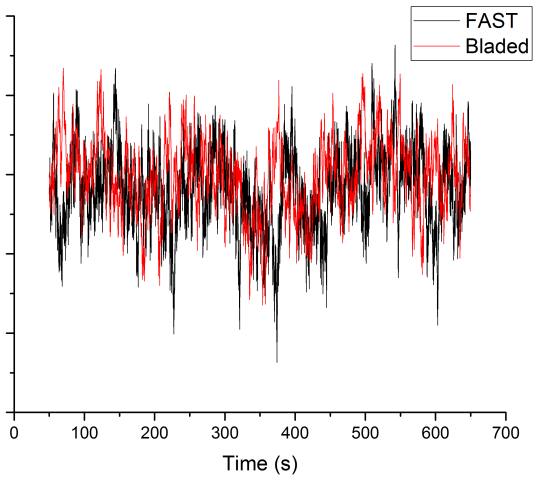

(a) Wind speed (m/s).

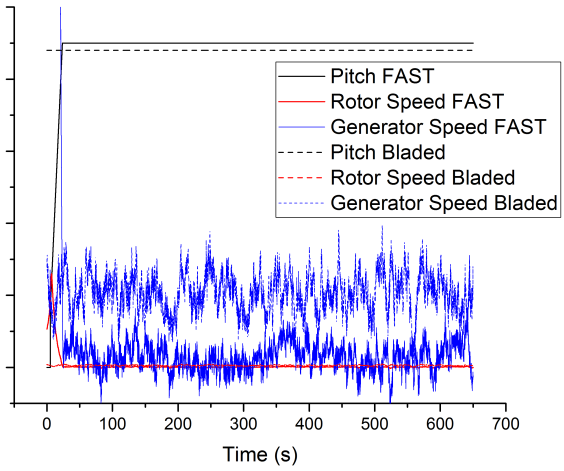

(b) Blade pitch angle (deg), rotor speed (rpm), and generator speed (rpm).

Figure 3.10.8.: DLC6.2 results comparison based in NREL FAST coordinate system.

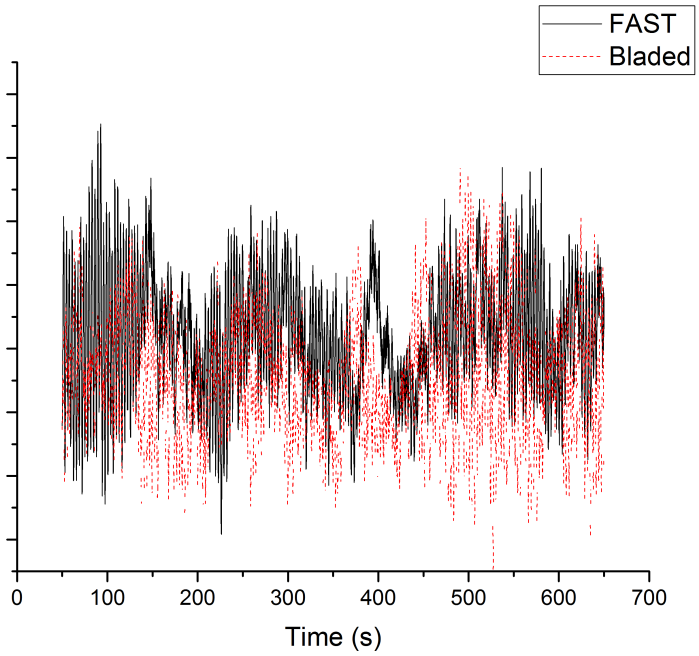

(c) Tower base forces in X-direction (kN).

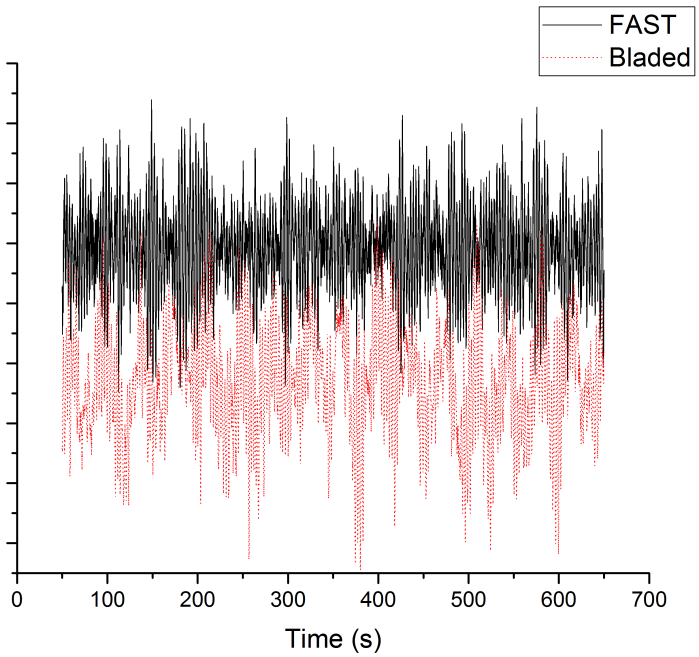

(d) Tower base forces in Y-direction (kN).

Figure 3.10.8.: DLC6.2 results comparison based in NREL FAST coordinate system.

This simulation exhibits rotor speeds close to zero. The tower base force on the Y-axis presents a difference regarding amplitude. GH Bladed reports larger amplitudes than FAST, and a shift in position, i.e. FAST oscillates above the Y-axis and GH Bladed below. The simulation also confirms that FAST predicts higher generator speeds than GH Bladed.

Figure 3.10.9a shows the same discrepancy pointed out in Figure 3.10.7c regarding the tower base force. Since DLC6.2 does not use active control, there is no difference due to the controller. The tower base moments on axes X (Figure 3.10.9b) and Z (Figure 3.10.9d) show how GH Bladed predicts higher amplitudes while on Y-axis, both codes showed similar results.

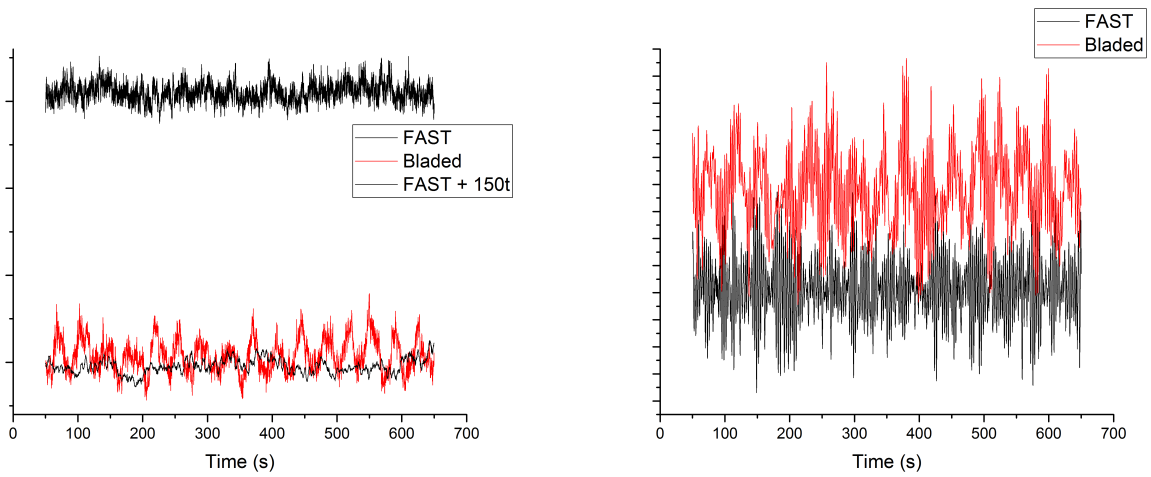

(a) Tower base forces (kN) in Z-direction.

(b) Tower base moments (kNm) in X-direction.

Figure 3.10.9.: DLC6.2 Tower base force (kN) and moment (kNm) results comparison based in NREL FAST coordinate system.

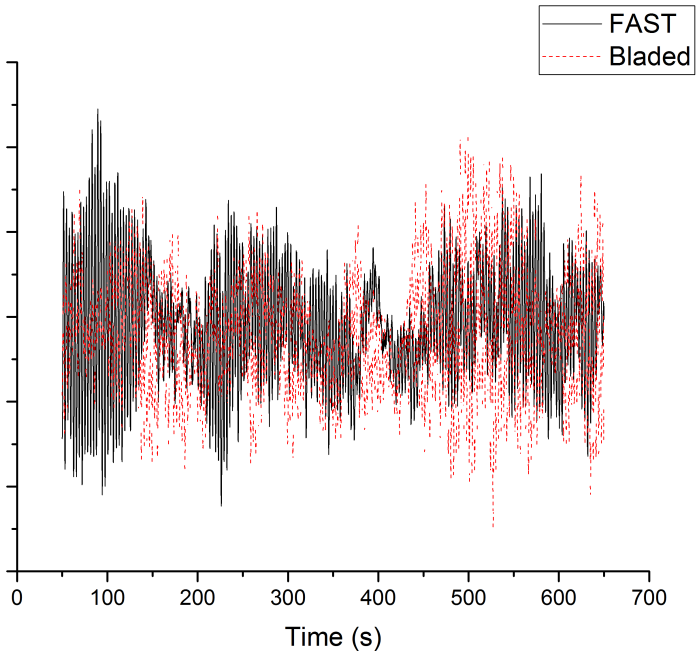

(c) Tower base moments (kNm) in Y-direction.

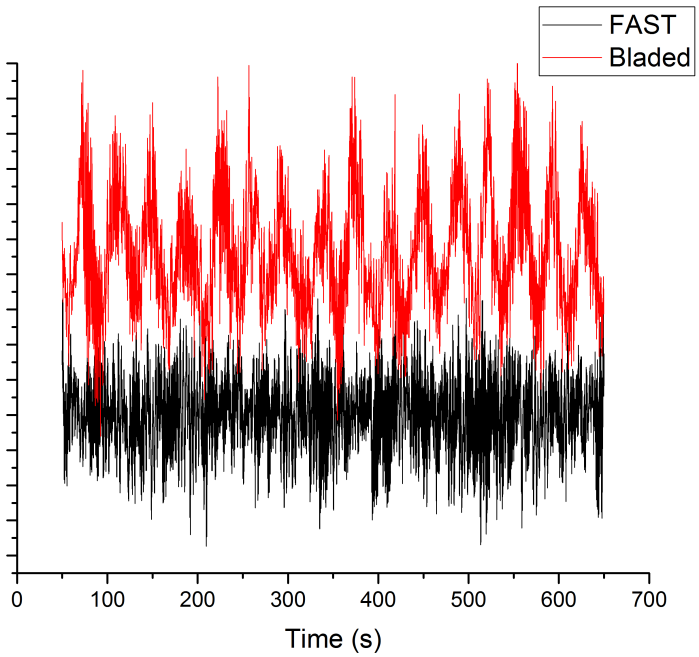

(d) Tower base moments (kNm) in Z-direction.

Figure 3.10.9.: DLC6.2 Tower base force (kN) and moment (kNm) results comparison based in NREL FAST coordinate system.

Table 3.9 presents the statistical differences between the NREL FAST results and the GH Bladed commissioning results for the DLC6.2.

Table 3.9.: Statistical differences between the NREL FAST results and the GH bladed commissioning results for the DLC6.2.

	Mean	SD	Minimum	Maximum
Wind1VelX (ms^{-1})	3.53	3.14	21.63	4.57
BldPitch1 ($^\circ$)	2.27	0.00	2.27	2.27
TwrBsFxt (kN)	27.55	3.68	114.04	11.95
TwrBsFyt (kN)	96.63	22.29	54.71	561.76
TwrBsFzt (kN)	15.98	46.39	16.37	14.99
TwrBsMxt (kNm)	96.26	21.42	742.32	55.25
TwrBsMyt (kNm)	14.41	6.35	16.66	10.17
TwrBsMzt (kNm)	127.25	40.18	194.07	74.70

The same comments made for the DLC1.1b and 2.3b regarding forces and moments differences can also be applied in DLC6.2.

3.10.5. Overall dynamic behaviour

In order to compare the overall dynamic behaviour, Table 3.10 presents the statistical differences between the NREL FAST results and the GH Bladed commissioning results combining all results of the DLCs 1.1, 2.3, and 6.2 shown in Table 3.1. All the forces have been transferred to the NREL FAST coordinate system for comparison purposes.

Table 3.10.: Statistical differences between the results.

	Mean	SD	Min	Max
Wind1VelX (ms^{-1})	1.67	4.58	10.67	4.32
BldPitch1 ($^\circ$)	13.60	6.66	0.76	2.80
RotSpeed (rpm)	10.20	63.88	7.90	21.30
GenSpeed (rpm)	10.20	63.88	7.89	21.43
TwrBsFxt (kN)	15.78	30.88	56.16	28.27
TwrBsFyt (kN)	38.91	18.75	45.21	21.76
TwrBsFzt (kN)	15.88	26.78	15.74	16.51
TwrBsMxt (kNm)	24.54	21.55	43.63	22.35
TwrBsMyt (kNm)	7.82	44.35	60.54	45.92
TwrBsMzt (kNm)	49.70	23.57	62.25	70.52
GenPwr (MW)	9.37	12.12	28.86	5.75
GenTq (kNm)	18.44	38.62	35.86	27.35

The Levenmouth model shows good agreement with the commissioning results. The discrepancies in the forces and moments are due to the different definitions of the transition piece and the substructure. Another reason is the controller used in the NREL FAST simulation is not the same as that used by the commissioning simulation, as stated previously. The behaviour of the pitch angle and rotor speed for DLC1.1b shows acceptable conformity (Figure 3.10.10) having into account that these results belong to the region $2\frac{1}{2}$, where maximum discrepancies were found (Figure 3.10.1) with the commissioning results.

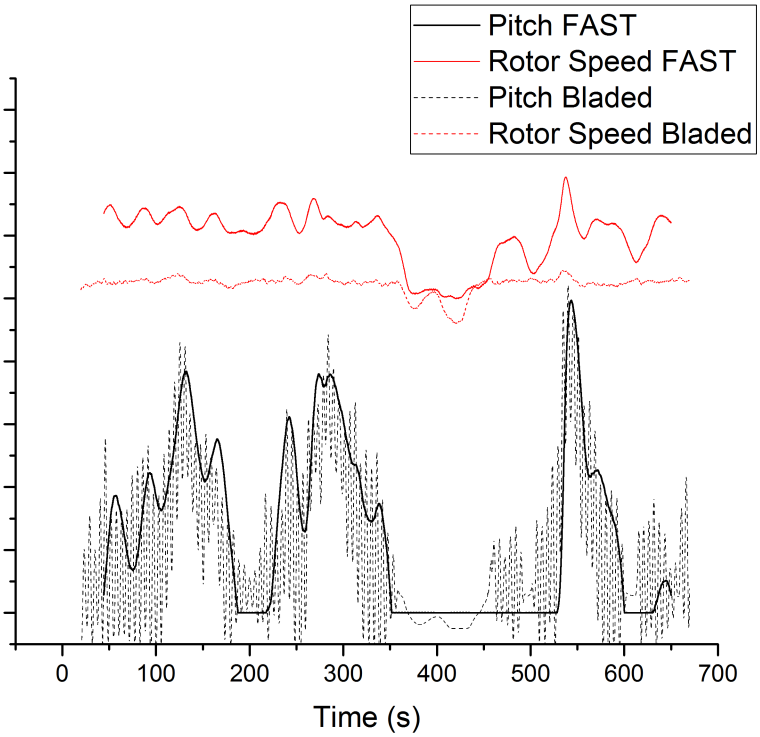

Figure 3.10.10.: DLC1.1b controller comparison, pitch angle (deg) and rotor speed (rpm).

The NREL-FAST model overestimates the rotor speed as well as the generator speed whereas underestimating generator torque and the power produced. Since the nominal values for rotor and generator speeds were correctly tuned, the differences must lie on the controller.

A comprehensive investigation of the pitch angle results shows that they follow the same general trend than commissioning results. The envelope of the blade pitch angle fits well with the commissioning results, but the inherent differences regarding the controller low-pass filters and gains, lead to significant statistical differences. Pitch mean values are slightly off due to the higher frequency of the commissioning results.

Figure 3.10.11a shows a comparison between the overall results of the NREL FAST simulation against the commissioning results. The discrepancies are within the expected

ranges, and the more substantial differences are related to DLC6.2.

Those differences must be analysed within the framework established by Figure 3.10.11b, which shows the discrepancies between the GH Bladed commissioning results in comparison to the GH Bladed Prototype analysis. This is based on the Levenmouth Class 1A conditions, i.e. a general Samsung S7.0-171 7MW wind turbine located in a given, but unknown, offshore site with wind conditions assimilated to IEC wind class IA, in comparison to the Samsung S7.0-171 7MW erected in Levenmouth, with its specific wind and sea state conditions.

Since this information is strictly confidential, a colour and pattern code has been used for the comparison. Green with a vertical pattern means differences up to 10%; yellow with a horizontal pattern means differences between 10% and 30%, and red with a crossed pattern means differences higher than 30%.

The differences observed between the NREL FAST and the GH Bladed commissioning load-matrixes are also related to the number of simulations executed. The commissioning results are based on approximately 3,000 simulations, whereas the NREL FAST results are based on 90 simulations for the whole set of DLCs. Each simulation uses wind speeds created from different random seeds to produce variability. Indeed, increasing the number of simulations/seeds will produce peak loads reducing the differences between both load-matrices. GH Bladed commissioning load-matrix matches better with GH Bladed Prototype Levenmouth Class 1A conditions load-matrix because they both are based on thousands of simulations.

		DLCs	Mx	My	Mz	Fx	Fy	Fz
Mx	Max	DLC6.2						
Mx	Min	DLC6.2						
My	Max	DLC2.2c						
My	Min	DLC2.3b						
Mz	Max	DLC1.3b						
Mz	Min	DLC1.3b						
Fx	Max	DLC1.3c						
Fx	Min	DLC2.3b						
Fy	Max	DLC6.2						
Fy	Min	DLC6.2						
Fz	Max	DLC6.2						
Fz	Min	DLC1.3c						

(a) NREL FAST VS GH Bladed.

		DLCs	Mx	My	Mz	Fx	Fy	Fz
Mx	Max	DLC6.2						
Mx	Min	DLC6.2						
My	Max	DLC2.2c						
My	Min	DLC2.3b						
Mz	Max	DLC1.3b						
Mz	Min	DLC1.3b						
Fx	Max	DLC1.3c						
Fx	Min	DLC2.3b						
Fy	Max	DLC6.2						
Fy	Min	DLC6.2						
Fz	Max	DLC6.2						
Fz	Min	DLC1.3c						

(b) GH Bladed vs GH Bladed prototype Levenmouth class 1A conditions.

Figure 3.10.11.: Load comparison.

3.11. Discussion and Conclusions

Accurate numerical models able to simulate the coupled dynamic response of realistic multi-MW turbines are needed to produce realistic load predictions.

The NREL FAST model developed during this study is stable and demonstrates reliable results. Hence, this model is an appropriate first step towards the virtualisation of the Levenmouth wind turbine, and the results obtained are valid to be used for loads

calculation in the initial stability analysis.

There is a concern regarding the tower base force in the Y-direction and tower base moment in the X-direction since the NREL FAST simulated values are very low compared to the commissioning results. The discrepancies between NREL FAST and GH Bladed results are related with the different approach used by the codes to calculate the loads, the different controllers used during the simulations, and differences regarding the definition of the systems, e.g. transition piece, substructure.

Because both codes show significant differences, these should be compared to SCADA data coming from the turbine to validate them.

Since the Levenmouth wind turbine has very flexible blades and NREL FAST ignores axial, and torsion Degrees of Freedom (DoFs), the use of BModes helps to overcome these limitations partially by implicitly accounting for these constraints [31].

Open-source coupled models like NREL FAST provide superior flexibility compared with commercial software, allowing the users to modify the code as appropriate. Since NREL FAST has been widely validated in the IEA Wind tasks 23 and 30 [66, 67], that makes it a suitable tool to virtualise wind turbines.

3.12. Recommendations

To improve the NREL FAST simulation of the Levenmouth wind turbine, the following future enhancements have been identified:

- The implementation of the simulator BeamDyn instead of ElastoDyn has the potential to improve the accuracy of the results. BeamDyn uses a nonlinear geometrically exact beam spectral FE blade theory which improves the structural dynamics results compared to ElastoDyn when used to model beams made of composite materials, initially curved and twisted, and subject to large displacement and rotation deformations such as this of the Levenmouth turbine blades.

- A deeper understanding of the controller operation is needed to develop more accurate filters leading to more accurate and precise simulations. The development of a re-tuned 64-bit controller will help to provide more stability to the simulations until the IP issues that prevent the use of the original controller are resolved.

- The addition of a hydrodynamic model will make the simulation more useful since it will allow forecasting the coupled behaviour of the system with different offshore substructures.

4. Baseline design

4.1. Introduction

This Chapter presents how the preliminary design of the Deep Turbine Installation-Floating (DTI-F) substructure and seakeeping system were conducted. The Chapter explains the existent relationships within the system leading to the principal dimensions of the substructure and mooring lines properties.

As explained in Section 1.5, the DTI-F is inspired in the design of the DTI-80F developed by Concrete Marine Solutions Ltd and QED Naval Ltd [22]. Therefore, it inherited the unique capability of raising and lowering the tower and nacelle set to simplify construction, installation, maintenance, and decommissioning. However, the DTI-F was designed as a hybrid structure with a frustum base built in steel and the main support column built with precast modular concrete sections whilst the DTI-F is a 100% modular concrete structure. Moreover, the original substructure had 80 metres of draft whereas the goal for the DTI-F is to reduce the draft up to approximately 60 metres. Therefore, the weights, volumes, and waterplane area for the new concept are expected to be different.

4.2. Parametric design

As any spar buoy-based FOWT concept, the DTI-F should meet a set of constraints. The buoyancy of the system must counter the mass of the tower and nacelle set plus the

own weight of the substructure. Therefore, enough void space must be allocated in the substructure to maintain the system afloat. This constraint is called floatability.

Another important constraint is the static intact stability. A floating substructure must have enough static stability to withstand the loads from the wind, waves, and the different operations, e.g. towing loads. The static stability of the floating body is determined by different factors:

- The difference between the vertical level of the metacentre and the centre of gravity (CoG), i.e. the metacentre height (GM) which must be bigger than one. This is the main requirement in terms of static stability for a spar-type FOWT.

- Even though this is not a requirement for a spar-type FOWT, it was agreed that the area under the righting moment shall be equal or greater than 130% of the area under the wind heeling moment previously calculated with NREL FAST.

- The maximum angle of inclination due to thrust steady loads of a constant wind at rated wind speed. Although this is only a guideline, the FOWT design shall aim to have a maximum angle of inclination of 4.5 degrees. Setting a maximum angle of inclination will provide the minimum total stiffness of the floating substructure.

Other constraints include fulfilling natural periods requirements, nacelle acceleration criteria, and setup a maximum heave and floater excursion. Regarding natural periods, in order to avoid resonant effects, the structure and the mooring system are designed in such a way that their resonant frequencies are shifted outside of the linear wave excitation range. To avoid possible couplings between inclinations and heave motions shift away their natural frequencies is also recommended. As a guideline, the nacelle acceleration shall be lower than 0.3 the acceleration of the gravity.

More constraints are imposed for damaged stability, towing operations, and dynamic stability but those are not going to be further discussed in this study.

Besides, the floating cylinder within the DTI-F must counteract the weight of the tower and nacelle set to enable its lifting process. In addition to that, the DTI-F needs a specific amount of ballast water for raising the tower and nacelle. Since any change in diameter or ballast will affect the total mass, an iterative process is needed to find all the appropriate parameters, i.e. substructure dimensions, floating cylinder dimensions, and amount of concrete and water ballast, that make the system fully-functional while fulfilling the above-mentioned constraints among others.

The spar diameter is one of the more significative parameters to consider while designing a spar-type FOWT. Small variations on the spar diameter induce remarkable differences in the total mass, and therefore affects the draft and the GM. Figure 4.2.1 presents the variation in draft, GM, and mass due to changes in spar diameter.

In summary, the floating system must be designed using a parametric approach. Therefore, a preliminary parametric design tool was employed to parametrise all the substructure dimensions while at the same time, volumes, masses and mass properties, and an early estimation of the main hydrostatic and hydrodynamic features of the floating system were calculated ensuring that all the above-mentioned constraints are met.

It is worth to state that the parametric tool developed in this study tackles the substructure dimensions, the position of the GM, the maximum angle of inclination and therefore the required stiffness, and the calculation of natural periods. The maximum heave, floater excursions and nacelle accelerations will be calculated using coupled simulations and the damaged stability and the stability during towing operations will be investigated by a third party and therefore are not going to be further discussed.

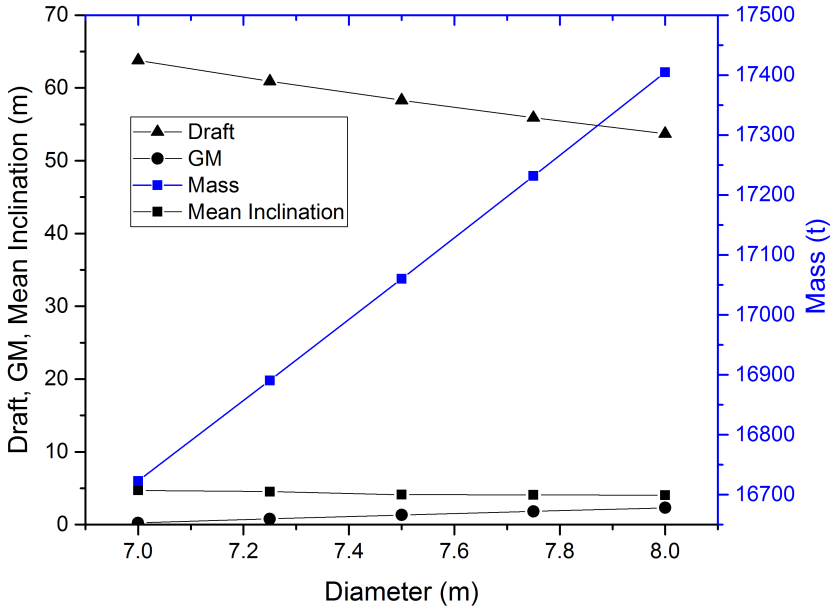

Figure 4.2.1.: Variation draft, GM, mass, and mean inclination at rated thrust due to spar diameter variation.

Another relevant parameter considered in the calculations was the wall thickness (Figure 4.2.2).The wall thickness is paramount regarding the structural constraints. The selection of the wall thickness was based on a structural analysis performed externally. The goal of the structural analysis was ensuring that the loads during operation, transport, and installation due to all external actions can be withstood by the structure. It implies the verification of bending, shear, torsion, and maximum crack width.

The parametric design tool also accounts for the weight of the suspended part of the mooring lines, the floating cylinder dimensions and the amount of water ballast needed to be able to raise the tower. After a few iterations, the outcome of the parametric design tool provides optimal results, defining shapes and dimensions fulfilling the functional requirements included in floating structures recommended practices [68]

.

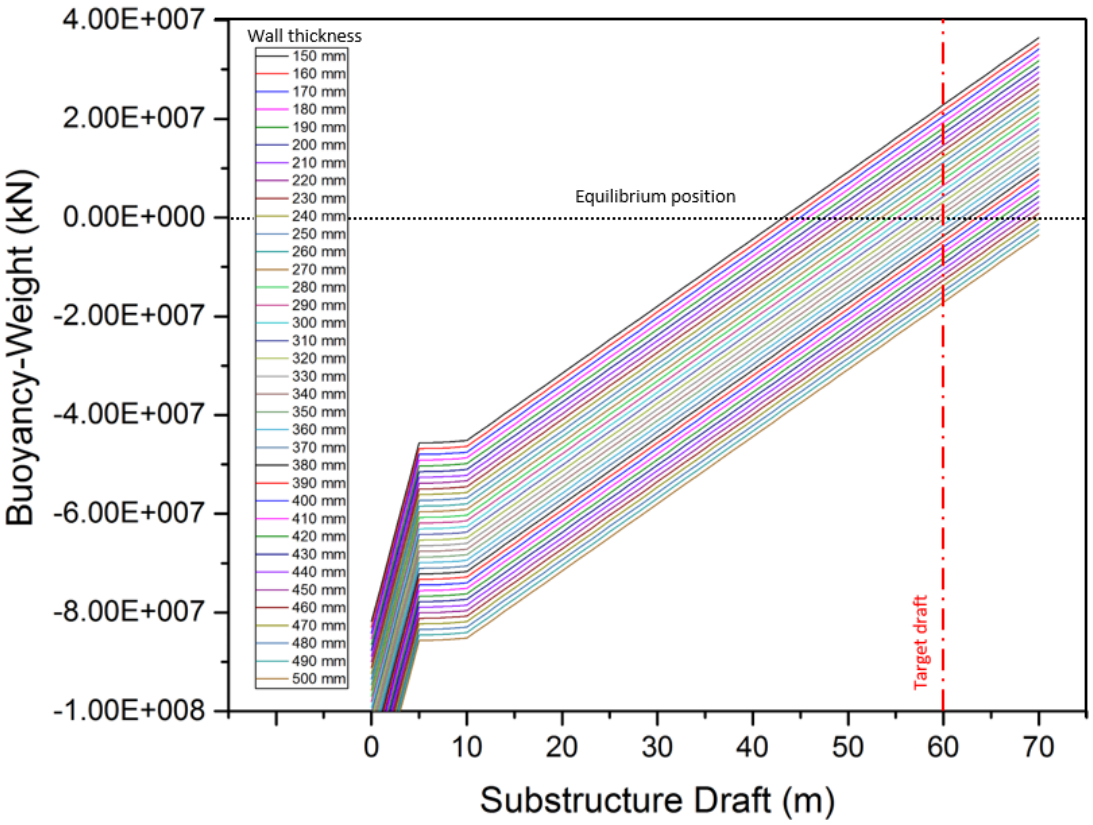

Figure 4.2.2.: Equilibrium position of the substructure for a given design with different wall thicknesses.

Three different catenary mooring configurations were proposed as depicted in Figure 4.2.3 and each of these configurations was considered during this early stage of development. Three lines distributed at 120 degrees were initially considered. Due to the concern regarding yaw motions, another three mooring lines configuration with a delta connection and four mooring lines distributed at 90 degrees configuration were also proposed. Keeping the natural periods of the floating system away from the resonance and controlling the global motions are the main design criteria considered.

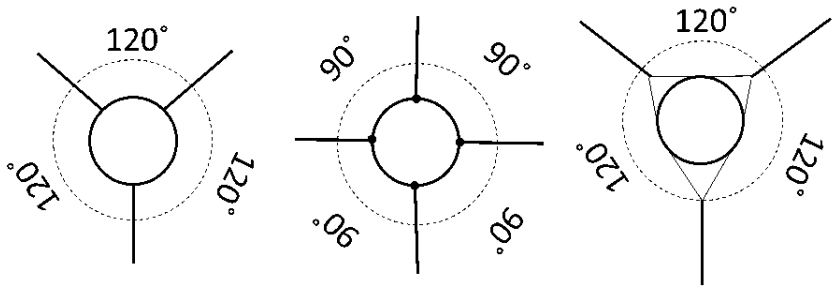

Figure 4.2.3.: Proposed mooring layouts.

The mooring line was designed to be in operation for the duration of the FOWT design life without replacement due to strength, fatigue, corrosion or abrasion issues. The final mooring line design consists of chains with three sections with different equivalent diameters, weight per length, and axial stiffness as shown in Figure 4.2.4.

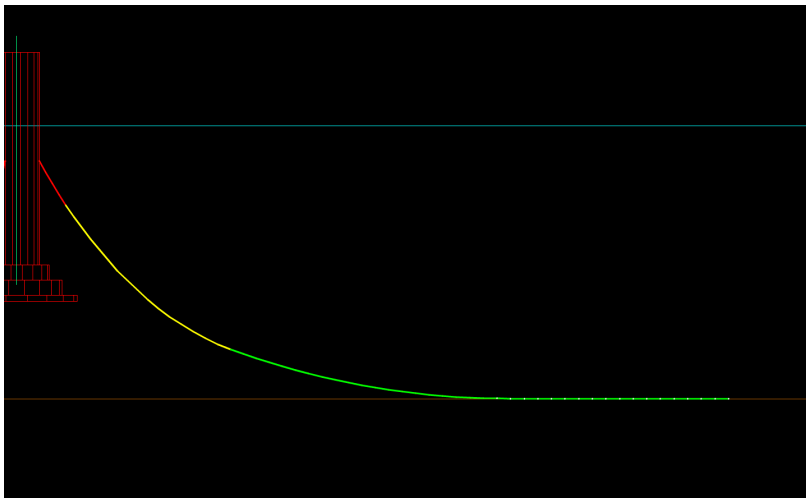

Figure 4.2.4.: Mooring design with three different sections highlighted in red, yellow, and green.

The load capacity of an anchor system depends on the interaction between the anchoring system and the seabed material. Two different anchoring systems have been proposed for the seakeeping of the DTI-F concept, i.e. gravity base and drag-embedded anchors. More sophisticated anchoring systems like suctions anchors or plates are more complex in terms of installation, and their costs are higher than well-established technologies like

drag anchors. Therefore, thirteen tonnes of nominal weight drag anchors were selected for the DTI-F system.

4.3. Concept dimensions

The DTI-F concept is a hybrid spar buoy-based floating offshore substructure designed and developed by Floating Wind Turbines (FWT) Ltd. It consists of two cylindrical and concentric walls joined by stiffener walls, a frustum, another wider base cylinder, and a heave plate.

The heave plate is the easiest solution to increase the weight in the lower part of the substructure while improving the heave motion by increasing the viscous damping. Other solutions such as hanging weights, truss sections or multi-heave plates structures are not going to be discussed in this work. The most relevant parameter regarding the heave plate performance is the ratio between the diameter of the heave plate and the main support column of the spar buoy.

Many studies [69, 70] suggest a ratio of around 2.84. Considering the added mass required to achieve the target in terms of heave natural period, in this study this value was reduced to 2.67.

The outer structure (a) is composed of a 15 m diameter cylinder that increases up to 30 m in diameter by means of a frustum-cone type structure, as depicted in Figure 4.3.1. Below the wider cylinder, there is a 40 m diameter water-entrapment heave plate that provides the required added mass to the floater.

The inner structure of the floater is composed of another hollow cylinder (b), 7 m in diameter. This hollow cylinder goes from the draft line to the bottom of the structure. The space between the two cylinders at the top (c) provides the necessary buoyancy to the floater. The void space in the wider cylinder at the bottom (d) is used to store the ballast water. This deposit, i.e. the wider cylinder, has different sealed tanks and stiffener

walls for structural reinforcement. Both the inner and wider cylinders are connected at the bottom end of the floater, allowing the tower and nacelle set to be raised and lowered down within the inner cylinder by flooding them using the ballast water (Figure 4.3.2). A 30 m height flotation cylinder, designed to counteract the weight of the tower and the nacelle, is installed at the bottom of the tower. This flotation cylinder is a critical component that allows both the tower and nacelle to float.

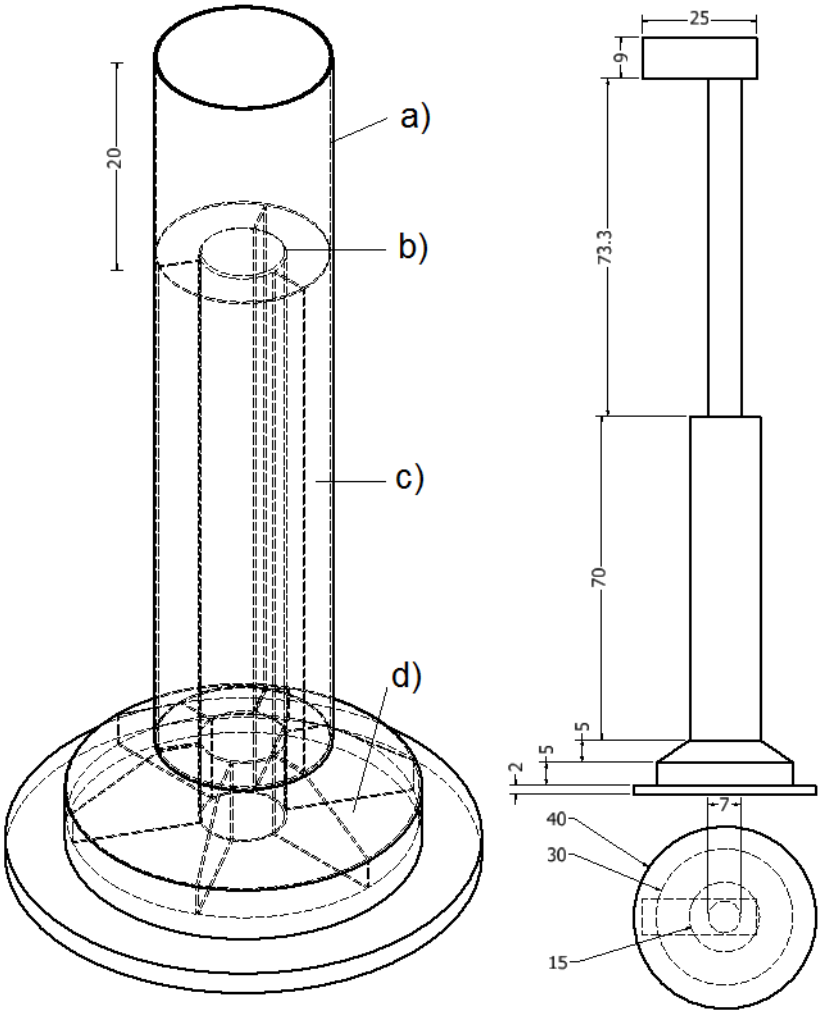

(a) Floater. (b) Complete system.

Figure 4.3.1.: DTI-F with dimensions in metres.

An active ballast system transfers water from the wider cylinder to the inner hollow cylinder to float the tower and nacelle set, allowing it to be raised and lowered, avoiding the use of expensive cranes during installation, maintenance and decommissioning processes.

The substructure has four boat landing areas, serviced by two remotely controlled lifts, ensuring at least one sheltered access point regardless of the wave direction.

A total of 553 m2 of deck space, located 20 m above the sea-level to avoid splashing waves, will give access to the facilities located within the substructure. It includes elevator accesses, a workshop, machinery rooms, structural tendons inspection access space, winches control room, IT, and communications space among others.

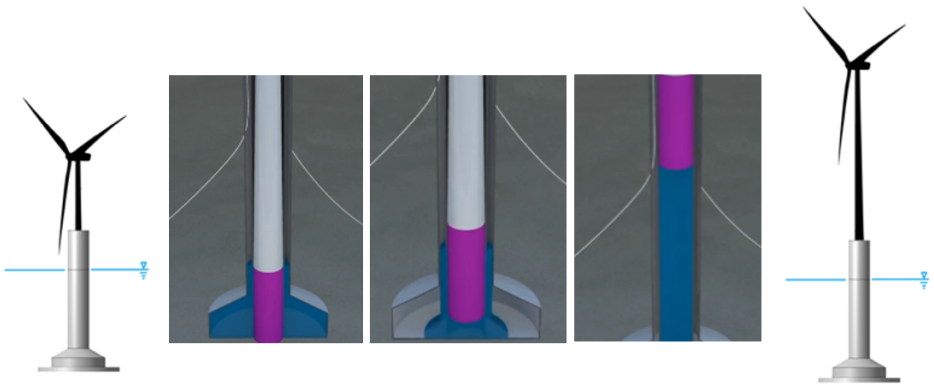

Figure 4.3.2.: Raising mechanism sequence using the flotation cylinder along with the ballast water to float the tower and nacelle set. Adapted from [22].

Each mooring line contains three different sections of 750, 550 and 165 kg/m respectively. Besides, 3 tonnes drag anchors were adopted to restrain the excursion of the floating system.

The floating substructure was designed to carry a standard 7 MW offshore wind turbine. However, the initial design is flexible allowing the operation of offshore wind turbines up to 15 MW with suitable modifications, i.e. increasing thickness of the walls, increasing the reinforcement capacity, increasing installation depth.

4.4. Construction and deployment

The author contribution to the development of the construction and deployment methods is limited to the calculations leading to the needed drafts during the different phases commented below.

The simple geometry of a spar buoy allows the use of a modular construction scheme. The precast concrete components can be fabricated off-site under controlled conditions, using simple formwork, and avoiding expensive slip forming. The reinforcement can be added in a controlled and efficient way of producing concrete precast modules. As precast concrete uses standard forms, modules can be produced in larger numbers, improving the economies of scale.

Construction will be carried out using a floating production line without the use of dry docks or similar facilities. Figure 4.4.1 illustrates a typical site layout including a batching plant, rebar and precast modules construction yards, the substructure assembly area, and the turbine assembly area.

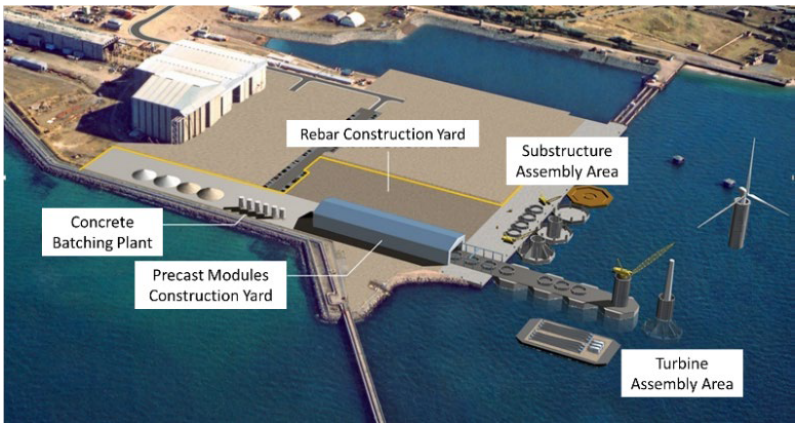

Figure 4.4.1.: Typical construction site layout. Adapted from [22].

The heave plate and the base sections are designed to be built on a submersible pontoon in shallow waters. With the base cast and afloat, precast modules are stacked along with the flotation cylinder (Figure 4.4.2a) and the corresponding tower sections (Figure

4.4.2b). Once the whole substructure is built, base and water ballast are added, and the substructure can be towed to a deeper assembly area (Figure 4.4.2c). Finally, the nacelle and blades will be assembled (Figure 4.4.2d), and the complete system can be tested at the quayside to allow for troubleshooting before installation in deep waters.

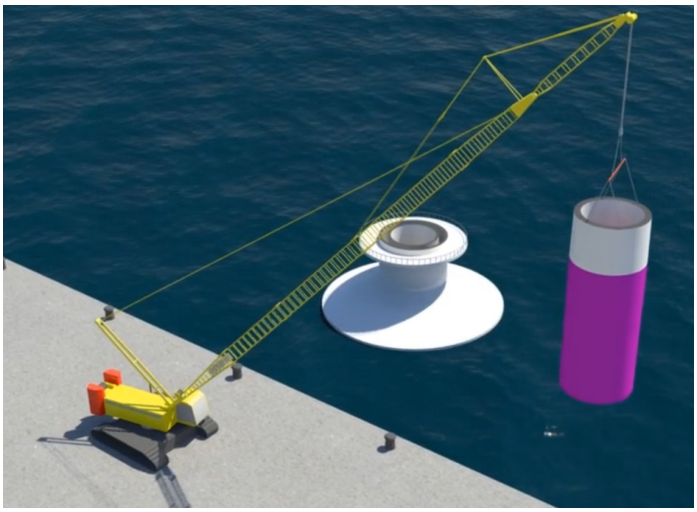

(a) Addition of the flotation cylinder at the assembly area.

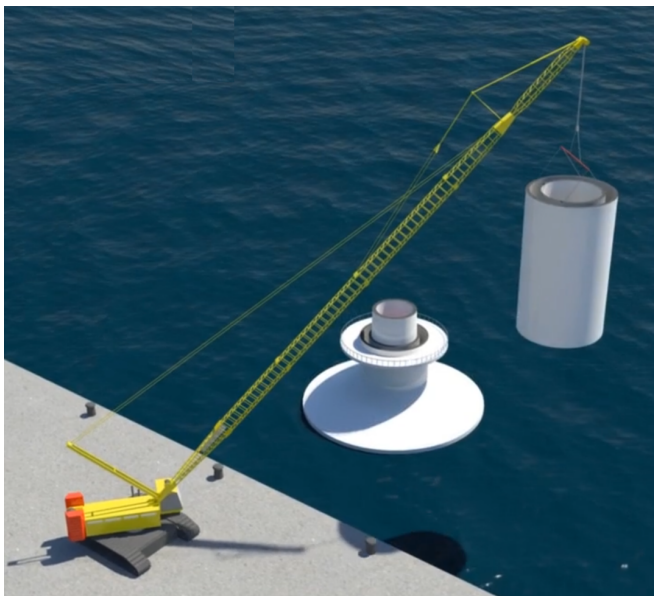

(b) Addition of the precast modules and tower sections.

Figure 4.4.2.: Construction and deploy methods. Adapted from [22].

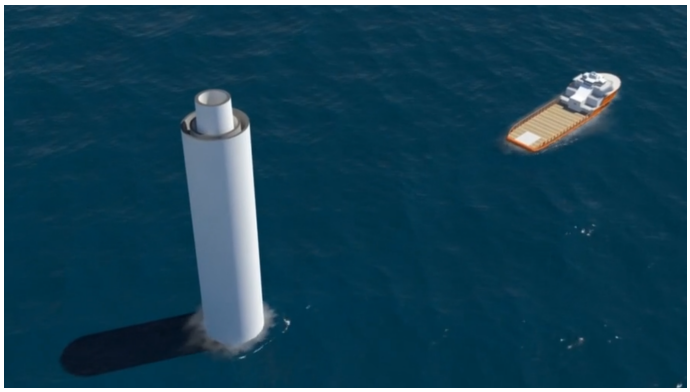

(c) Substructure towed to the turbine assembly area.

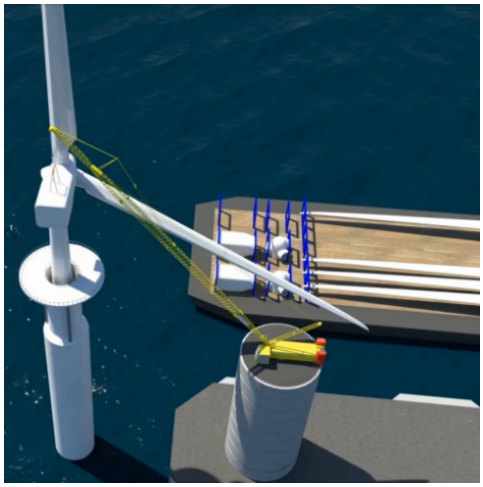

(d) Nacelle, rotor and blades fitted, and ready to be tested at turbine assembly area.

Figure 4.4.2.: Construction and deploy methods. Adapted from [22].

To face the construction and deployment phase with guaranties, it is necessary to calculate the required draft during the construction of the substructure, the assembly of the different subsystem, the commissioning of the FOWT, and first stages of the deployment, i.e. before the FOWT reaches deep-waters.

Once the initial design is established, a first forecast of the different weights and submerged volumes involved in each of the different construction stages. The mentioned weights and submerged volumes can be processed to predict the required drafts.

Figure 4.4.3 presents the depths required at each of the different construction stages. The DTI-F substructure requires less than 10 m depth for the construction early stages and from 10 to 25 m depth to complete floater construction.

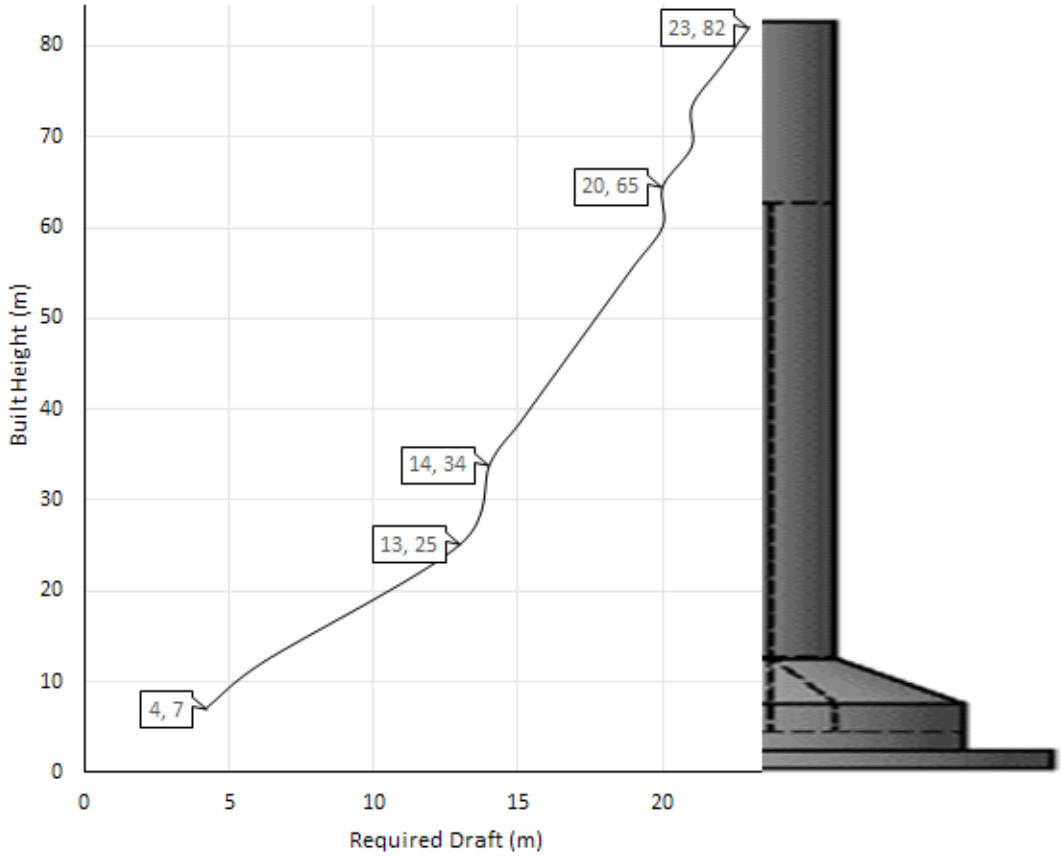

Figure 4.4.3.: Needed draft during construction.

Figure 4.4.4 presents the draft requirements from the assembly phase to the commissioning stage. It includes the addition of the base ballast, the fitting of the nacelle, the rotor, the blades and the transfer of the ballast water until the full commissioning of the system with the tower erected and the turbine ready to be tested.

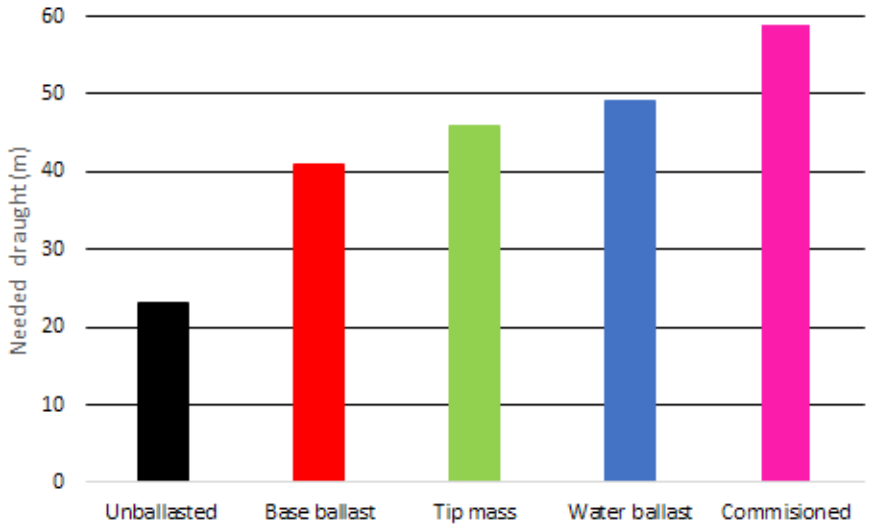

Figure 4.4.4.: Draft required to deliver the substructure.

4.5. Summary

The baseline design of the DTI-F system has been carried out using a concrete spar buoy-based floater supporting the Levenmouth wind turbine (7MW). The results are a good indication that the fundamental design of the concept is technically feasible.

Installation and construction methods have been designed to minimise offshore operations. The raising mechanism allows for installation and maintenance avoiding the use of heavy lifting cranes.

Further optimisation of the system can be achieved by using a two-bladed wind turbine. Two-bladed wind turbines exhibit lower power performance than a three-bladed wind turbine. However, the cost reduction in materials along with a slightly longer blade will counteract this lower power output. Besides, the two-bladed wind turbine geometry allows lowering the nacelle with the blades in horizontal position. Therefore, the installation and maintenance operations can be performed only at 20 m above the sea level which has the potential to drastically reduce the costs.

The parametric design adopted has demonstrated been a useful tool to conduct an

early design in terms of dimensions while producing overall results as volumes, masses and mass properties, and an early estimation of the main hydrostatic and hydrodynamic features of the floating system.

A 350 mm wall thickness was selected to achieve the desired draft while fulfilling design and structural constraints. A final draft of 62 m was achieved reducing the initial draft in 18 m.

The preliminary design has reduced the draft while using a heavier material by increasing the diameter of the spar buoy. Increasing the spar buoy diameter will have important hydrodynamic consequences which will be discussed later in Chapters 5 and 6.

A mooring system consisting of lines with three different sections has been designed and fine-tuned in terms of length, pretensions, and anchors position to reduce the floater response and protect the export cable from undesired loads. Drag anchors have been chosen to restrain the excursion of the floating system since drag anchors are a well understood technology with many years of experience applied in oil and gas platforms. Three different mooring line configurations are considered during the first iteration design.

All the results from the calculations performed by the parametric design tool meet the design basis document, i.e. FWT Ltd standard specifications and details of the DTI-F concept.

5. Experimental methods and analysis techniques for FOWT

5.1. General

Floating offshore wind turbines (FOWTs) are complex systems. Besides the complexity that the WT introduces into the system by itself, floating platforms are also subjected to hydrodynamics interactions with the moorings, waves and currents. To predict realistic hydrodynamic responses of FOWTs, full-scale tests on the relevant environment, i.e. open sea, are the most reliable method. However, full-scale testing requires considerable effort and it is expensive. Although tank testing is subjected to undesirable scaling effects [71], small models are less costly and easier to handle. They require less staff, shorter set up and testing time. Therefore, scale model testing is commonly accepted to be the first step to evaluate concept feasibility [72] or component performance [69] before moving to large/full-scale developments.

Based on the design developed in the previous Chapter, a scale model of the DTI-F concept was built and tested to assess its hydrodynamic behaviour, and further de-risk the new floating concept.

The following objectives are identified for the experimental campaign:

(1) Characterise the unmoored DTI-F substructure hydrodynamically i.e. no mooring lines and 'soft' mooring lines, by calculating natural periods, damping ratios and

response amplitude operators (RAOs).

(2) Evaluate the advantages and disadvantages of different catenary mooring configurations, i.e. three lines, four lines, and three lines with a delta connection, by calculating natural periods, damping ratios. Use the produced results as a basis for mooring system selection.

(3) Characterise the DTI-F substructure hydrodynamically with the chosen mooring configurations by calculating its RAOs.

(4) Evaluate the hydrodynamic loading on mooring lines.

(5) Based on the measurements, to validate the numerical models of the DTI-F concept with the chosen mooring configuration.

(6) Provide statistical information about the overall performance of the floating system in realistic sea states.

The following Sections describe details of the facilities, model details, experimental setup, methodology and analysis techniques employed during the experimental campaign of the DTI-F (Sections 5.2 to 5.12). The results analysed are reported from Section 5.13 onwards.

5.2. Facilities

This Section introduces the facilities used to perform the testing campaign of the DTI-F.

5.2.1. Lir NOTF

The first experimental campaign was carried out in the Ocean Wave Basin of the Lir NOTF in Cork, Ireland. The basin (Figure 5.2.1) is 15.14 m long, 25.85 m wide.

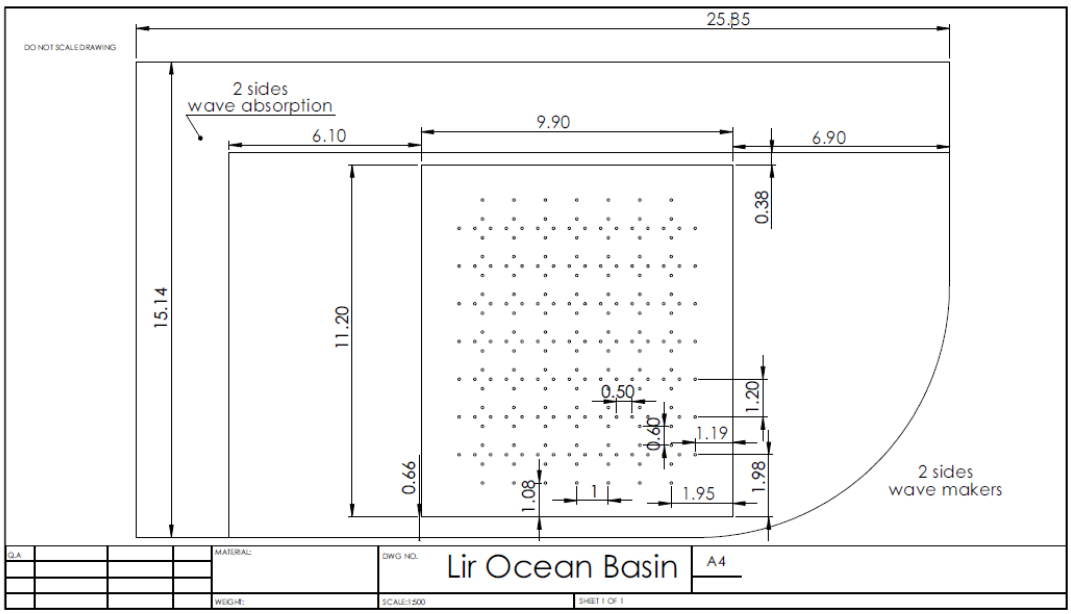

Figure 5.2.1.: Wave basin geometry and lengths at Lir NOTF.

Its 11.2 × 10 m deep section is equipped with a movable floor plate (Figure 5.2.2). The working water depth is set to 2 m to conduct the testing.

Figure 5.2.2.: Wave basin picture showing the movable floor in a raised position at Lir NOTF.

The basin (Figure 5.2.3) is equipped with 80-hinged wave paddles located on two sides of the basin allowing for adjustable wave directions. The two other sides of the basin are equipped with a beach, i.e. a wave absorber structure. The paddles can generate peak

wave conditions with a significant wave height (H_s) of 0.16 m, peak wave period (T_p) of 1.4 s, and maximum wave height (Hmax) of 0.32 m [73], which makes it ideal to test operational conditions for 1:45 scale models such as the one considered in this study.

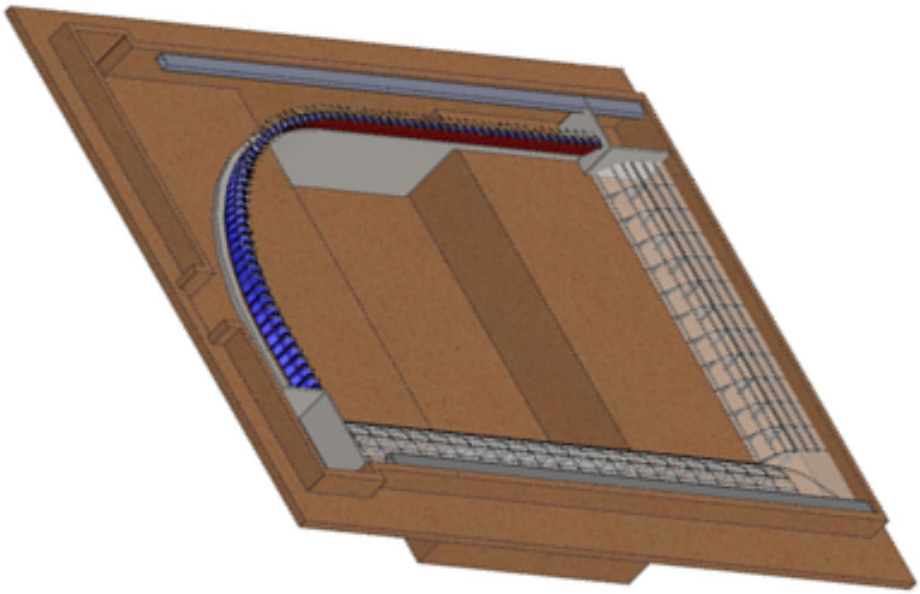

Figure 5.2.3.: Wave basin 3D draw showing the 80-hinged paddles (in blue), the beach structure (in grey) and the deeper central basin at Lir NOTF.

5.2.2. FloWave OERF

Complementary hydrodynamic testing was performed at the FloWave Ocean Energy Research Facility (OERF) in Edinburgh, Scotland. FloWave OERF is a circular wave and current testing tank (Figure 5.2.4). The basin is equipped with 168 active-absorbing hinged wavemaker paddles situated around the circumference of the tank. In addition 28 flow drivers will generate current systems.

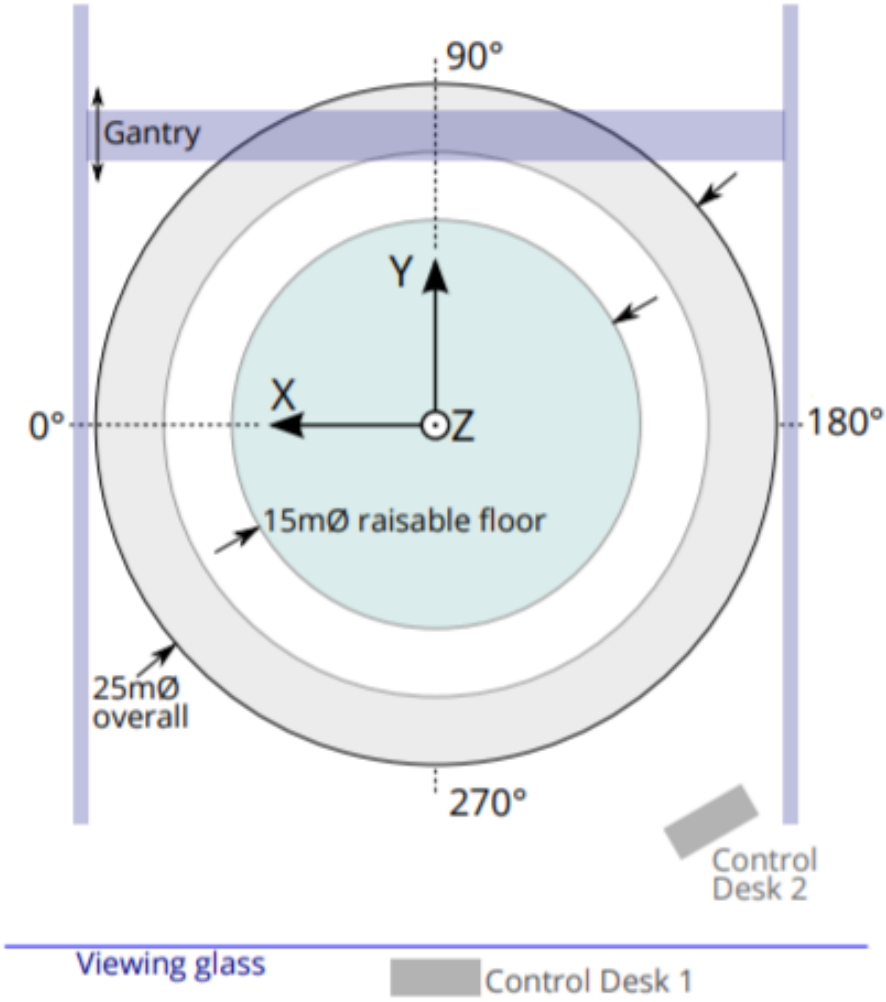

Figure 5.2.4.: Basin layout. Modified from [74].

The multidirectional wave and current basin is optimised for wave heights up to 0.45 m at wave period of 2 seconds (Figure 5.2.5) and can generate currents up to 1.6 m/s [74]. This offers sea state conditions for testing floating wind turbines at scales up to 1:45.

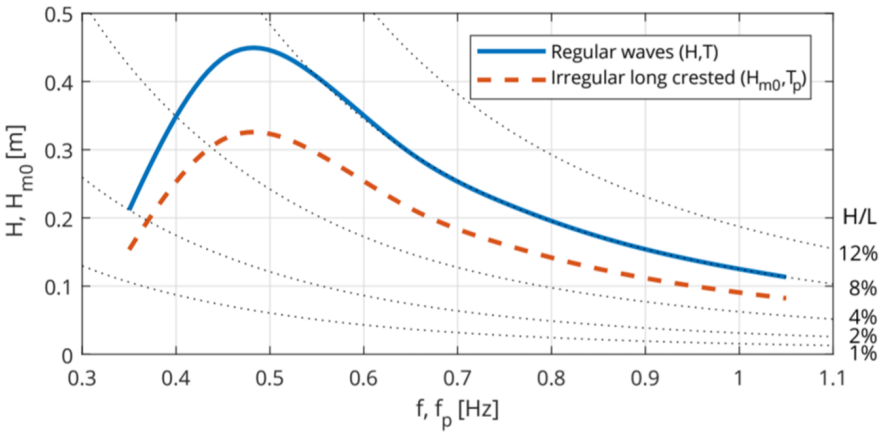

Figure 5.2.5.: FloWave OERF approximate tank performance.

There is a 15 m diameter movable floor in the centre of the tank that can be raised above the water level (Figure 5.2.6) to facilitate model installation and reconfiguration. The working water depth was set to 2 m to conduct the testing.

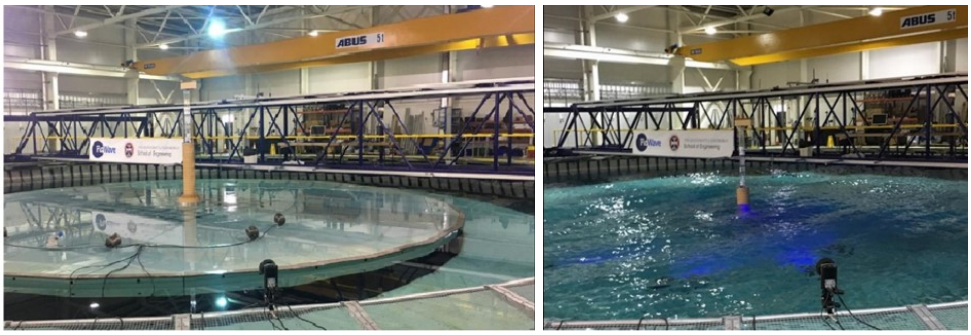

(a) Movable floor in a raised position. (b) Underwater optical tracking system.

Figure 5.2.6.: Wave basin picture showing the movable floor and the underwater optical tracking system.

5.2.3. Structural laboratory

In order to perform the catenary axial stiffness testing on the mooring line chains, the structural laboratory at the University of Edinburgh's Engineering School located in the William Rankine building was used. The premises have an Instron 4500 Series Universal

Testing Machine (Figure 5.2.7).

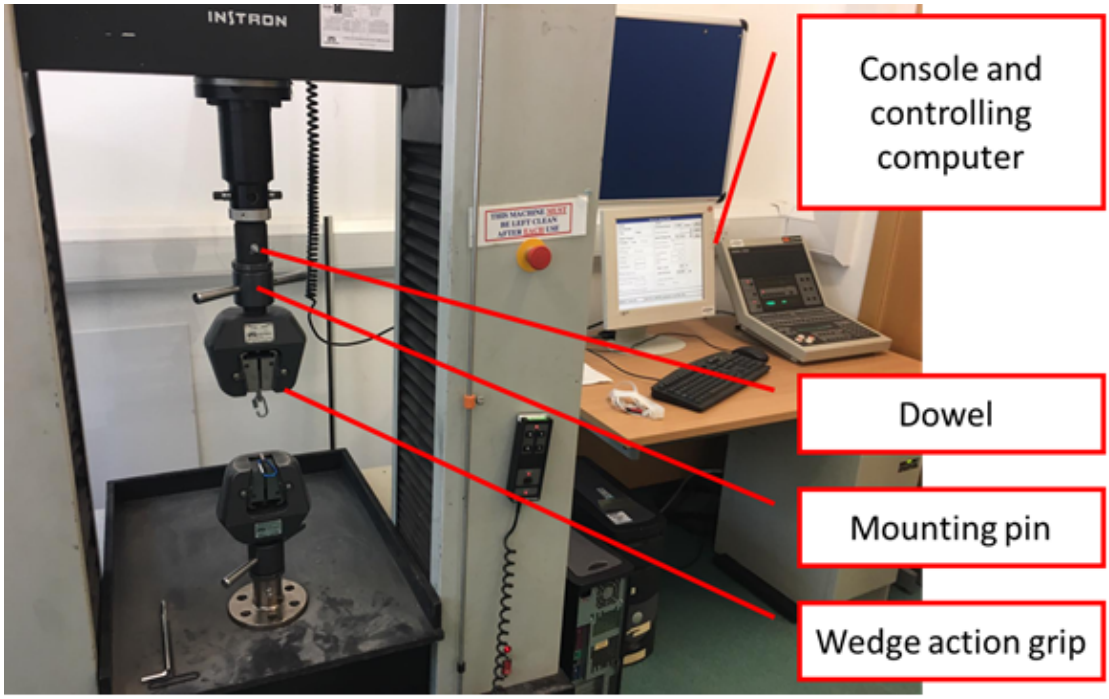

Figure 5.2.7.: Instron 4500 Series Universal Testing Machine showing the console and controlling computer, the wedge action grip, the mounting pin, and dowel used to secure the mounting pin to the testing frame.

A 100 kN rated capacity ($\pm 2N$) wedge action grip was mounted in the load frame by attaching the mounting pin to the frame adapter and securing it with a dowel. A specimen, i.e. 20 cm of chain, was attached to the wedge action grip using a perforated plate and a quick link (Figure 5.2.8).

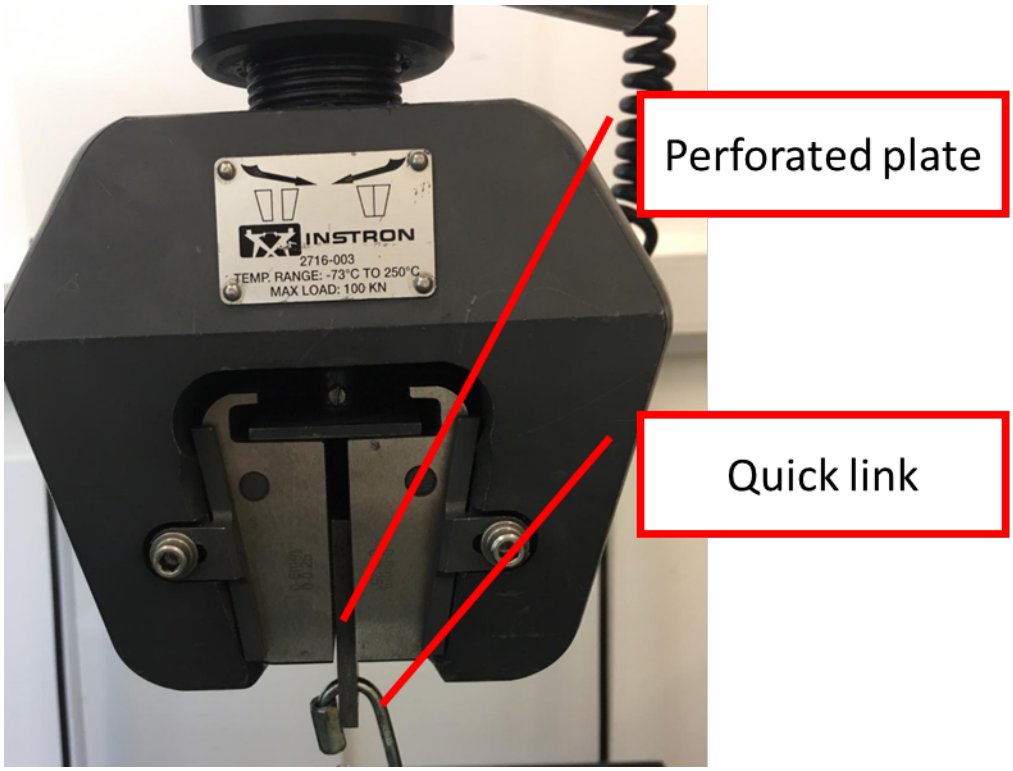

Figure 5.2.8.: 100 kN rated capacity wedge action grip showing the perforated plate and the quick link used to attach the chain specimen.

5.3. Scale model

A 1:45 rigid model of the DTI-F system was machined (milling machine accuracy=$\pm 0.5mm$) and assembled (Figure 5.3.1) in the FloWave OERF workshop. It was constructed of divinycell closed cell foam sections with aluminium interfaces and heave plate. The design includes approximately 10 kg of moveable ballast in the upper cylinder to adjust the final draft and centre of gravity (CoG). The scale factor (1:45) was chosen to allow the correct representation of water depth in the testing environment.

The scale model was designed to preserve geometric and dynamic similarities. Geometric and dynamic similarity implies a unique scale ratio for the entire linear dimension and a constant ratio between the forces in both model and full-scale. Therefore, geomet-

ric and dynamic similarity together imply that flow and model will have geometrically similar motions in model and full-scale which is known as kinematic similarity.

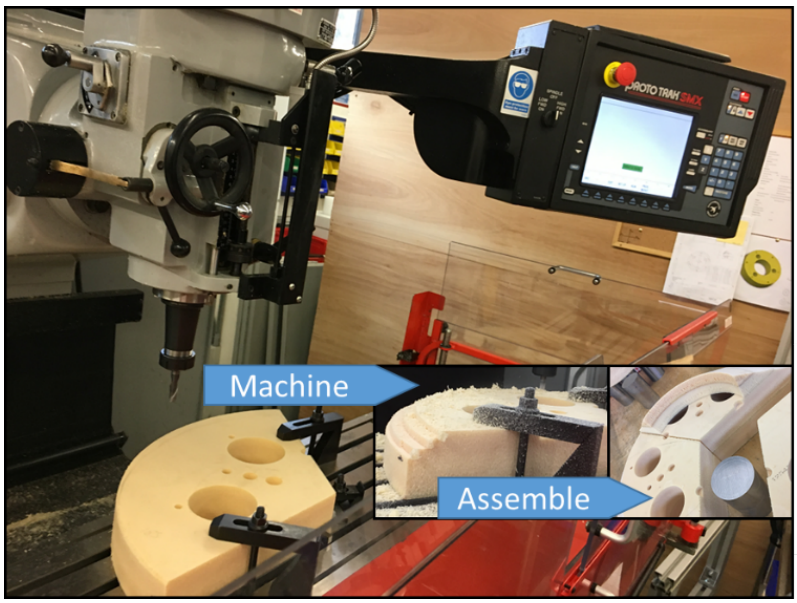

Figure 5.3.1.: Milling machine ready to cut a piece, working on the frustum, and a view showing how some of the pieces were assembled.

Due to the unfeasibility of simulating all the dimensionless numbers at the same time, i.e. it is unfeasible to simulate Froude and Reynolds number concurrently, the scale model was designed to preserve the Froude hydrodynamic similitude. Therefore, the proposed scaling maintains the following dimensionless numbers:

- Froude number, which is the ratio of water particle velocity to wave velocity.
- Keulegan-Carpenter number, which accounts for the relative excursion of a water particle during a wave cycle, and
- The aerodynamic Lock number, which is the ratio of the aerodynamic forces and the inertia forces.

The dimensionless numbers that are not conserved:

- The Reynolds number in the air and the water. The Reynolds number is the ratio of inertial forces and the viscous forces.
- The Weber number, which measures the balance of surface tension to inertial loads.
- The Strouhal number in water and air, which describes the oscillatory behaviour of fluids.
- The Mach number, which is the ratio of the relative flow velocity to the sound velocity.
- The Tip Speed Ratio, which is the ratio between the tangential speed of the tip of a blade and the actual speed of the wind.

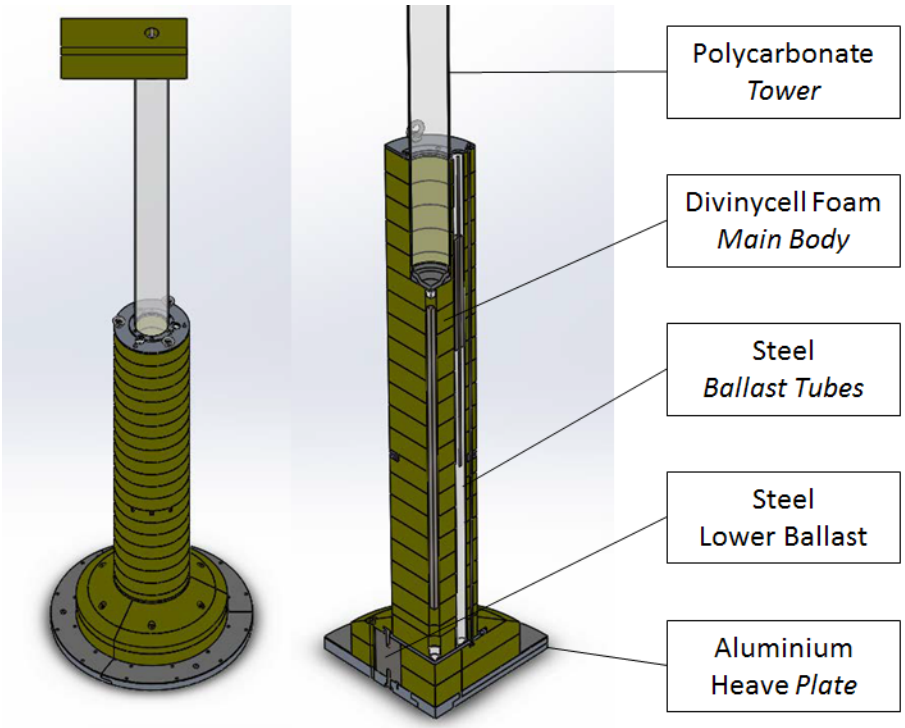

Figure 5.3.2.: Manufacture design of the DTI-F. The drawing on the right is a quadrant showing the inner structure.

The scaling relationships [75] utilised to obtain the appropriate scale factors are shown

in Tables 5.1 and 5.2, where β is an adimensional free parameter allowing for adjustment of a laboratory wind speed beyond strict Froude scaling and the length scale ratio λ is defined by:

$$\lambda = \frac{L_p}{L_m} \tag{5.3.1}$$

Where 'p' and 'm' subscripts stand for prototype scale and model-scale respectively, and L is the representative length.

Table 5.1.: FWT scaling factors. ρ_w denotes the water density.

Property	Scaling factor
Length	λ
Area	λ^2
Volume	λ^3
Mass	$(\rho_{wp}/\rho_{wm})\lambda^3$
Mass moment of inertia (J)	$(\rho_{wp}/\rho_{wm})\lambda^5$
Area moment of inertia (I)	λ^4
Water velocity	$\lambda^{1/2}$
Air velocity	$\lambda^{1/2}\beta^{-1}$
Acceleration	1
Time	$\lambda^{1/2}$
Frequency	$\lambda^{-1/2}$
Angle	1
Force	$(\rho_{wp}/\rho_{wm})\lambda^3$
Moment	$(\rho_{wp}/\rho_{wm})\lambda^4$
Stiffness (E)	$(\rho_{wp}/\rho_{wm})\lambda$
Stress	$(\rho_{wp}/\rho_{wm})\lambda$
Power	$(\rho_{wp}/\rho_{wm})\lambda^{7/2}$
Thrust coefficient (C_T)	$(\rho_{wp}/\rho_{wm})\lambda^2\beta^2$

Table 5.2.: Wind and waves scaling factors.

Property	Scaling factor
Geometric height (z)	λ
Wind speed (V)	$\lambda^{1/2}\beta^{-1}$
Turbulent wind frequency (f)	$\lambda^{-1/2}$
Turbulence intensity	1
Wind profile power coefficient (α)	1
Water depth	λ
Velocity	$\lambda^{1/2}$
Significant wave height	λ
Peak period	$\lambda^{1/2}$
Wind-wave misalignment	1

Table 5.3 presents the dimensions of the scale model 'as constructed' and Table 5.4 shows the theoretical mass properties of the new designed 1:45 scale CAD model and the percentual difference with the target values, i.e. 1:45 scale values from the full-scale CAD model. The tower and nacelle were modelled to match the mass distributions of the Levenmouth (Samsung Heavy Industries - S7.0-171) demonstration WT as described in [76]. The tip mass distribution accounts for the whole system, i.e. blades, rotor, and nacelle.

Table 5.3.: DTI-F scale to 1:45. All dimensions are provided in millimetres.

	Height	Width	Lenght	Diameter
DTI-F	3651	-	-	-
Tip mass	200	178	556	-
Tower	1628	-	-	156
Top cylinder	1556	-	-	333
Frustum	111	-	-	-
Base cylinder	111	-	-	667
Heave plate	44	-	-	889

Table 5.4.: DTI-F mass properties scale to 1:45 and difference with the target values.

	Mass (kg)	CoG Z (mm)	I_{xx} (kgm^2)	I_{yy} (kgm^2)	I_{zz} (kgm^2)
Model	186	447	126	126	10
%	0	0	8	8	-5

5.4. Mooring configurations

The mooring lines were modelled by means of chains. Three different catenary mooring configurations have been proposed for the seakeeping of the DTI-F concept, i.e. (i) three lines distributed at 120 degrees, (ii) four lines distributed at 90 degrees, and (iii) three lines distributed at 120 degrees with a delta (Δ) connection (Figure 5.4.1).

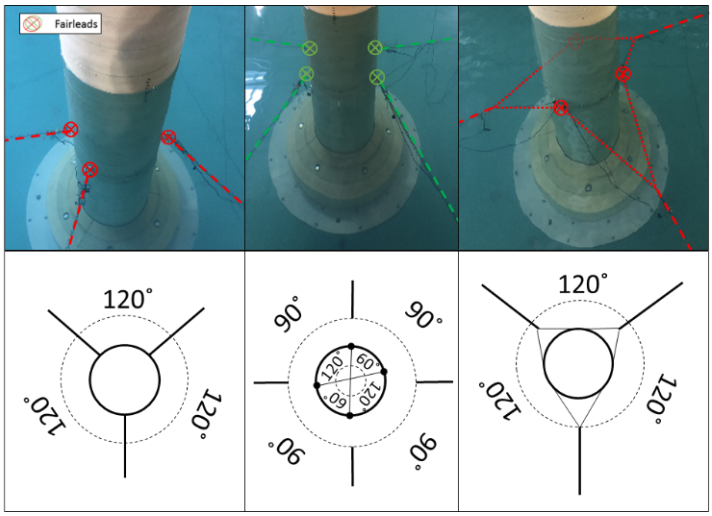

Figure 5.4.1.: Different mooring configurations.

The experiments at Lir NOTF were the basis for seakeeping system selection. Therefore, only the most efficient mooring configuration, i.e. three mooring lines, was tested further at FloWave OERF. Figure 5.4.2 presents the different mooring layouts used at Lir NOTF, whereas Figure 5.4.3 shows the physical arrangement used at FloWave OERF for testing the three mooring lines configuration.

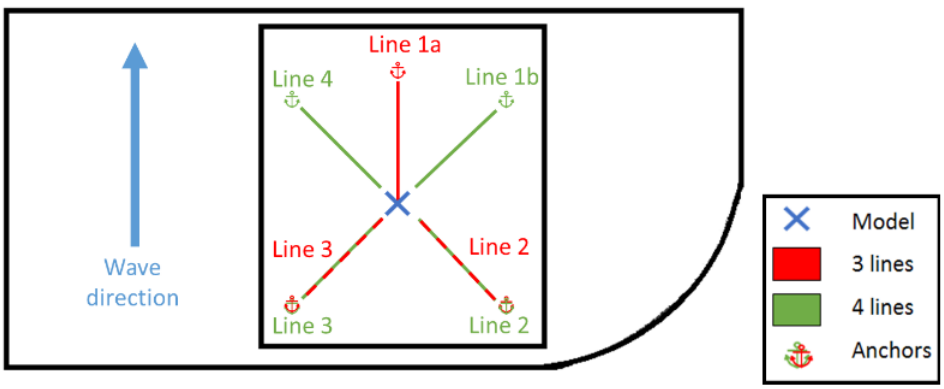

Figure 5.4.2.: Lir NOTF mooring layout.

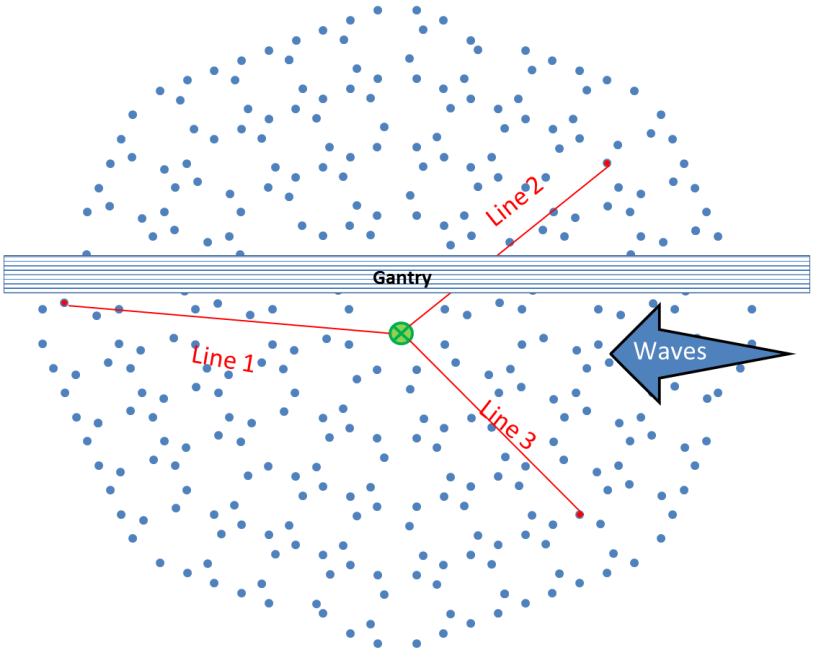

Figure 5.4.3.: Mooring physical arrangement used at FloWave OERF.

Tables 5.5 and 5.6 provide the position of the fairleads for the three and four mooring layouts respectively. All the dimensions provided are related to the scale model with the origin of the coordinate system centred on the lower part of the heave pate, i.e. the vertex in the right quadrant shown in Figure 5.3.

Table 5.5.: Fairleads position in millimetres for the three-mooring layout .

	x (mm)	y (mm)	z (mm)
Line 1	167	0	822
Line 2	-83	144	822
Line 3	-83	-144	822

Table 5.6.: Fairleads position in millimetres for the four-mooring layout.

	x (mm)	y (mm)	z (mm)
Line 1	167	0	822
Line 2	0	167	822
Line 3	-167	0	822
Line 4	0	-167	822

The length and weight are the main factors influencing the behaviour of a mooring line. Tables 5.7, 5.8 and 5.9 provide the mooring line features as tested in Lir NOTF and FloWave OERF respectively. Every line was divided into three different sections, each segment is lighter than its predecessor (Figure 5.7). The mass per unit length of the first section of the chain, the one attached to the model, was 0.37 kg/m, followed by a 0.27 kg/m section, and a lighter 0.08 kg/m section linked to the anchoring point in the floor of the basin.

Table 5.7.: Mooring features for the three-mooring configuration as tested at Lir NOTF.

	Length (m)	Weight (kg)
Line 1	5.11	1.42
Line 2	5.32	1.07
Line 3	5.32	1.07

Table 5.8.: Mooring features for the three-mooring configuration as tested at FloWave OERF.

	Length (m)	Weight (kg)
Line 1	5.70	1.19
Line 2	5.70	1.19
Line 3	5.70	1.19

Table 5.9.: Mooring features for the four-mooring configuration as tested at Lir NOTF

	Length (m)	Weight (kg)
Line 1	5.35	1.01
Line 2	5.32	1.07
Line 3	5.32	1.07
Line 4	5.35	1.02

In order to characterise the three-mooring line with delta connection, an additional 0.44 m and 0.4 kg must be added on top of the three mooring lines configuration values to account for the delta connection setup (illustrated later in Figure 17).

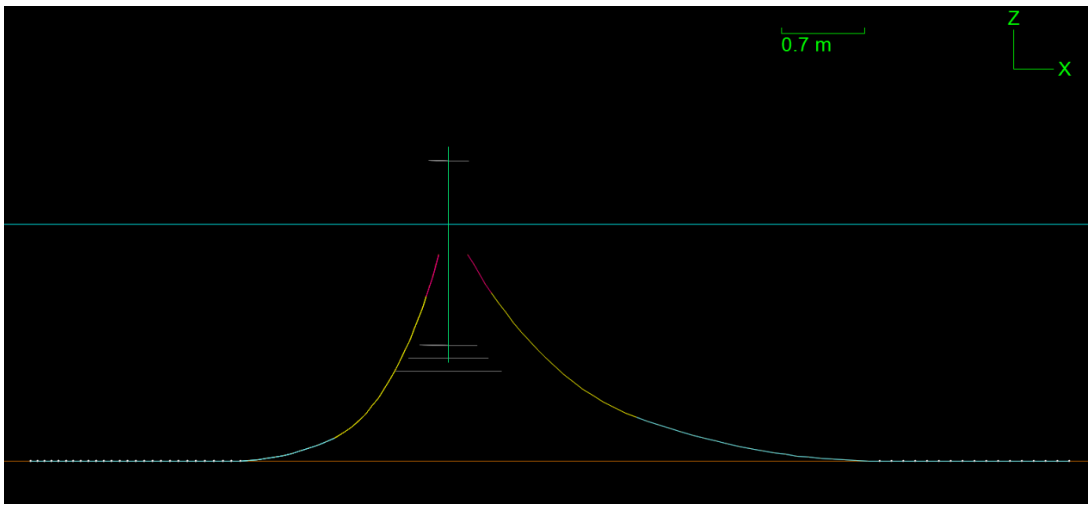

Figure 5.4.4.: Mooring line layout showing the in three different sections in red (0.37 kg/m), yellow (0.27 kg/m), and blue (0.08 kg/m) respectively.

Free floater testing was conducted using two different approaches. At Lir NOTF the floater was strictly free-floating whereas a fine elastic rubber line, i.e. 'soft' mooring configuration, was used at FloWave OERF.

5.5. Instrumentation

The instrumentation listed below were used during the testing, to measure the wave surface elevations in the tank, the loads in the mooring lines, and the motions of the floating platform:

- The generated wave heights were measured using six resistive twin-wire probes (Figure 5.5.1) with an accuracy of ±0.3 mm. Wave probes were connected to a Churchill control amplifier at Lir NOTF meanwhile a National Instruments PXI and CompactDAQ system was used at FloWave OERF.

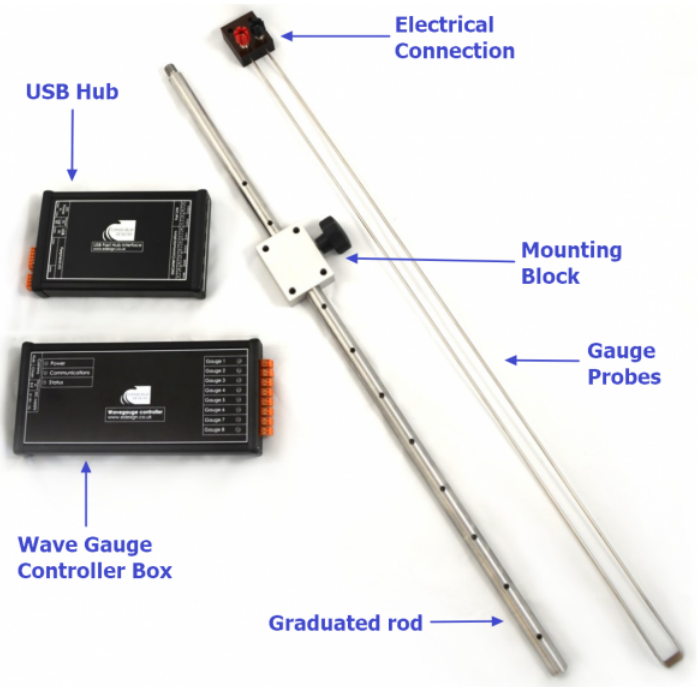

Figure 5.5.1.: Edinburgh Designs resistive wave gauges [77].

- The mooring line tensions were measured at Lir NOTF using four force transducers located between the fairleads and the mooring line. Two different types of transducers, i.e. s-beam and ring (Figure 5.5.2), were used to compare results. For the delta connection configuration, the transducers were installed between the delta

lines and the mooring line as shown in Figure 5.5.3. The weight of the submersible s-beam load cells is 8.5 g, their capacity is 22.2 N, and their accuracy is ±0.02 N.

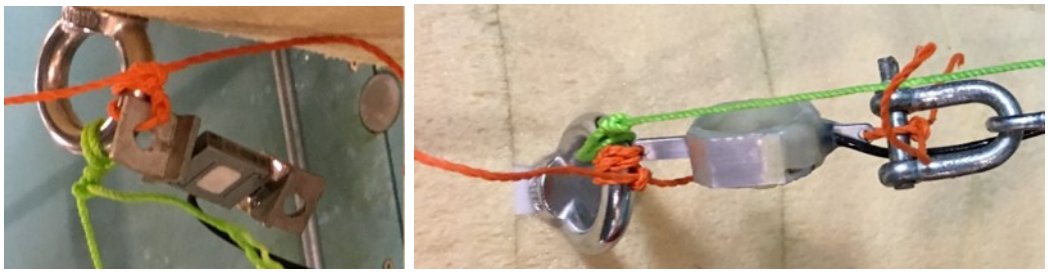

(a) S-beam transducer. (b) Ring transducer.

Figure 5.5.2.: Force transducers.

- The six degrees of freedom (DOF) motions of the floating platform were measured using an optical tracking system. The Qualisys ProReflex MCU was used at Lir NOTF meanwhile Oqus 7+ cameras were used at FloWave OERF. Both systems present an accuracy of ±0.01 mm.

- Qualisys Oqus 5+ underwater cameras were used at FloWave OERF to record the three degrees of freedom (DOF) motions of mooring lines. The accuray of the underwater optical tracking system is ±0.1mm.

The resistive twin-wire probes and the force transducers are analogue output measuring equipment. They are designed to generate a current signal (or analogue voltage) which is linearly proportional to the measured parameter. Therefore, analogue instruments need calibration to find out the proportionality constant. On the contrary, the Qualisys system is an instrument with digital output, i.e. with a characteristic digital signal protocol. It is complex dealing with different types of concurrent signals, and getting the whole system simultaneously triggered is a challenge. Transducers apart, the system needed to perform measurements within the tank facility includes amplifiers, signal conditioning system, i.e. filters, AD converters; data store and a communication system, e.g. cabling, wireless.

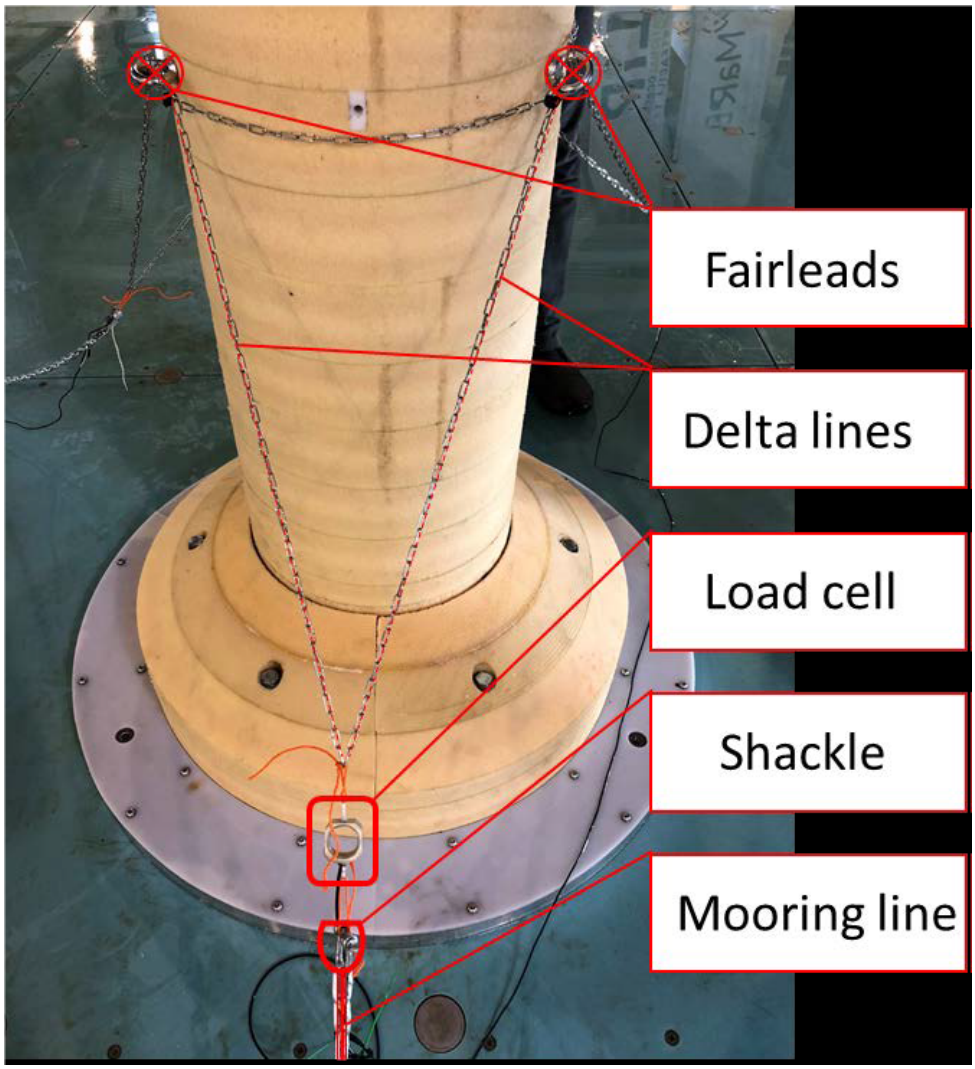

Figure 5.5.3.: Detail of the delta connection setup.

5.6. Testing conditions

Two different groups of experiments regarding the characterisation of FOWT are described and commented: 'dry' and 'wet' tests. 'Dry' tests comprise inclination, swing, and mooring line tensile tests. Inclination and swing test were carried out within FloWave OERF premises, the tensile tests were performed in the above-mentioned structural lab, whereas 'wet' tests i.e. static, quasi-static, and hydrodynamic tests, were conducted in

the two aforementioned wave basins.

Static and quasi-static tests were performed in still water conditions to determine the draft of the model and the mooring line stiffness.

Free decay tests were carried out for heave, pitch and roll modes of motion, whereas stiffness decay tests were also conducted for the surge, sway, and yaw modes of motions. The objective is to define the resonance properties and hydrodynamic coefficients for the free floater and the complete system including the three different mooring line configurations.

Regular wave testing, simulating waves with amplitudes of 44, 100, and 110 mm and periods ranging from 0.70 to 3.33 s were carried out to compute the displacements and the cable force response amplitude operators (RAOs). These tests correspond to wave with a period from 4.7 to 22.4 s and height from 2 to 5 m at full scale, which represents moderate to rough operational sea states, but not extreme sea states at the Peterhead site.

Three random sea states were generated using the Joint North Sea Wave Observation Project (JONSWAP) spectrum with H_s of 40, 101, and 150 mm and T_p of 0.89, 1.27, and 1.41 s were also tested. The experiments using random wave also included line lost tests. The line lost tests were performed using the mentioned JONSWAP irregular seas but releasing some of the mooring lines sequentially during the test.

Table 5.10 summarises the experiments conducted at Lir NOTF and FloWave OERF respectively.

Table 5.10.: Summary of the test programme conducted.

Type of tests	Tests @ Lir NOTF	Tests @ FloWave OERF
Free decay tests	9	21
Stiffness decay tests	36	41
Regular wave tests	88	139
Irregular wave tests	26	9

5.7. Wave quality

The wave quality at Lir NOTF is depicted in Figure 5.7.1. It has been found that the wave height produced during regular wave experiments, i.e. 44 and 110 mm for Lir NOTF, is smaller than the target. The 44 mm waves were off by 23% for low frequencies arising until 27% for higher frequencies. The 110mm waves present a 10% discrepancy with the target for low frequencies while for higher frequencies the experimental wave matches the target adequately. The wave heights produced during random wave experiments were off by 7% and 4% for waves of 150 mm and 1.41 s, and 101 mm and 1.27 s respectively, whereas the random waves produced with a H_s of 40 mm and a T_p of 0.89 s matched the target. Regarding the periods, the overall matching reaches 96% although specific cases are off by 7%.

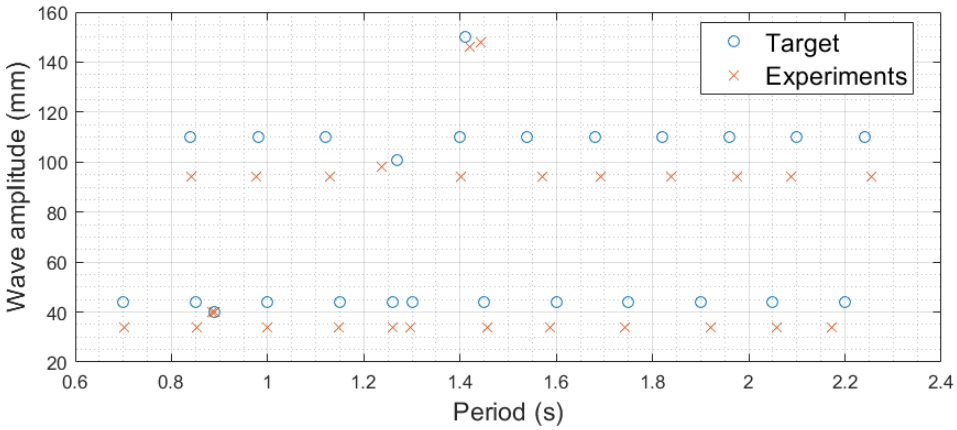

Figure 5.7.1.: Wave quality at Lir NOTF.

The quality of the waves at FloWave OERF is shown in Figure 5.7.2. Once again, the wave height of the experiments is smaller than the target wave. However, due to the smaller target wave height, i.e. 20 mm instead of 44 mm, the wave height produced presents an overall 5% discrepancy with the target wave height. It is worth noting that two cases, i.e. regular wave with a period of 0.5 s, and random wave with a peak period of 1.27 s reach the 18% discrepancy in wave height. Regarding the periods, the overall

matching reaches 99% although specific cases were off by 5%.

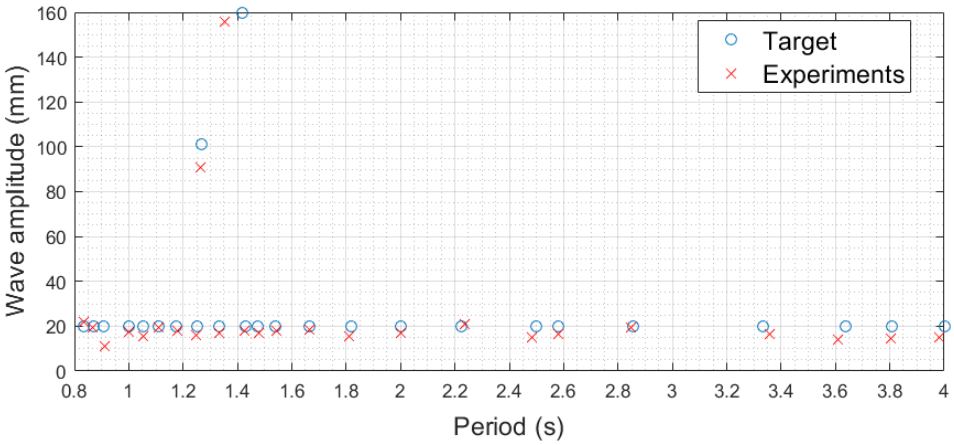

Figure 5.7.2.: Wave quality at FloWave OERF.

Figure 5.7.3 shows a typical wave profile for a regular wave recorded at Lir NORT. Figure 5.7.3a shows the wave height as recorded for a target wave of 44 mm height and a period of 0.85 s, and Figure 5.7.3b presents an ampliation of the record showing how the experimental wave compares with the target wave. Figure 5.7.5 presents similar results to the ones shown in Figure 5.7.3 but recorded in FloWave OERF. Therefore, the target wave height is 40 mm and the target regular period is 0.87 s. Figures 5.7.4 and 5.7.6 show a typical wave profile and spectral density for irregular waves recorded at Lir NORT and FloWave OERF respectively. Figures 5.7.7 and 5.7.8 present the part of the record used for the wave quality assessment. Only initial transients caused by the start-up condition of the wavemaker and last cycles of the record are excluded for the analysis. The reflected waves are included in the analysis.

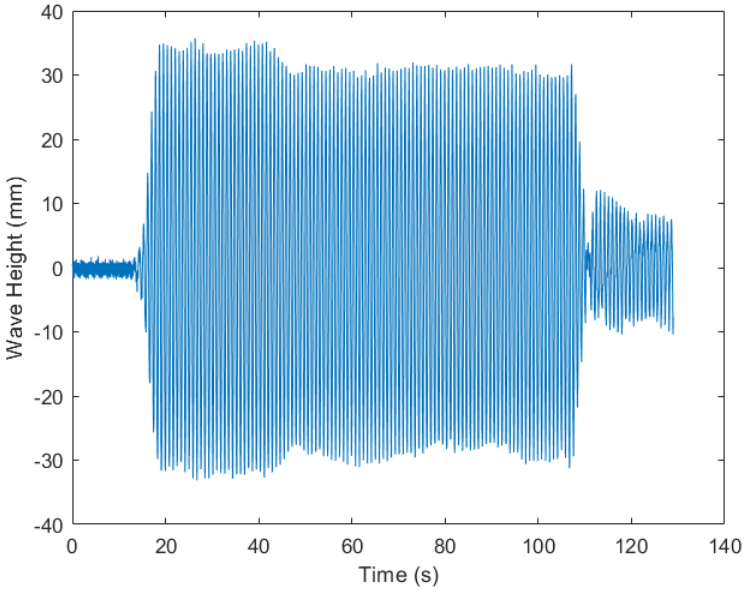

(a) Wave height as recorded for a target wave of 44 mm height and a period of 0.85 s.

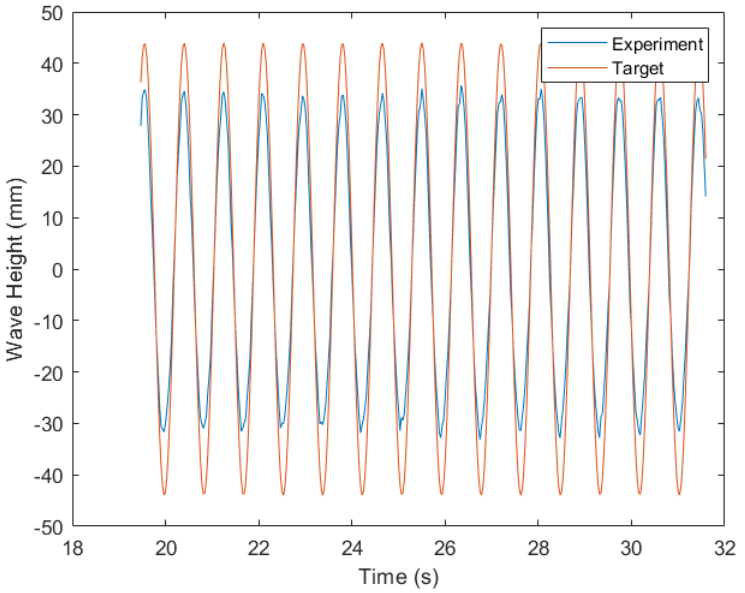

(b) Zoom of the record comparing the experimentally produced wave with the target wave.

Figure 5.7.3.: Regular wave profiles recorded at Lir NOTF.

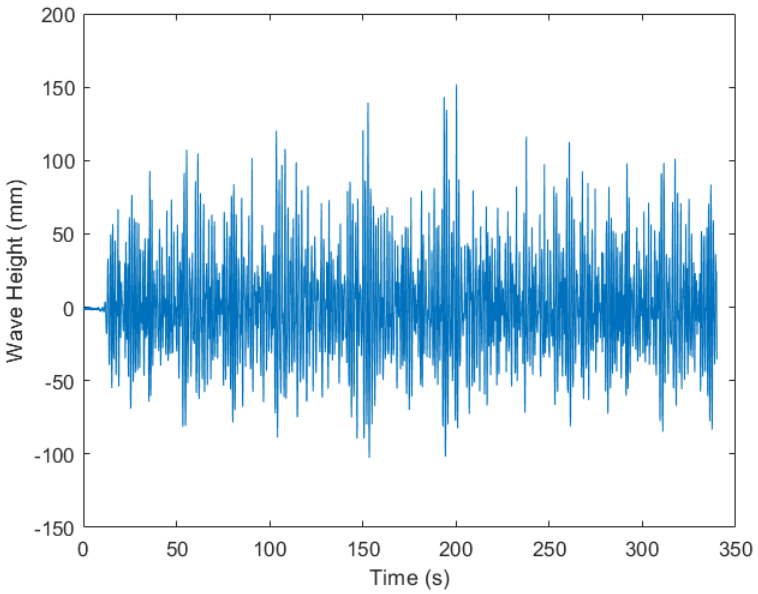

(a) Records for H_s of 150 mm and T_p of 1.41 s

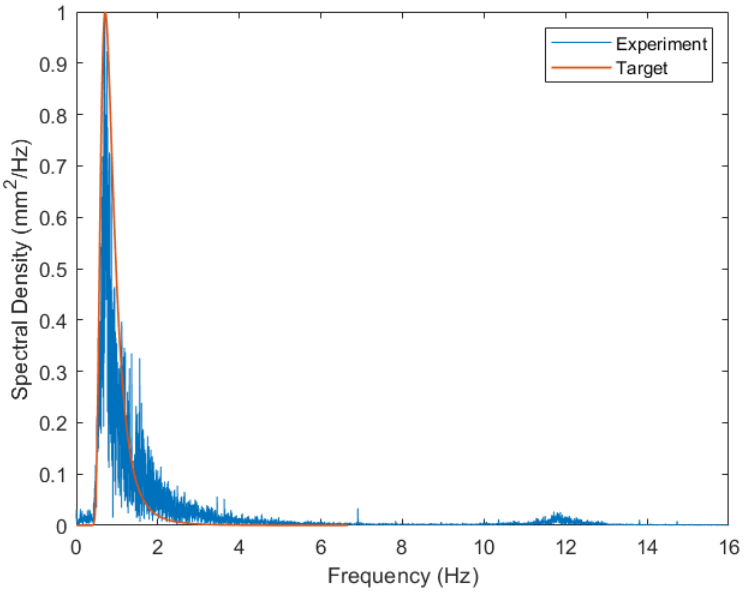

(b) Spectral density for H_s of 150 mm and T_p of 1.41 s.

Figure 5.7.4.: Wave profile and spectral density for irregular waves recorded at Lir NOTF.

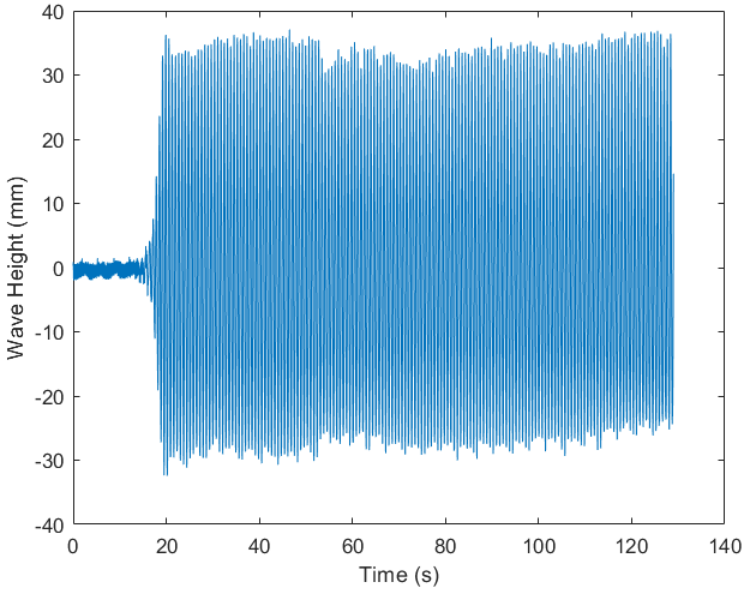

(a) Wave height as recorded for a target wave of 40 mm height and a period of 0.87 s.

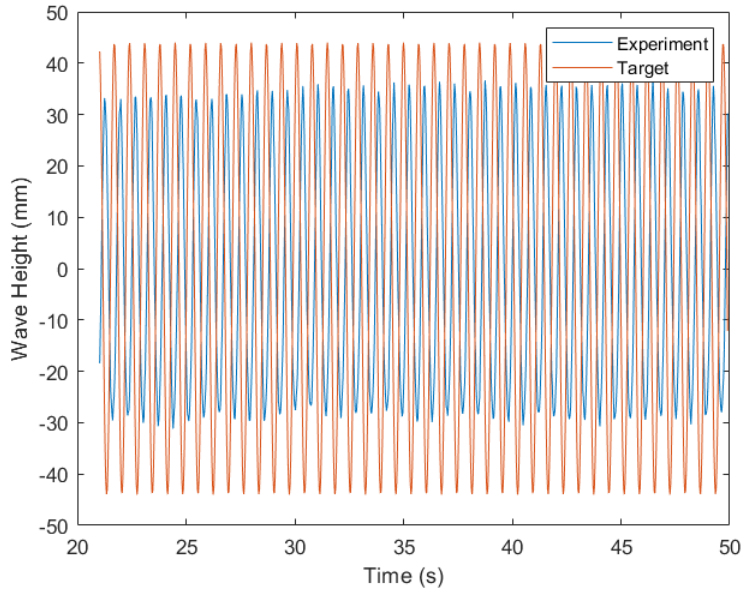

(b) Zoom of the record comparing the experimentally produced wave with the target wave.

Figure 5.7.5.: Regular wave profiles recorded at FloWave OERF.

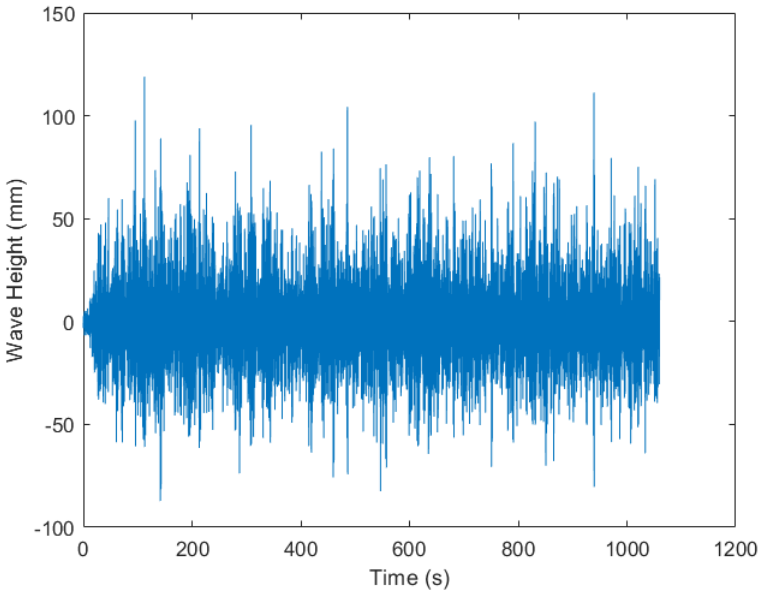

(a) Records for a H_s of 101 mm and T_p of 1.27 s.

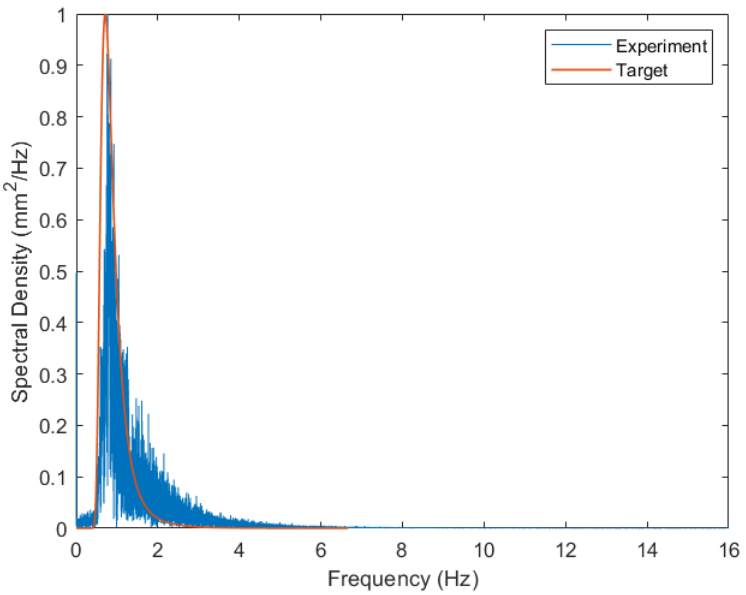

(b) Spectral density for a H_s of 101 mm and T_p of 1.27 s.

Figure 5.7.6.: Wave profile and spectral density for irregular waves recorded at FloWave OERF.

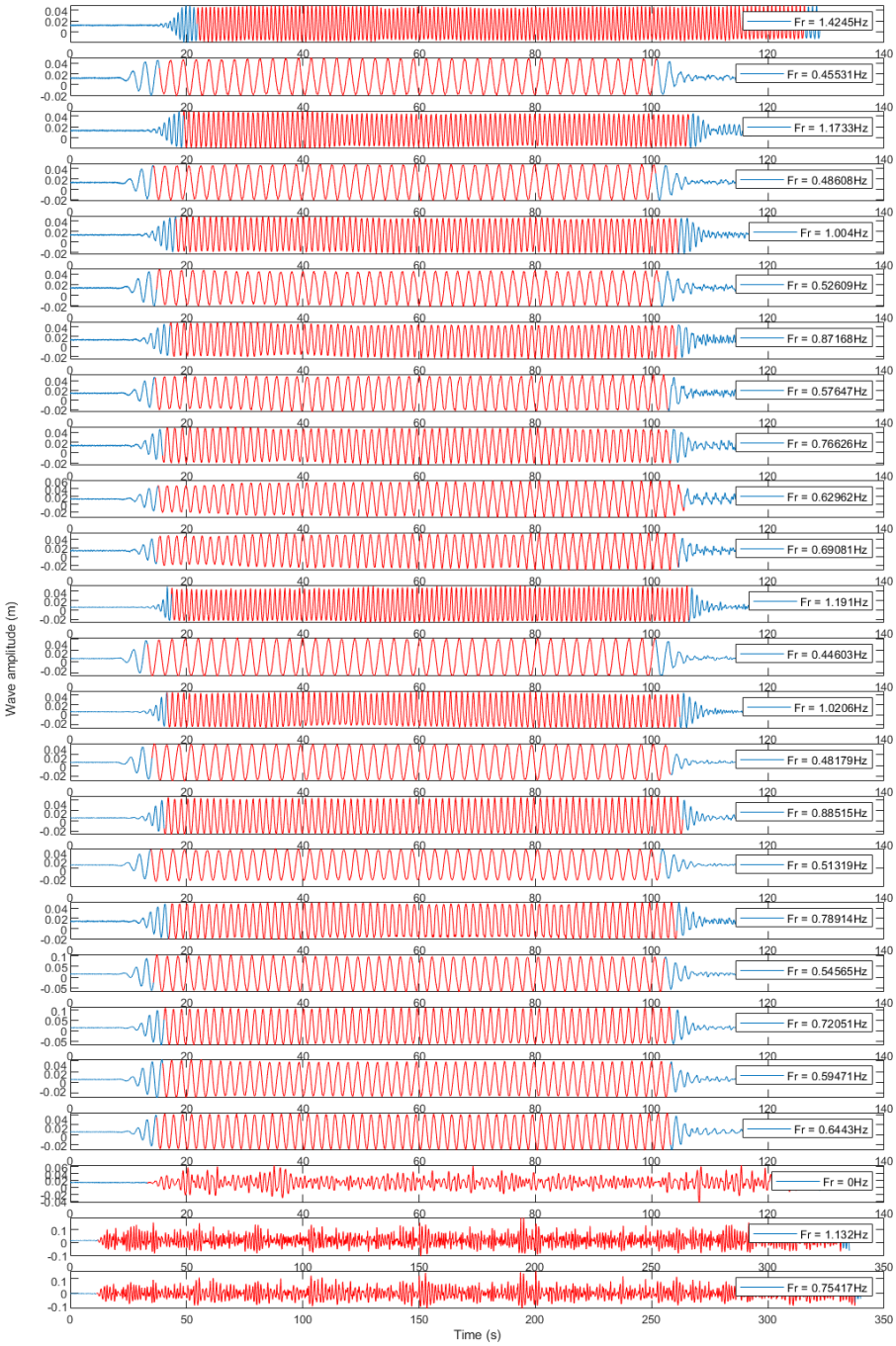

Figure 5.7.7.: Full record of the wave probe and the part used for wave quality analysis highlighted in red for the experiments conducted in Lir NOTF.

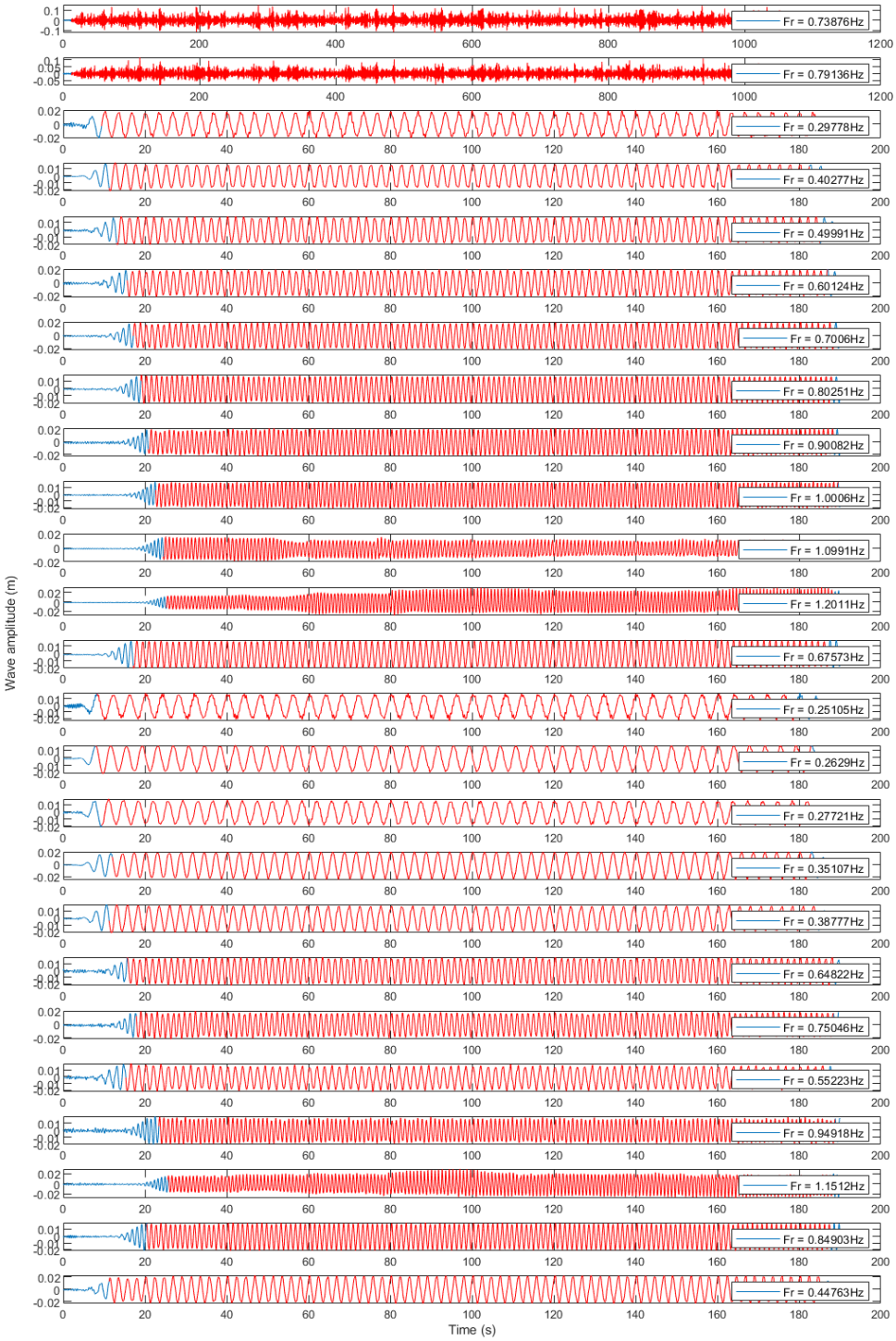

Figure 5.7.8.: Full record of the wave probe and the part used for wave quality analysis highlighted in red for the experiments conducted in FloWave OERF.

5.8. Dry tests

Several experimental techniques are included within the category of dry tests when refereeing to FOWT. Usually, the term applies to wind tunnel testing. However, other experiments such as inclination tests, swing tests, and catenary axial stiffness tests are also covered.

Inclination and swing tests are conducted using a tilting test rig. The testing rig consists of a free frame able to swing within the base frame. The contact between the two frames has been designed to minimise the loss of energy while swinging. The setup is a pendulum arrangement where the oscillation period of the frame alone or a system (frame plus model) can be calculated. First, the rig natural period of oscillation is calculated, i.e. frame without the model. Then the model is tested along with a known mass situated sequentially at different heights to find the CoG of the model. Finally, the model is tested with two additional masses situated at a known distance from the frame oscillation centre, and the period of the whole system is measured. Using the pendulum equations and knowing the oscillation period of the frame alone, the MoI of the model can be calculated. The setup used to perform the mass properties testing, i.e. CoG height and MoI, is shown in Figure 5.8.1. The tilting test rig includes the base and the free frames, a high accuracy inclinometer, and the digital acquisition (DAQ) system including a computer to record the oscillation data. Further information regarding inclination and swing tests can be consulted in [78, 79].

Figure 5.8.1.: Tilting test rig.

The catenary axial stiffness experiment was conducted after the two hydrodynamic tests to validate the elastic modulus of the mooring lines. The stiffness of a line is the stress-strain relationship. The elastic modulus is the product of the stiffness and the initial length of the sample (20 cm) divided by the cross-sectional area of the sample. The cross-sectional area of the chain must be calculated based on the equivalent diameter (0.0033 m) of the chain. It is important to test the chain up to the level of loads reached during the hydrodynamic testing. Figure 5.8.2 shows the setup explained in Section 5.3 along with the chain sample as tested in the structural laboratory.

Figure 5.8.2.: Catenary axial stiffness experiment as performed in the structural laboratory.

Figure 5.8.3 presents the typical result of a catenary axial stiffness testing with a fitted regression line. The slope of the regression line is equivalent to Young's modulus of the chain.

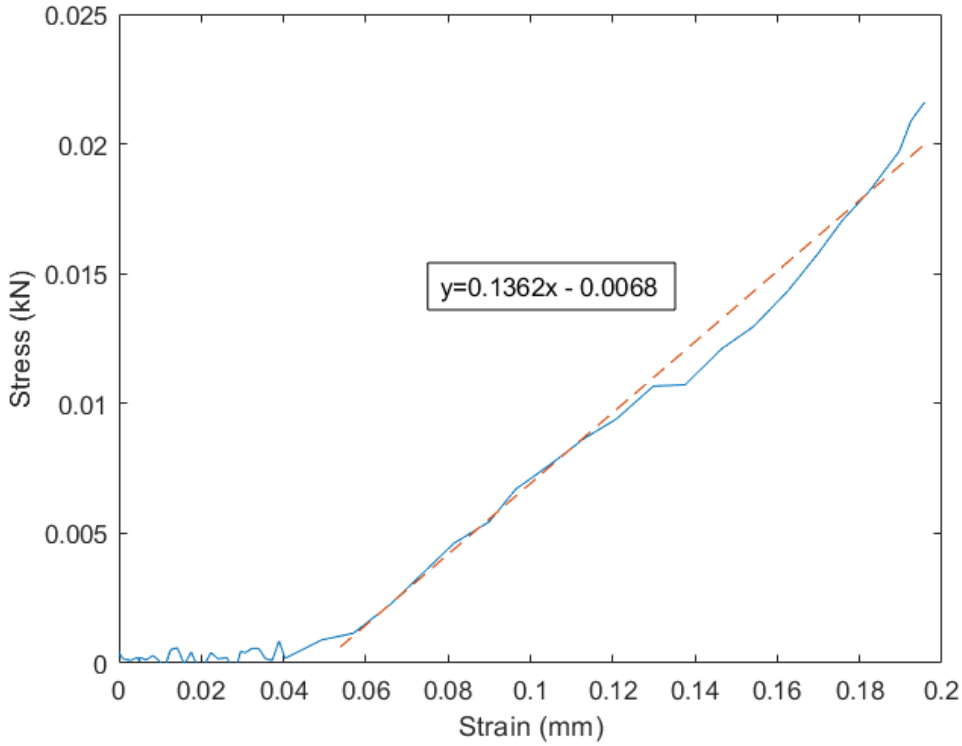

Figure 5.8.3.: Result of a catenary axial stiffness testing.

5.9. Static and quasi-static testing

As aforementioned, the main objective of the static testing is determining the draft of the floating system with and without the mooring lines. Figure 5.9.1 shows the initial draft of the floater with and without mooring lines, as tested at Lir NOTF. Static testing also provides information regarding the heel and trim of the floater. Figure 5.9.2 shows the trim and heel of the free floater at Lir NOTF.

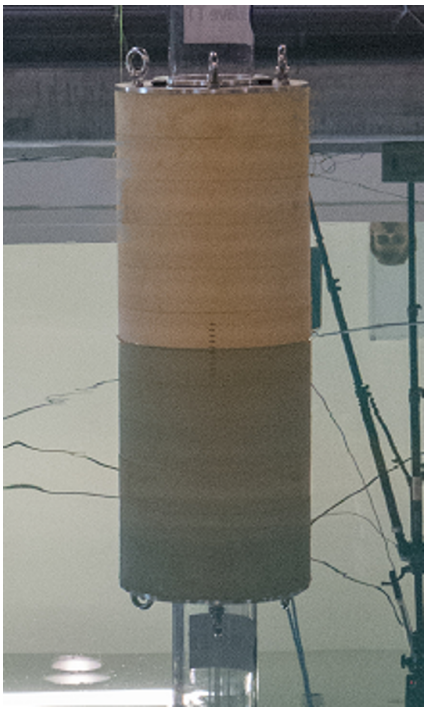

(a) Draft of the floater without mooring lines.

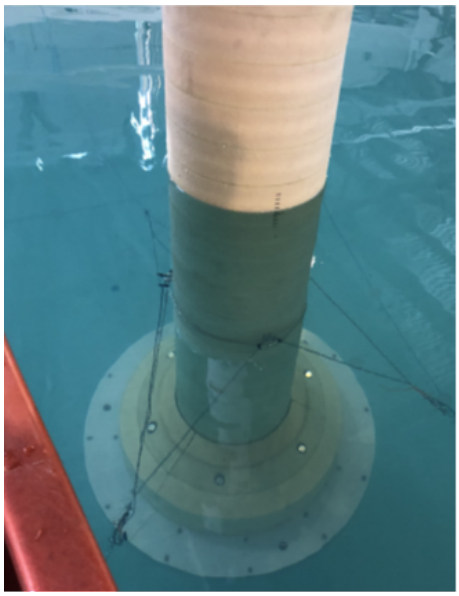

(b) Draft of the floater with three mooring lines.

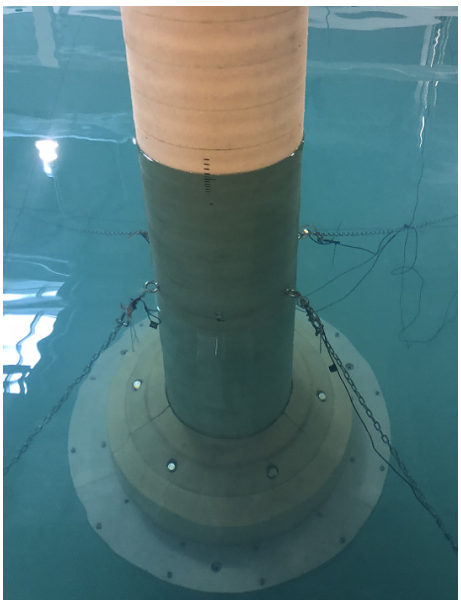

(c) Draft of the floater with four mooring lines.

Figure 5.9.1.: Draft of the floater as tested at Lir NOTF.

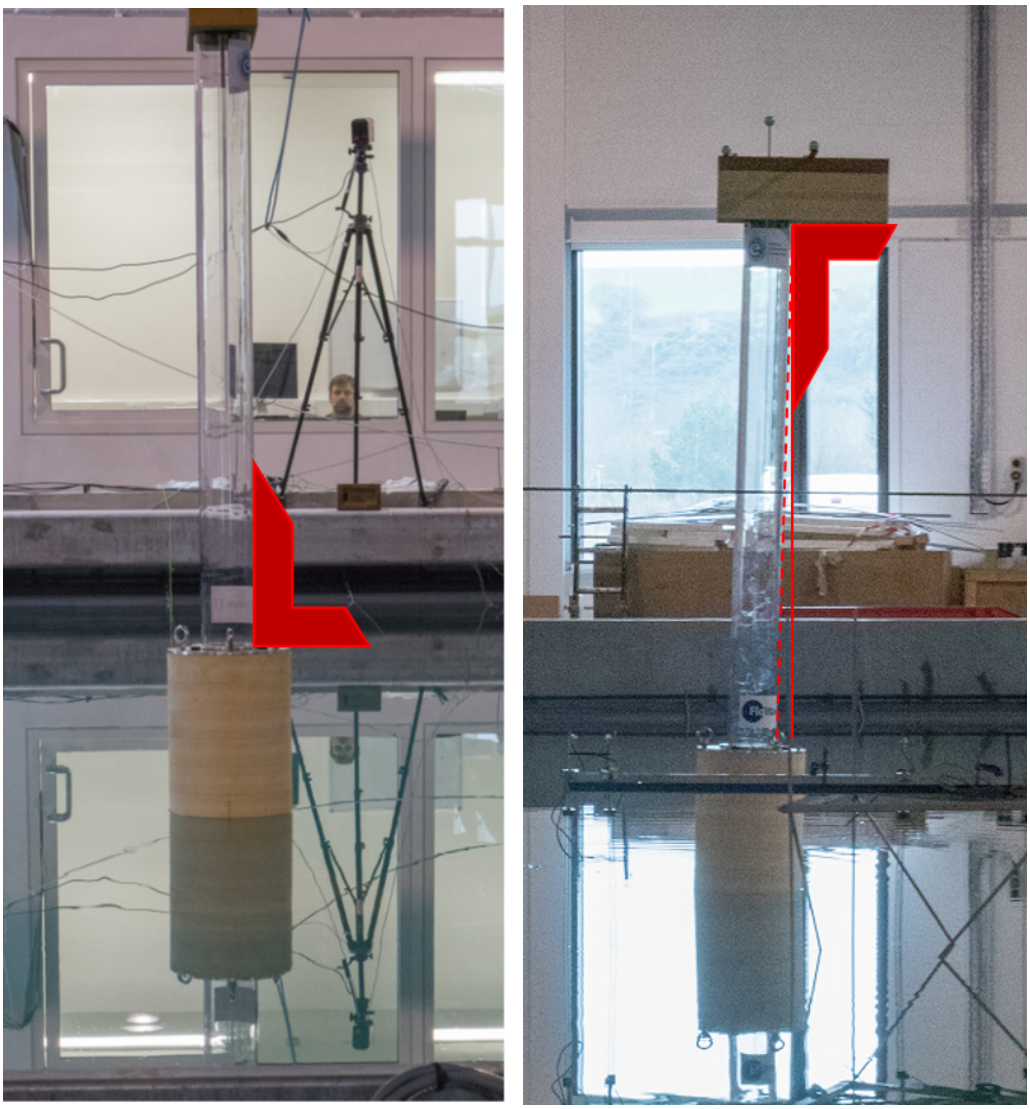

(a) Trim of the free floater.

(b) Heel of the free floater.

Figure 5.9.2.: Static testing at Lir NOTF.

Figures 5.9.3 and 5.9.4 show the initial draft of the floater with the 'soft' and the catenary mooring respectively, as tested at FloWave OERF. One of the objectives of the testing at FloWave OERF was to eliminate any trim or heel on the model in still water conditions. Therefore, the model was re-ballasted until it looked trimmed and heeled at zero degrees, i.e. no trim or heel. Thorough checking of the draft and trim and heel angles were performed in both basins.

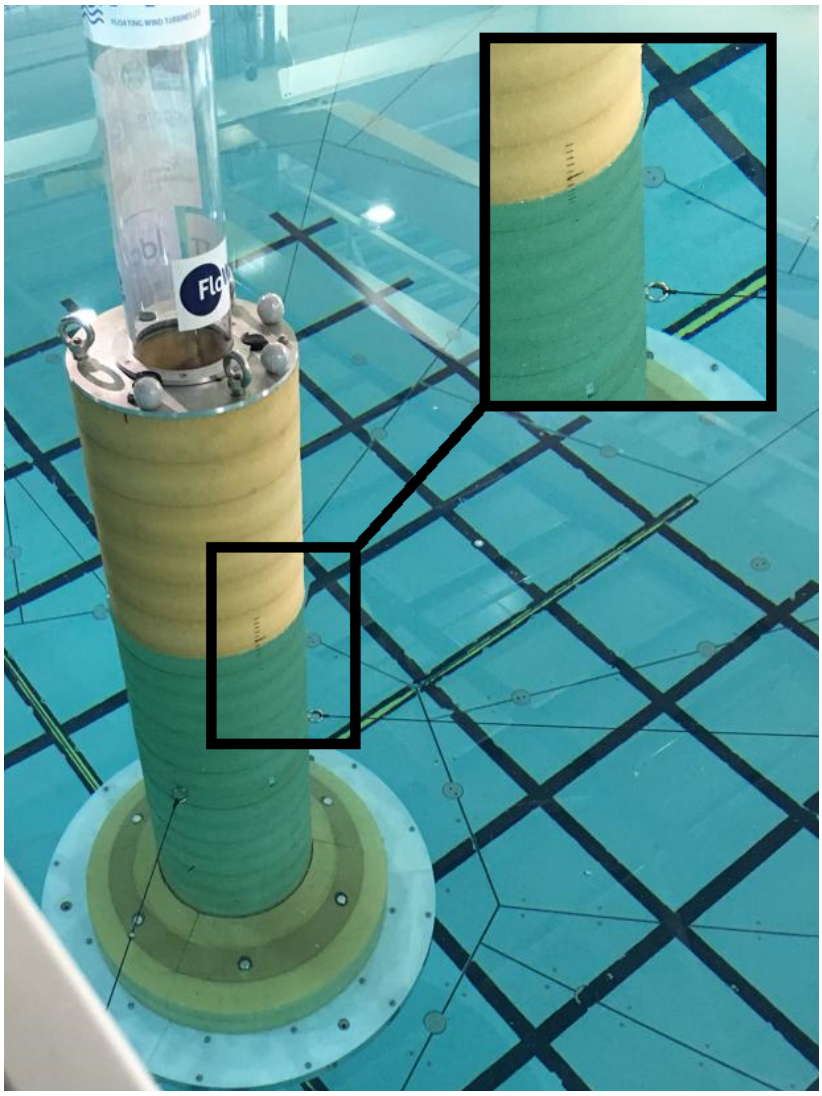

Figure 5.9.3.: Draft of the floater with the 'soft' mooring lines, as tested at FloWave OERF.

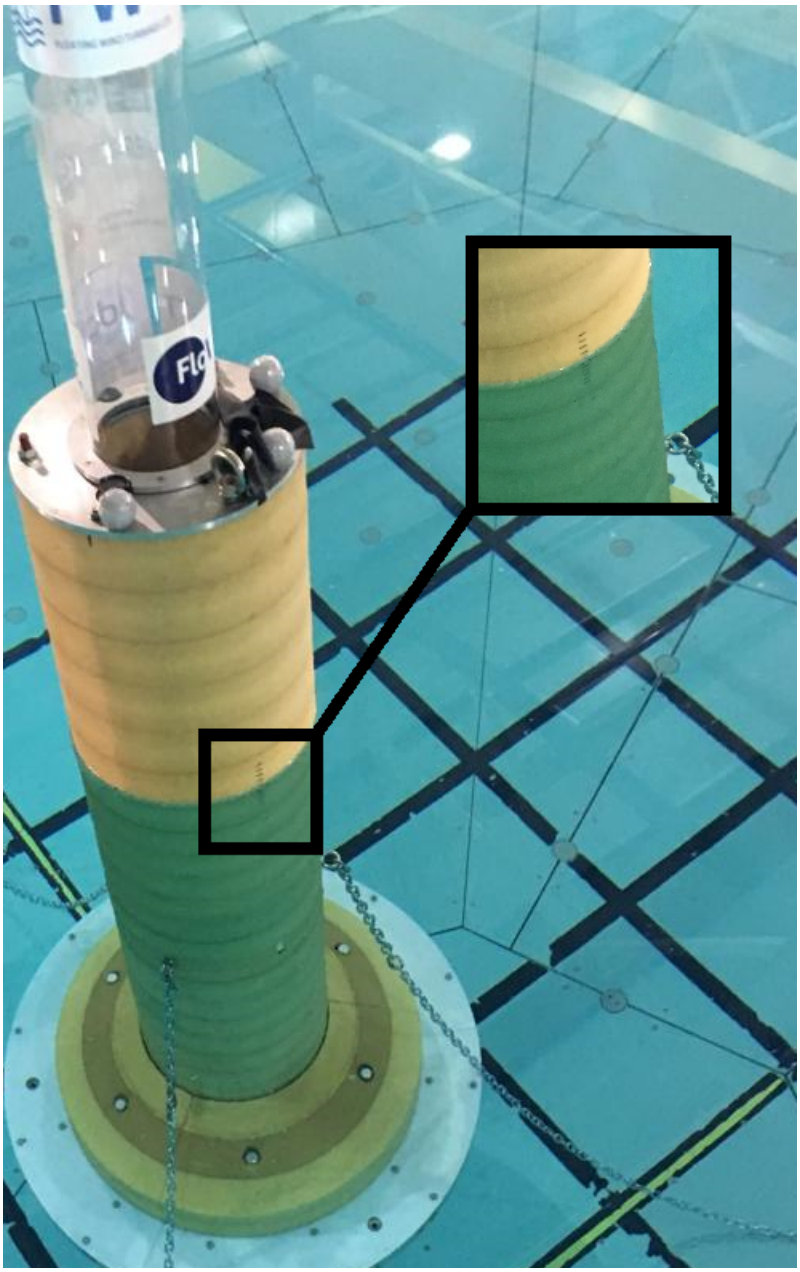

Figure 5.9.4.: Draft of the floater with the catenary mooring lines, as tested at FloWave OERF.

Quasi-static tests were carried out to identify the line stiffness in a certain direction. The test is conducted in still water conditions. A string is attached at the CoG height of the model on the opposite side to the line that must be tested (Figure 5.9.5). By hanging

a set of weights sequentially, the horizontal position, i.e. surge, of the floater changes, and by plotting the change of horizontal position of the floater against the tensions induced by the hanging weights, the global mooring line stiffness can be identified. This experiment was conducted only in FloWave OERF.

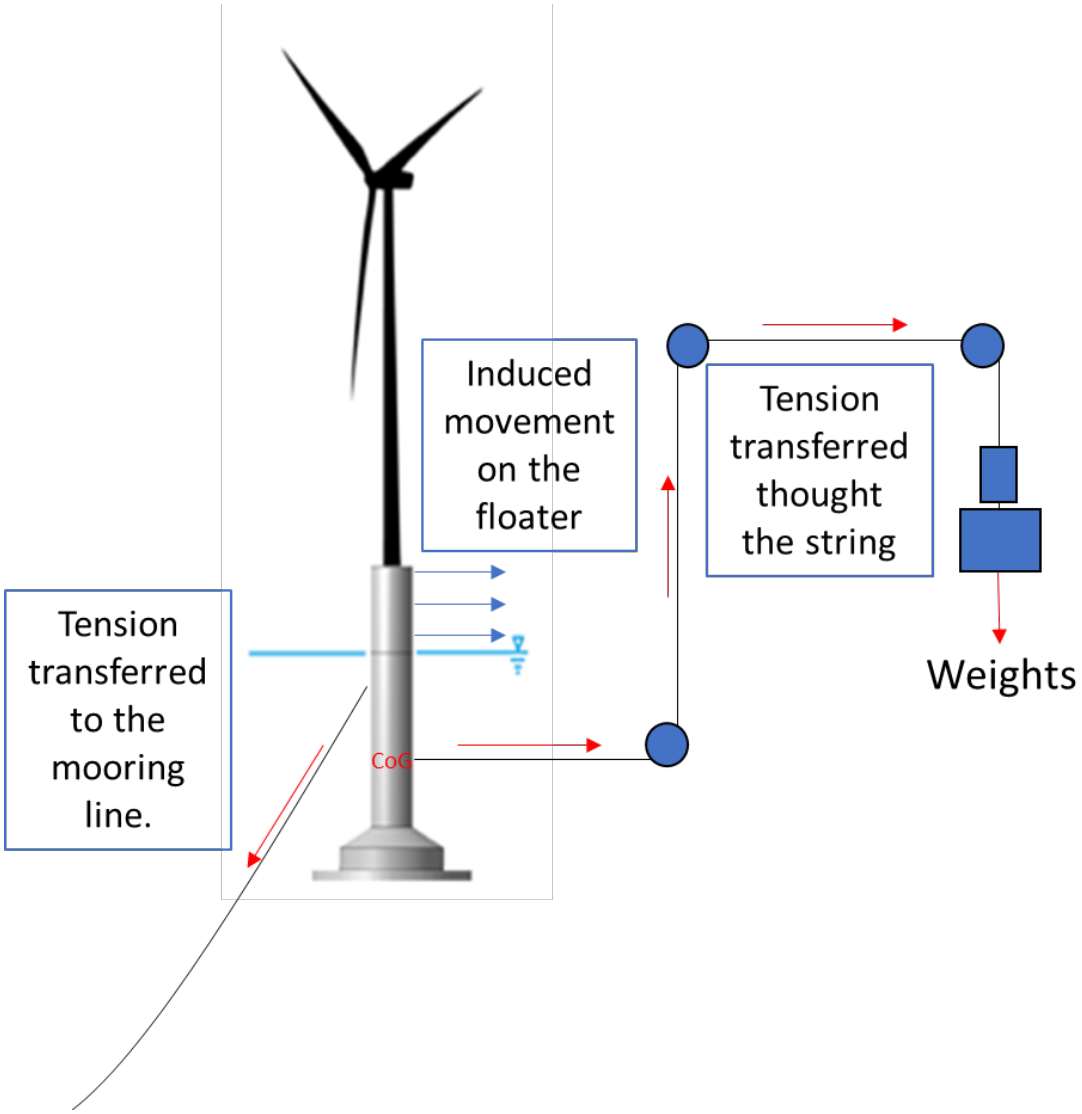

Figure 5.9.5.: Setup used to test the line stiffness in surge at FloWave OERF.

5.10. Decay testing

To experimentally obtain the resonance properties and hydrodynamic coefficients for the free floater and the complete floating system including the three different mooring line configurations, free decay and stiffness decay tests were performed at Lir NOTF and FloWave OERF. Free decay tests were carried out for heave, pitch and roll modes of motion, whereas stiffness decay tests were also conducted for the surge, sway, and yaw modes of motions. The decay testing at Lir NOTF was the basis for mooring configuration selection. Therefore, only the selected mooring line configuration was further checked at FloWave OERF.

5.10.1. Free decay testing

Free decay tests were carried out with no moorings attached at Lir NOTF, whereas a 'soft' mooring configuration, i.e. fine elastic rubber line, was used at FloWave OERF. Lir NOTF facilities lacked the gantry, i.e. footbridge, when the tests were conducted. Therefore, a boat was used to approach the model and provide the excitation for the test.

Each set of tests was repeated several times, e.g. three times at Lir NOTF and six times at FloWave OERF, to check for experimental bias. These experiments were conducted by applying a prescribed displacement in heave, pitch and roll from the stationary equilibrium position, and cautiously releasing the model allowing it to free oscillate.

Figure 5.10.1 presents an overview of the typical record obtained from a heave free decay test at Lir NOTF. Figure 5.10.2 shows heave free decay test results as recorded at FloWave OERF. Both records include the surge, sway, roll, pitch, and yaw motions occurring simultaneously. It is essential to verify that the magnitude of the tested motion is larger than the other modes of motion to ensure that most of the energy within the system has been employed to produce the tested motion.

To compute overall damping coefficients and natural frequencies, the procedure explained in [80] has been followed. Overall damping can be split into its linear (radiation damping) and quadratic (viscous damping) components using the procedure explained in [81] and shown in Figure 5.10.3. An example of how to apply step by step the methodology is presented in [82].

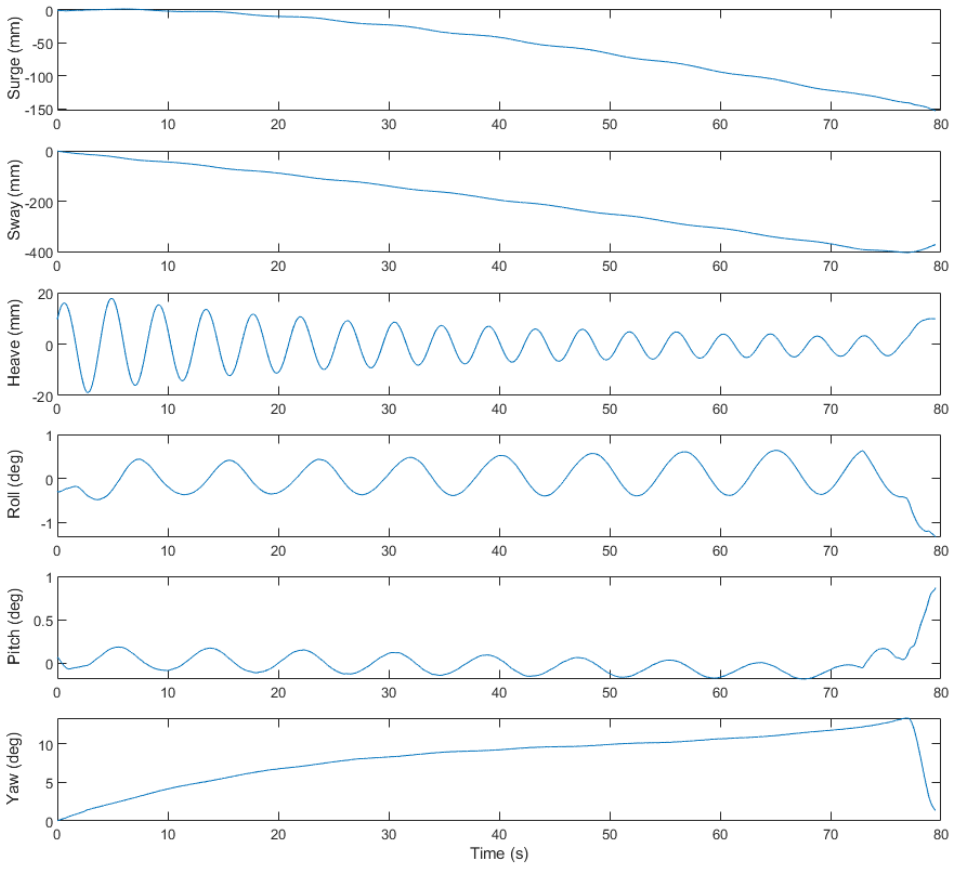

Figure 5.10.1.: Typical record of a heave free decay test at Lir NOTF.

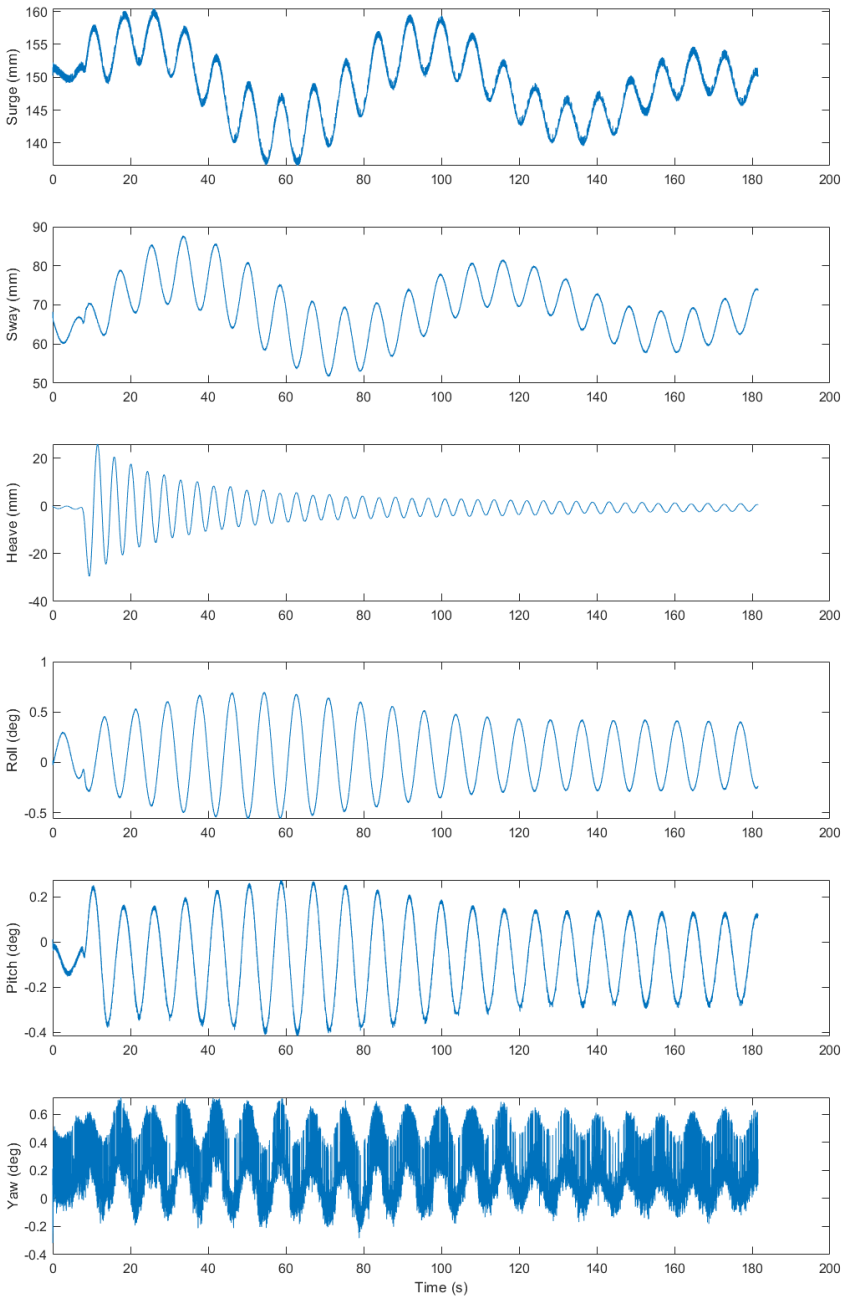

Figure 5.10.2.: Typical record of a heave free decay test at FloWave OERF.

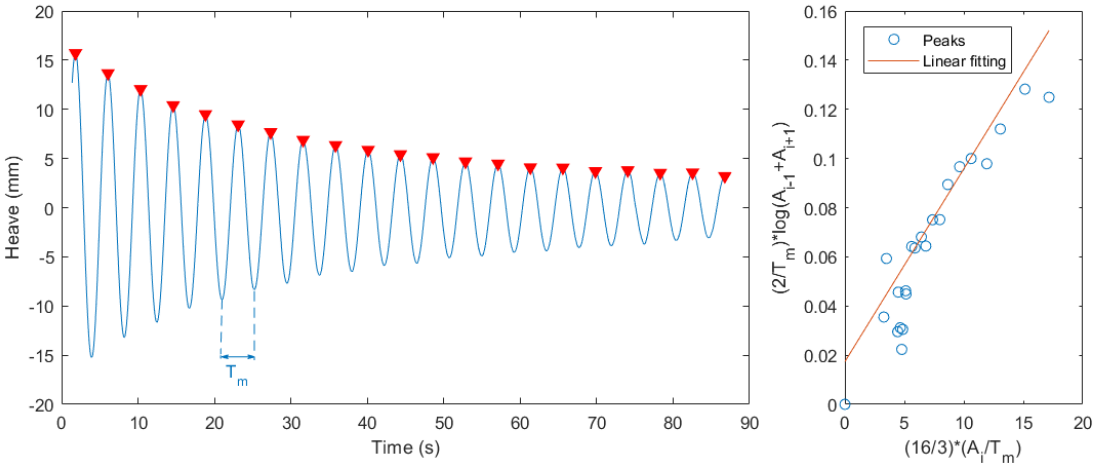

Figure 5.10.3.: Procedure to split damping into linear damping (radiation damping) and quadratic (viscous damping) components using the method explained in [81].

5.10.2. Stiffness decay testing

Stiffness decay tests in heave, surge, sway, yaw, pitch, and roll modes of motion were carried out to define the resonance properties and hydrodynamic coefficients of the floating system including the three different mooring line configurations. As in the case of the free decay tests, the stiffness decay experiments were performed by applying displacement to the moored floater in all six modes of motion and then releasing it. The mooring system counteracts the excitation and moving the floater back to the stationary equilibrium position, the whole system starts to oscillate, i.e. dissipate energy. Again, a boat was used (Figure 5.10.4) to approach the model and provide the excitation for the test at Lir NOTF whereas the gantry was used at FloWave OERF.

Figure 5.10.4.: Method used at Lir NOTF to approach the model and provide the excitation for the free decay experiment since the facilities lacked gantry when the tests were conducted.

Figure 5.10.5 presents the typical record from a heave free decay test as performed at Lir NOTF. It is worth noting the effect of the boat movement at the beginning the record in the sixth time series labelled WP for wave probe. Using the same procedures mentioned for the analysing of the free decay tests, the natural frequencies and damping coefficients for the floating system including the mooring lines were calculated and damping was split into its linear (radiation damping) and quadratic (viscous damping) components.

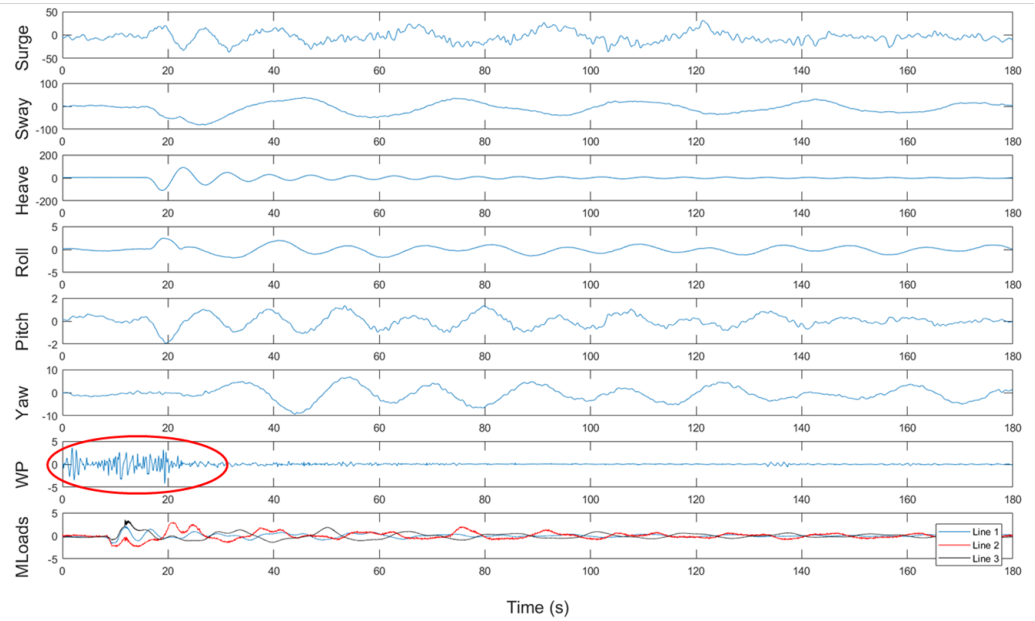

Figure 5.10.5.: Typical record obtained from a heave stiffness decay test as performed at Lir NOTF.

5.11. Regular wave testing

Regular wave tests aim to evaluate the behaviour of the system in a controlled environment by assessing the RAOs. RAO is a non-dimensional transfer function relating the wave elevation and the response amplitude for a certain degree of freedom used to evaluate the performance of the structure in the frequency domain. Regular wave testing was performed for both moored and 'free floater' conditions although the 'free floater' testing was conducted only at FloWave OERF and using the 'soft' mooring line configuration to avoid excessive drift. Moored regular testing included experiments with the three different mooring configurations, i.e. three, four, and three mooring lines with delta connection at Lir NOTF but only the three mooring line configuration at FloWave OERF. Figures 5.11.1 and 5.11.2 show typical records obtained from regular testing at Lir NOTF and FloWave OERF respectively.

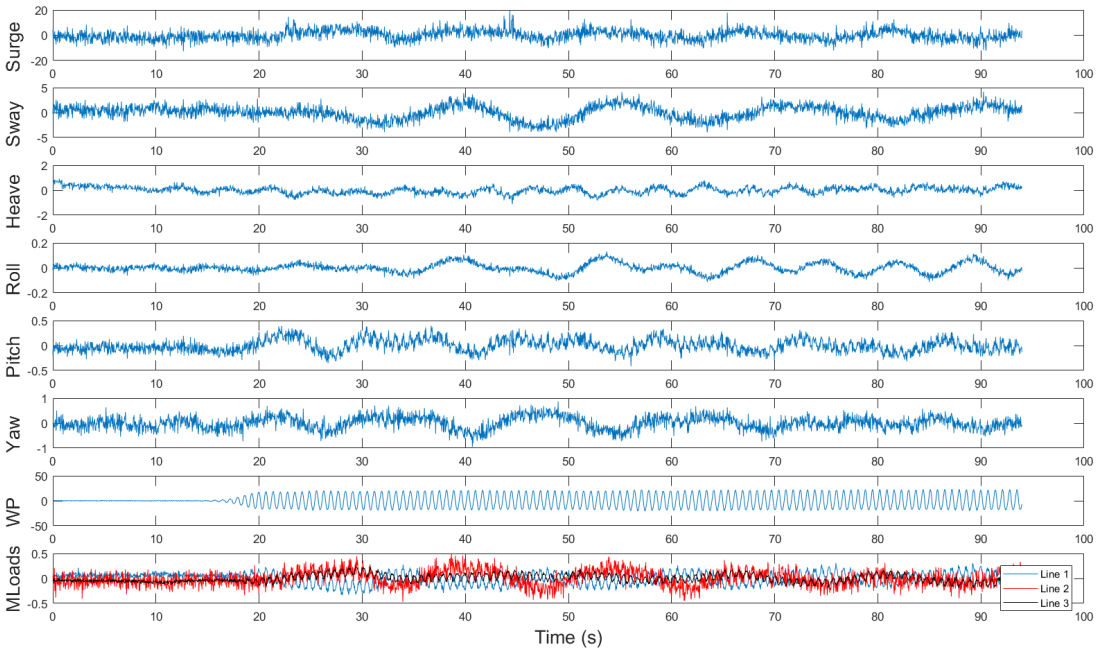

Figure 5.11.1.: Typical records obtained from regular testing at Lir NOTF. Results expressed in millimetres, degrees, and Newtons.

Figure 5.11.1 presents the responses of the six modes of motion of the floater, the record of the wave probe, and the mooring line tensions whereas Figure 5.11.2 lacks tensions records.

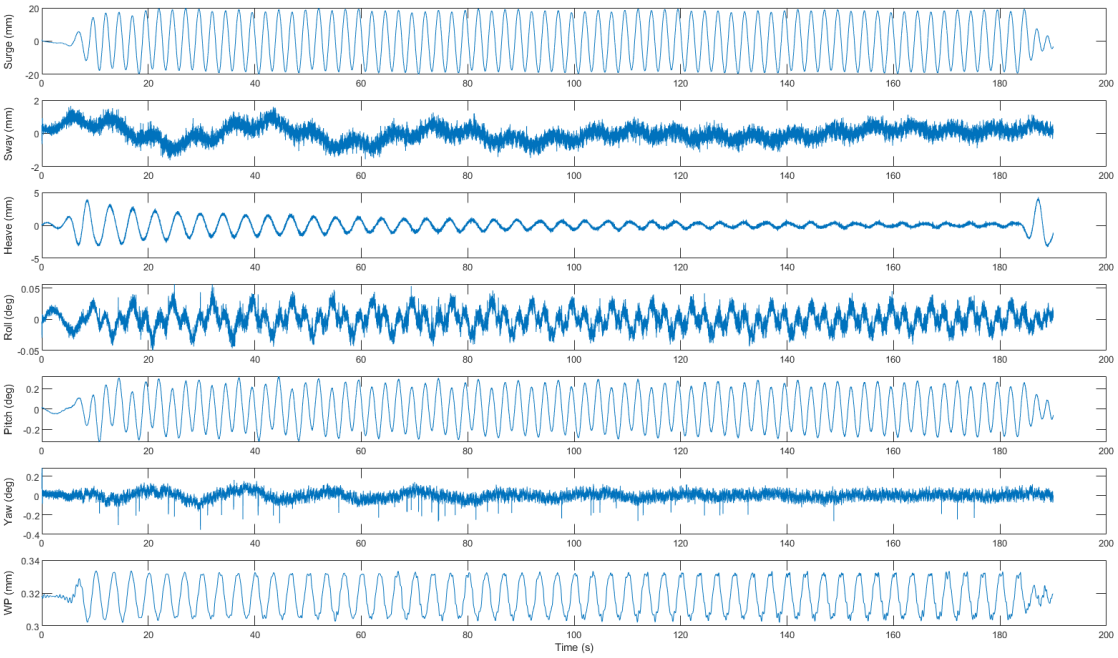

Figure 5.11.2.: Typical records obtained from regular testing at FloWave OERF.

It is worth noting, that the regular wave test records are noisier in Lir NOTF than in FloWave OERF, i.e. records in Figure 5.11.1 is noisier that records in Figure 5.11.2. Regardless of the quality of the data, the most challenging aspect regarding the RAO computation is choosing the part of the record to be analysed. It is a subjective task that requires experience, and a deep understanding of the objectives sought. This is discussed later in Section 5.15. Figure 5.11.3 presents 'the RAO amplitude for the different DoF obtained using different time windows. It gives an idea of the dispersion of the data, and where they tend to concentrate. The first five time windows analysed differ on the part of the record used for the calculations, whereas the last five time windows show the results for a time window that goes increasing in size.

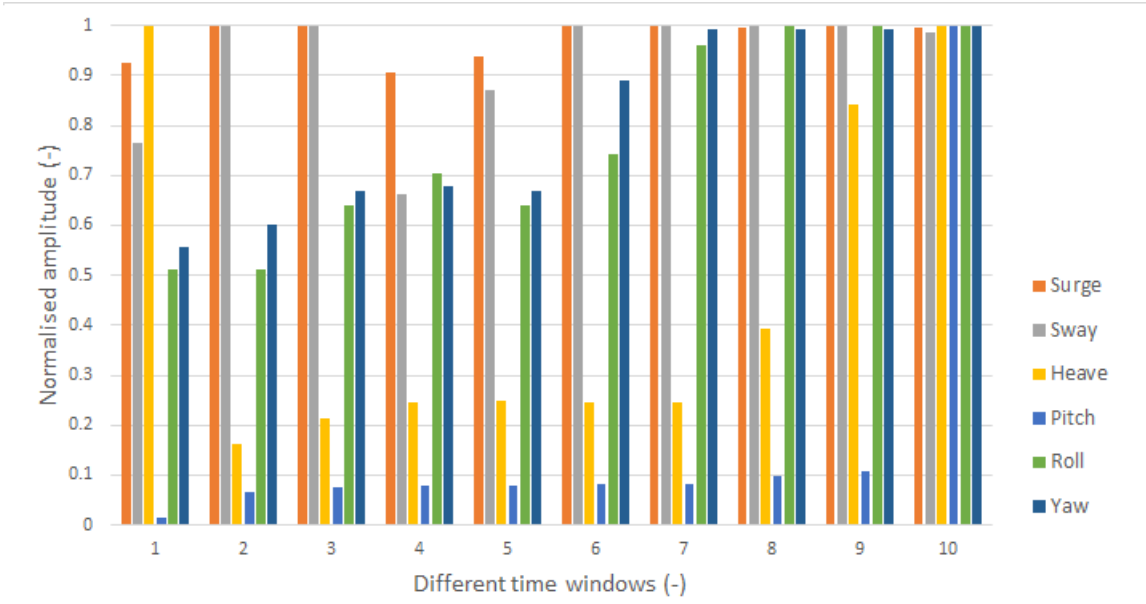

Figure 5.11.3.: RAO amplitude for the different DoF obtained using different time windows.

5.12. Irregular wave testing

The analysis of random seas is rather complex than regular ones but offers a prediction of the behaviour of the floating system in realistic environmental conditions. Beyond the quasi-periodic results obtained by regular wave testing, irregular waves tests may highlight coupled behaviours, e.g. surge-pitch coupling, triggered by non-linear forces acting at periods different than the investigated with regular waves [84]. Figures 5.12.1 and 5.12.2 show typical records obtained from irregular wave testing at Lir NOTF and FloWave OERF respectively. Note that the length of the records was increased from five to eighteen minutes to fully develop the irregular sea.

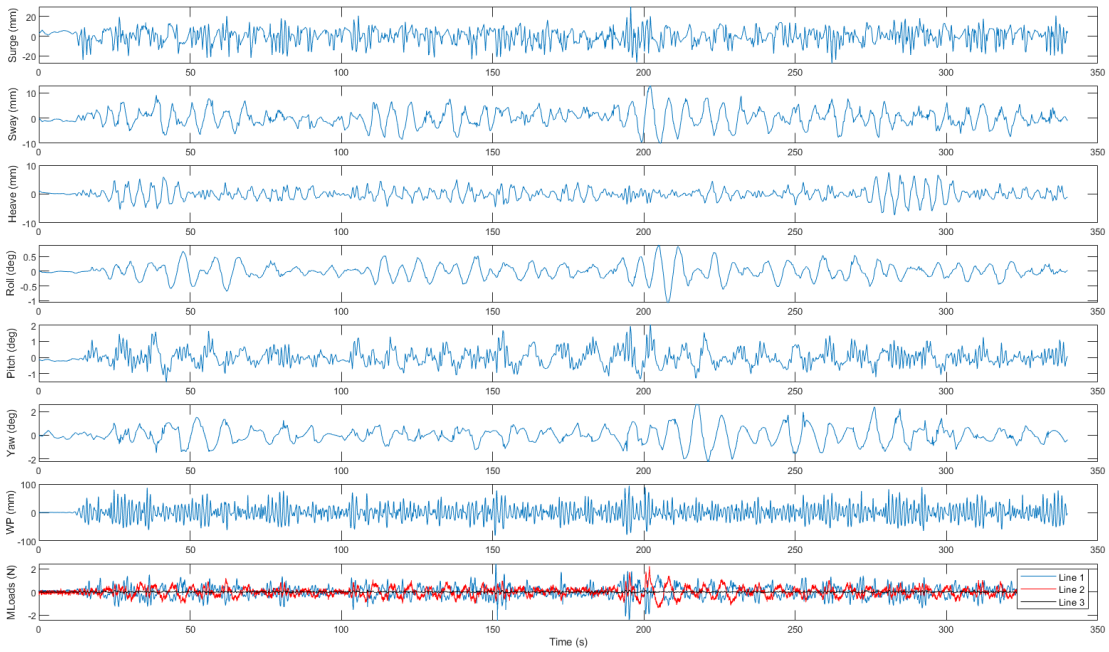

Figure 5.12.1.: Typical records obtained from irregular wave testing at Lir NOTF. Results expressed in millimetres, degrees, and Newtons.

As mentioned before for regular waves, the RAO is a useful tool to analyse the results of random wave testing. In this case, the RAO equivalent is called non-dimensional displacement and is calculated using the square root of the relationship between the energy distribution of the response in a certain degree of freedom, i.e. response spectrum instead of amplitude, divided by the energy distribution of the excitation which produced the mentioned response. The whole record is used to produce the non-dimensional displacements, therefore, the problem related to choosing the right part of the record does not apply to the analysis of irregular waves.

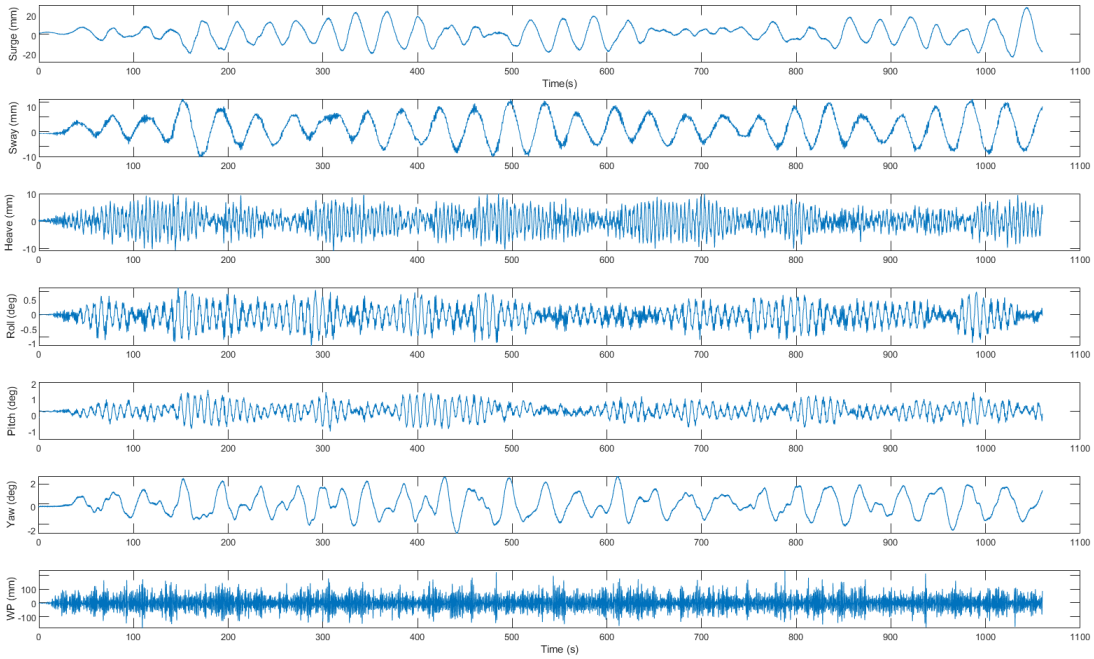

Figure 5.12.2.: Typical records obtained from irregular wave testing at FloWave OERF. Results expressed in millimetres and degrees.

5.13. Results @ Lir NOTF

This Section presents the experimental results obtained at Lir NOTF. Table 5.11 presents the results of the static tests, i.e. draft, trim and heel. There were no quasi-static tests conducted in Lir NOTF but since force transduces were installed between the fairleads and the mooring line attachment (Figure 5.5.3), there is a record of the pretension values. Table 5.12 shows the pretensions recorded for each mooring line configuration.

Table 5.11.: Static tests results. Draft is presented in millimetres and the inclination in degrees

	Draft / Inclination
Free-floating condition	1320
Three mooring lines	1375
Three mooring lines with Δ connection	1380
Four mooring lines	1390
Endwise or trim	-1.4
Sideways or heel	0

Table 5.12.: Mooring line pretension in Newtons.

	Line 1	Line 2	Line 3	Line 4
Three mooring lines	11.2	7.3	8.0	-
Three mooring lines with Δ connection	12.9	7.5	6.7	-
Four mooring lines	9.5	9.5	6.8	6.8

Figure 5.13.1 shows the analysis of the results for the three repetitions of the heave free decay experiments and therefore, the source of the data used to calculate the properties of the oscillating system, i.e. logarithmic decrement and natural frequency. For each repetition, two different sets of data have been produced and analysed. The first set of results was produced by fitting a damped sinusoidal curve (Figures 5.13.1a, 5.13.1c, 5.13.1e), whereas the second set of data uses a peak finding process along with the fitting of an exponential curve (Figure5.13.1b, 5.13.1d, 5.13.1f). Table 5.13 shows the results of three different heave free decay tests for testing repeatability and reproducibility purposes. Tables 5.14 and 5.15 present the same results for pitch and roll free decay tests.

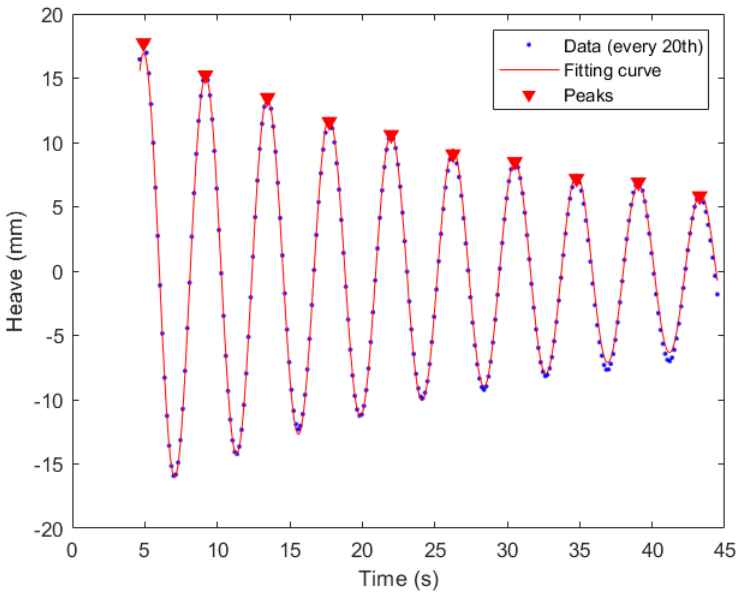

(a) Fitting with a damped sinusoidal curve.

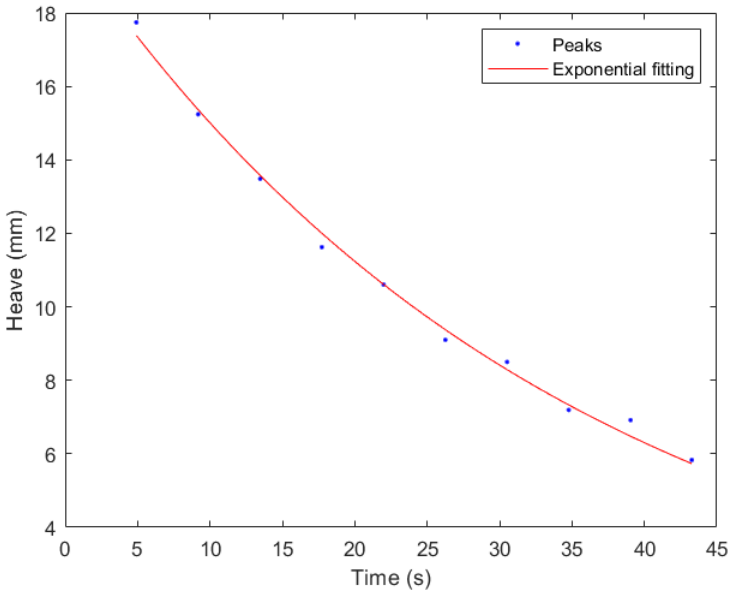

(b) Exponential fitting of the peaks shown in 5.13.1a.

Figure 5.13.1.: Results of the three heave free decay experiments.

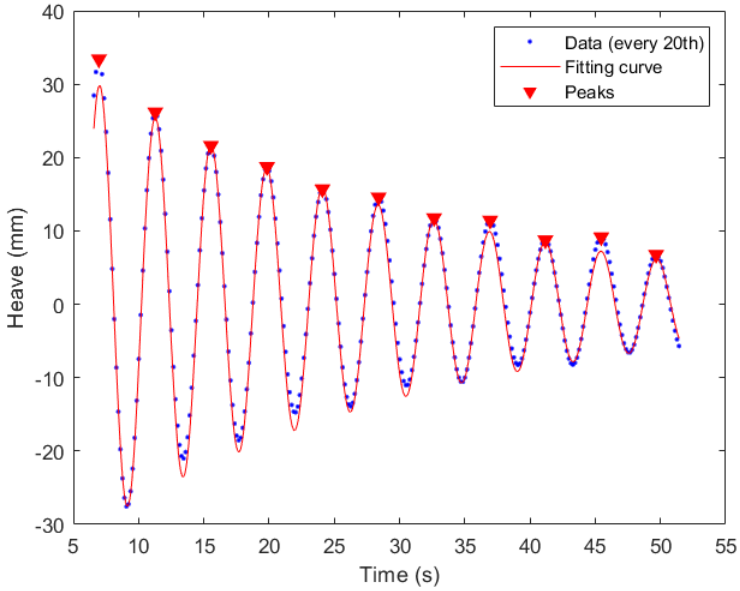

(c) Fitting with a damped sinusoidal curve.

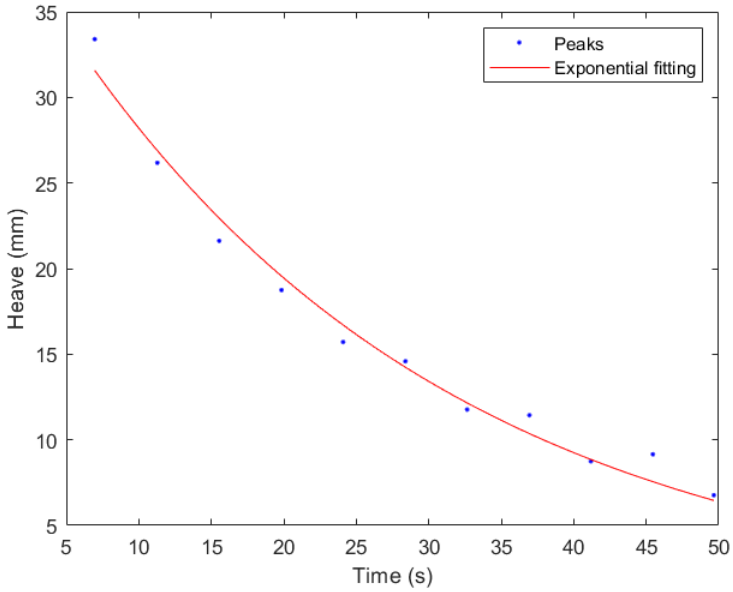

(d) Exponential fitting of the peaks shown in 5.13.1c.

Figure 5.13.1.: Results of the three heave free decay experiments.

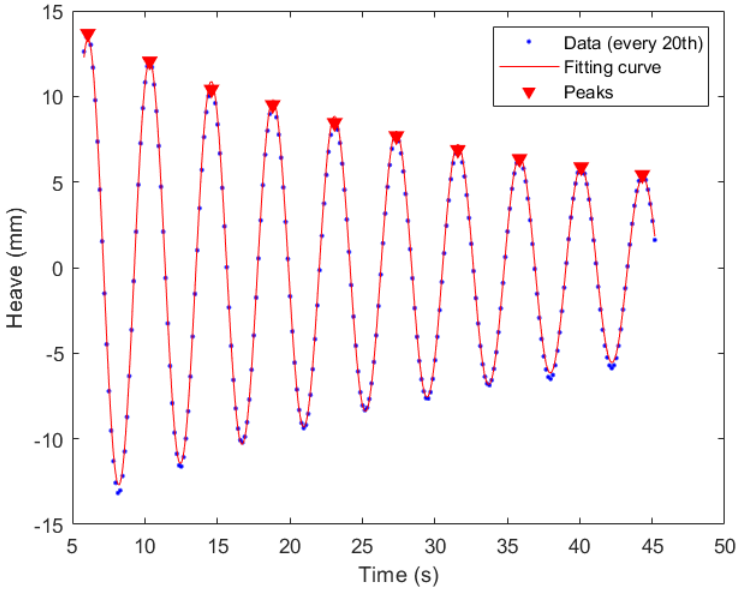

(e) Fitting with a damped sinusoidal curve.

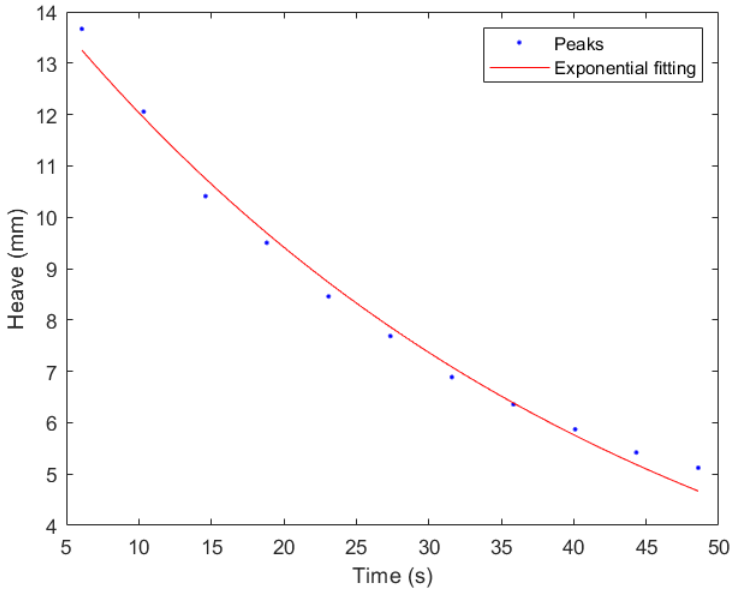

(f) Exponential fitting of the peaks shown in 5.13.1e.

Figure 5.13.1.: Results of the three heave free decay experiments.

Table 5.13.: Heave free decay tests results.

	Damping Coefficient (-)		Natural Period (s)	
	Set 1	Set 2	Set 1	Set 2
Test 1	0.0046	0.0043	4.268	4.268
Test 2	0.0043	0.0044	4.267	4.255
Test 3	0.0044	0.0043	4.254	4.254

Table 5.14.: Pitch free decay tests results.

	Damping Coefficient (-)		Natural Period (s)	
	Set 1	Set 2	Set 1	Set 2
Test 1	0.0025	0.0021	8.148	8.181
Test 2	0.0024	0.0021	8.183	8.184
Test 3	0.0025	0.0020	8.180	8.181

Table 5.15.: Roll free decay tests results.

	Damping Coefficient (-)		Natural Period (s)	
	Set 1	Set 2	Set 1	Set 2
Test 1	0.0025	0.0021	8.174	8.180
Test 2	0.0021	0.0021	8.163	8.175
Test 3	0.0022	0.0021	8.169	8.152

Table 5.16 presents a summary of the free decay testing results. Natural period is presented in both experimental and full-scale.

Table 5.16.: Summary of the free decay results. Natural periods shown in seconds.

	Damping Coefficient (-)	Natural Period	Full-scale Natural Period
Heave	0.0044	4.261	28
Pitch	0.0008	8.184	54
Roll	0.0008	8.173	54

In order to compute the resonance properties of the floating system with the three different mooring line configurations, the same procedure explained for the free decay testing was followed, i.e. producing results from two different set of data. Again, the first set of data was produced by fitting a damped sinusoidal curve, whereas the second set of data uses a peak finding process along with the fitting of an exponential curve. Figures 5.13.2 and 5.13.3 show examples of the data obtained, and the analysis performed for the stiffness decay tests in heave, surge, sway, and pitch, roll, and yaw modes of motion for the three mooring line configuration respectively.

The same procedure was followed to produce the properties of the oscillating system, i.e. logarithmic decrement and natural frequency, for the four and three with delta connection mooring line configurations. A summary of the result obtained is presented in Table 5.17. Table 5.18a presents the damping coefficients natural period of resonance of the floating system at testing scale, whereas Table 5.18b presents the natural periods of resonance of the floating system for the three mooring line configurations considered at full-scale.

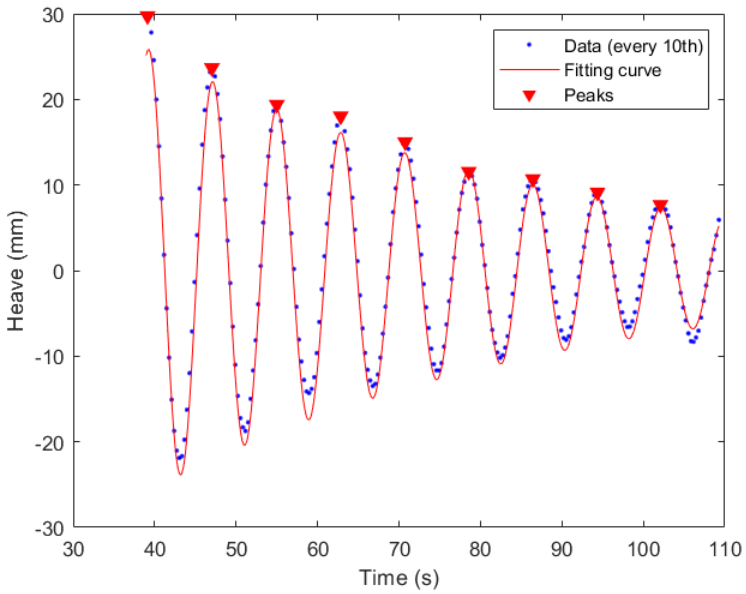

(a) Fitting of the testing results with a damped sinusoidal curve.

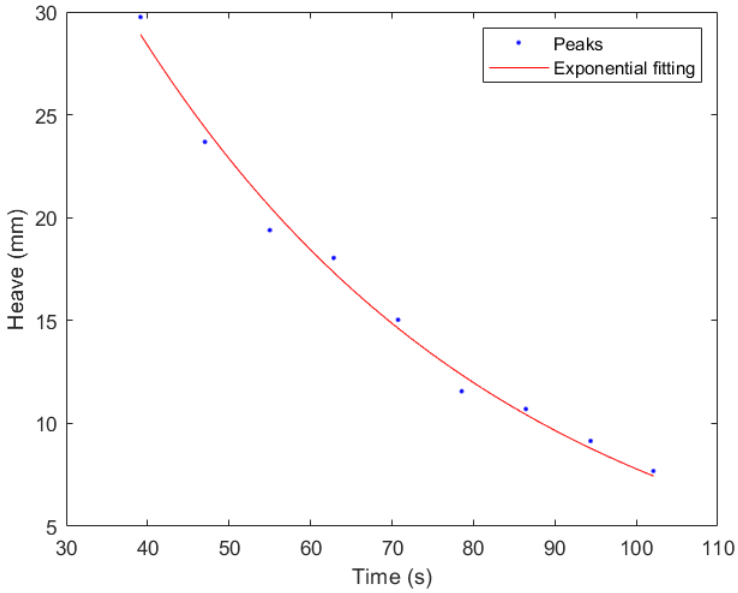

(b) Exponential fitting of the peaks shown in 5.13.2a.

Figure 5.13.2.: Stiffness decay test results for the translational modes of motion.

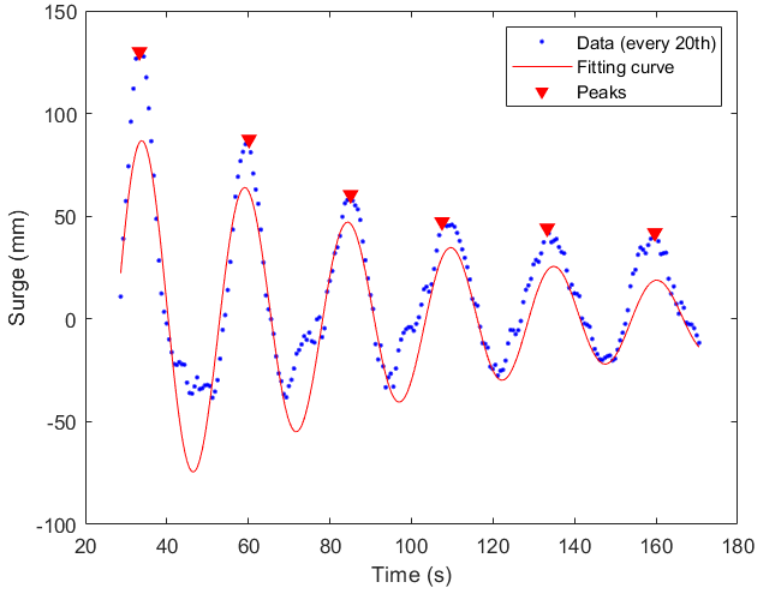

(c) Fitting of the testing results with a damped sinusoidal curve.

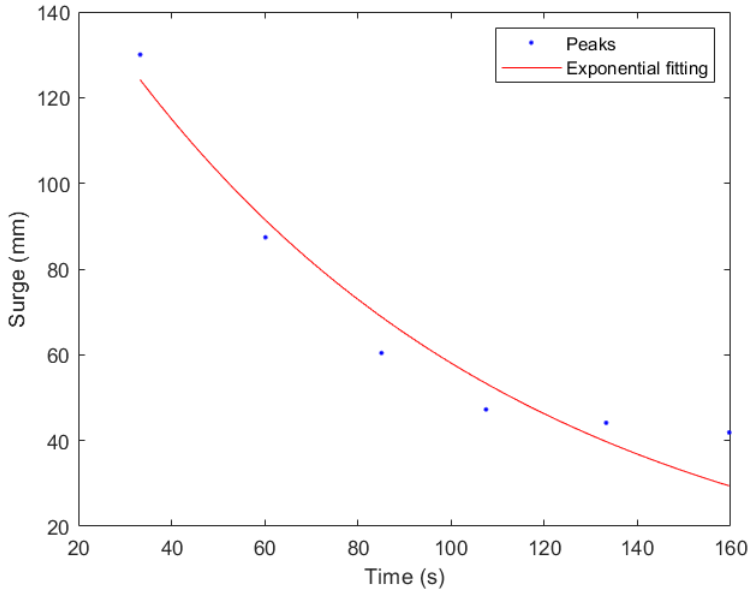

(d) Exponential fitting of the peaks shown in 5.13.2c.

Figure 5.13.2.: Stiffness decay test results for the translational modes of motion.

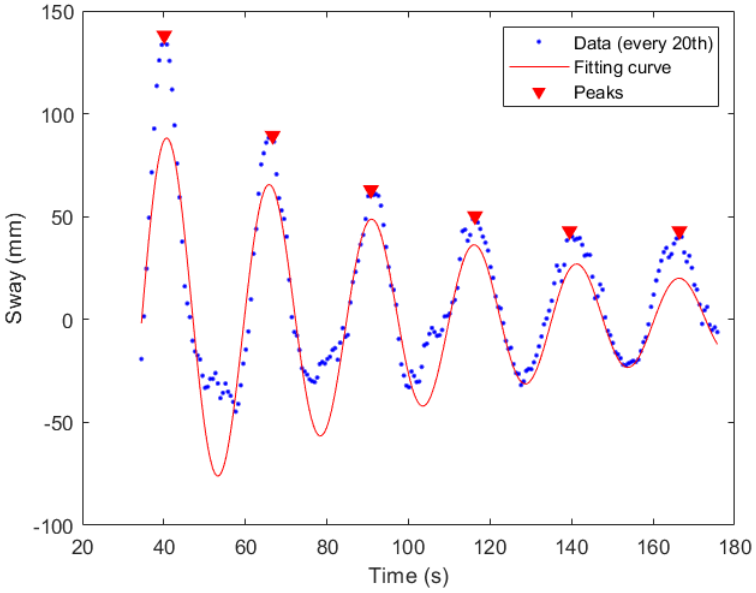

(e) Fitting of the testing results with a damped sinusoidal curve.

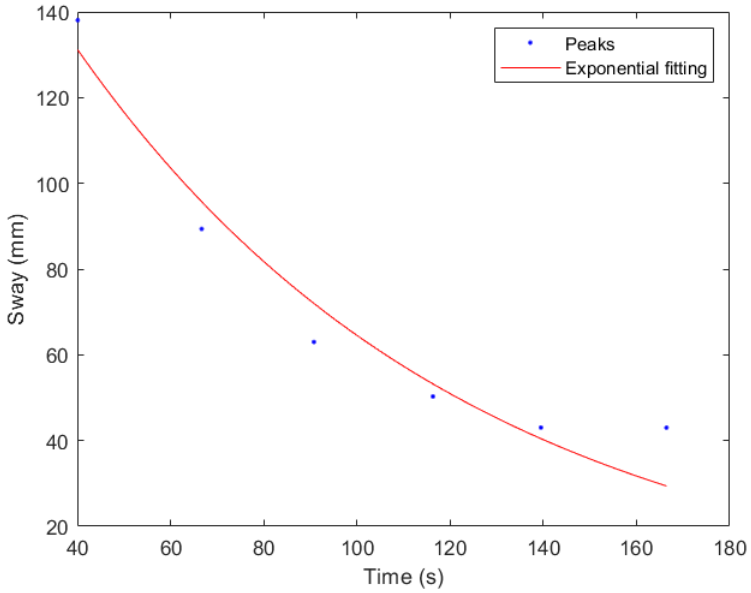

(f) Exponential fitting of the peaks shown in 5.13.2e.

Figure 5.13.2.: Stiffness decay test results for the translational modes of motion.

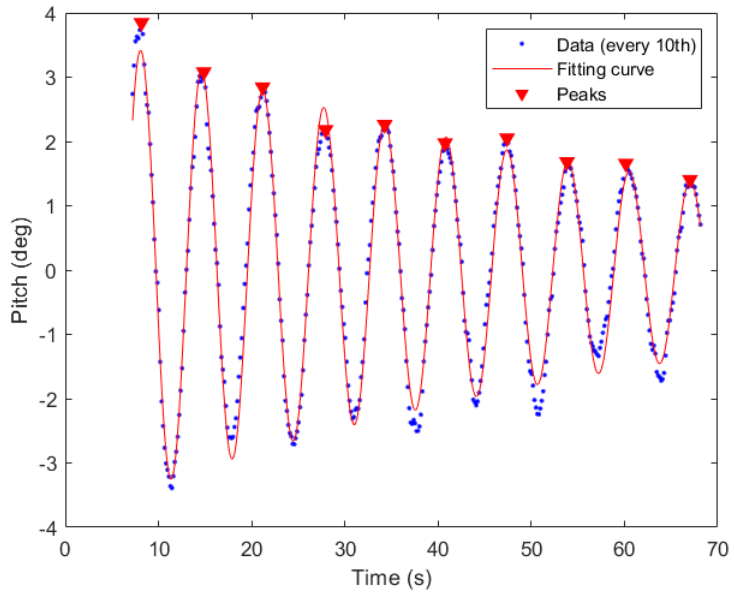

(a) Fitting of the testing results with a damped sinusoidal curve.

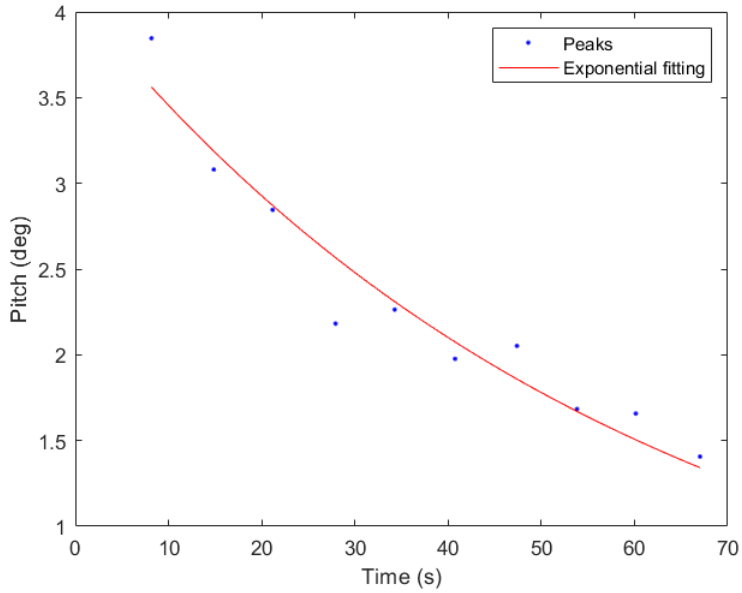

(b) Exponential fitting of the peaks shown in 5.13.3a.

Figure 5.13.3.: Stiffness decay test results for the rotational modes of motion.

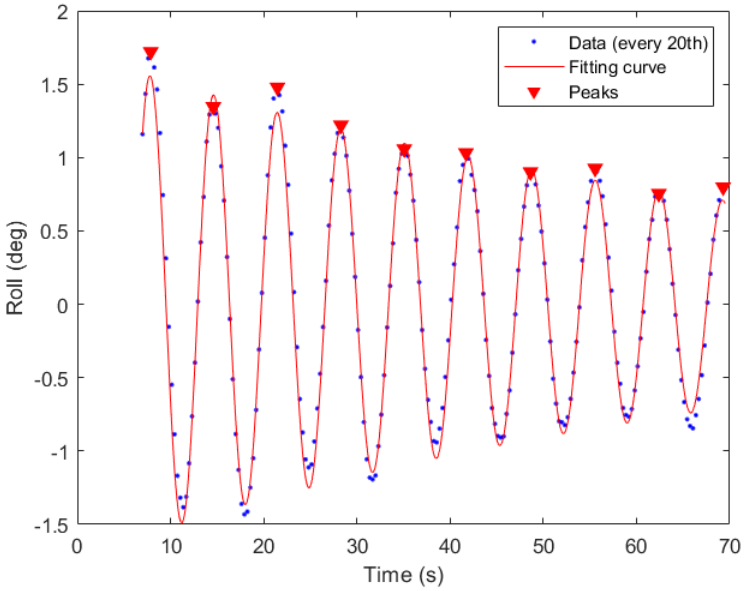

(c) Fitting of the testing results with a damped sinusoidal curve.

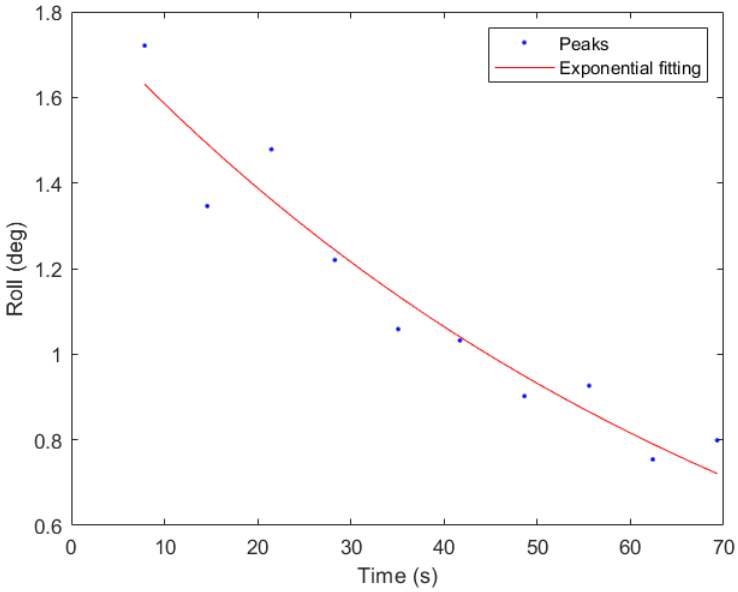

(d) Exponential fitting of the peaks shown in 5.13.3c.

Figure 5.13.3.: Stiffness decay test results for the rotational modes of motion.

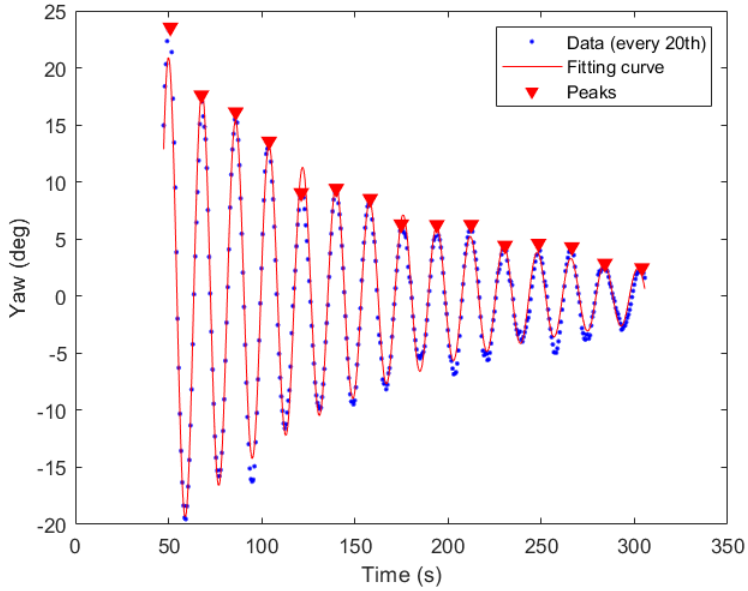

(e) Fitting of the testing results with a damped sinusoidal curve.

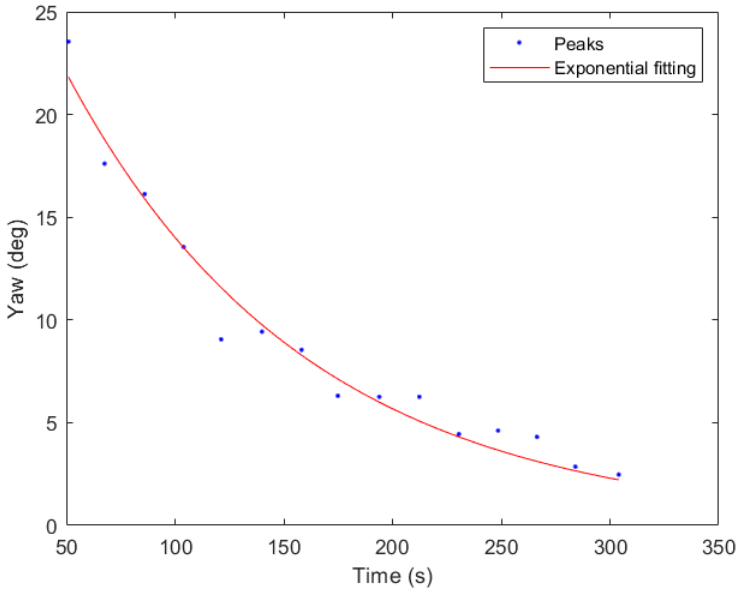

(f) Exponential fitting of the peaks shown in 5.13.3e.

Figure 5.13.3.: Stiffness decay test results for the rotational modes of motion.

Table 5.17.: Summary of the result obtained during the stiffness decay testing for the three (3), four (4), and three with delta connection (Δ) mooring line configurations.

	Damping coefficient (-)			Model-scale natural period (s)		
Mooring configuration	3	Δ	4	3	Δ	4
Heave	0.004	0.004	0.004	4.203	4.203	4.203
Surge	0.002	0.002	0.002	25.234	25.002	24.884
Sway	0.002	0.002	0.002	15.151	14.851	11.101
Pitch	0.001	0.001	0.001	7.379	8.181	7.383
Roll	0.001	0.001	0.001	7.352	8.171	7.264
Yaw	0.001	0.005	0.002	18.055	6.209	10.385

(a) Damping coefficient and natural period of resonance at testing scale.

	Full-scale natural periods (s)		
Mooring configuration	3	Δ	4
Heave	28	28	28
Surge	169	169	167
Sway	102	100	74
Pitch	50	55	50
Roll	50	55	49
Yaw	121	42	70

(b) Natural period of resonance at full-scale shown.

As stated before, the regular wave records shown in Figure 5.11.1 are noisier than the ones depicted in Figure 5.11.2. The same comment is valid for the random wave experiments, i.e. records in Figure 5.12.1 are noisier during the regular and random wave testing than records in Figure 5.12.2. Therefore, precaution must be taken when analysing the results obtained in Lir NOTF since the data is subject to high uncertainty.

Figure 5.13.4 shows wave probe, surge, pitch and heave time series for a regular wave test with a wave height of 44 mm and a period of 2.22 s.

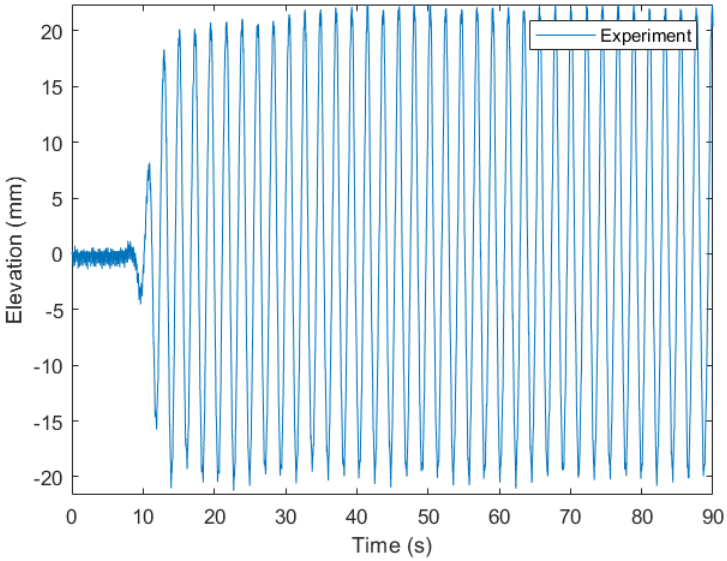

(a) Wave probe.

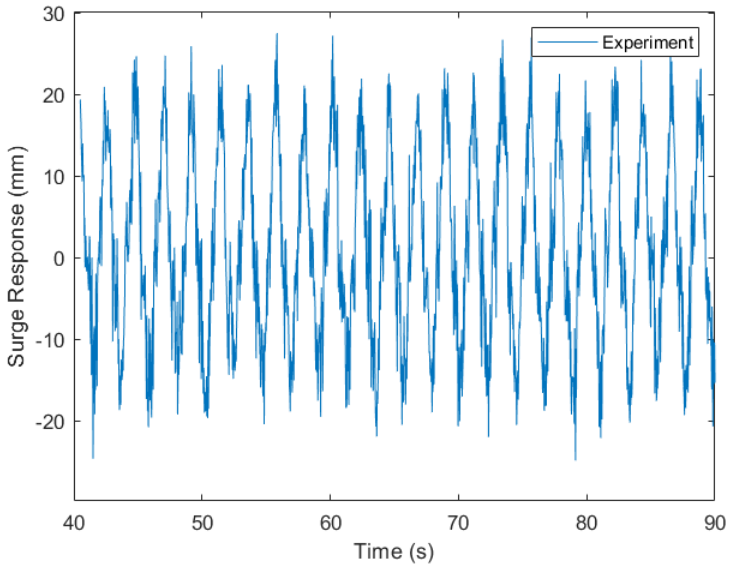

(b) Surge.

Figure 5.13.4.: Recorded time series for a regular wave test.

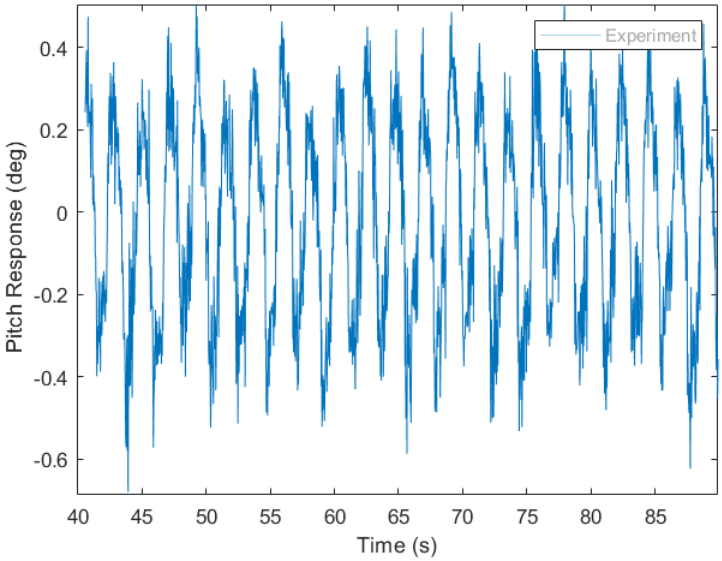

(c) Pitch.

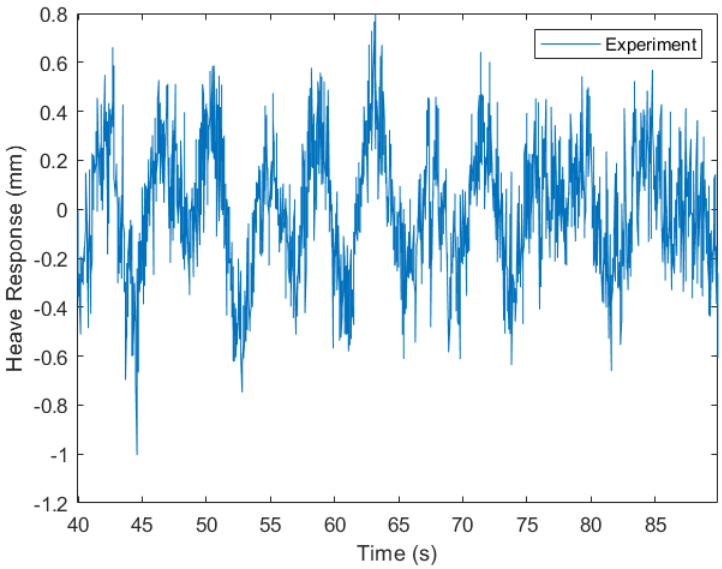

(d) Heave.

Figure 5.13.4.: Recorded time series for a regular wave test.

The full record of the wave probe is depicted in Figure 5.13.4a. Figures 5.13.4b, 5.13.4c, and 5.13.4d present the records for the surge, pitch and heave time series starting at 40

s to avoid transients.

Figure 5.13.5 presents wave probe, surge, pitch and heave time series for an irregular wave test with a significant wave height of 40 mm and a peak period of 0.89 s.

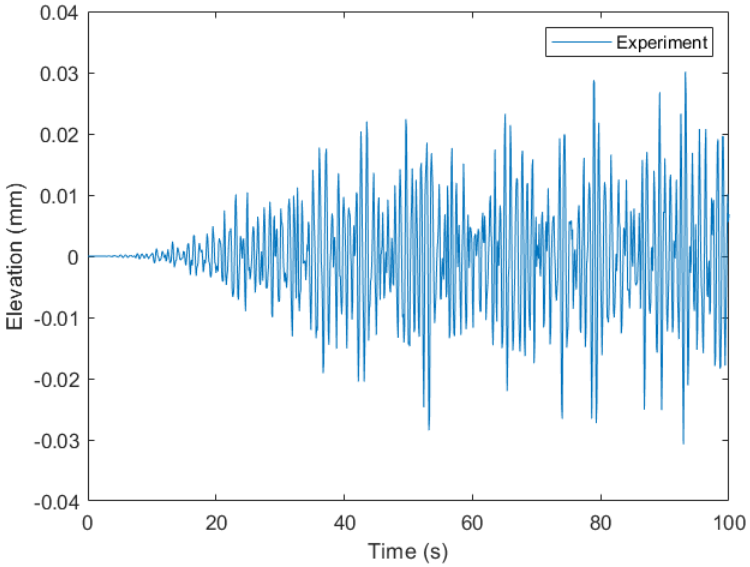

(a) Wave probe.

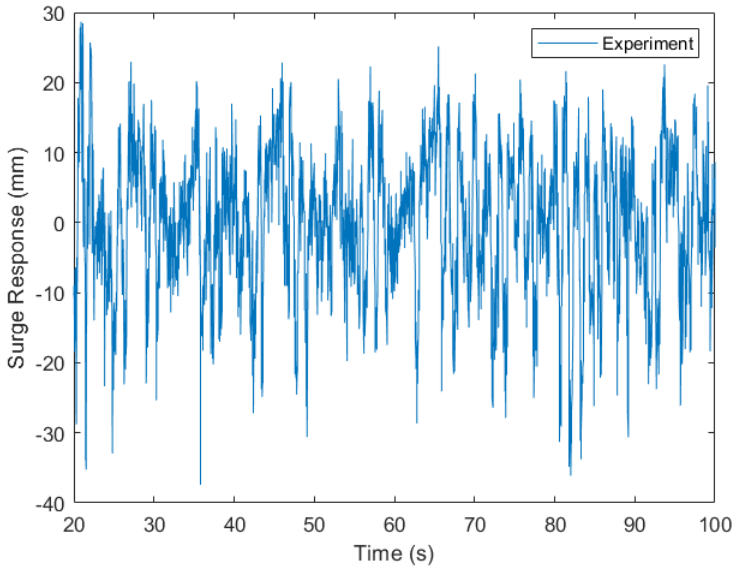

(b) Surge.

Figure 5.13.5.: Recorded time series for an irregular wave test.

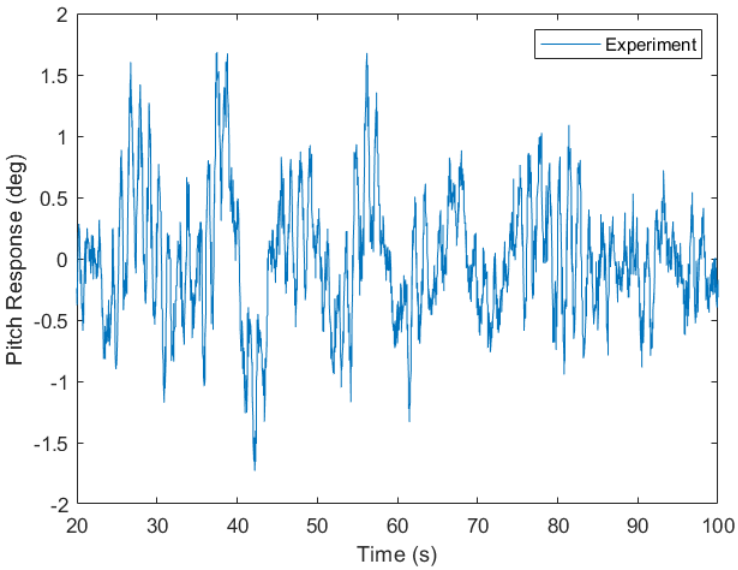

(c) Pitch.

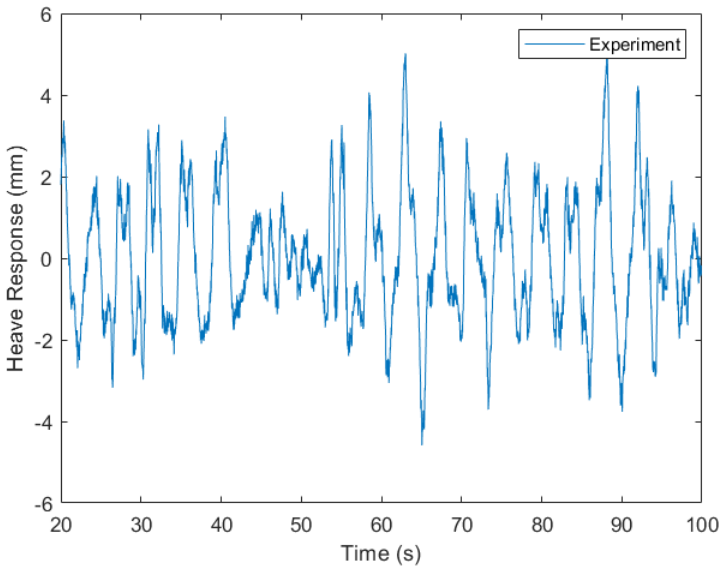

(d) Heave.

Figure 5.13.5.: Recorded time series for an irregular wave test.

The full record of the wave probe is depicted in Figure 5.13.5a. Figures 5.13.5b, 5.13.5c, and 5.13.5d present the records for the surge and pitch time series starting at 20 s to

avoid transients. Figure 5.13.6 presents the spectral densities of the records shown in Figure 5.13.5.

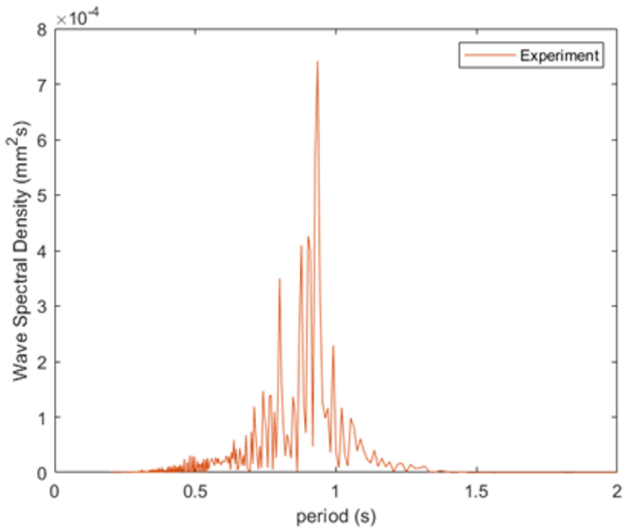

(a) Wave probe.

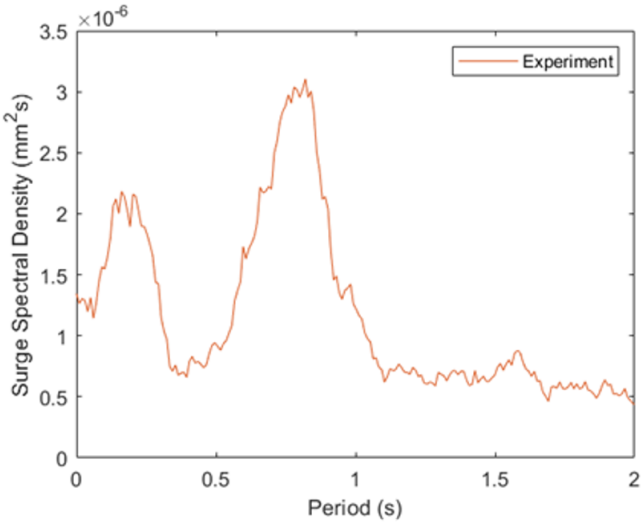

(b) Surge.

Figure 5.13.6.: Spectral densities of the wave probe, surge, pitch and heave experimental records for an irregular wave test with a significant wave height of 40 mm and a peak period of 0.89 s.

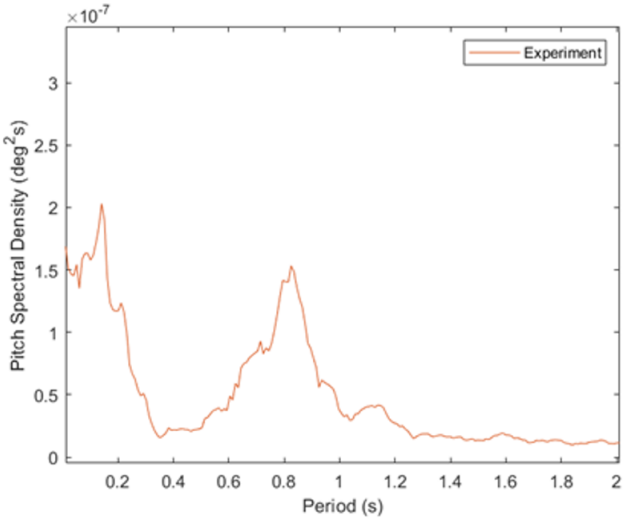

(c) Pitch.

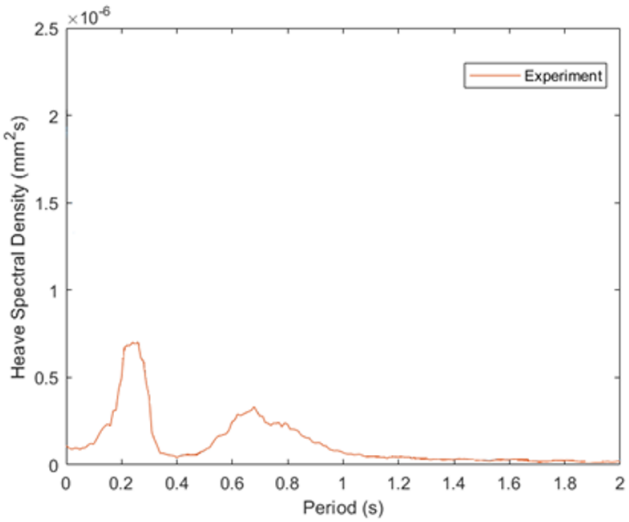

(d) Heave.

Figure 5.13.6.: Spectral densities of the wave probe, surge, pitch and heave experimental records for an irregular wave test with a significant wave height of 40 mm and a peak period of 0.89 s.

A summary of regular and random wave tests results is shown in Figures 5.13.7 and 5.13.8 in terms of RAO.

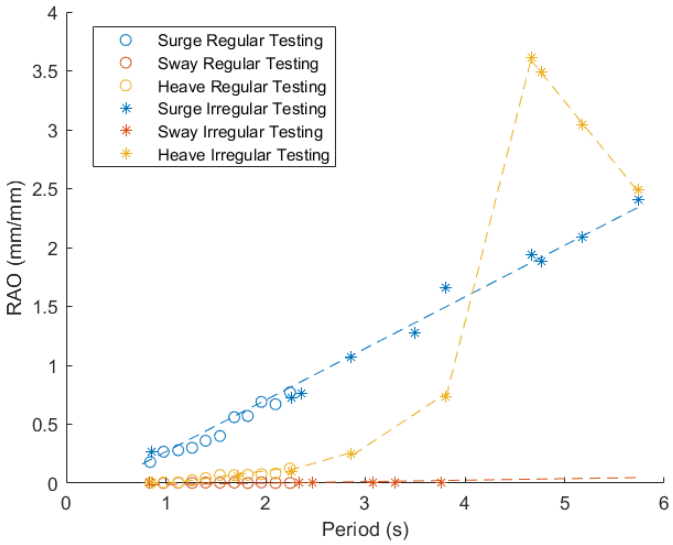

Figure 5.13.7.: Summary of regular and random wave tests results in terms of translational RAOs.

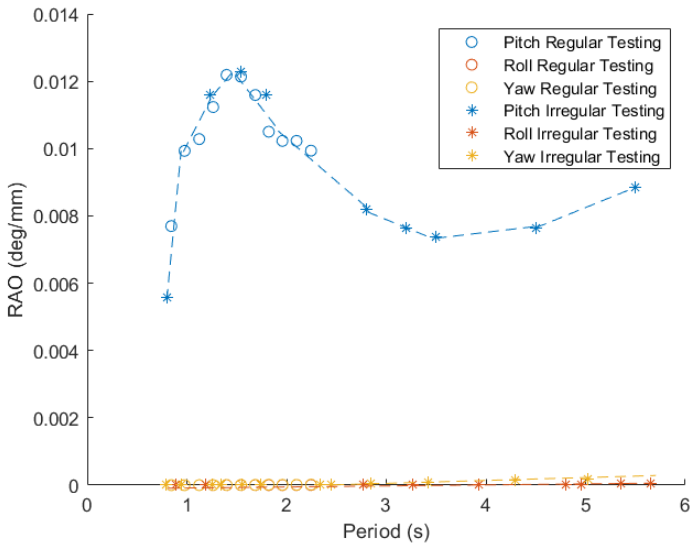

Figure 5.13.8.: Summary of regular and random wave tests results in terms of rotational RAOs.

5.14. Results @ FloWave OERF

This Section presents the experimental results obtained at FloWave OERF. The results of the dry tests are presented in table 5.18.

Table 5.18.: Dry tests results.

Inclination test (m)	0.489
Swing test (kgm^2)	135.398
Chain stiffness (kN/m)	750.000
Elastic modulus (kN/m^2)	$2.280x10^7$

Table 5.14 presents the results of the static test, i.e. draft, trim and heel. The position of the markers installed in the mooring lines was recorded during the static test to calculate the pretension of the system. Figure 5.14.1 presents the profile of the mooring line in still water conditions, indicating a pretension of 11 N. The results of the quasi-static tests are presented in Figure 5.14.2 indicating the tension in the mooring lines for a given surge offset.

Table 5.19.: Static tests results.

	Draft (mm) or Inclination (deg)
Free-floating condition	1320
Three mooring lines	1375
Endwise or trim	0
Sideways or heel	0

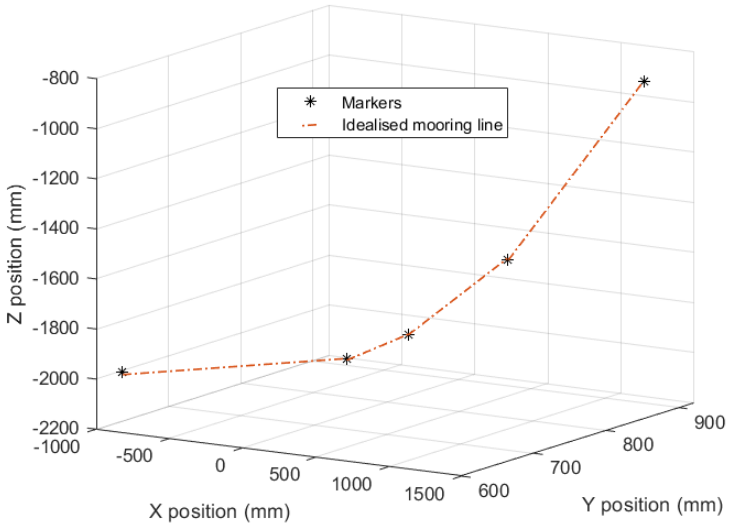

Figure 5.14.1.: Mooring line layout in still water conditions.

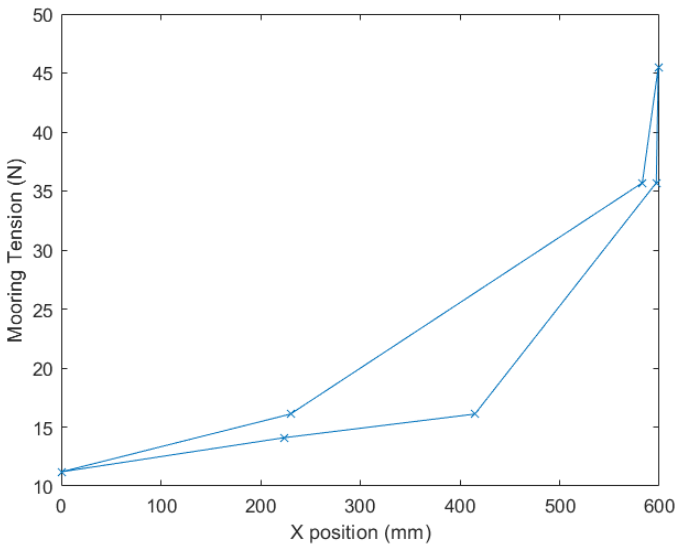

Figure 5.14.2.: Mooring stiffness for the floating system.

Tables 5.20 and 5.21 present a summary of the free decay and stiffness decay testing results in both experimental and full-scale

Table 5.20.: Summary of the free decay results.

	Damping Coefficient (-)	Natural Frequency (Hz)	Full-scale Natural Period (s)
Heave	0.0040	0.235	28
Pitch	0.0008	0.123	54
Roll	0.0008	0.123	54

Table 5.21.: Summary of the stiffness decay results.

	Damping coefficient (-)	Model-scale natural frequency (Hz)	Full-scale natural period (s)
Heave	0.0035	0.236	28
Surge	0.0041	0.032	207
Sway	0.0041	0.026	253
Pitch	0.0093	0.132	51
Roll	0.0081	0.132	51
Yaw	0.0011	0.049	137

Figures 5.14.3 to 5.14.7 show the six DoF motion response of the model for regular waves with 40 mm of wave height and a period of 0.35, 0.4, 0.9, 1.2, and 0.2625 Hz respectively.

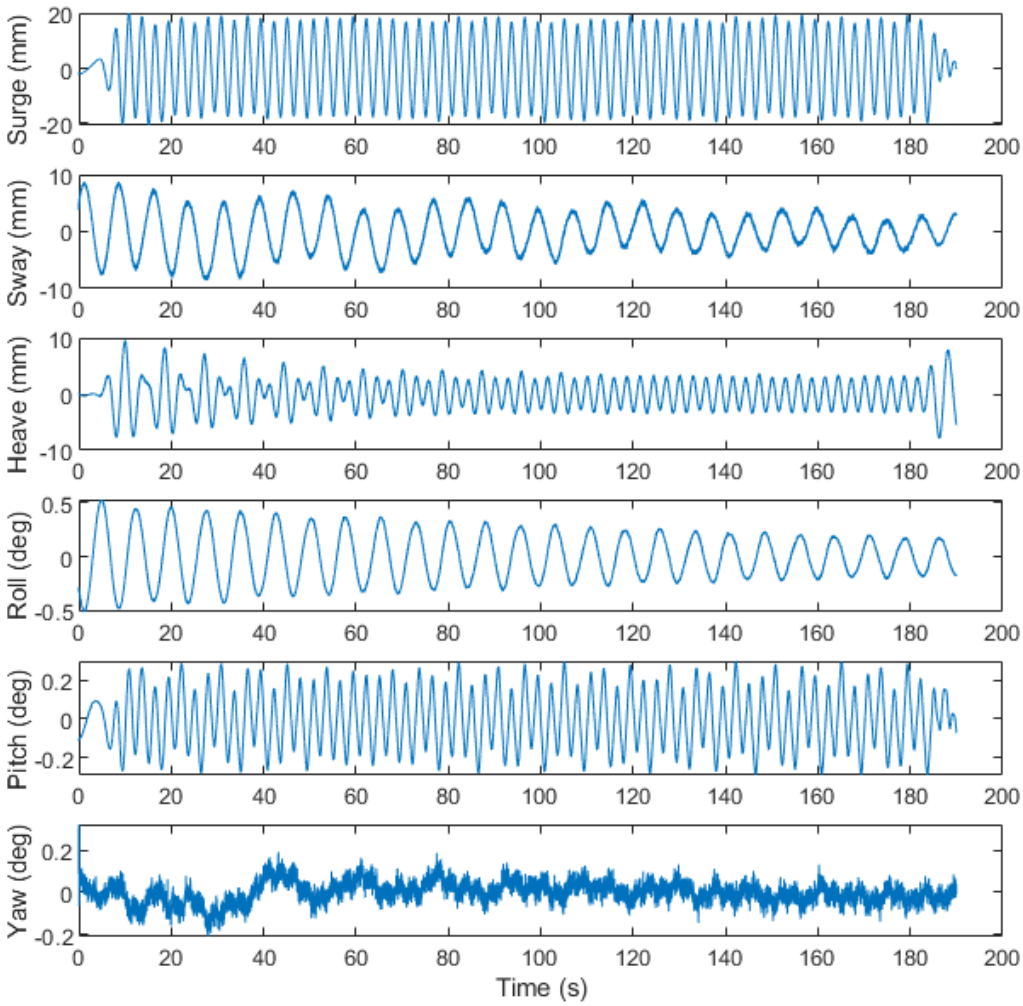

Figure 5.14.3.: Motion response for regular waves with a frequency of 0.35 Hz.

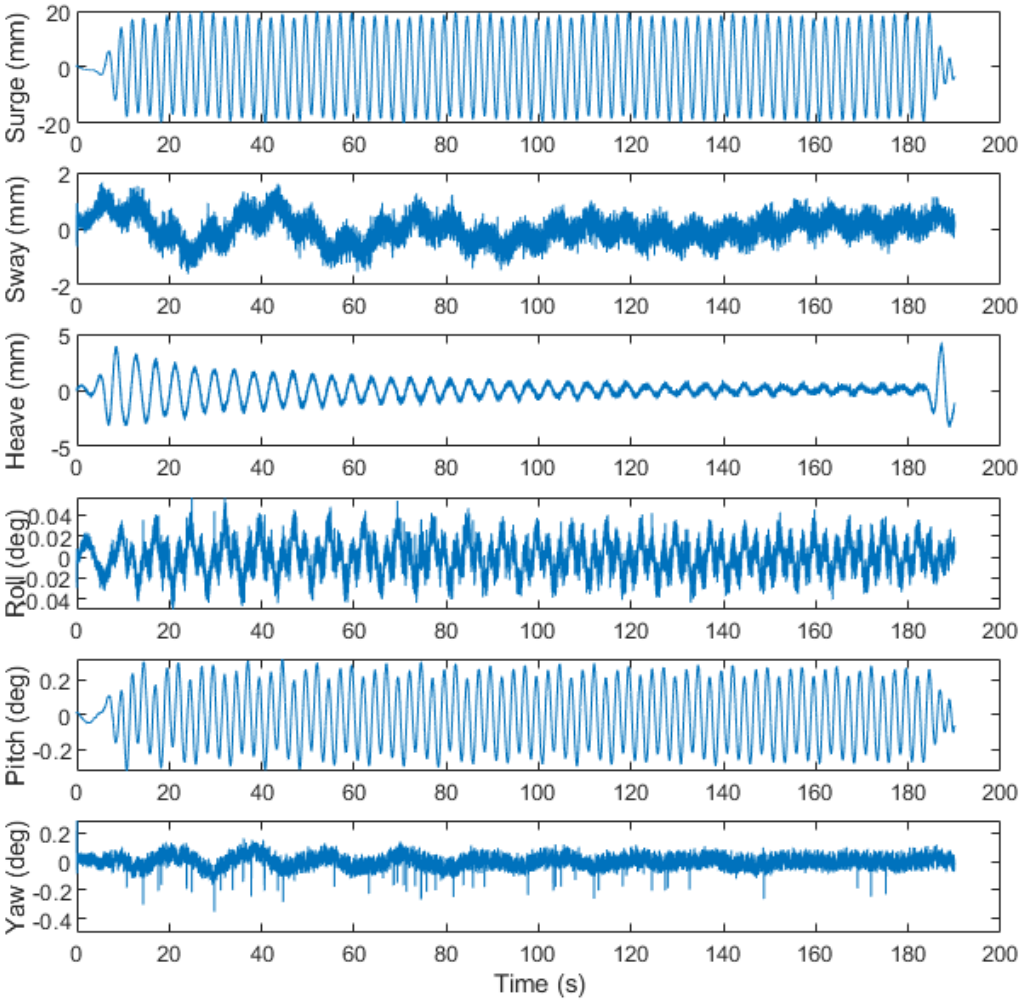

Figure 5.14.4.: Motion response for regular waves with a frequency of 0.4 Hz.

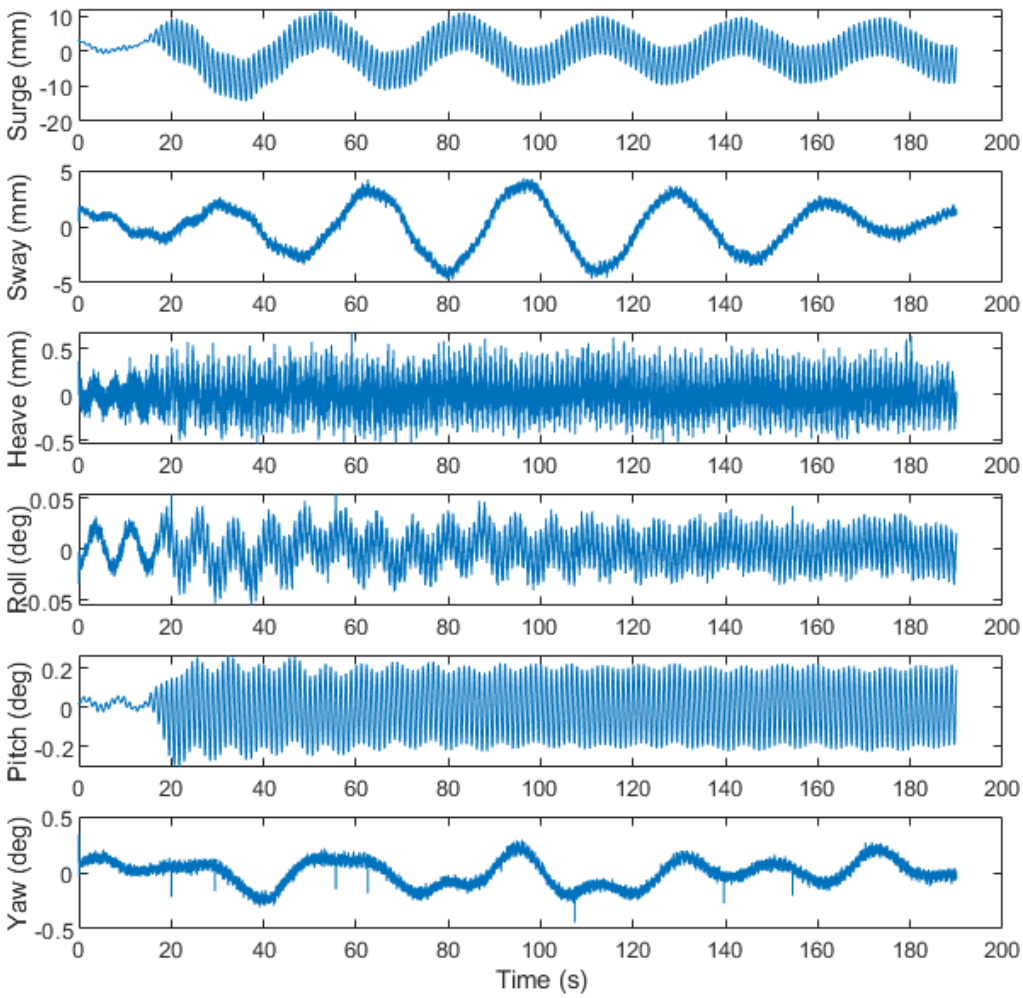

Figure 5.14.5.: Motion response for regular waves with a frequency of 0.9 Hz.

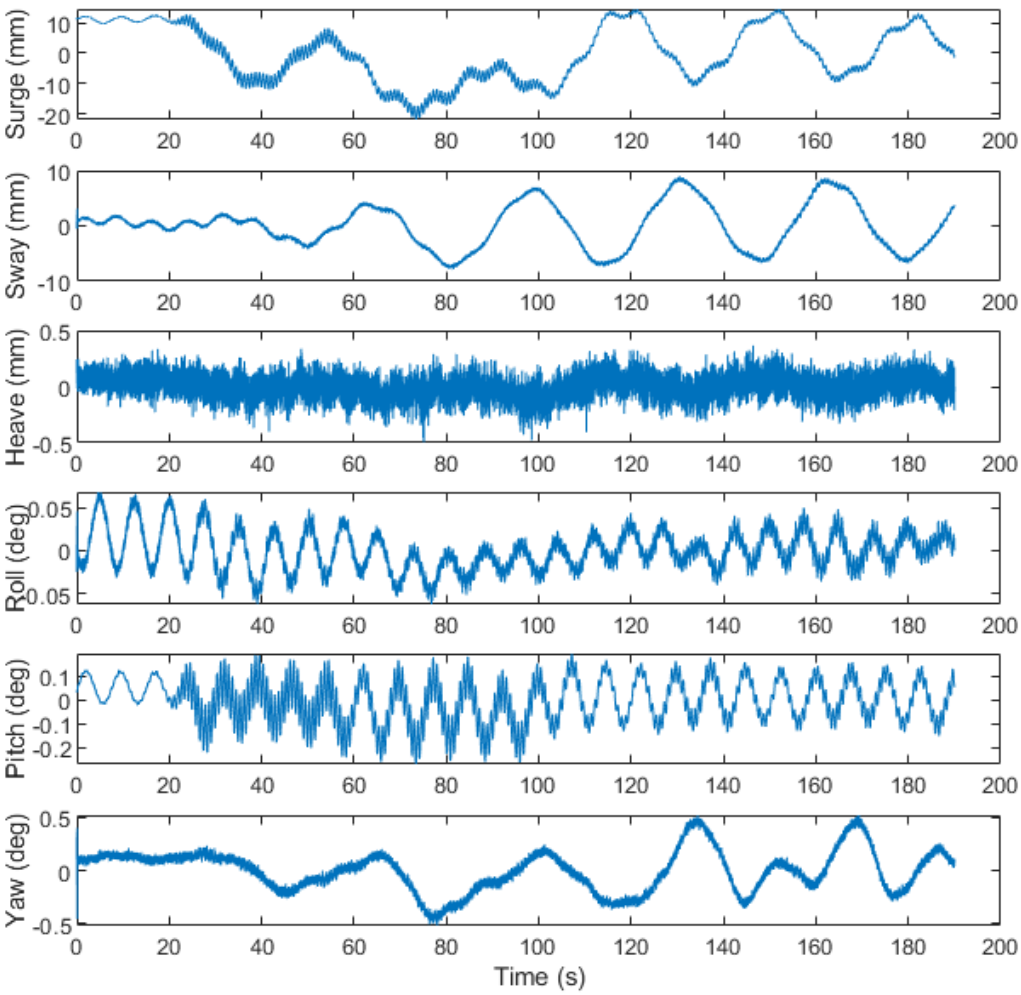

Figure 5.14.6.: Motion response for regular waves with a frequency of 1.2 Hz.

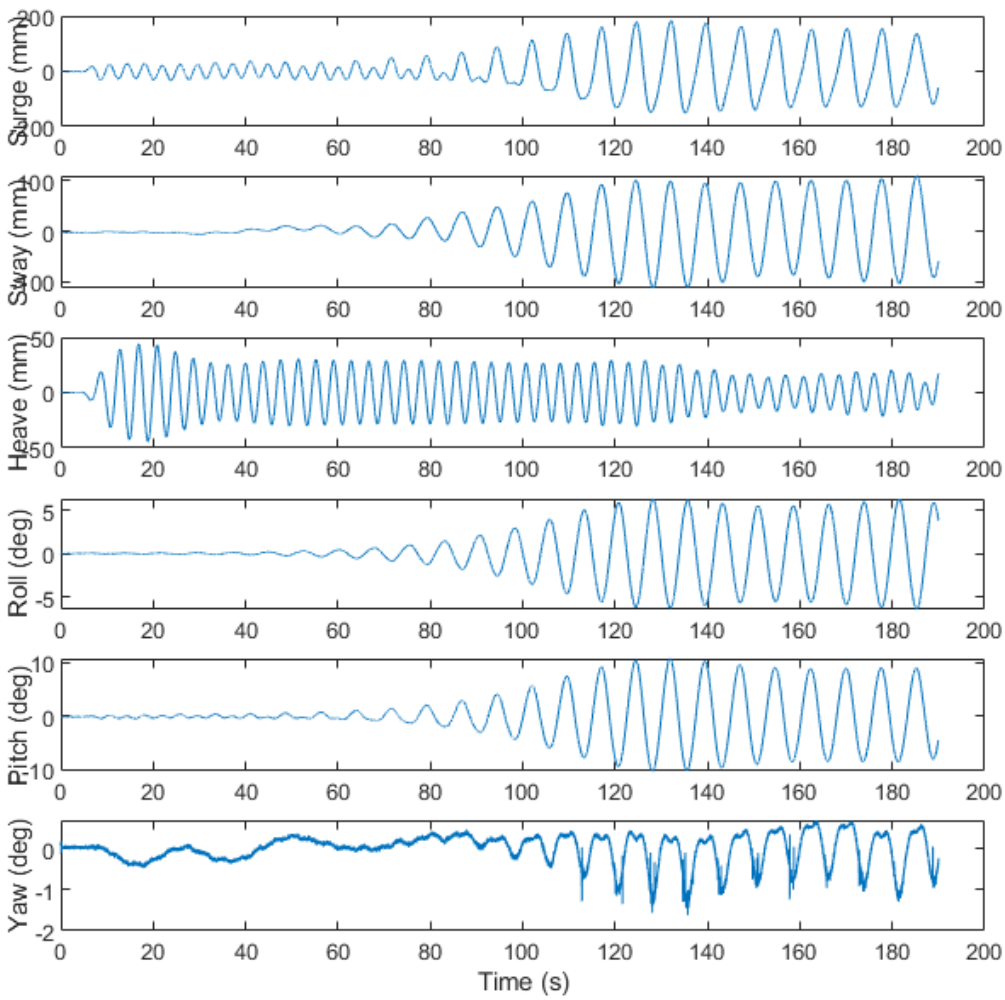

Figure 5.14.7.: Motion response for regular waves with a frequency of 0.2625 Hz.

Figures 5.14.8 to 5.14.13 present the results of the regular wave test in terms of RAOs and Figure 5.14.14 shows similar results but computed using irregular wave testing results.

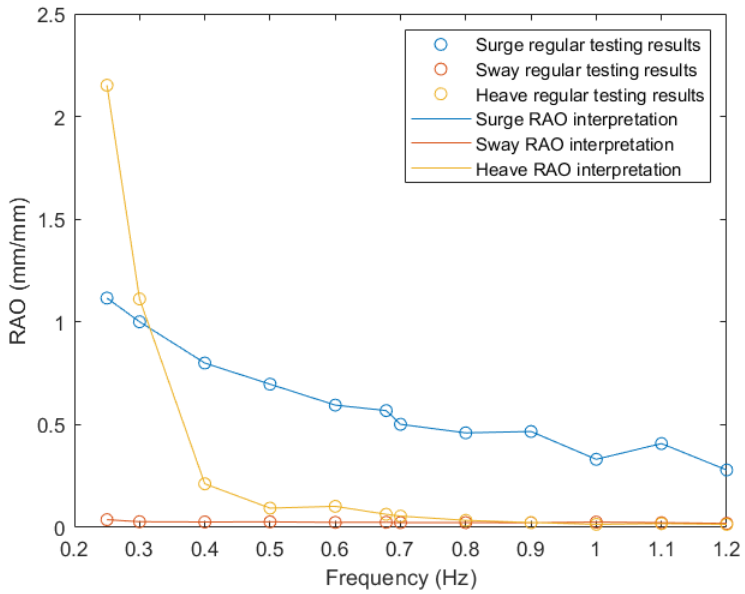

(a) Translational RAOs.

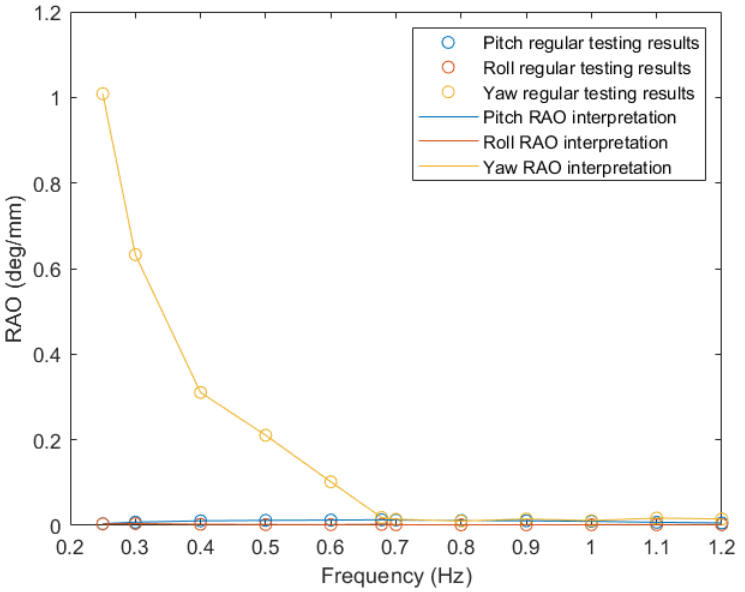

(b) Rotational RAOs.

Figure 5.14.8.: RAOs for the free floater condition in head seas, i.e. with waves impacting at zero degrees.

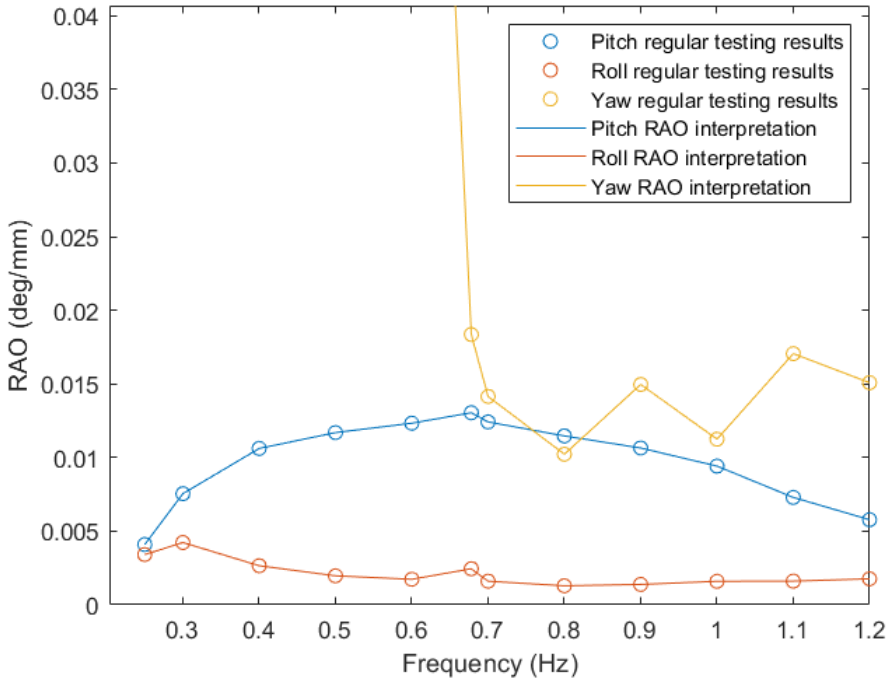

Figure 5.14.9.: Zoom in view of the rotational RAOs shown in Figure 5.14.8b.

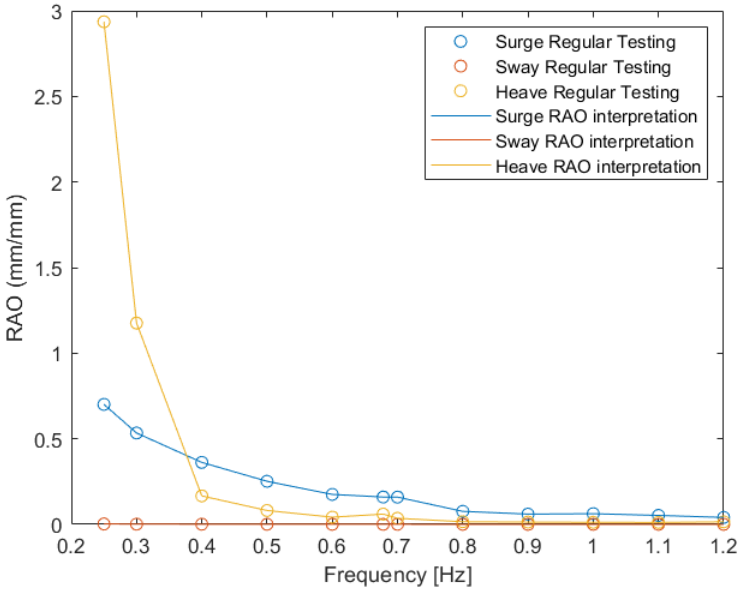

(a) Translational RAOs.

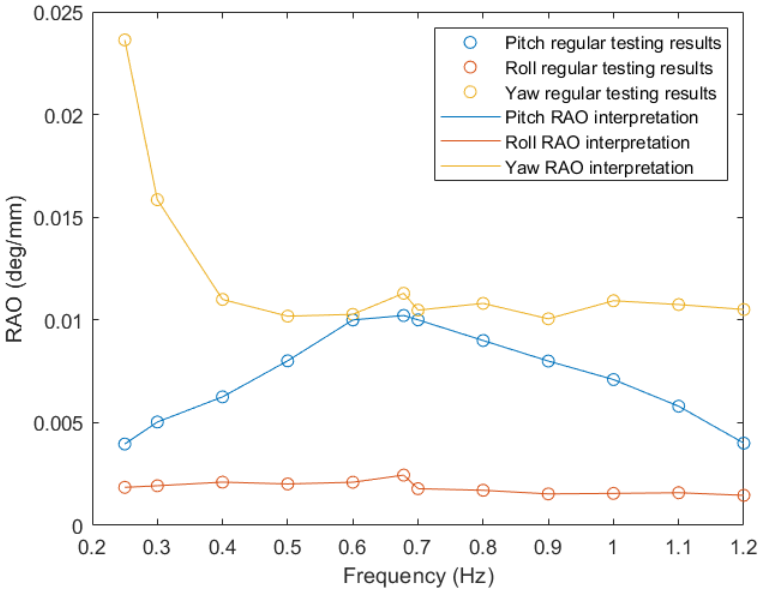

(b) Rotational RAOs.

Figure 5.14.10.: RAOs for the moored condition in head seas.

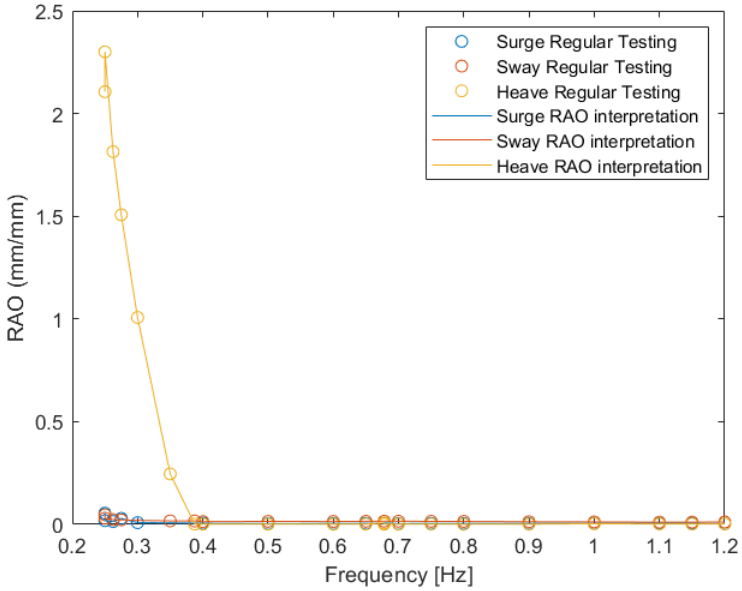

(a) Translational RAOs.

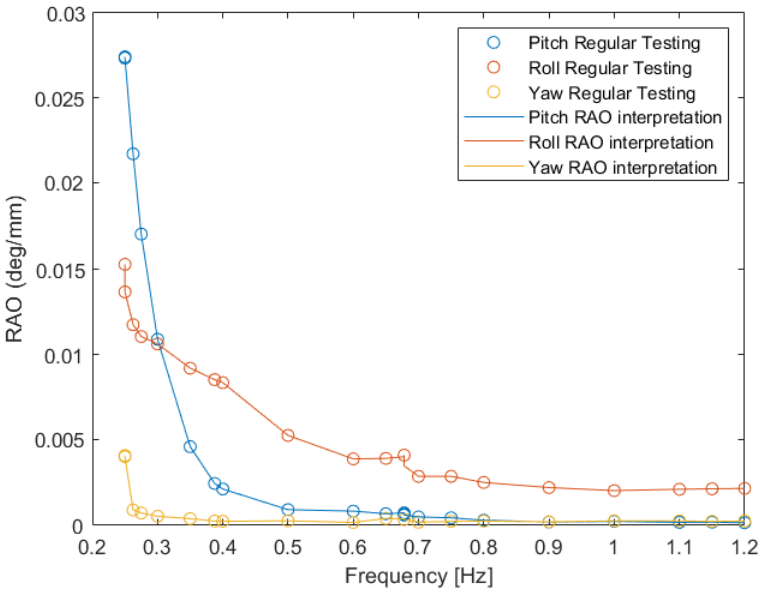

(b) Rotational RAOs.

Figure 5.14.11.: RAOs for the moored condition in bow seas (with waves impacting at forty-five degrees).

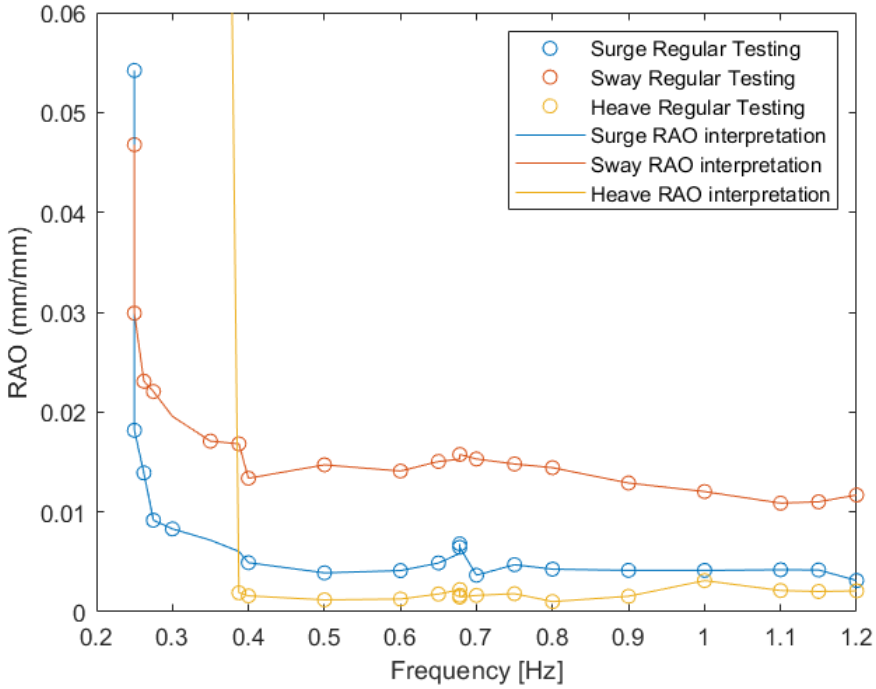

Figure 5.14.12.: Zoom in view of the translational RAOs shown in Figure 5.14.11a.

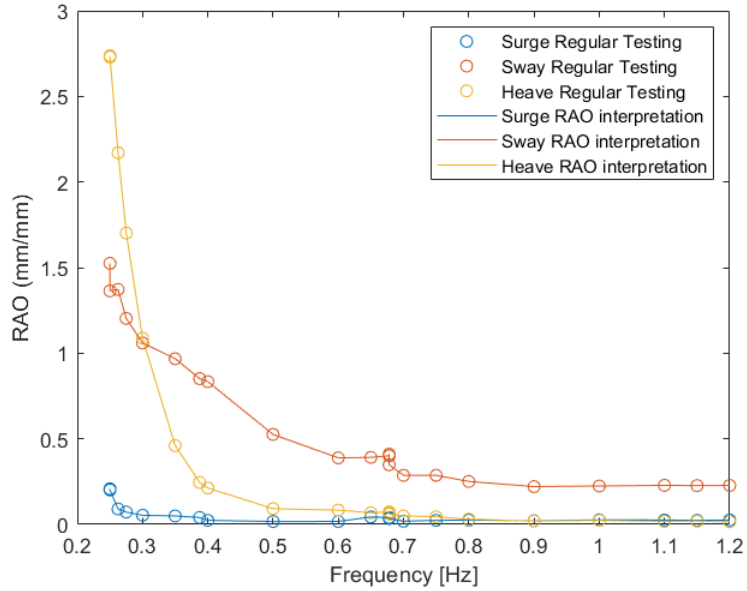

(a) Translational RAOs.

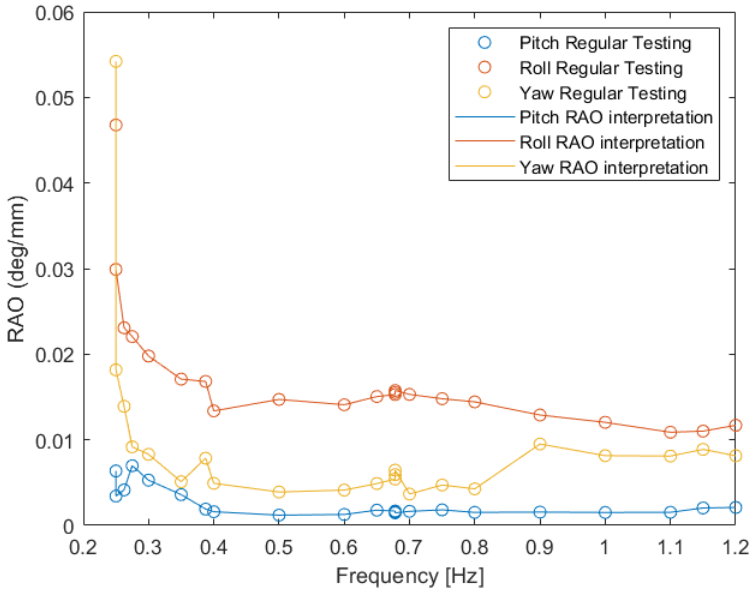

(b) Rotational RAOs.

Figure 5.14.13.: RAOs for the moored condition in beam seas, i.e. with waves impacting at ninety degrees.

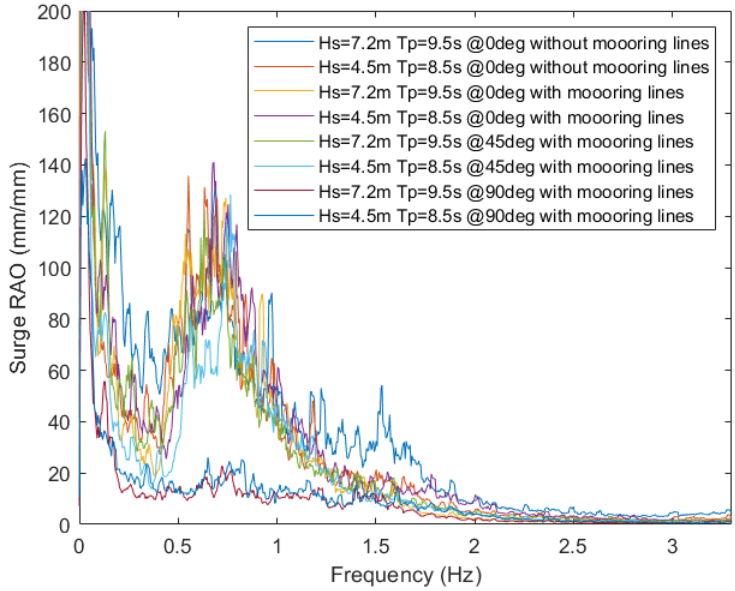

(a) Surge.

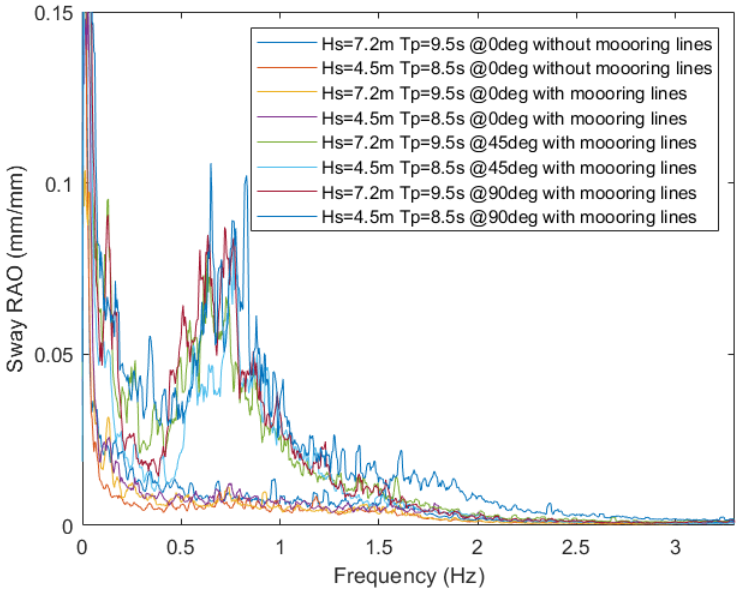

(b) Sway.

Figure 5.14.14.: RAOs from different irregular waves.

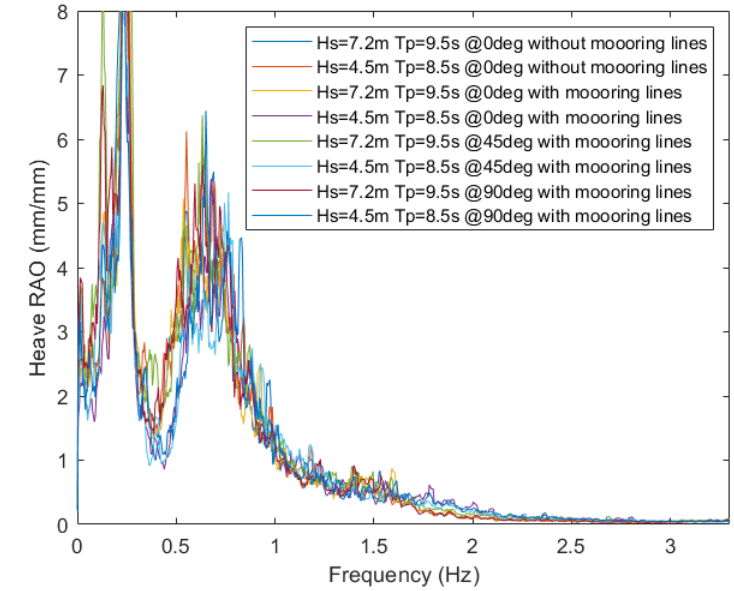

(c) Heave.

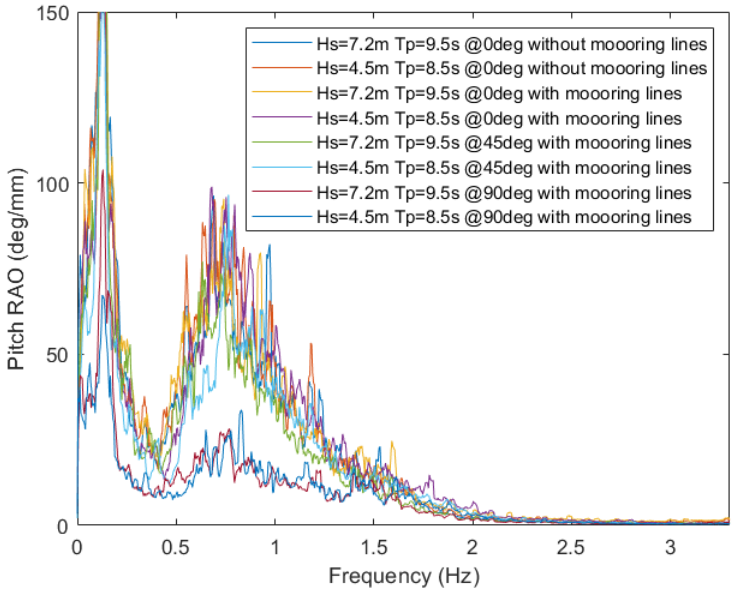

(d) Pitch.

Figure 5.14.14.: RAOs from different irregular waves.

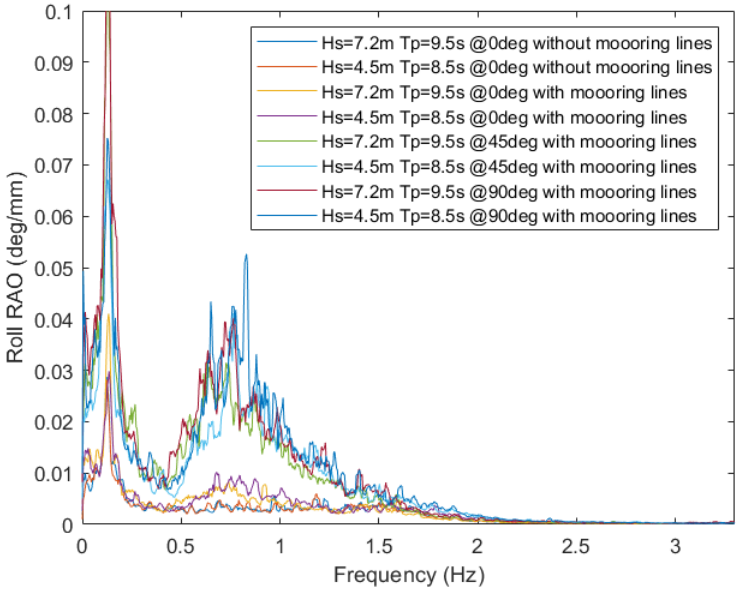

(e) Roll.

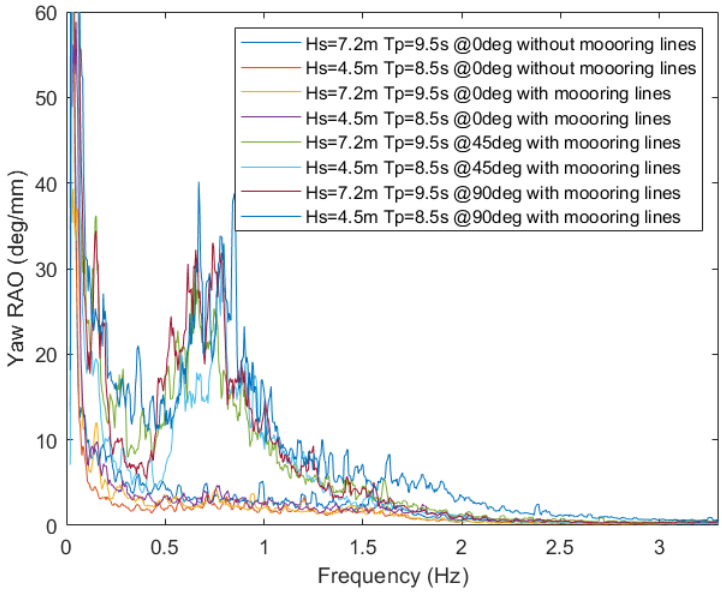

(f) Yaw.

Figure 5.14.14.: RAOs from different irregular waves.

5.15. Discussion

This Section presents the discussion of the results presented in the two previous Sections, i.e. the results obtained during the testing campaigns performed in Lir NOTF and FloWave OERF. The investigation gives insight into the model, the facilities used for hydrodynamic testing and the wave quality delivered. It also covers a wide range of experimental investigations including preliminary 'dry' testing, static and quasi-static testing, decay testing, and regular and random wave experiments.

As mentioned before in Section 5.3, the model has been scaled using the Froude number, because in this case, the Reynolds number in the flow is above the critical value for the transition to turbulence. Therefore, the flow is turbulent with relatively weak effects of drag on the process compared with the effects of gravitational free-surface waves, i.e. free surface flows are governed by gravity forces. As a result of the Froude scaling, viscous effects must be compensated for when translating results to full scale and during the validation of numerical models.

Similarly, the use of the Froude number provides a correct scaling of the weight of the mooring line which ensures appropriate restoring forces and inertial loads. However, hydrodynamic loads due to viscous drag are not considered and must be considered when translating results to full scale and during the validation of numerical models.

After the scaling process, the physical model was designed using a computer-aided design (CAD) tool. The scale model as built show discrepancies with the theoretical model initially proposed in CAD. The tolerances of the milling machine are of the order of three millimetres. The position of the CoG matched perfectly the theoretical assumption. However, the theoretical mass distribution in terms of MoI was between 8 and 5% off compared to the theoretical full-scale mass distribution (Table 5.4).

Even though it is not a common practice, performing inclination and swinging tests is the only way to tune or validate the position of the CoG and the MoI of the physi-

cal model. Regarding that, the moveable ballast in the upper cylinder (Figure 5.3) was enough to perfectly match the theoretical height of the CoG (Table 5.11). Further improvement of the MoI results can be achieved by implementing a trial and error approach during the swing tests, but this method was out of the scope due to time limitations.

The discrepancies regarding the tolerance of the milling machine are neglectable, but the divergencies regarding mass distribution must be considered when translating results to full scale and during the setup of numerical models.

As stated in Section 5.4 the most relevant parameters to properly model a catenary mooring line are the weight per unit of length and the equivalent diameter of the chain although other parameters like the axial stiffness should also be considered. Axial stiffness influences the line catenary shape, and it is relevant to the surge, sway and yaw motions. Moreover, cable displacements decrease with increase in axial stiffness while the cable tensions increase with the increase in axial stiffness. The scaling of the weight per unit of length and the equivalent diameter is covered by Froude laws and geometric scaling respectively. However, to deduce the axial stiffness of the line used during the hydrodynamic experiments the chain must be tested as explained in Section 5.8. The experimental axial stiffness must be used during the setup of numerical models. Another solution would be introducing springs accounting for the difference in elastic modulus between the real and the tested chain, but this approach was out of the scope due to time limitations.

As stated in Section 5.2, two hydrodynamic experimental campaigns have been performed in two different tank facilities, Lir NOTF and FloWave OERF. The facility used for testing is a relevant aspect of the experimental campaign and it influences the results until a certain degree. The most characteristic difference between the two facilities employed for this study is the shape of the wave basin. Lir NOTF basin has a rectangular shape with one of its vertices curved (Figures 5.2.5, 5.2.6, and 5.4.3) whereas FloWave OERF is a circular one. Accordingly, Lir NOTF basin is equipped with active-absorption

paddles and an absorbing beach, whereas FloWave OERF relays on force-feedback active-absorption paddles to dissipate the wave energy by generating an inverse wave which cancels out the incoming wave.

As a result, the reflection pattern of the two facilities is notably different. As shown in Figures 5.7.1 and 5.7.2, the quality of the regular waves is similar in both basins when referring to the generated periods. However, the generated wave heights are closer to the requested ones in FloWave OERF, even though both basins deliver smaller waves than requested. Figures 5.7.3 and 5.7.5 also show lower reflections in FloWave OERF than in Lir NOTF, and a more accurate sinusoidal shape on the crest of the generated waves. However, an overall check of the sinusoidal shape in Figures 5.7.7 and 5.7.85.7.8 reveals that the wave shape quality is better in Lit NOFT. Regarding irregular waves (Figures 5.7.4 and 5.7.6), both basins have similar performance, but showing higher spectral density overtaking the target spectra in Lir NOTF.

Any inaccuracy in terms of period or wave height must be considered during the setup of numerical models. Period and wave height inaccuracies can also lead to erroneous RAO interpretations since the ratio between response and excitation must be reported against the period of the excitation.

In free-floating conditions, before attaching the mooring lines, the draft of the model was 1320 mm at both basins. Trim and heel angles were -1.4 and 0 degrees at Lir NOTF whereas there was no trim at FloWave OERF. The trim of a floating structure is the difference between the forward and aft draft. A negative trim means that the aft draft is greater than the forward draft and the floating structure is usually described as trimmed by the stern. The difference in draft shown in Figures 5.9.1a and 5.9.3 is justified because of the trim, i.e. apparent draft in Lit NOFT is larger than the apparent draft in FloWave OERF, but numerically the draft is the same since the apparent draft at Lir NOTF must be reduced by the sinus of the trim angle.

After the attachment of the three mooring line configuration, the measured draft in-

creased in 55 and 65 mm at Lir NOTF and FloWave OERF respectively. Again, the cause of the discrepancy lays on the fact that the floater was trimmed by the stern at Lir NOTF. The design of the three mooring line configurations was different in Lir NOTF and in FloWave OERF. In Lir NOTF the free-floating structure had a designed trim that would be countered by the asymmetric three mooring line configuration described in Table 5.7, whereas a non-trimmed floating structure was tested in FloWave OERF along with a symmetric three mooring line configuration (Table 5.9). The only premise when designing the two different three mooring line configurations was to maintain the final draft constant at 1375 mm which was achieved. In Lir NOTF two extra mooring lie configuration were tested, i.e. three mooring lines with delta connection and four mooring lines. The draft of the DTI-F increased 5 mm when the delta connection was attached to the system and 15 mm when the four mooring lines were connected.

In absence of underwater markers in Lir NOTF and force transducers in FloWave OERF, correlating the data obtained from both methodologies is the only way of analysing the pretension in both basins. Figure 5.14.1 shows the position of the underwater markers at FloWave OERF from where the amount of suspended chain can be inferred and therefore the weight of the suspended chain which eventually will translate into pretension for still water conditions. The objective when designing the FloWave OERF three mooring line configuration was obtaining similar pretensions compared with the previous testing performed at Lir NOTF. Therefore, as expected, the pretension computed at FloWave OERF matches the results recorded in Lir NOTF up to 97% being a 3% higher in FloWave OERF.

The results of the quasi-static tests present an important feature of a mooring line, the restoring force of the floating system. This is a mandatory check while validating hydrodynamic numerical modelling.

Regarding the free decay results, no remarkable differences were found between the two methods used to calculate the results, i.e. fitting a damped sinusoidal curve, peak

finding plus fitting of this peaks with an exponential curve (Figure 5.13.1 and Tables 5.13, 5.14, and 5.15); however, following the common practice in testing tanks, the fitting of a damped sinusoidal curve method was used for reporting the results (Tables 5.16 and 5.20). No remarkable differences were found between the tests conducted in Lir NOTF and FloWave OERF with the maximum disagreement being lower than 1%.

The stiffness decay results obtained in Lir NOTF were the basis for mooring configuration selection. Since the results of the oscillations tests for the four mooring lines and the three mooring lines with delta connection configurations do not improve the resonance properties of the system, only the three mooring lines configuration was further considered. Comparing the results obtained in both basins demonstrates how small changes in the mooring lines lead to differences regarding the response of the floating body. The three mooring lines configuration was longer and lighter at FloWave OERF, but most relevant than that, at Lir NOTF the mooring system was asymmetric, i.e. one of the lines was heavier than the other two. Even though the average suspended weight was similar in both basins, the natural periods of oscillation were different for all the modes of motion except heave. The other modes of motion, i.e. surge, sway, pitch, roll, and yaw match up to 82, 67, 98, 97, and 88% respectively. The reason for this mismatch is the fact that the heave plate intercepted the mooring line while swinging during some of the tests, truncating the oscillatory motion as can be seen in Figures 5.13.2c and 5.13.2e. The records of the tests performed at FloWave OERF do not present this anomaly.

As explained in Section 5.11, different RAOs can be computed from the same source data depending on the part of the record analysed (Figure 5.11.3). RAOs are normally used to assess the frequency-domain linear wave-body response of floating structures. Therefore, they are transfer functions defined only when motion can be assumed linear. Accordingly, the RAOs results presented before were computed using only the linear part of the motions record. The trends are in line with typical results for a spar buoy wind concept [18, 84, 85, 86].

Assessing which part of the record is linear or not is not a trivial task. Figures 5.14.3 to 5.14.7 show how the records of a regular test can vary according to the frequency of the excitation wave. The surge response, for example, starts in Figures 5.14.3 and 5.14.4, i.e. 0.35 and 0.4 Hz respectively, with a quasi-harmonic behaviour oscillating up and down at wave excitation frequency during the whole record. In this case, it is advised to analyse the beginning of the record avoiding the initial transients, i.e. from 5 to 25 s. This interval of analysis ensures the use of a minimum of two complete cycles to compute the RAO. From 25 s onwards the record is contaminated with undesirable hydrodynamic effects such as reflections. As the frequency of excitation is increased, e.g. Figure 5.14.5 with a regular wave of period 0.9 Hz, the natural frequency of the mooring line is over-imposed to the wave excitation harmonic motion. Now, the analysis must be constrained to a smaller record, e.g. from 15 to 20 s, since with a smaller interval we can analyse even more cycles than before while avoiding undesirable hydrodynamic effects More complex responses are obtained for higher frequencies, e.g. Figure 5.14.6 with a regular wave of period 1.2 Hz. As the frequency increases, the wave takes longer to reach the model, but a few seconds of record account for several cycles.

Particularly relevant is the case shown in Figure 5.14.7. The record shown, correspond to a regular wave with a frequency of 0.2625 Hz. Following the previous reasoning, it is expected with a quasi-harmonic behaviour, however, this frequency is close to the heave resonant wave condition, and non-linear behaviour arises presenting a complex surge-pitch coupled response.

Figures 5.13.7 and 5.13.8 include the results of the random waves testing conducted in Lir NOTF in terms of RAO. The trends match with the regular results as suggested by the line joining both results.

The RAOs produced during the irregular wave testing conducted in FloWave OERF are presented in Figure 5.14.14. The Figure presents the results split in modes of motion, i.e. surge, sway, heave, pitch, roll, and yaw. However, each Figure includes the results

from two irregular waves, i.e. H_s equal to 4.5 and 7.2 m and T_p of 8.5 and 9.5 s, for head, bow and beam seas, i.e. 0, 45, and 90 degrees, and with and without mooring lines. This way of presenting the results highlights the relationship existent between surge and pitch responses since they show smaller response for beam seas than for head and bow seas, i.e. surge and pitch motions are dominated by the wave excitation in head and bow seas. In Figure 5.14.14a, i.e. surge RAO, leaving the wave excitation apart, the surge and pitch resonant frequencies are also highlighted. The heave resonant frequency is also depicted but presenting a smaller peak. In Figure 5.14.14d, i.e. pitch RAO, and again leaving the wave excitation apart, clear pitch, surge and heave peaks are depicted.

This way of presenting the results, also draws special attention to the sway, roll, and yaw modes of motion relationship since bow and beam seas present higher response than head seas, i.e. sway, roll, and yaw motions are also dominated by the wave excitation in head and bow seas. Figure 5.14.14b, i.e. sway RAO, presents sway, pitch and heave resonant peak along with the wave excitation. Figures 5.14.14e and 5.14.14f, i.e. roll and yaw RAOs, show roll, surge and heave resonant peak. However, heave peaks are relatively small.

5.16. Conclusions

Hydrodynamic testing of a 1:45 Froude scaled model of the DTI-F concept has been carried out in two different wave basins for three different mooring configurations, i.e. three lines distributed at 120 degrees, four lines distributed at 90 degrees, and three lines distributed at 120 degrees with a delta connection.

The requested wave periods were adequately reproduced in both basins. However, the wave amplitudes were 25% off at Lir NOTF, and 5% off at FloWave OERF for regular waves, and 6% off and 18% off respectively for irregular waves.

Free decay, stiffness decay, regular wave, and irregular testing were performed. The

hydrostatic behaviour and resonance properties of the floater were experimentally determined.

The full-scale natural period results show that all six degrees of freedom are longer than the linear wave excitation for all the mooring configurations tested, as the ocean waves contain first harmonic wave energy in the period range of 5 - 25 seconds. For a spar buoy-based FOWT the natural periods in surge, sway and yaw should be larger than 100 seconds, 20-35 seconds for heave, and 50-90 seconds for roll and pitch [68]. Therefore, the results meet the constraints specified in the relevant standards. Comparing the results to the Equinior's (Statoil formerly) Hywind project results [20], the DTI-F concept has a 25% longer surge period, a similar heave period, a 75% longer pitch and roll periods, and a 95% longer yaw period.

The damping obtained while performing decay tests has been split into its radiation and viscous components, i.e. linear and quadratic damping, to be introduced in future numerical modelling.

Stiffness decay tests served as justification for the mooring configuration choice. Since no improvement regarding natural periods of oscillation was achieved by increasing the number of mooring lines nor by including the delta connection, the three mooring lines configuration was selected, and the four and three mooring line with delta connection configurations were not further considered.

Regular and irregular wave tests results were discussed in terms of RAOs. The RAOs variability regarding the part of the record used to calculate them has been discussed.

Irregular wave tests were performed for two different sea states representing two rough operational conditions. The results give will help to validate future numerical modelling developments.

The differences shown between the results obtained in Lir NOFT and FloWave OERF basins are mainly due to slight differences in the scale model e.g. trim, and the different mooring layout used.

6. Numerical methods for the FOWT

6.1. General

Due to the existing strong coupling between aerodynamics and hydrodynamics that the FOWTs exhibit, it is desirable to perform fully-coupled simulations of the system. However, during the design and in the early stages of the development, the different interactions explained before can be isolated and simulated independently before joining them in a fully-coupled simulation, in order to reduce the level of complexity. This study thus deals solely with the uncoupled hydrodynamic behaviour of the DTI-F system. To compute the hydrodynamic behaviour of FOWT, the literature offers a wide range of techniques available to researchers. The most common empirical method used is Morison's equation [88]. Increasing the computational effort, the use of the Potential Flow (PF) models to compute linear wave-structure interaction using the 3D panel method is another widely used technique due to its well-balanced accuracy against computational effort ratio. However, in the PF theory viscosity is ignored; if the role of viscosity is important, Morison type models may be imposed to improve PF results. Finally, when considering advanced numerical methods, Computational Fluid Dynamics (CFD) models [88, 89] present a better agreement with experimental results giving details of the flow at very local regions within the fluid domain. However, the use of CFD is limited for large multi-body systems at early design stages may be impractical due to the computational effort involved. This study focuses on setting up an ANSYS AQWA simulation of the

DTI-F concept without mooring lines. Subsequently, the ANSYS AQWA results are used as an input to simulate the platform and mooring dynamics using OrcaFlex. ANSYS AQWA 19.1 is a commercial software package using diffraction potential theory with an imposed Morison drag term. OrcaFlex 10.2 is a dynamic mooring analysis commercial software package able to perform complex simulations including VIV effects among others. Other numerical simulation tools were used to perform the whole analysis. Both ANSYS AQWA and OrcaFlex software include drawing capabilities, but they lack mass distribution properties calculation. Mass distribution properties such as the height of the centre of gravity (CoG) and moments of inertia (MoI) are necessary inputs for ANSYS AQWA, and since ANSYS AQWA provides input to OrcaFlex, these results are also necessary to run OrcaFlex simulations. To calculate the initial mass distribution properties of the full-scale system the Autodesk Inventor computer-aid design (CAD) software was used in this study. In order to validate the initial hull design, the Bentley MAXSURF's integrated naval architecture tools were used. MAXSURF ensures a fast and accurate analysis of hull hydrostatics, equilibrium and stability including essential characteristics such as endwise and sideways inclination (trim and heel). The modelling with MAXSURF was performed by a researcher at the University of Strathclyde. Therefore, only the results that are relevant to this research will be analysed, and there is no further reference to how to model with MAXSURF. This scheme has been followed twice in order to produce two sets of simulations, one validated against the testing performed in Lir NOTF and another one validated against the FloWave OERF results. Next Sections describe the functionalities of the different software packages mentioned before. The different numerical tools are presented following the order in which they are used for this investigation. The description is limited to the functionalities used during this research.

6.2. Modelling in Autodesk Inventor

Inventor 2016 R3 is a 3D CAD parametric modelling tool. It is mainly an application for 3D mechanical design, simulation, visualisation, and documentation developed by Autodesk. Invertor was used to perform the baseline design of the concrete floater (Figure 6.2.1a) and the full-scale floating system (Figure 6.2.1b), i.e. substructure, ballast water, flotation cylinder, tower, and nacelle set, i.e. nacelle, rotor, and blades, using the dimensions presented in Section 4.2.

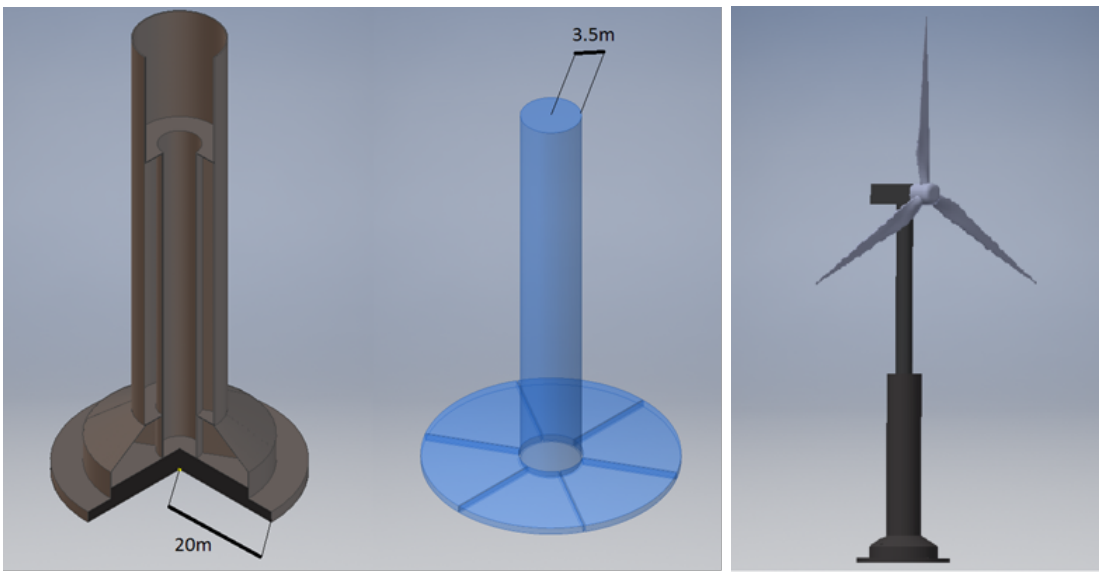

(a) Three quarter section view of the concrete floater and a zoom in the ballast water body as distributed into the floater in the raised tower and nacelle position.

(b) Full-scale complete free floating system.

Figure 6.2.1.: Baseline design of the DTI-F concept.

Complex geometries can be parametrically defined. A material density can be linked with every different part producing a reliable computation of the overall mass, area, volume, position of the CoG, and mass moments and products of inertia.

6.3. Notes on the wave forces on a floating body

To compute the hydrodynamic forces due to the wave interaction with a floating body, its inertial and viscous components must be calculated. Inertial forces, i.e. Froude-Krylov, diffraction, and radiation forces, arise from potential flow wave theory. The Froude-Krylov force is dominant when the characteristic dimension of the floating body, e.g. the top cylinder diameter of the spar buoy, is much smaller than the wavelength. It means that the floating body does not modify the incident wave field, and therefore, the diffracted and radiated wave potential can be ignored. Contrarily, diffraction or scattering force prevails when the characteristic dimension of the floating body is not much greater than the wavelength, meaning that the wave field near the floating body will be affected even if it is stationary. Radiation forces, controlled by the added mass, damping, and restoring terms, are the results of a structure forced to oscillate at wave excitation frequency in its 6 DoF with no incident waves (Figure 6.3.1).

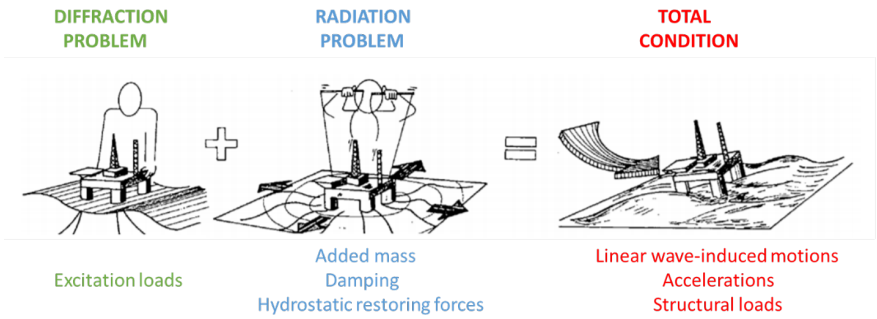

Figure 6.3.1.: Inertial forces on linear potential theory.

Viscous forces, i.e. form drag and friction drag, are associated to flow separation. Therefore, they are relevant in the proximity of a boundary layer with small Reynolds number, being the former the ratio of inertial to viscous forces within a fluid subjected to relative inertial movement, i.e. different fluid velocities.

Figure 6.3.2 presents the dominant loading regimes [90] affecting a structure as a function of wave height (H), structure diameter (D) and wave length (λ). The Figure shows

the relevant hydrodynamic regimes for the structure and sea states under consideration. The DTI-F floater falls into the 'all inertia' and the 'diffraction' regimes. For large wavelength waves the floater behaviour will be more influenced by Froude-Krylov forces. However, for small wavelength waves diffraction will be dominant. Moreover, for large wave heights a small drag component should be added. Even tough survivability analysis is out of the scope, it is worth noting that for extreme waves, i.e. waves whose height is more than twice the H_s, the drag component grows, and viscous effect should also be considered.

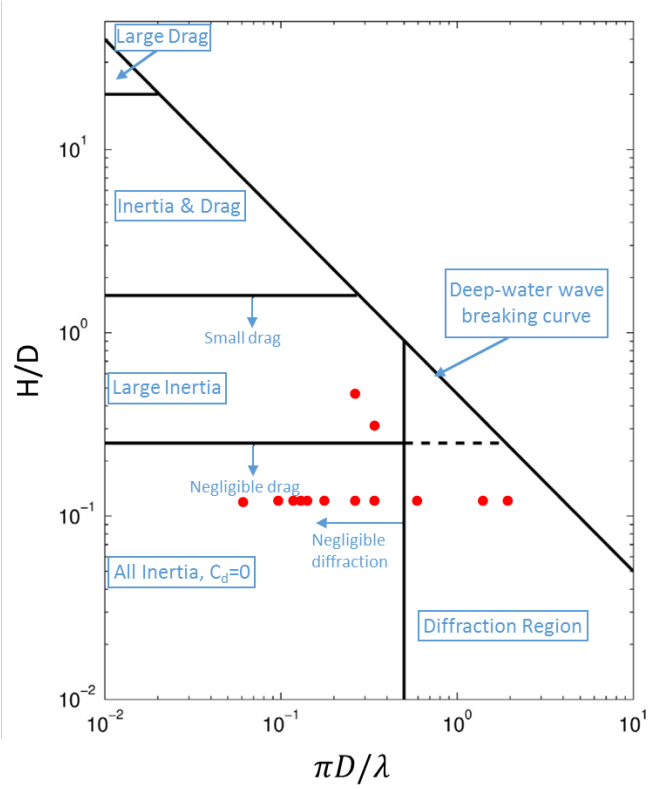

Figure 6.3.2.: Relative importance of viscous effects and different types of potential flow effects. Modified from [90]. The red dots represent the waves tested.

In addition, the theory used to generate waves will depend on the wave height and the depth of the studied site. The distinction between deep and shallow water is determined by the ratio of water depth to wavelength. In deep water, linear wave theory is valid for

small waves. As the wave height increases Stokes theory becomes more relevant, and its order of approximation raises proportionally to the wave height [91]. Figure 6.3.3 presents the approximate ranges of applicability of different wave theories and the relevant ones for the structure and sea states under consideration.

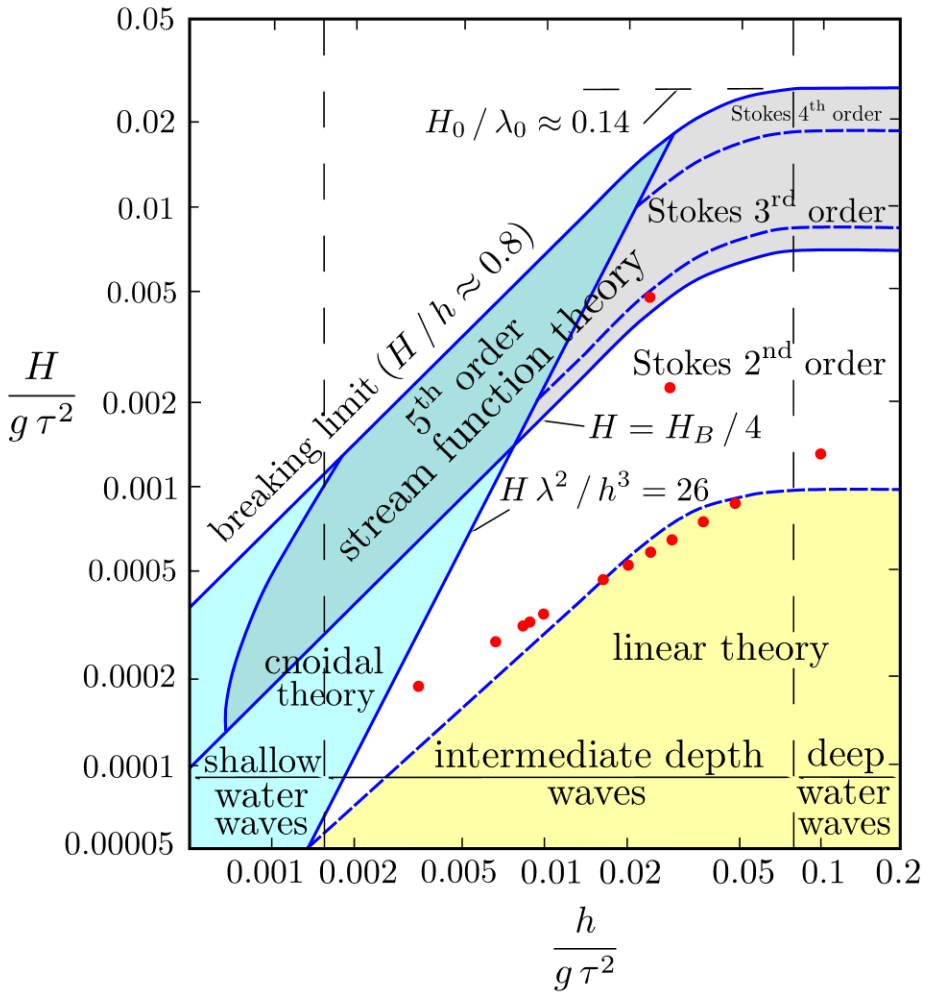

Figure 6.3.3.: Ranges of applicability of different wave theories as a function of function of the wave height (H), structure diameter (D) and water depth (h). Modified from [91]. The red dots represent the waves tested.

6.4. Modelling in ANSYS AQWA

ANSYS AQWA 19.1 is an engineering analysis suite of tools to investigate waves, wind, and current effects on both fixed and floating structures [92, 93]. AQWA [94] uses basic hydrodynamic 3D potential theory to calculate the motion results, and it also uses Morison's Equation and Morison linearization to calculate the hydrodynamic forces (Figure 6.4.1). It assumes an ideal fluid with an existing velocity potential and uses linear hydrodynamic theory.

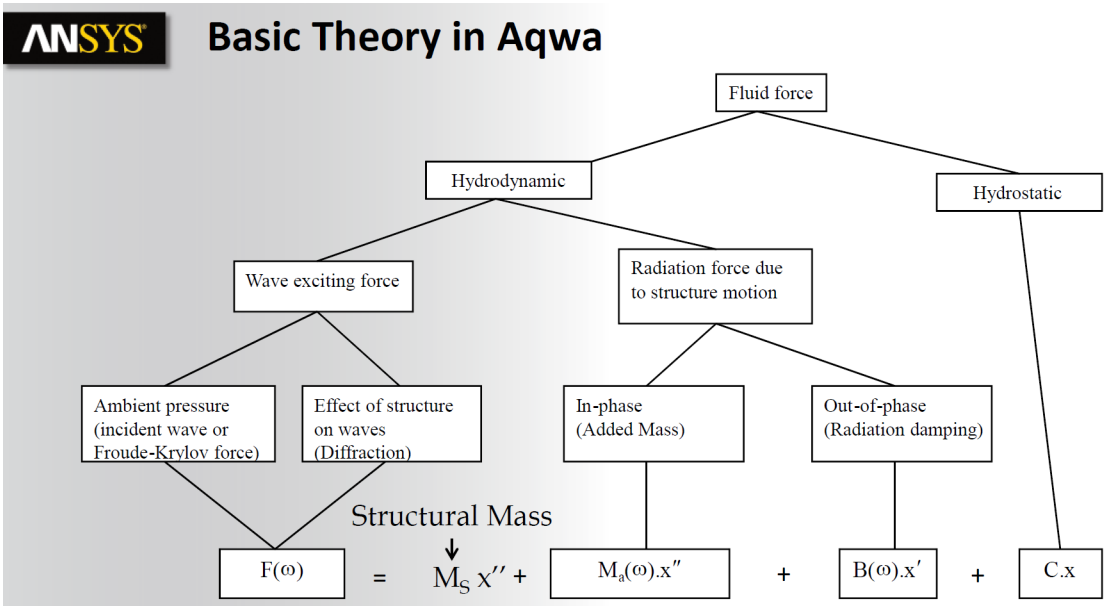

Figure 6.4.1.: Basic theory in ANSYS AQWA [94].

Three core programs within the AQWA suit have been used to compute the diffraction analysis, the static and dynamic equilibrium positions, response amplitude operators (RAOs) and some frequency domain as well as time-domain results. Only the diffraction results, the RAOs and the time series for the free decay tests will be discussed in this study.

AQWA-Line is a 3D diffraction and radiation analysis program working in the frequency domain. It provides hydrostatic analysis and hydrodynamic coefficients to be

used in other programs, both within and outwith the AQWA suit. AQWA-Librium [95] provides the equilibrium position, the eigenvalues of the linearised stiffness matrix to obtain static stability, and the static and dynamic stability results. AQWA-Fer calculates the RAOs and motions due to high and low frequencies. The suit works under ANSYS Workbench project management environment [96]; therefore, the capabilities of the above-mentioned core programs are used through two analysis systems, Hydrodynamic Diffraction (HD) and Hydrodynamic Response (HR). The HD system provides hydrostatic results, RAOs, radiation damping, and added mass. The HR system provides static stability, frequency and time domain dynamic responses.

Two sets simulations were developed to assess the responses of the free-floating system, the first one models the full-scale system whereas the second set models the scale testing performed in Lir NOTF and FloWave OERF. Since the initial conditions were slightly different in the two wave basins, different numerical models were developed and subsequently validated against experimental results.

6.4.1. Modelling the DTI-F system without moorings

This Section explains the workflow to set up an ANSYS AQWA simulation under the Workbench environment [96]. The starting point for modelling with ANSYS AQWA is defining the geometry to analyse. As explained before, the full-scale structure was already modelled in Autodesk Inventor. However, for the diffraction analysis a simplified version of the CAD model was used, i.e. shell or thin solid. DesignModeller or SpaceClaim, the CAD tools provided by ANSYS easily perform this operation. Obtaining a scaled technical draw of the simplified version is also straightforward, being only a matter of introducing the scaling parameter. A few critical steps must also be followed within the ANSYS CAD systems before being able to use it as an ANSYS AQWA geometry, e.g. the structure must be sliced by the water plane, and then the two resulting parts must be joined together into a new part. The experiments conducted in Lir National Ocean

Test Facility (NOTF) present an initial trim. Therefore, one of the simulations was set up replicating this inclination in the floater.

Valid geometries can be imported from DesignModeller or SpaceClaim to the geometry component system. The geometry component system groups all the input parameters regarding the model geometry and the modelling of the still-water condition environment, e.g. structural mass, position of CoG, MoI, water depth, water density, water size among others.

Before importing the whole project information to an HD analysis system, the geometry must be discretised (Figure 6.4.2). The process of discretising a geometry is called meshing and it will affect the results if the quality of the mesh is poor i.e. elements aspect ratio higher than 30, skewness higher than 0.9, or minimum orthogonal quality lower than 0.15.

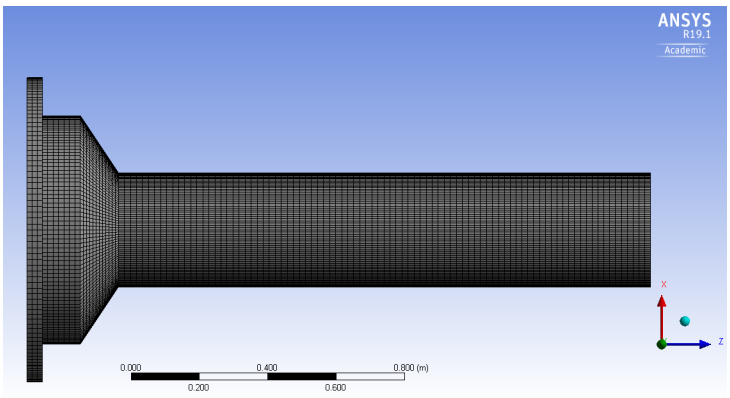

Figure 6.4.2.: Discretization of the concrete substructure for the diffraction analysis.

Only a successfully meshed geometry can be shared between the geometry component system and the HD system. Within the HD system, analysis settings including wave directions and frequencies must be introduced along with all the desired results.

The results of an HD system include hydrostatic results, RAOs, radiation damping and added mass among others. The HD system shares its results with one or several HR systems, e.g. stability analysis, time response, frequency response. The stability

analysis system computes the static and dynamic stability positions. Time response systems calculate specified response time series, e.g. three different HR systems were configured to replicate the heave, pitch and roll free decay tests conducted in Lir NOTF and FloWave OERF. Frequency response calculates significant motions for the floating system due to wave (high frequency) and drift (low frequency) frequencies.

The results are presented in different formats, i.e. graphical results in the screen, exportable results spreadsheet, and output file with LIS extension (Figure 6.4.3). LIS outputs are ASCII files containing the model definition, some analysis parameters and the analysis results [97].

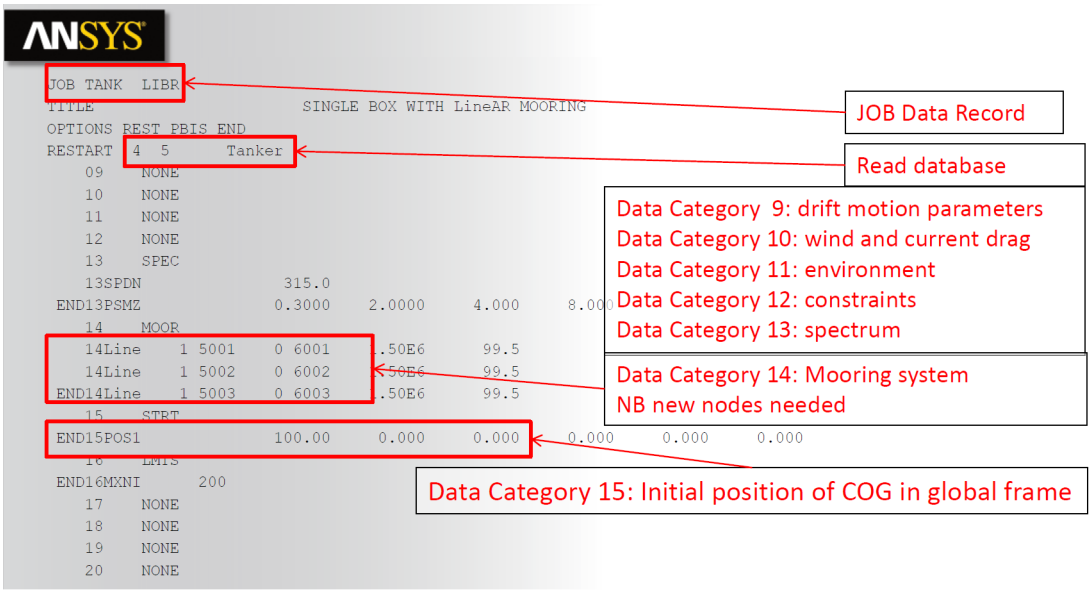

Figure 6.4.3.: Detail of a LIS file with comments [97].

6.4.2. Simulations setup

Three models were developed to assess the response of the floating structure. A full-scale model based on the dimensions calculated in Section 4.2 which is not going to be further discussed, and another two based on the dimensions provided in Table 6.1 of Section 5.3 to replicate the testing conditions in Lir NOTF and FloWave OERF. The common

parameters introduced in the geometry component system are presented in Table 6.2a whereas the parameters differing in Lir NOTF and FloWave OERF are presented in Table 6.2b.

Table 6.1.: Parameters used for the Lir NOTF and FloWave OERF numerical simulations.

	Scale model
Structural mass (kg)	186
Height of CoG (m)	0.447
Draft (m)	1.320
Water depth (m)	2
Water density (kg/m^3)	1000
Water size (m)	0.5x0.5

(a) Common parameters.

	Lir NOTF	FloWave OERF
Trim	-1.4	0
I_{xx}, I_{yy}, I_{zz} (kgm^2)	126, 126, 9.8	135, 135, 10

(b) Differing parameters in Lir NOTF and FloWave OERF simulations.

The MoI (I_{xx}, I_{yy}, I_{zz}) used for the Lir NOTF simulation correspond to the theoretical values calculated by Autodesk Inventor while the ones used for the FloWave OERF simulation are the results obtained during the swing testing explained in Section 5.8.

Both models present a high-quality mesh, i.e. elements aspect ratio equal to 23, skewness equal to 0.7, and minimum orthogonal quality of 0.17; with a total of 39287 elements of which 19321 are diffracting nodes. The rest are non-diffracting elements, i.e. elements over the waterline. The maximum element size was 0.0295m allowing for a maximum wave frequency of 3.553 Hz. These figures demonstrate that the smallest wavelength in the frequency analysis is captured by 7-panels or 7-panel sizes fit into the smallest

wavelength.

In both cases, eight wave directions were considered in the HD analysis at intervals of 45 degrees and ranging from 0.45 to 3 Hz at equispaced intervals of 0.16 Hz.

Three HR systems were set up to reproduce the conditions of the free decay testing in heave, pitch and roll modes of motion conducted in both basins, i.e. Lir NOTF and FloWave OERF. Before starting these simulations, another HR system takes care of calculating the static stability position of the spar buoy using all the information introduced before. Once the static stability position is set as initial point for the time domain simulation, an initial displacement (or inclination) is imposed on the floating system and the simulation starts. The floating body tends to return to its static stability position due to the restoring moments showing a characteristic damped sinusoidal response.

The initial numerical model underestimated or overestimated some of the hydrodynamic parameters. Therefore, additional damping and drag must be introduced into the model to calibrate it against the testing records. In addition, the stiffness and the added mass had to be tuned in order to match the testing results. Further comments on the calibration process will be discussed later in Section 6.6.

6.5. Modelling in OrcaFlex

This Section introduces the workflow to set up an OrcaFlex hydrodynamic model. The starting point for modelling in OrcaFlex environment is defining the floating system to be analysed [98]. In OrcaFlex, the relevant objects to model a FOWT are the vessel, the buoy, and the mooring line objects. Besides, a line object could be used for modelling FOWTs, but this approach is not going to be further commented since it would model a flexible substructure, and this is out of the scope.

The vessel object is the best suited to simulate objects behaving in the diffraction regime although spar buoys do have limited diffraction capability. Any vessel type can

be defined within OrcaFlex by using a diffraction code, e.g. ANSYS AQWA, WAMIT, Sesam, to obtain stiffness, RAOs, quadratic transfer functions (QTFs) and frequency-dependent added mass and damping. As explained before, the ANSYS AQWA LIS results file provides all the needed parameters to set up a vessel object in OrcaFlex automatically, i.e. the code determines the relation between the OrcaFlex vessel and ANSYS AQWA origins and axes and uses these relationships during the import process to set the reference origins and mass/inertia matrix appropriately in OrcaFlex [99]. The 6D buoy object can be tailored in terms of geometry and hydrodynamic parameters, e.g. drag and added mass among others, to create hydrodynamically accurate components. It models marine structures that can be fixed to the seabed, moored or free-floating.

The 6D buoy object uses Morison's equation to simulate objects which are dominated by the inertia (and/or drag) regime, i.e. FOWT characteristic diameter much smaller than the wavelength [100]. The 6D buoy object can be connected to other objects. Therefore, it gives rise to utilisation of hybrid buoy-vessel models [101].

The mooring line object models cables, hoses, chains or other similar devices. OrcaFlex uses a lumped mass model to simulate the mooring lines. Each line consists of a limited number of lumped masses (nodes) joined by massless springs systems (segments). Each segment represents a discrete part of the line, whose properties have been lumped at the nodes at its ends [102]. OrcaFlex uses three different spring-dampers systems (Figure 6.5.1) to model the axial and torsional stiffness and damping, and the bending properties of the mooring lines.

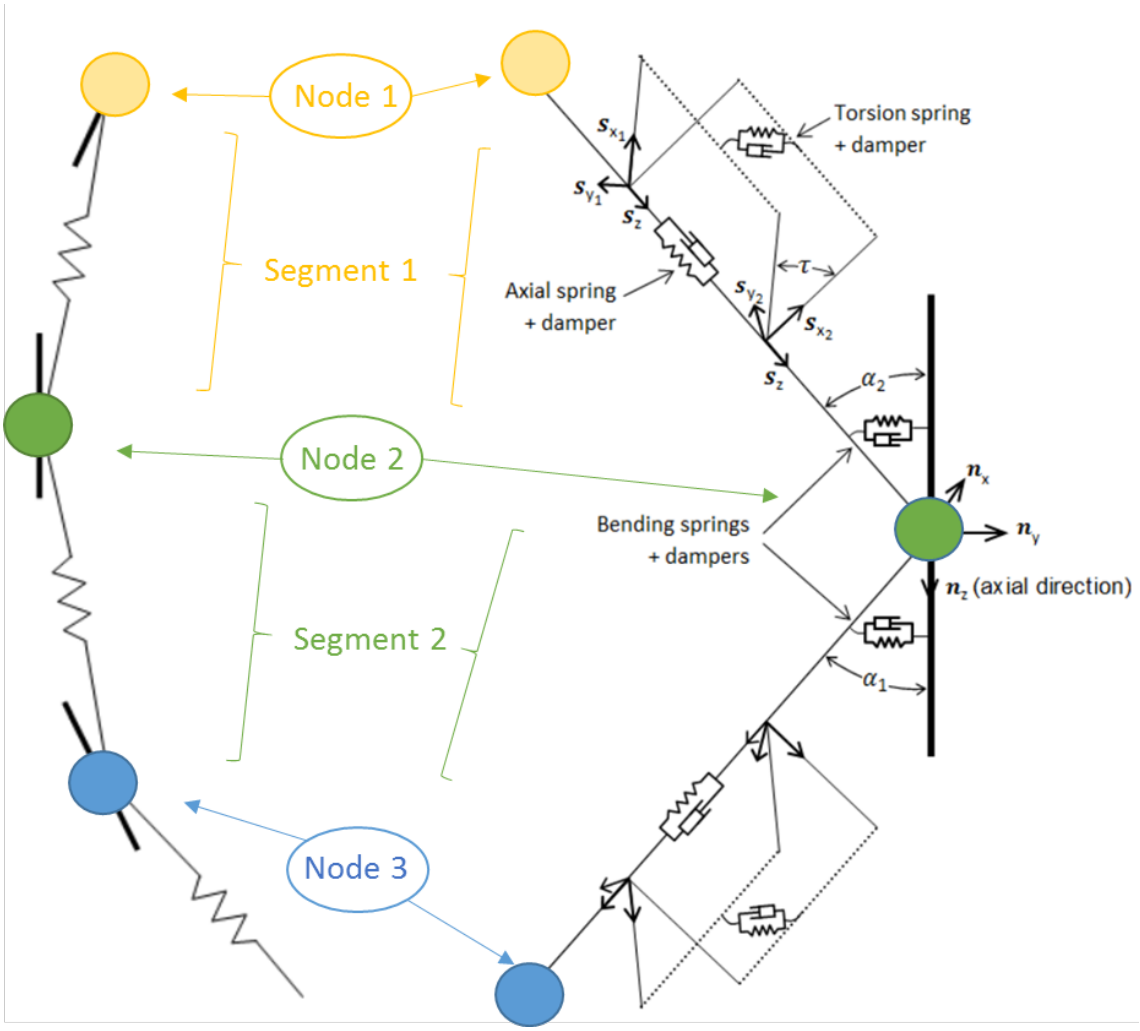

Figure 6.5.1.: Discretised mooring line model and the correspondent structural model. Modified from [102].

Table 6.2 presents a comparison between ANSYS AQWA and OrcaFlex capabilities.

Table 6.2.: Comparison between ANSYS AQWA and OrcaFlex capabilities. LM and FE stand for lumped mass and finite elements respectively.

	Tension/Bending/Torsion	LM/FE	Non-linear Stiffness
ANSYS AQWA	Yes/Yes/No	LM	Yes
OrcaFlex	Yes/Yes/Yes	LM	Yes

(a) Dynamic cable solver.

	Diff/Rad	Morison	Diff/Rad Input	2^{nd} order Wave Effects
ANSYS AQWA	Yes	Yes	No	Yes
OrcaFlex	No	Yes	Yes	Yes

(b) Hydrodynamic analysis.

	Linear	Stokes	Stream	Irregular
ANSYS AQWA	Yes	2^{nd}	Yes	Yes
OrcaFlex	Yes	5^{th}	Yes	Yes

(c) Wave theory.

6.5.1. Modelling the DTI-F in OrcaFlex

As introduced earlier, there is a variety of options to model FOWTs. Models relying on 6D buoys are the optimal choice for slender structures. When a floating structure increases its characteristic diameter until a certain threshold, a vessel object will better capture the diffraction and radiation effects. Therefore, 6D buoys have been the choice for most of the studies on spar buoy-based FOWTs since spar buoys have a limited diffraction capability. However, as shown in Figure 6.3.2, the DTI-F concept lays on the diffraction regime for high-frequency waves. Consequently, a hybrid buoy-vessel model has been developed to properly account for all the inertia components using both a vessel and a 6D buoy objects, rigidly connected to the vessel.

The first step to set up a hybrid buoy-vessel simulation is to model the floating structure as a vessel, and then connecting the mooring lines. Then, a 6D buoy must be connected to the vessel origin. It should be noted that vessel objects can be only 'master' objects, i.e. vessel object cannot be connected to another object and become 'slave'. Therefore,

the mooring lines must be also connected to the vessel object.

The 6D buoy object will deal with the mass, the mass moments of inertia and the position of the CoG whereas the vessel object will allocate the hydrodynamic stiffness, added mass, and damping. Therefore, the mass properties will be set as negligible in the vessel and the 6D buoy will lack stiffness, added mass, damping which will be provided by the vessel object.

To properly replicate testing results, the vessel must be set up to i) include the six DoF in the static analysis, ii) to 'Calculated (6DOF)' for the primary motion, iii) to 'None' for the superimposed motion; and turn on all 'Included Effects'.

Regarding the modelling of the mooring lines, a dynamic approach was adopted. However, before the dynamic analysis takes place, the static equilibrium position must be obtained by using an iterative process. Performing a robust and accurate statics convergence solution will save time during the simulation since un-necessary transients will be avoided [103].

6.5.2. Simulation setup

Two different models were developed to simulate the testing campaigns conducted in Lir NOTF and FloWave OERF.

Both models share the same general setup, including the implicit integration method and the international system of units. However, they have different geometries since the experiment in Lir NOTF was performed with -1.4 degrees of trim. These geometries are linked to vessel objects.

The OrcaFlex vessel object receives inputs from the LIS file generated in ANSYS AQWA. Therefore, most of the parameters will be properly and automatically input in the right place by the importing tool. It is strongly advised to double-check that every value is correctly input regarding reference origins and axis. Some of these values must be redistributed in the 6D buoy object and set to zero in the vessel object, as explained

before.

Setting up the mooring lines will be the main task in OrcaFlex (Figure 6.5.2). After placing a line object in the model environment, the type of mooring line, the number of different sections, and the length of each section must be provided. Generic values for catenary lines can be obtained directly from the Line Type Wizard tool within OrcaFlex, but since the provided parameters are generic using real data pertaining to the chain would be a better approximation. The DTI-F models incorporate as much manufacturer-provided parameter as has been possible. Moreover, the relevant testing was conducted to ensure maximum reliance with the input parameters and avoiding differences between experimental and numerical setup.

Once the first line object is configured and connected to the vessel and the anchoring point, a useful Rotation tool helps to symmetrically distribute the rest of the lines, fairleads, and anchoring points.

At this stage, the model is ready to perform the static analysis. If the results of the static analysis are satisfactory, the model is ready to execute the dynamic analysis. However, before conducting the dynamic simulation, it is possible to check the pretension existing on the floating system. If the pretension values are no accurate enough, OrcaFlex provides the Line Set-up Wizard tool which, given a certain pretension value, adjusts the length of the line or the position of the anchor point to match that pretension value. The Line Set-up Wizard tool was used to match the pretension level in the model simulating the experiments conducted in Lir NOTF since there were available load cell readings.

Another important check before conducting the dynamic simulation would be the mooring stiffness. The mooring stiffness provides the restoring forces/moments for surge, sway, and yaw modes of motion. The combination of pretensions and mooring stiffness matching the experimental setup, along with a reasonable floating object model leads to an accurate and high-performance dynamic simulation.

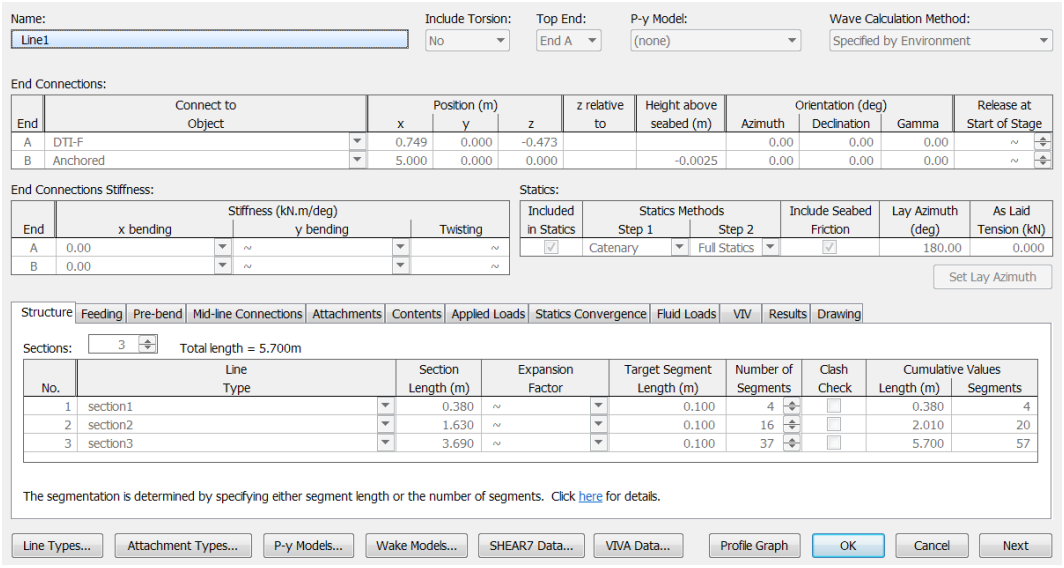

Figure 6.5.2.: Screenshot of the line data editor within OrcaFlex.

Regarding the environment, the dynamic viscosity of the water and the density must be setup. It can seem trivial, but normal full-scale simulations use a water density of 1025 kg/m^3 corresponding to seawater, whereas scale testing simulations use freshwater density, i.e. 1000 kg/m^3. Other line-seabed interaction parameters can be defined along with the wave regime, currents and wind. The present study uses generic line-seabed interaction parameters and does not account for current or wind loading.

The waves were produced specifically to match every single experiment using the adequate wave theory as shown in Figure 6.3.3. The JONSWAP spectrum was used to generate the appropriate random seas. The irregular waves tested were simulated for three hours as the international standards recommend. It was ensured that the H_{max} in each simulation was larger than 1.87 times H_s for every JONSWAP spectrum tested. Six seed were used for each wave condition and only the maximum responses were extracted to evaluate the global performance at this stage.

6.6. Results and validation

This Section will present the results of the numerical models developed to simulate the Lir NOTF and FloWave OERF experimental campaigns.

6.6.1. Simulation of the Lir NOTF experiments

The draft in still water conditions was matched by the numerical models. Both ANSYS AQWA and OrcaFlex have shown excellent agreement with the testing records without and with mooring lines attached respectively. As stated before, the trim was imposed in both models.

The initial pretension calculated by the numerical model was between 4 to 6% off in comparison to the pretension recorded in the basin. Therefore, the pretension listed in Table 5.12 of Section 5.13 for the three mooring lines configuration, i.e. 11.2, 7.3 and 8.0 N, were introduced using the above-mentioned Line Set-up Wizard tool in the numerical model. The tool changed the anchor points location to match the provided pretensions. The maximum change in the position of the anchor point per component was 32 mm which correspond to a 0.8% of the total distance between the vertical of the floating body and the initial anchoring point.

Table 6.3 presents the natural period of oscillation (w_n) and damping coefficients (ζ) computed by ANSYS AQWA compared with the testing results. Figure 6.6.1 depicts the results of the ANSYS AQWA simulation of the free decay testing in heave, pitch, and roll modes of motion compared with the testing results. Table 6.4 presents the simulated natural periods of oscillation and the damping coefficients of the DTI-F system for the three mooring lines at 120 degrees configuration compared with the testing results. Figure 6.6.2 shows the results of the numerical model simulating the stiffness decay test of the DTI-F system for the three mooring lines at 120 degrees configuration in heave, surge, and sway compared with the testing results.

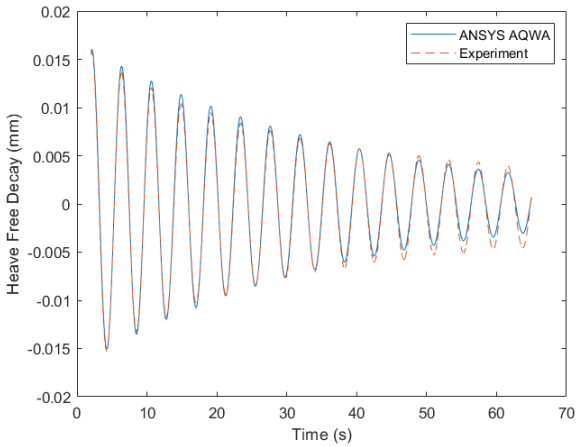

(a) Heave.

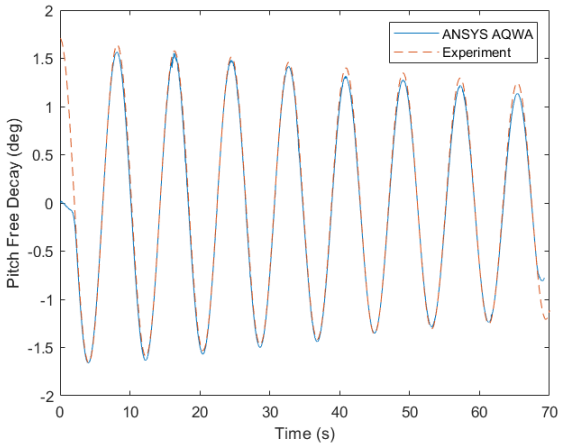

(b) Pitch.

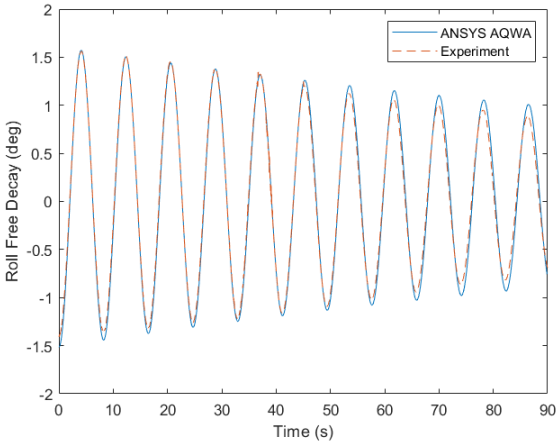

(c) Roll.

Figure 6.6.1.: Free decay simulation validated against the testing results.

Table 6.3.: Resonance properties of the free floater.

	ANSYS AQWA		Free decay test		% difference	
	f_n (Hz)	ζ (-)	f_n (Hz)	ζ(-)	f_n(%)	ζ (%)
Heave	0.235	4.14×10-3	0.235	4.40×10-3	0.00	5.91
Pitch	0.122	8.11×10-4	0.122	8.00×10-4	0.00	1.38
Roll	0.122	7.61×10-4	0.122	8.00×10-4	0.00	4.88

Table 6.4.: Resonance properties of the DTI-F system.

	ANSYS AQWA		Free decay test		% difference	
	f_n (Hz)	ζ (-)	f_n (Hz)	ζ (-)	f_n(%)	ζ (%)
Surge	0.039	1.91x10^{-3}	0.040	1.97x10^{-3}	2.50	3.05
Sway	0.066	2.37x10^{-3}	0.066	2.17x10^{-3}	0.00	8.44
Heave	0.235	3.78x10^{-3}	0.238	3.54x10^{-3}	1.26	6.35
Pitch	0.076	1.54x10^{-3}	0.076	1.23x10^{-3}	0.00	20.13
Roll	0.074	1.28x10^{-3}	0.073	1.01x10^{-3}	1.35	21.09
Yaw	0.056	1.36x10^{-3}	0.055	1.79x10^{-3}	1.79	24.02

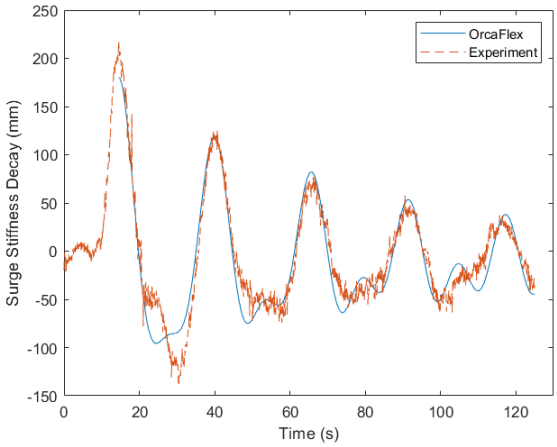

(a) Surge.

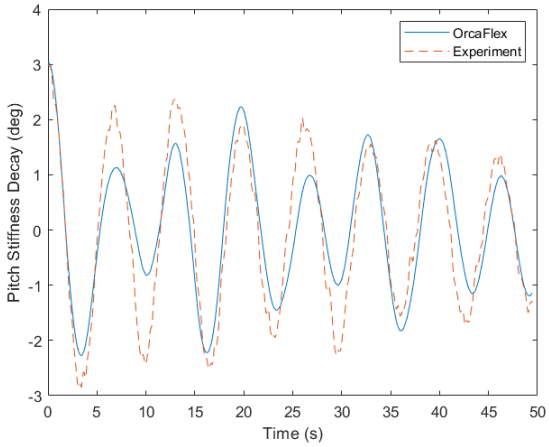

(b) Pitch

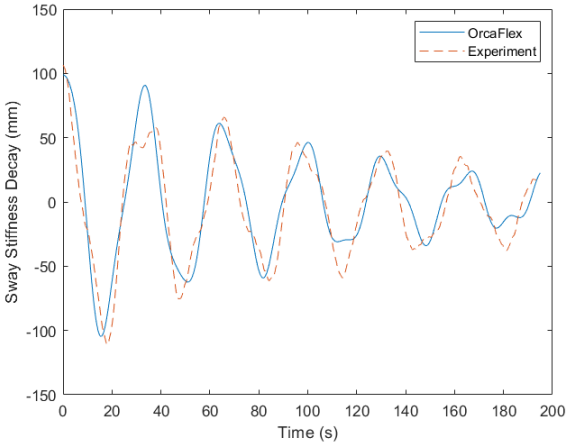

(c) Sway.

Figure 6.6.2.: Stiffness decay simulation results for the three mooring lines at 120 degrees configuration compared with the testing results.

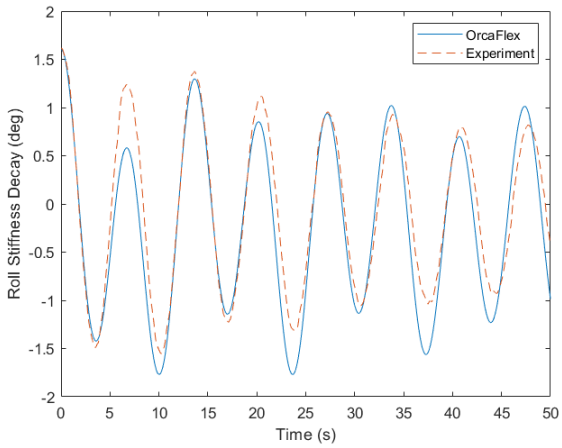

(d) Roll.

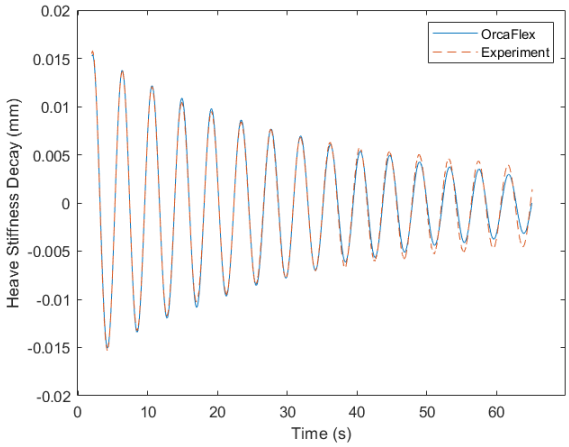

(e) Heave.

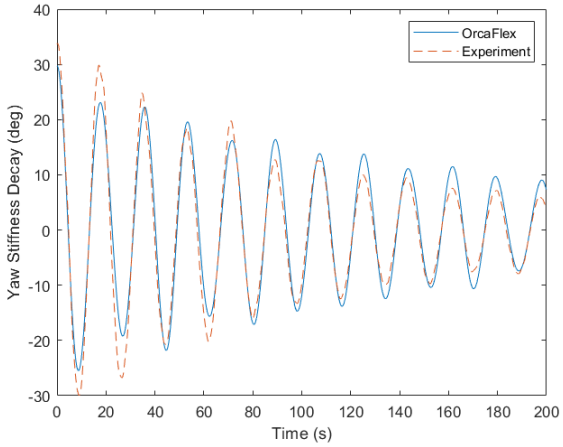

(f) Yaw.

Figure 6.6.2.: Stiffness decay simulation results for the three mooring lines at 120 degrees configuration compared with the testing results.

Figure 6.6.3 presents the calculated RAOs for the three mooring lines at 120 degrees configuration in surge, sway, heave, roll, pitch and yaw. Figure 6.6.4 shows the results of a regular wave test simulation with a wave height of 44 mm and a period of 2.22 s and an irregular wave (JONSAWP spectrum with wave significant height of 40 mm and a peak period of 0.89 s) in terms of wave elevation, surge and the pitch responses, both compared with the testing results. Figure 6.6.6 shows the spectral densities of the irregular wave time series depicted in Figure 6.6.5.

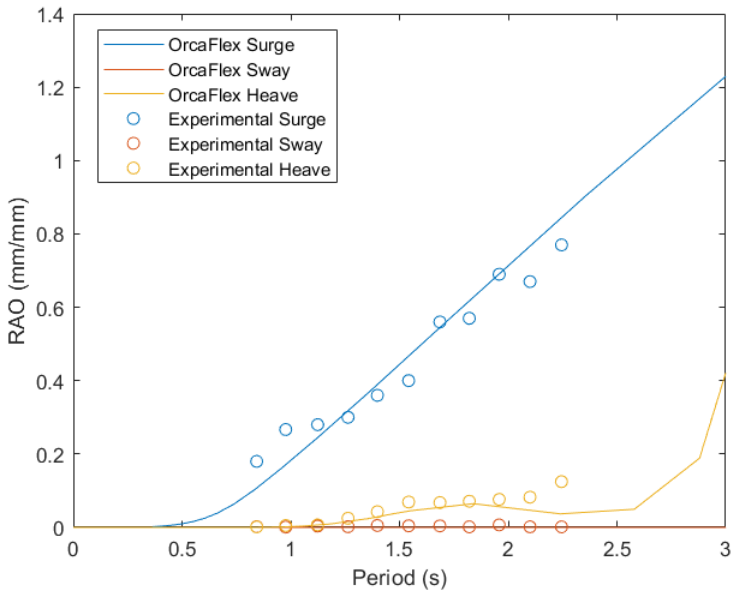

(a) Translational RAOs.

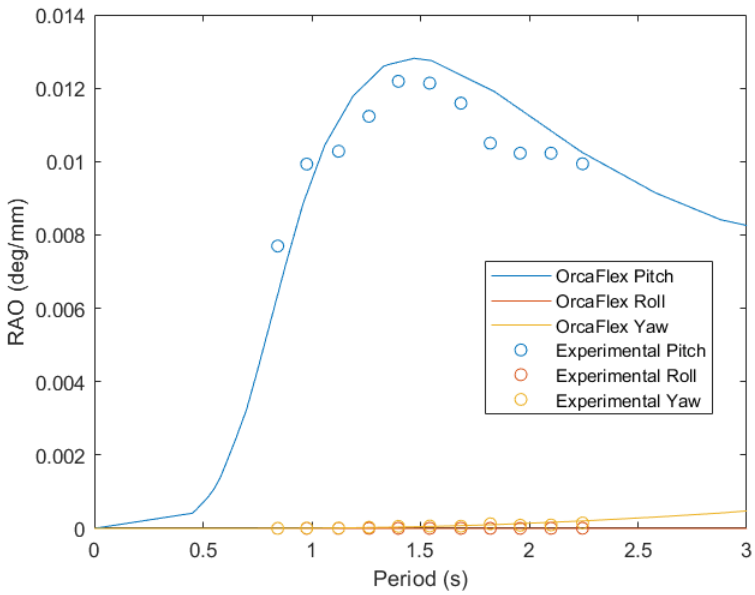

(b) Rotational RAOs.

Figure 6.6.3.: Simulated and experimental RAOs.

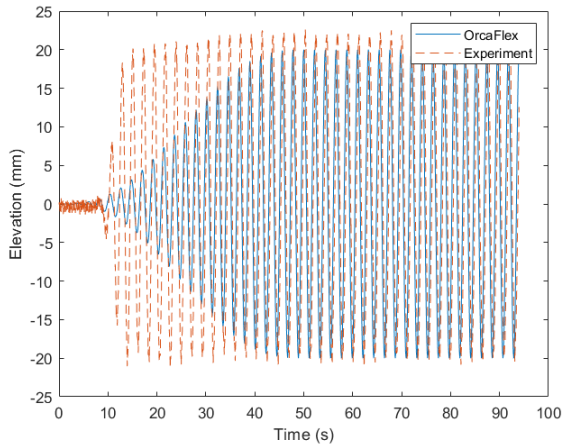

(a) Regular wave elevation.

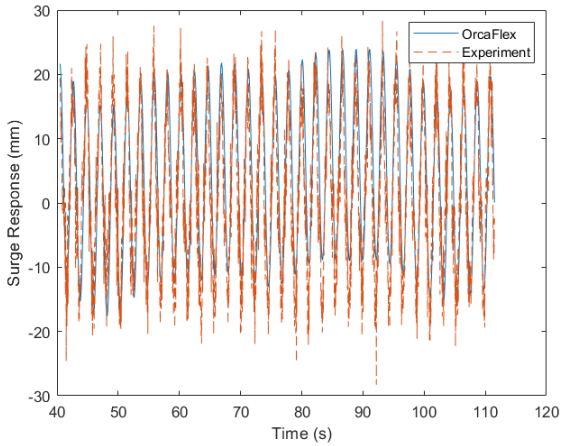

(b) Surge for the regular wave.

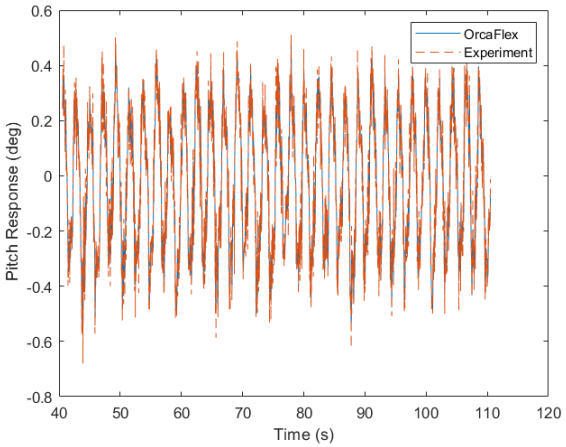

(c) Pitch for the regular wave.

Figure 6.6.4.: Simulated and experimental regular wave testing responses.

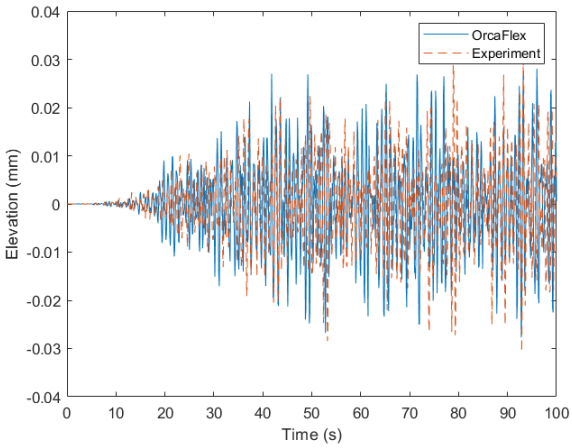

(a) Irregular wave height.

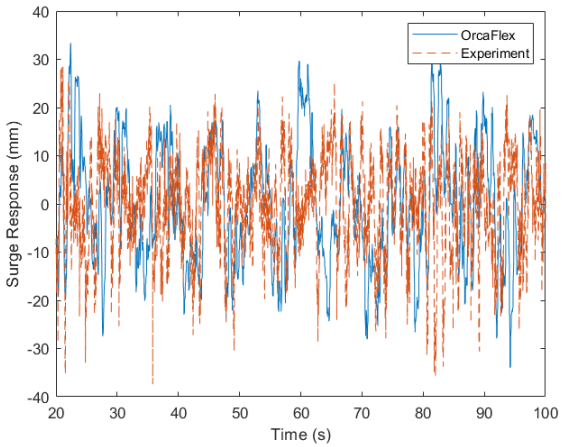

(b) Surge for the irregular wave.

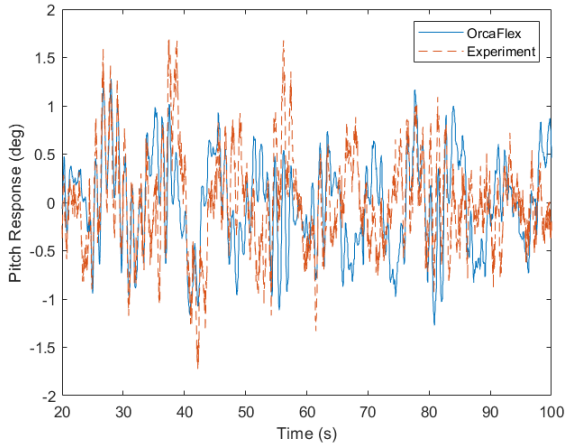

(c) Surge for the irregular wave.

Figure 6.6.5.: Simulated and experimental irregular wave testing responses.

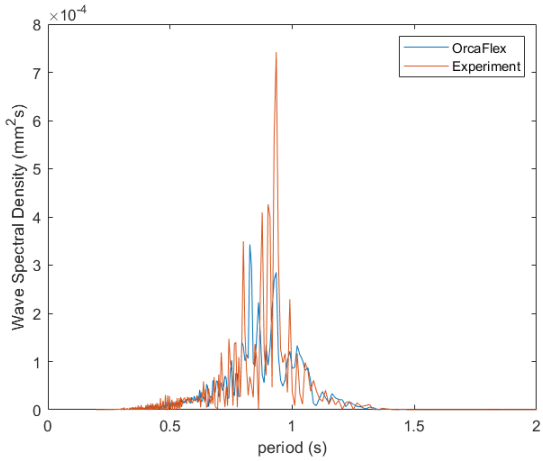

(a) Wave height spectral density.

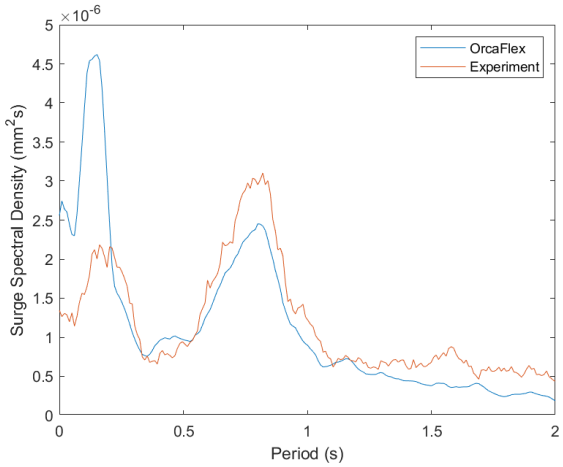

(b) Surge spectral density.

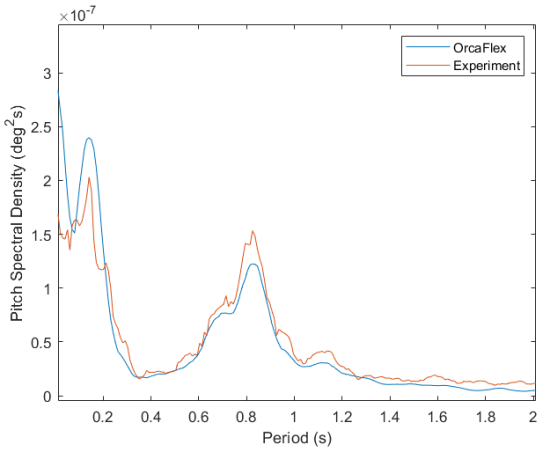

(c) Pitch spectral density.

Figure 6.6.6.: Spectral densities of the time series shown in Figure 6.6.5.

6.6.2. Simulation of the FloWave OERF experiments

The draft in still water conditions was perfectly matched with the numerical models. Both ANSYS AQWA and OrcaFlex have shown excellent agreement with the testing records without and with mooring lines attached respectively.

Since the testing setup used in FloWave OERF did not include force transducers, no mooring tension records are available, and therefore the pretension either. However, the experimental setup included underwater cameras able to trace the underwater markers installed in Line 1. Processing the position of the underwater markers, the catenary shape can be envisaged, and therefore pretensions can be estimated. Figure 6.6.7 presents a comparison of the simulated versus experimental mooring line shape in still water conditions, and Figure 6.6.8 presents the results of the simulation of the quasi-static test.

Figure 6.6.9 shows the results of the simulation of the free decay testing, and Table 6.5 presents the numerical modelling damping and natural period of oscillation results of the free-floating system. Table 6.6 and Figure 6.6.10 present the simulated results of the stiffness decay testing.

A comparison of the simulated RAOs for the free-floating and moored conditions validated with the regular testing results is depicted in Figures 6.6.11 and 6.6.12.

Table 6.5.: Comparison of the simulated resonance properties of the free floater and testing results.

	ANSYS AQWA		Free decay tests		% difference with testing		% difference with Lir NOEF model	
	f_n (s)	ζ (-)	f_n (s)	ζ (-)	f_n (s)	ζ (-)	f_n (s)	ζ (-)
Heave	0.235	4.18×10^{-3}	0.235	4.40×10^{-3}	0.00	5.00	0.00	0.96
Pitch	0.122	8.06×10^{-4}	0.122	8.00×10^{-4}	0.00	0.74	0.00	0.62
Roll	0.122	7.96×10^{-4}	0.122	8.00×10^{-4}	0.00	0.50	0.00	4.62

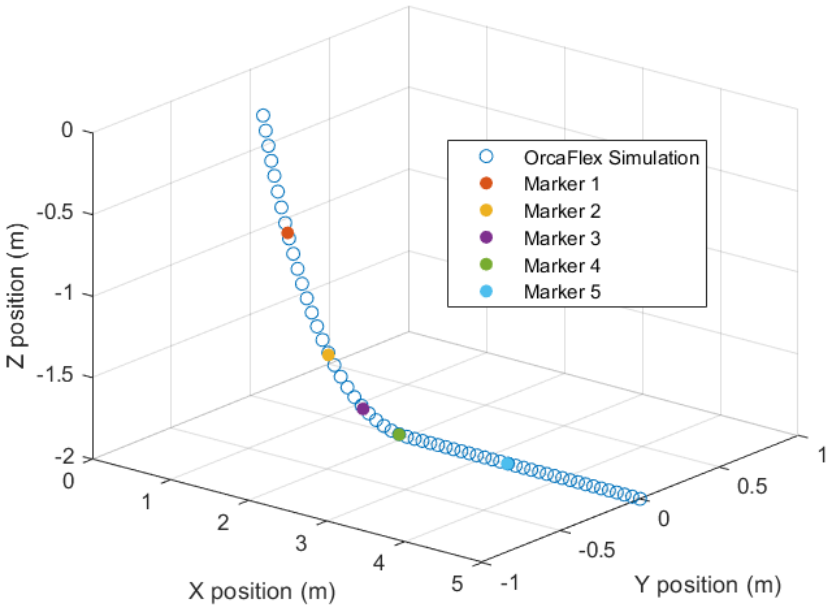

Figure 6.6.7.: Validated mooring lines shape.

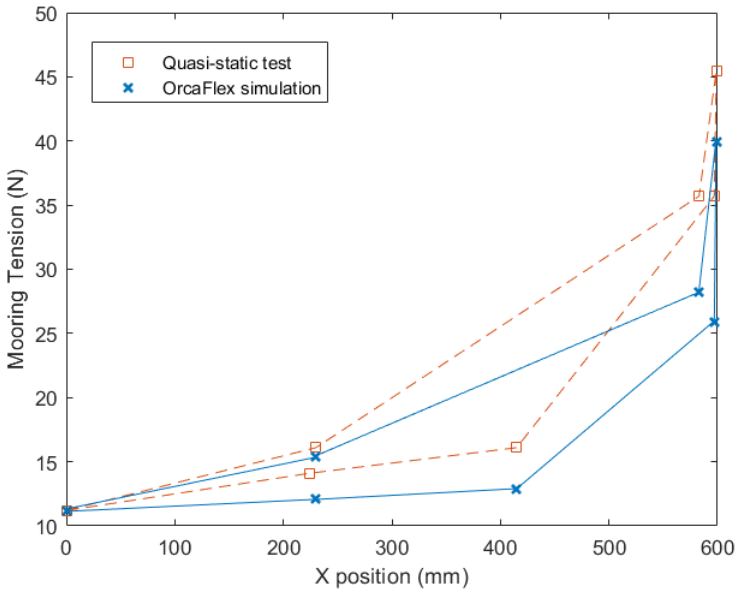

Figure 6.6.8.: Simulated catenary axial stiffness testing.

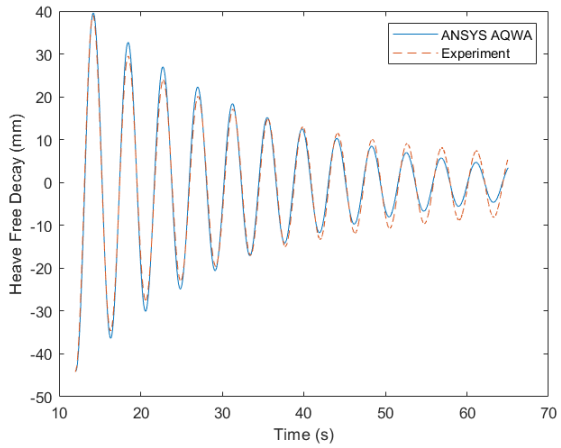

(a) Heave.

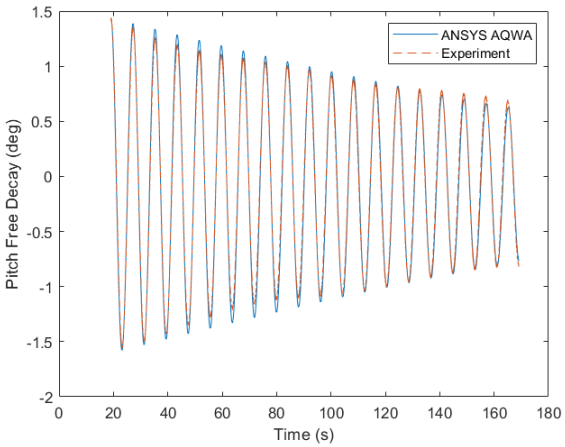

(b) Pitch.

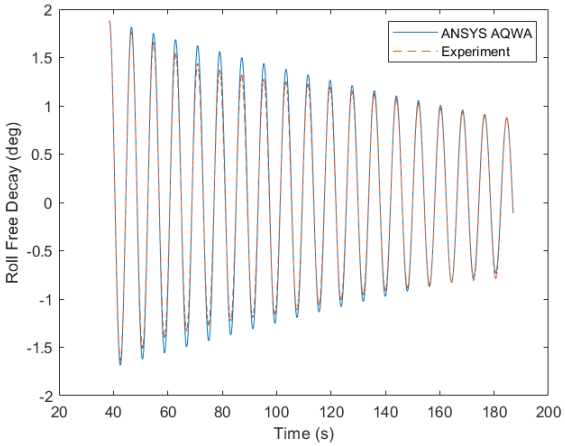

(c) Roll.

Figure 6.6.9.: Validated free decay simulation.

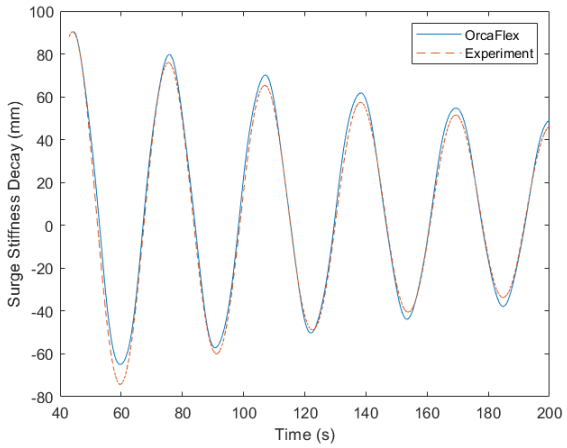

(a) Surge.

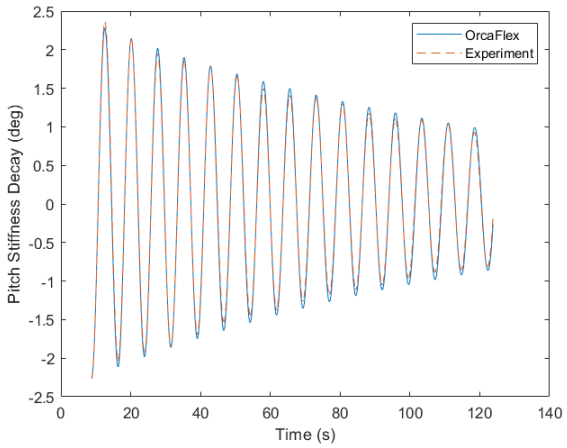

(b) Pitch.

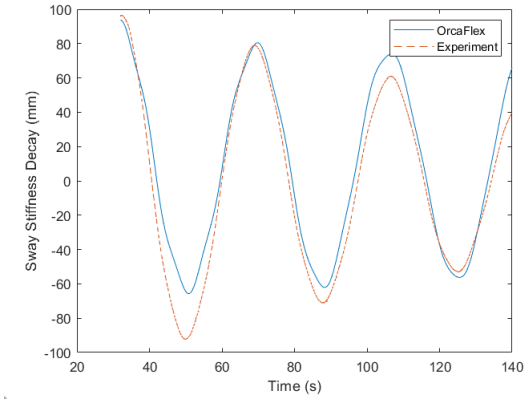

(c) Sway.

Figure 6.6.10.: Validated stiffness decay simulation.

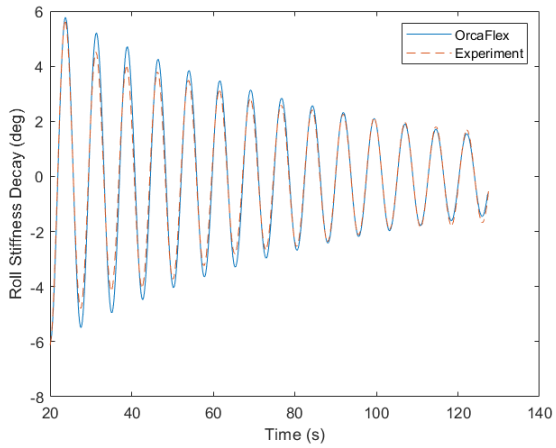

(d) Roll.

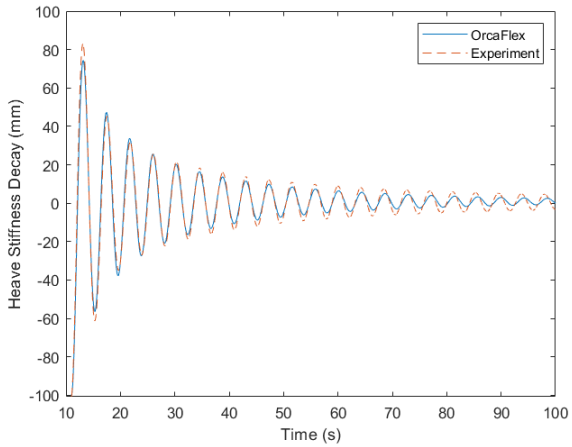

(e) Heave.

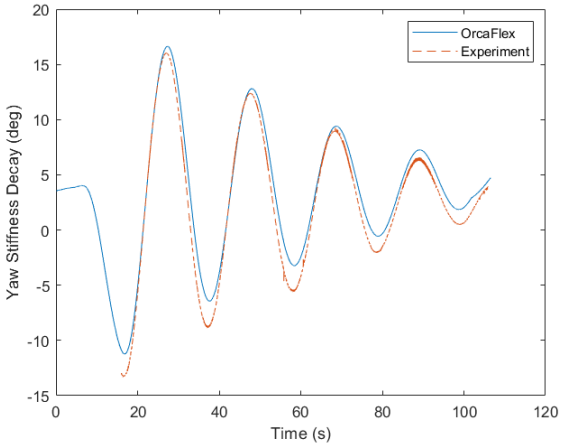

(f) Yaw.

Figure 6.6.10.: Validated stiffness decay simulation.

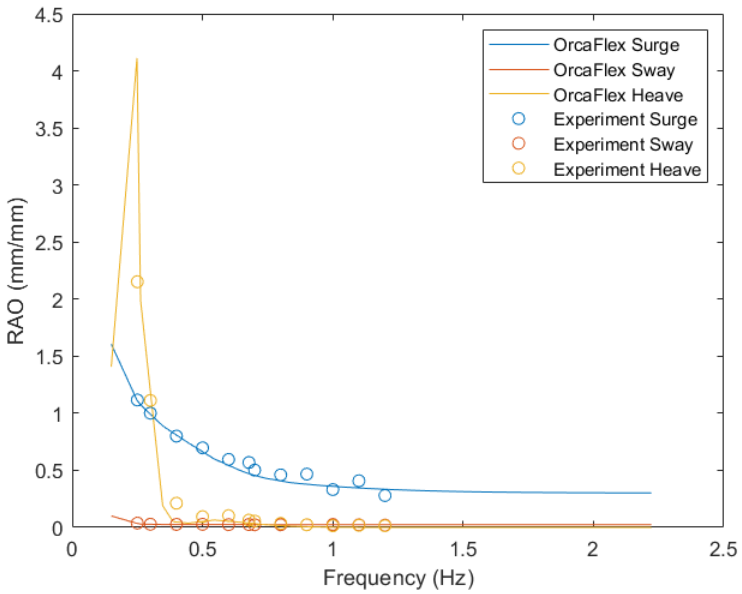

(a) Translational RAOs.

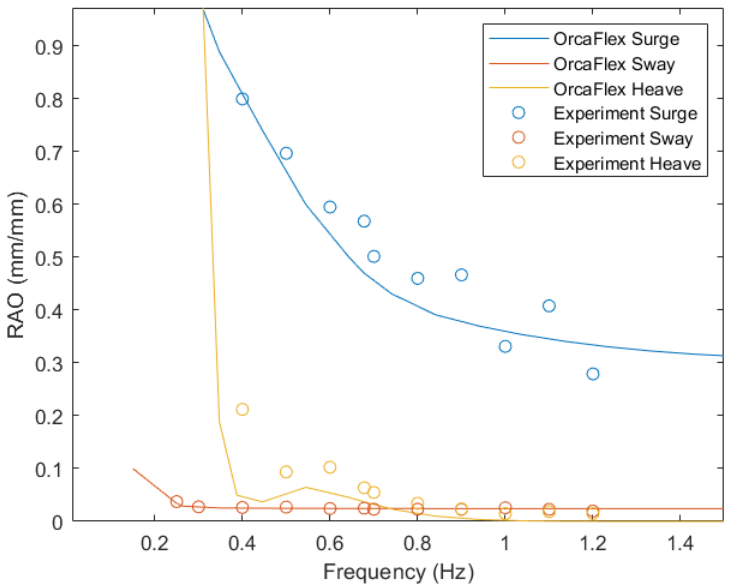

(b) Zoom in view of Figure 6.6.11a.

Figure 6.6.11.: Simulated RAOs for the free-floating condition in heading seas validated with the regular testing results.

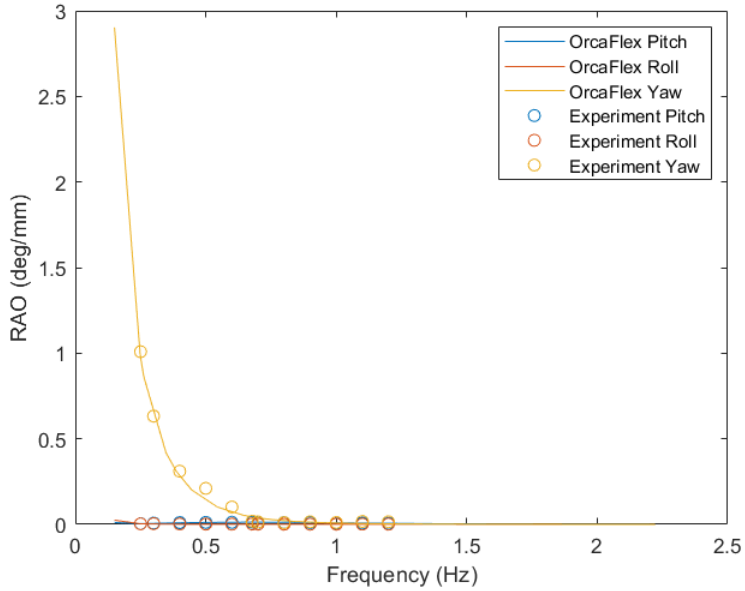

(c) Rotational RAOs.

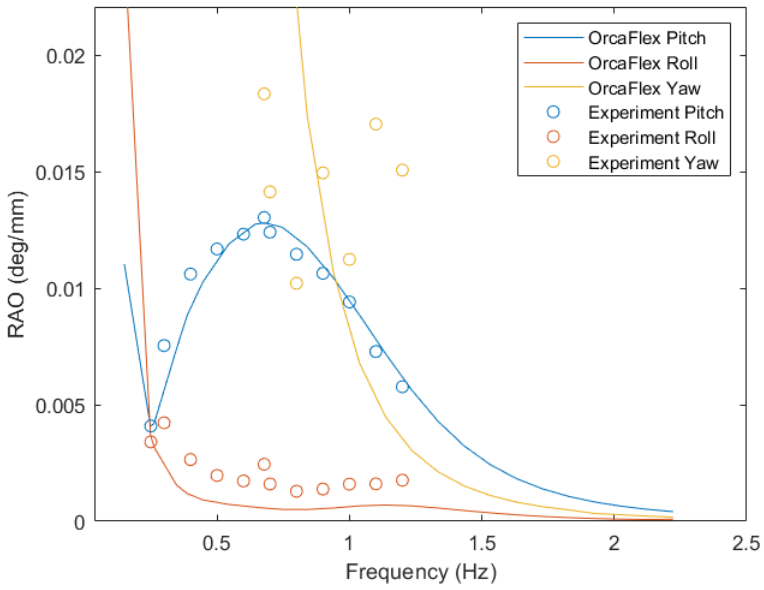

(d) Zoom in view of Figure 6.6.11c

Figure 6.6.11.: Simulated RAOs for the free-floating condition in heading seas validated with the regular testing results.

Table 6.6.: Comparison of the simulated resonance properties of the moored DTI-F system.

	OrcaFlex		Stiffness decay test		% difference	
	f_n(Hz)	ζ (-)	f_n(Hz)	ζ(-)	f_n	ζ
Surge	0.032	3.86×10^{-3}	0.032	4.10×10^{-3}	0.00	3.50
Sway	0.025	3.75×10^{-3}	0.026	$4.10\times10\text{-}^{-3}$	4.00	9.33
Heave	0.237	3.80×10^{-2}	0.236	3.56×10-2	0.42	6.32
Pitch	0.132	7.46×10^{-3}	0.132	9.25×10^{-3}	0.00	7.67
Roll	0.131	8.92×10^{-3}	0.132	8.11×10^{-3}	0.75	9.08
Yaw	0.048	1.13×10^{-3}	0.049	1.10×10^{-3}	2.04	2.56

Figure 6.6.13 shows the results of a regular wave test simulation with a wave height of 40mm and a frequency of 0.3 Hz in terms of wave elevation, surge and the pitch responses, both compared with the testing results. Figure 6.6.14 presents the same results for another wave with the same wave height and a frequency of 1.2 Hz.

Figure 6.6.15 shows the wave height, heave, pitch, and surge responses for an irregular wave experiment with 101 mm of wave height and a peak period of 1.27 s. Zoom in view of the time series is also provided to better assess the level of agreement.

Figure 6.6.16 presents the wave height, heave, pitch, and surge spectral density for an irregular wave test with 101 mm of wave height and a peak period of 1.27 s. Vertical dotted lines highlight the peak responses and the resonant frequency is also provided.

In Figure 6.6.17, the non-dimensional displacement calculated from the irregular sea simulations with a significant wave height of 4.5 m and a peak period of 8.5 s are depicted along with their equivalents recorded during the testing.

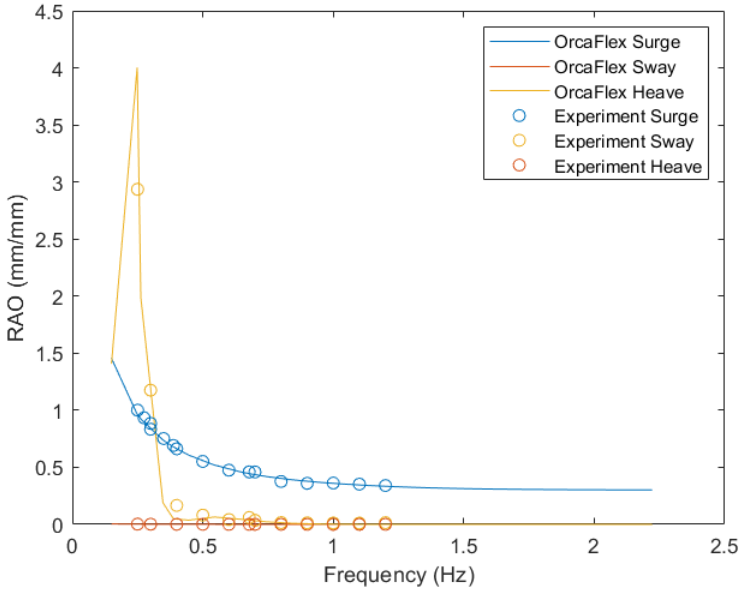

(a) Translational RAOs.

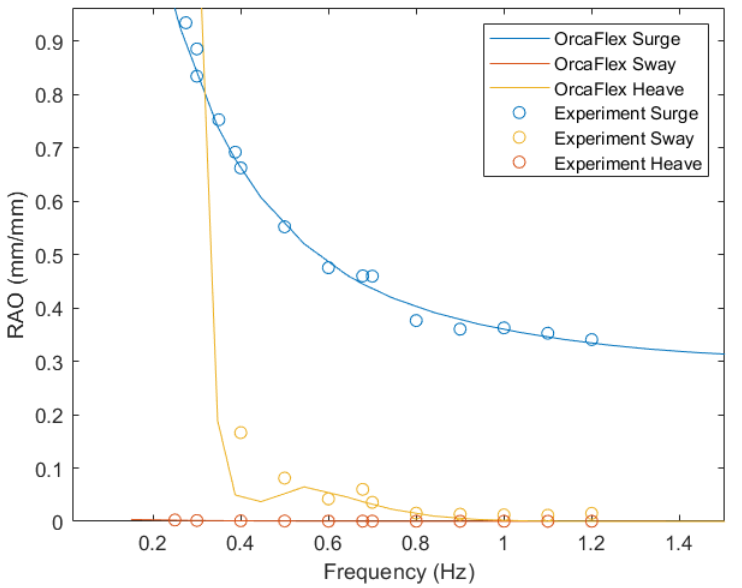

(b) Zoom in view of Figure 6.6.12a.

Figure 6.6.12.: Simulated RAOs for the moored condition in heading seas validated with the regular testing results.

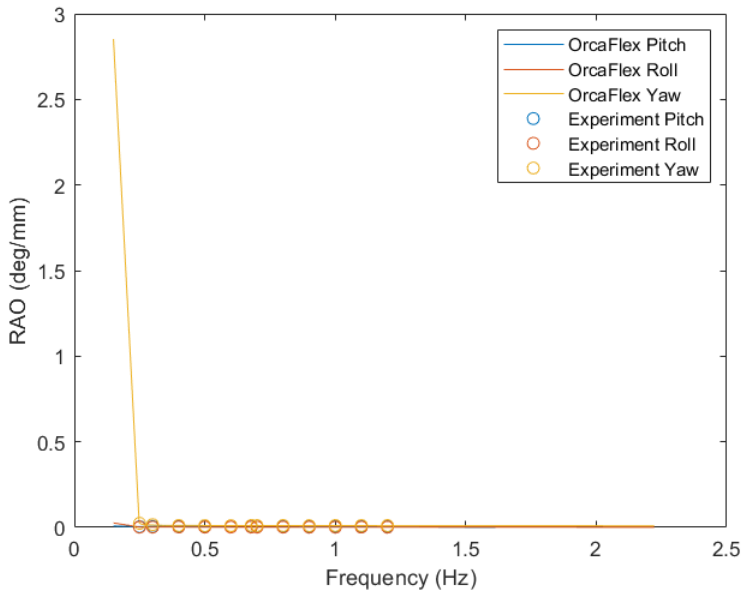

(c) Rotational RAOs.

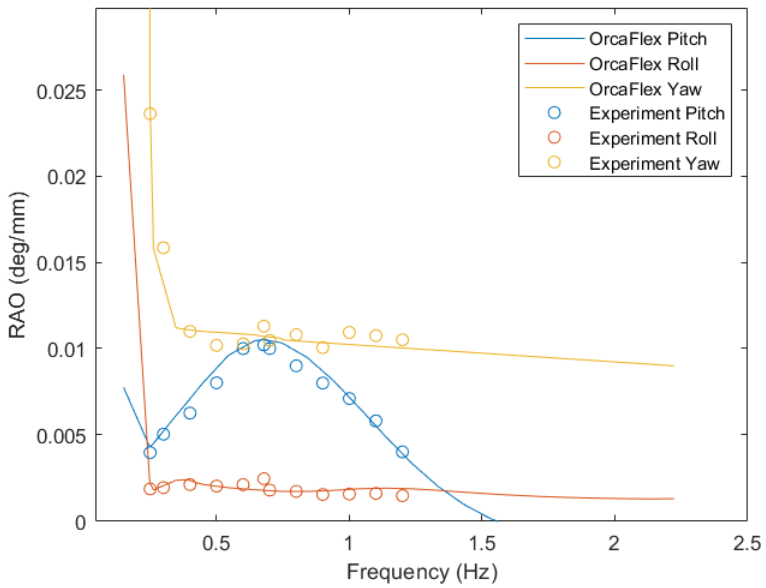

(d) Zoom in view of Figure 6.6.12c.

Figure 6.6.12.: Simulated RAOs for the moored condition in heading seas validated with the regular testing results.

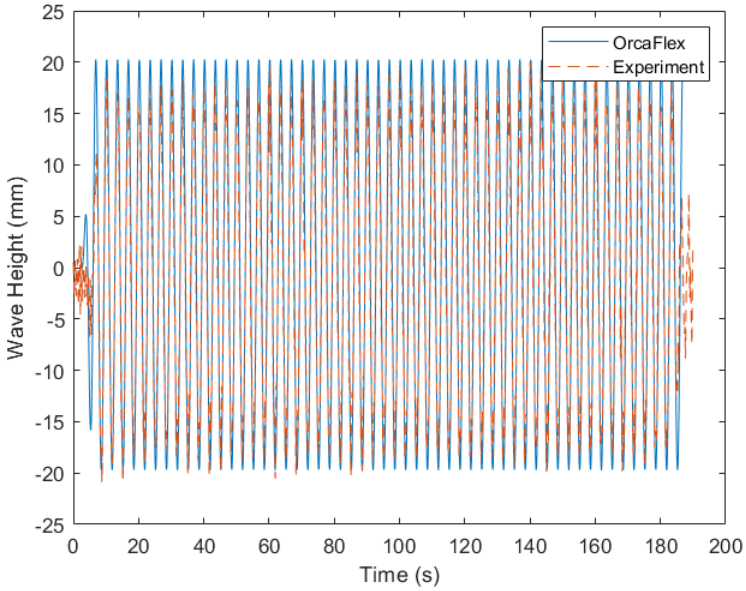

(a) Wave height.

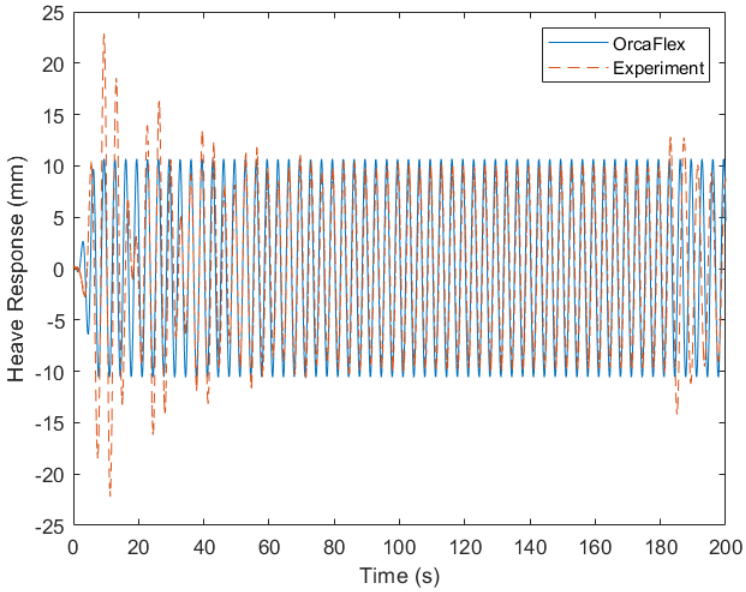

(b) Heave.

Figure 6.6.13.: Simulated time series compared with regular testing results.

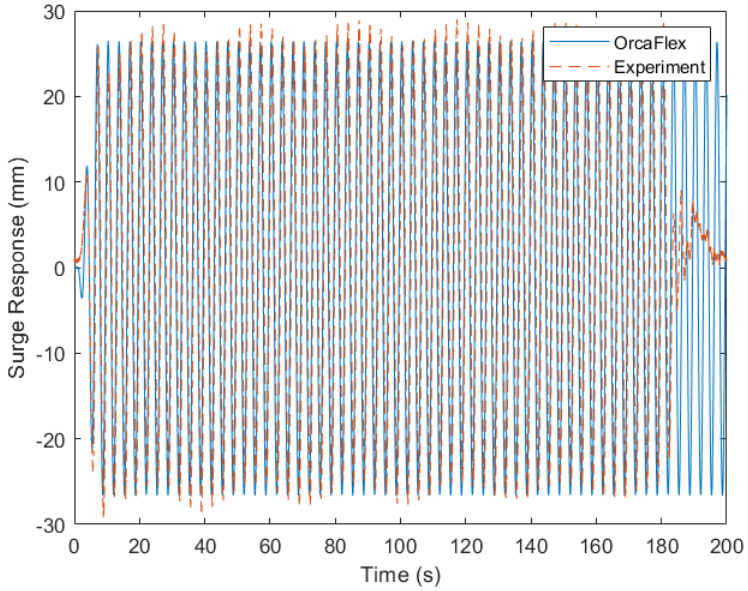

(c) Surge

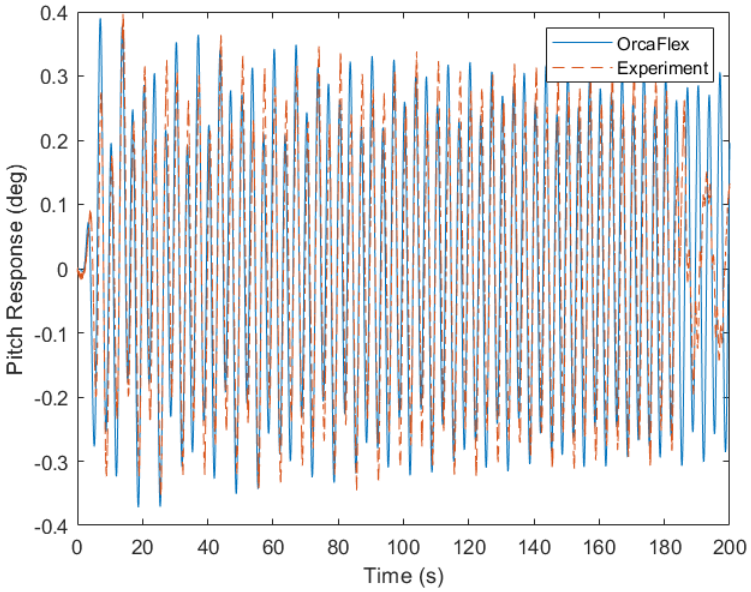

(d) Pitch.

Figure 6.6.13.: Simulated time series compared with regular testing results.

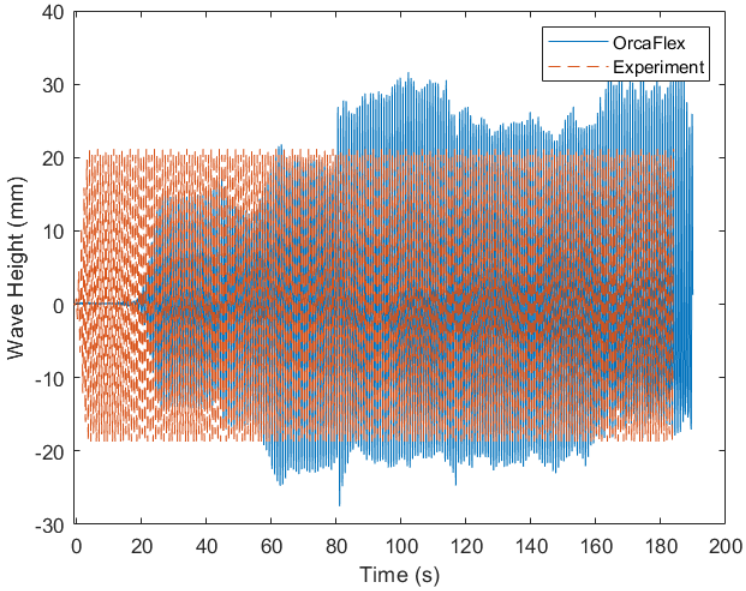

(a) Wave height.

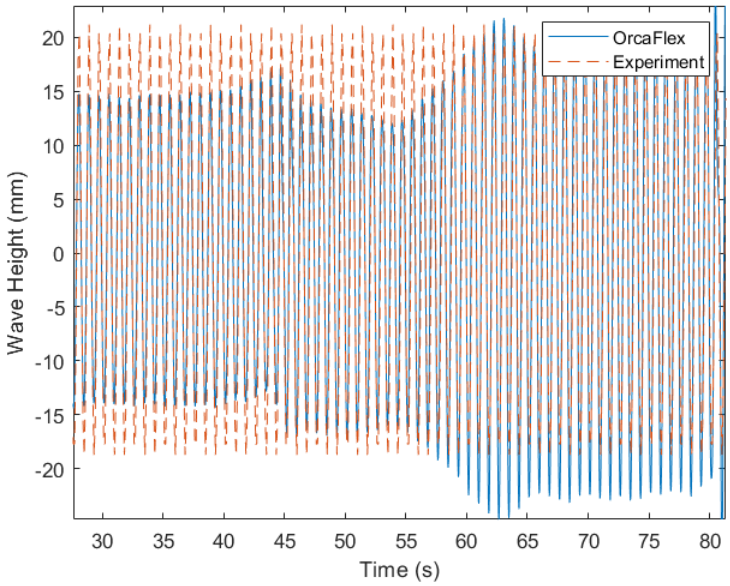

(b) Zoom in view of Figure 6.6.14a.

Figure 6.6.14.: Simulated time series compared with regular testing results.

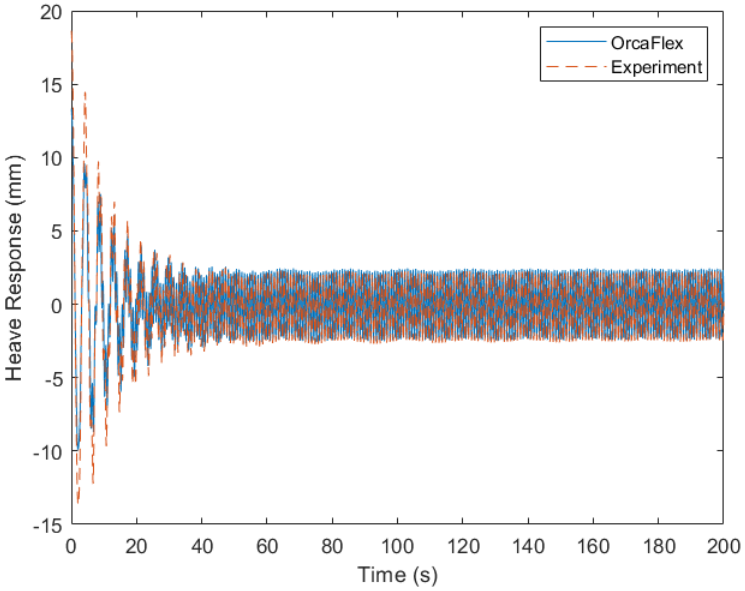

(c) Heave.

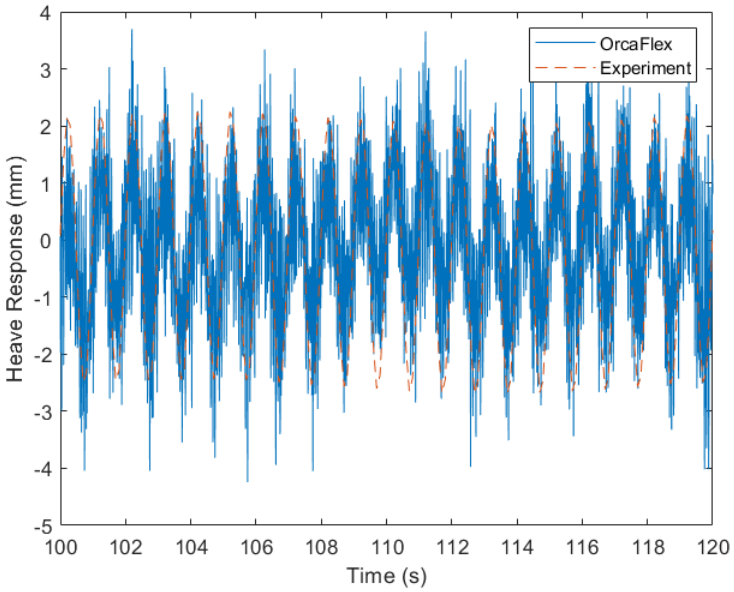

(d) Zoom in view of Figure 6.6.14c.

Figure 6.6.14.: Simulated time series compared with regular testing results.

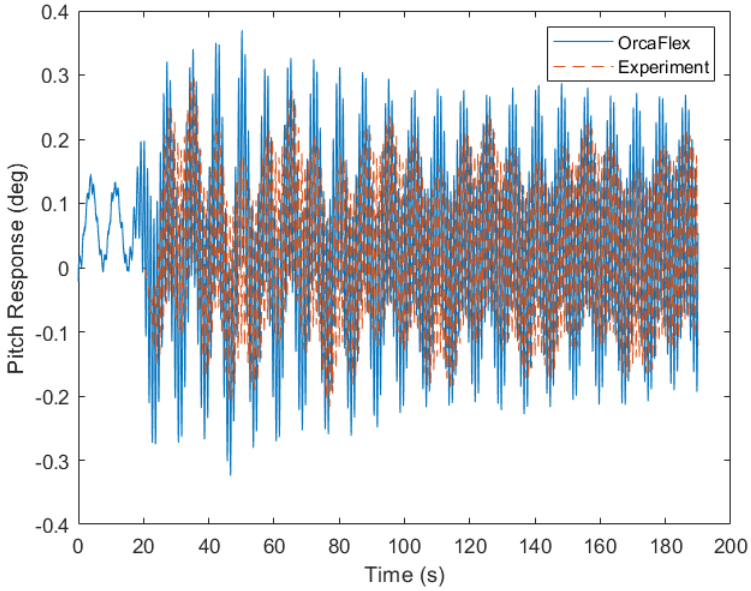

(e) Pitch.

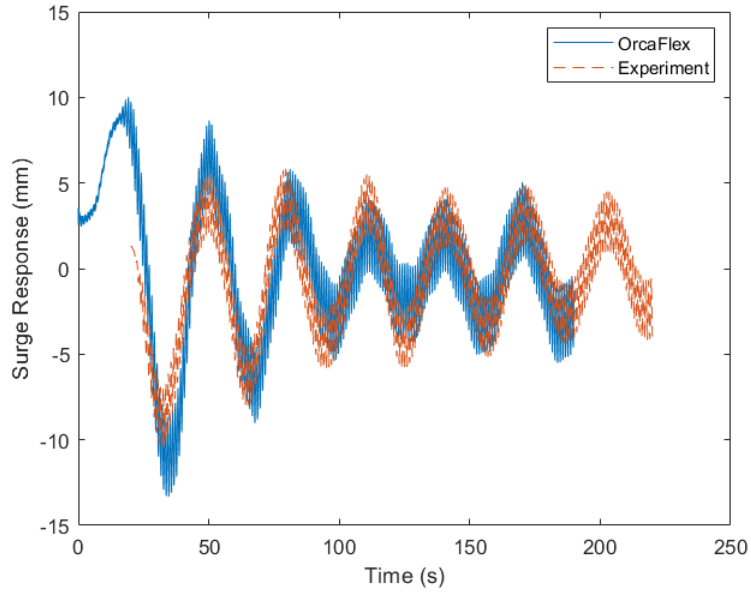

(f) Surge.

Figure 6.6.14.: Simulated time series compared with regular testing results.

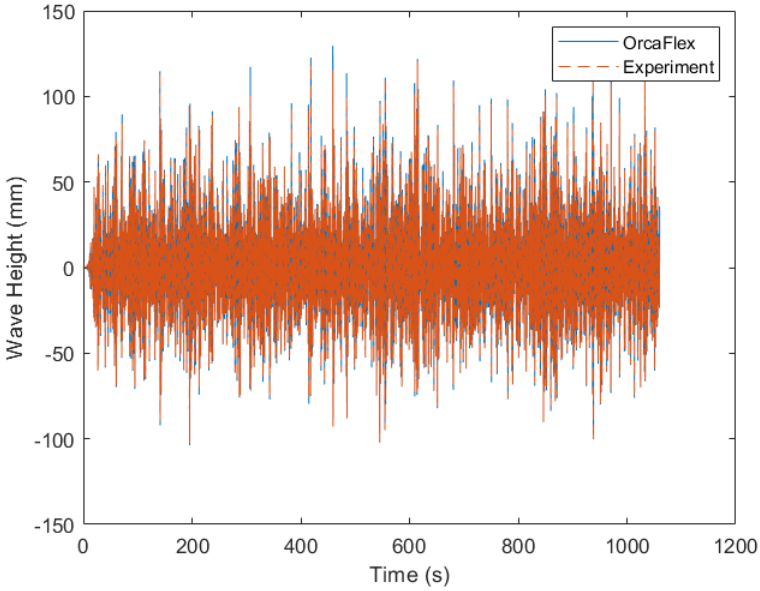

(a) Wave height.

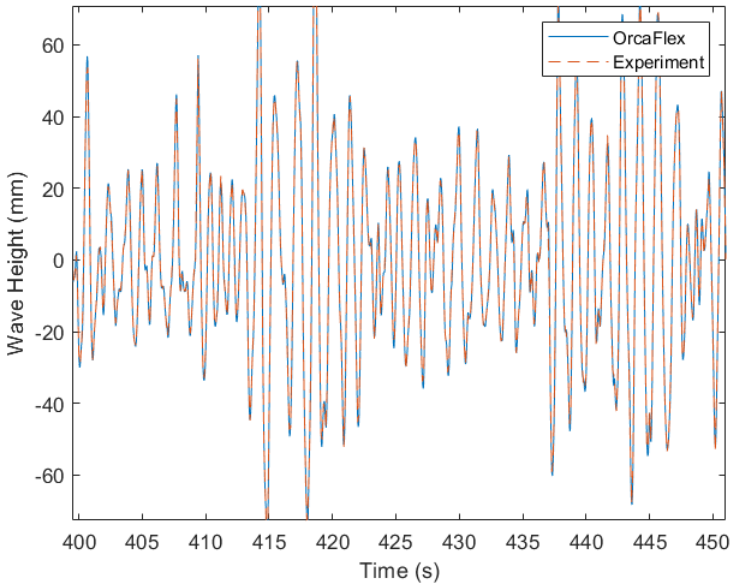

(b) Zoom in view of Figure 6.6.15a.

Figure 6.6.15.: Simulated responses compared with irregular testing results.

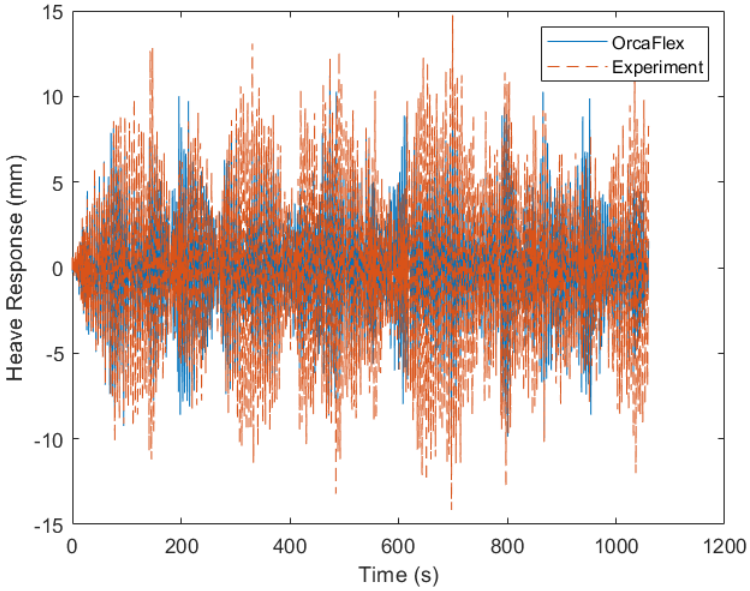

(c) Heave.

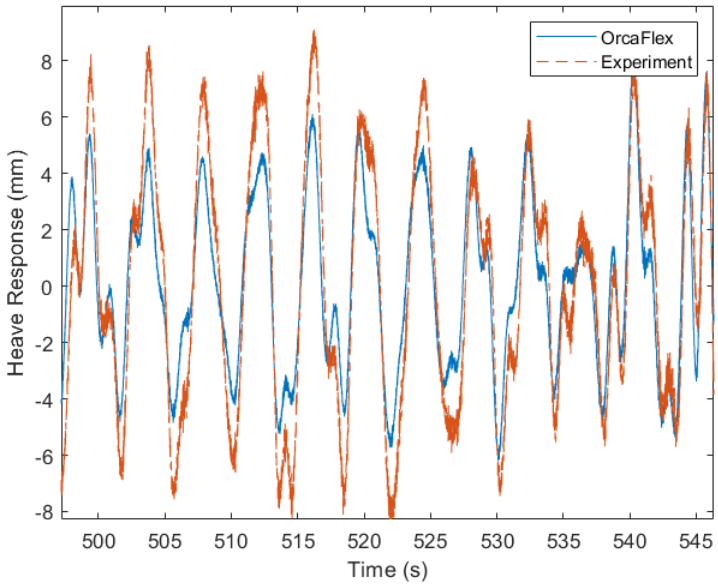

(d) Zoom in view of Figure 6.6.15c.

Figure 6.6.15.: Simulated responses compared with irregular testing results.

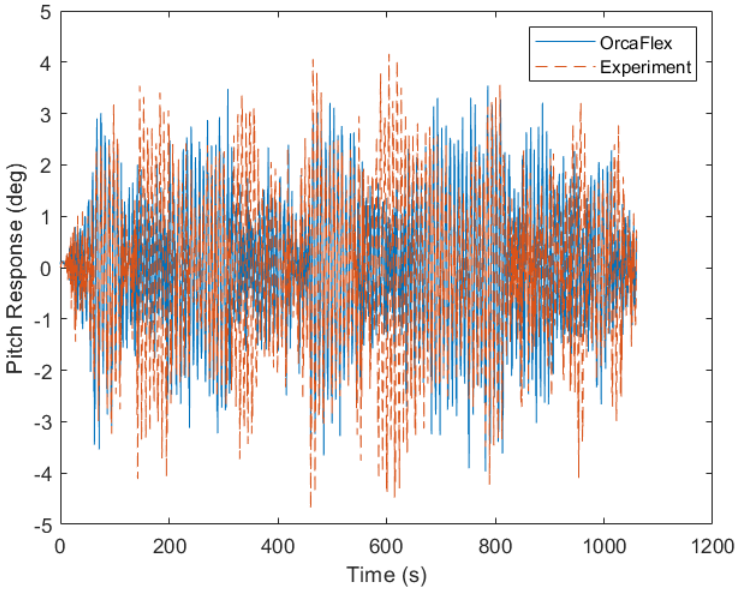

(e) Pitch.

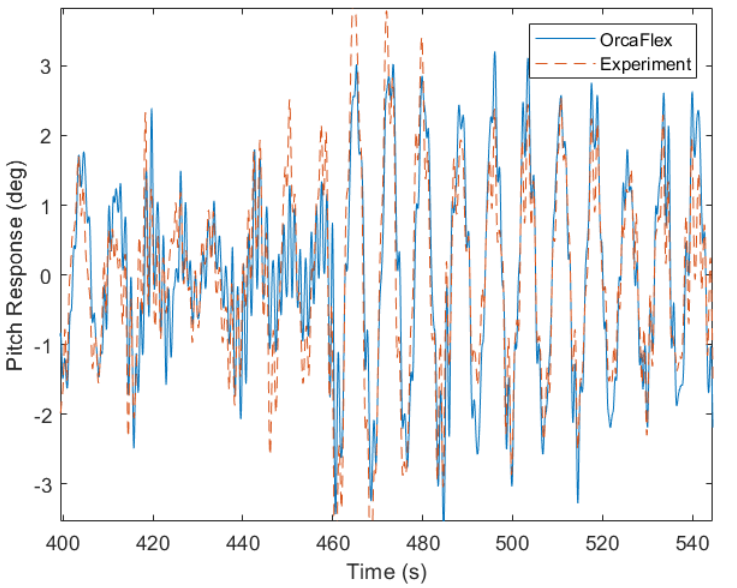

(f) Zoom in view of Figure 6.6.15e.

Figure 6.6.15.: Simulated responses compared with irregular testing results.

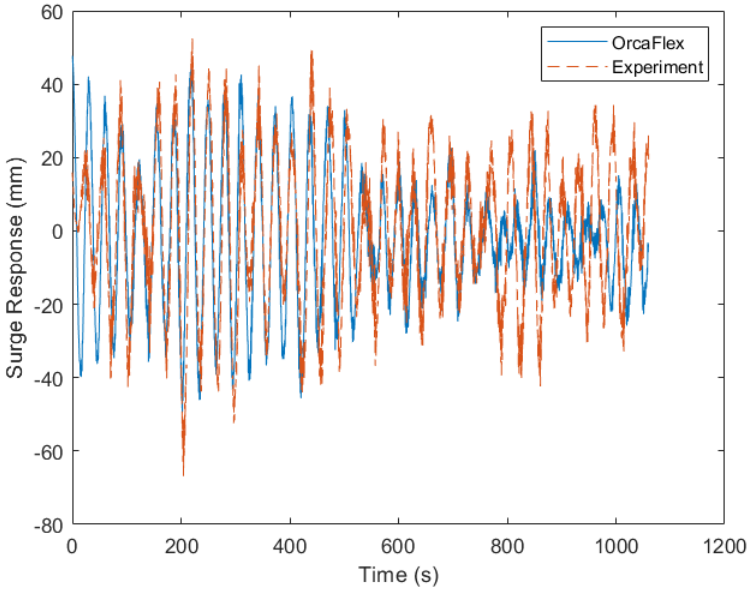

(g) Surge.

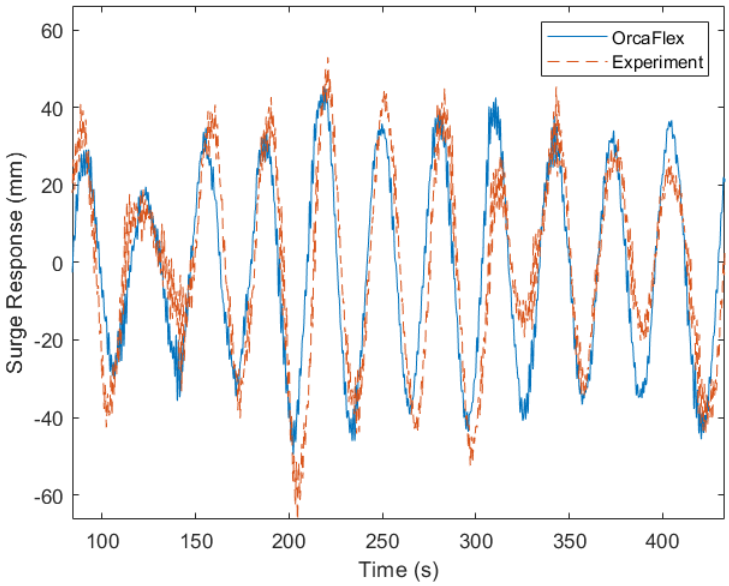

(h) Zoom in view of Figure 6.6.15g.

Figure 6.6.15.: Simulated responses compared with irregular testing results.

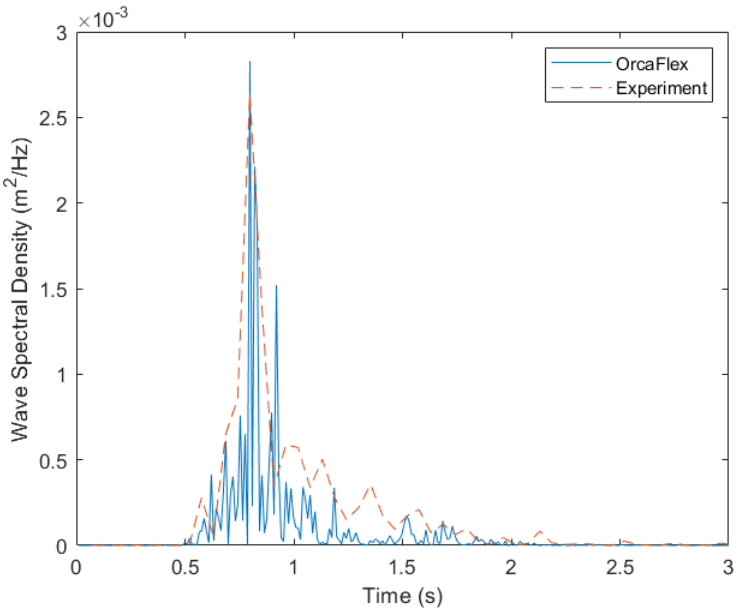

(a) Wave record.

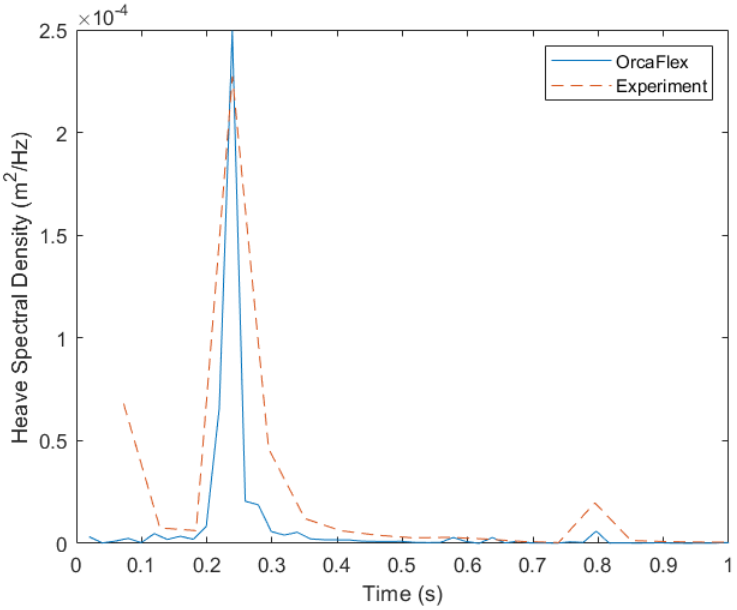

(b) Heave.

Figure 6.6.16.: Spectral density results for an irregular wave with 101mm of wave height and a peak period of 1.27s.

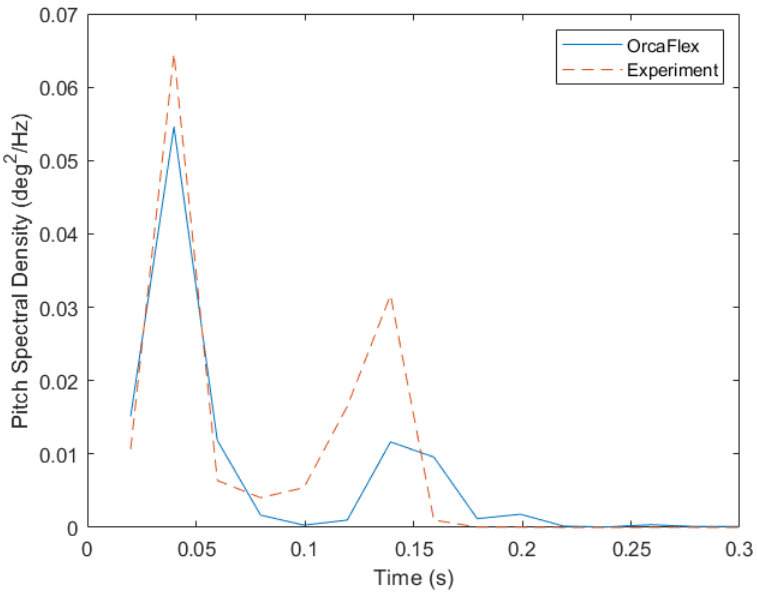

(c) Pitch.

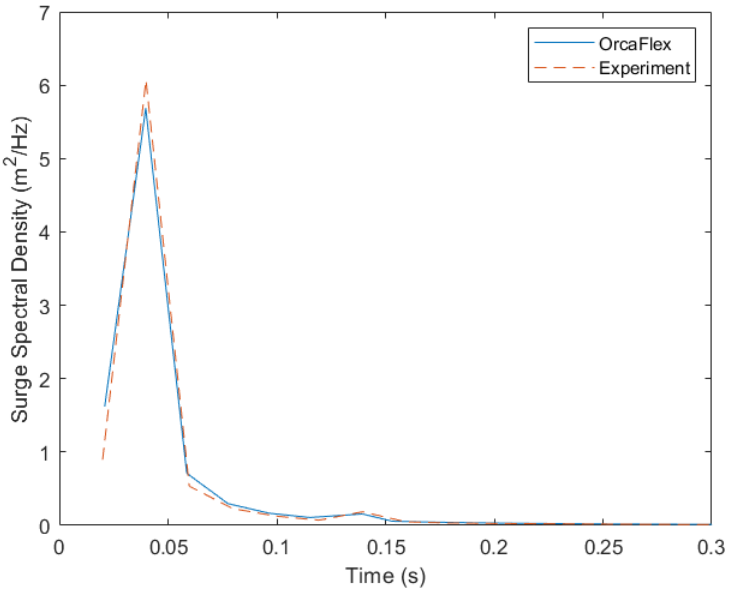

(d) Surge.

Figure 6.6.16.: Spectral density results for an irregular wave with 101mm of wave height and a peak period of 1.27s.

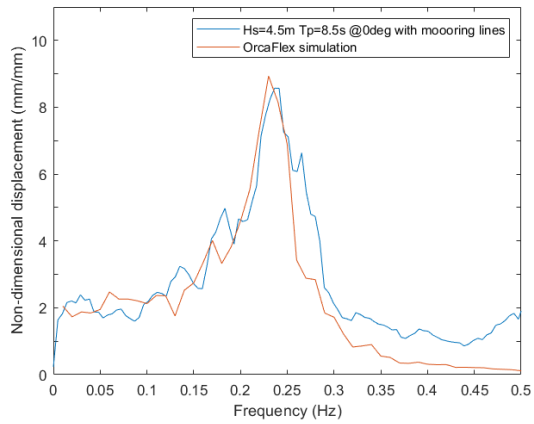

(a) Heave.

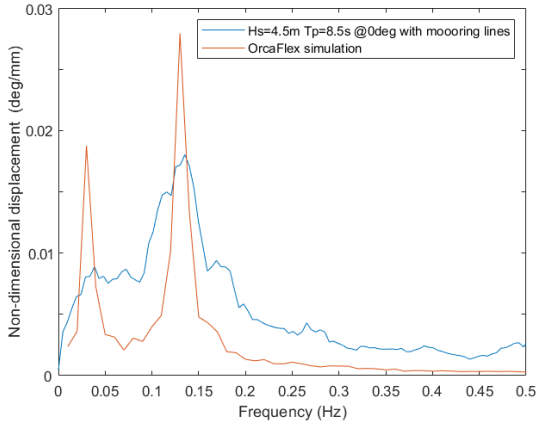

(b) Pitch.

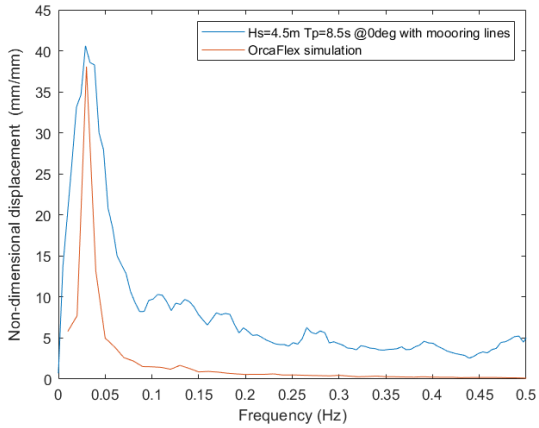

(c) Surge.

Figure 6.6.17.: Non-dimensional displacement calculated from the irregular sea simulations and compared with the relevant experiment.

6.7. Discussion

This Section presents the discussion of the results presented in the previous Section, i.e. Results and validation.

The building process of a hydrodynamic simulation started defining the geometry to be analysed. Beyond the direct output of a CAD tool, i.e. the scale model draws or virtual geometry, which is fundamental to perform a simulation, the geometry model can compute the position of the CoG and the MoI of the geometry. These parameters are critical for the correct setup of posterior hydrodynamic models. However, they must be validated against experimental data as shown in Section 5.3. The hydrodynamic models simulating the experiments conducted in Lir NOTF used the virtual mass properties as calculated by Inventor since the relevant testing to validate the mass properties was performed afterwards as part of the FloWave OERF campaign. On the other hand, the hydrodynamic models simulating the experiments conducted in Lir NOTF used the validated mass properties. The virtual mass properties as calculated by Inventor and the experimental value show agreement up to 92%. Therefore, it is not expected significant differences in hydrodynamic response due to the differences in mass distribution properties. Compared with the design values presented in Section 4, the CAD calculated mass distribution properties, i.e. position of the CoG and the MoI, present an agreement of up to 89%. Differences arise because the parametric design tool accounts only for simple geometries such as cylinders or frustum i.e. shapes that can be parametrised analytically, while the CAD tool considers real-live objects joining surfaces smoothly and using sophisticated tools like sweep, revolve, or chamfer allowing to perform a more accurate representation of the floating system.

As mentioned in Section 5.15, during the testing conducted in Lir NOTF the free-floating structure had a designed trim that would be countered by the asymmetric three mooring line configuration. In order to calculate accurately the trim of the floater, and

therefore, the needed difference in mass per unit of length in the mooring lines to account for the trim and leave the structure completely vertical, a MaxSurf model was used. The mass model was also useful to calculate the mass relocation for the second testing where there was no trim and the mooring system was symmetric, i.e. the three mooring lines are identical.

ANSYS AQWA was used to compute the diffraction and radiation analysis of the DTI-F scale model since Figure 6.3.2 shows how the DTI-F scale model behaves within the diffraction regime for some of the wave's condition tested. Moreover, for the random wave experiments with higher wave heights, the scaled model lays within the large inertia regime with small but not negligible drag. Therefore, a drag component must bet set up to account for the large inertia regime while modelling experiments with random waves. The initial draft is input in ANSYS AQWA; therefore, it does not need to be validated. However, the model calculates the unbalanced forces by checking that the centre of buoyancy (CoB) and CoG are aligned, and their magnitudes are counteracted at the defined draft line. These values are reported as the ratio of the out of balance forces in a certain degree of freedom divided by the total mass of the floating system and are in the order of 10^{-9} for the X and Y-components and 10^{-6} for the Z-component, meaning that the out of balance forces are negligible. It is worth to state that the numerical model simulating the experiments conducted in Lir NOTF had out of balance forces up to 16% higher than the numerical model simulating the experiments conducted in FloWave OERF, even though they both remain in the above-mentioned orders of magnitude. This difference stems from the difficulties of modelling a floating body with an initial trim in ANSYS AQWA which makes it more complicated to produce a geometry that remains stable in still water conditions.

The initial ANSYS AQWA models had to be adjusted in terms of damping, hydrodynamic stiffness and added mass in order to match testing free decay results. Due to the theory used, ANSYS AQWA does not account for drag and underestimates damping.

Drag is important for matching time series and damping contributions to the diffraction analysis are important. Therefore, special care has been taken while tuning the damping and drag in ANSYS AQWA. In the Lir NOTF model, 20 N/(m/s) of frequency-independent damping was added in heave, whereas 0.030 and 0.035 N/(°/s) were added in pitch and roll modes of motion. Moreover, the hydrodynamic stiffness was reduced in the heave mode of motion by 0.39% of the originally calculated by the code. Small corrections, i.e. 0.0019%, were also applied in the pitch and roll hydrodynamic stiffness. The added mass had to be modified by 0.96% in the heave mode of motion, and 0.16% in the pitch and roll modes of motion. In the FloWave OERF model, 36 N/(m/s) of frequency-independent damping was added in heave, whereas 0.042 and 0.044 N/(°/s) were added in pitch and roll modes of motion. The added mass had to be increased by 0.88% in the heave mode of motion and 0.13% in the pitch and roll modes of motion.

The calibrated models simulated free decay time series showing excellent agreement with the testing results for both experiments, i.e. Lir NOTF and FloWave OERF. Simulated free decay natural periods match perfectly testing results, whereas damping ratios match up to 95% in the worse cases, i.e. roll mode of motion. The overall matching of the simulated time series shed correlation values of 0.9975 for the free decay tests performed in Lir NOTF and 0.9925, 0.9971, and 0.9986 for the heave, pitch, and roll experiments conducted in FloWave OERF.

The high degree of matching between testing responses and simulation results indicates that the diffraction analysis results will be adequate input for the following hydrodynamic model developed in OrcaFlex.

To properly replicate testing results in OrcaFlex, after introducing all the diffraction analysis results from ANSYS AQWA, the calculation on the vessel object must be set up to i) include the six DoF in the static analysis, ii) to 'Calculated (6DOF)' for the primary motion, iii) to 'None' for the superimposed motion; and turn on all 'Included Effects'. Calculated primary motion will let the floating system respond to the tensions in the

moorings. In addition, the floating system's motion contributes to tension and curvature in the moorings. Adding all the possible included effects will ensure that first-order wave loads, added-mass and damping effects are considered along with second-order loads, i.e. slow drift and sum-frequency loads.

Before starting with the dynamic simulations, static and quasi-static checks are needed. Since the pretension has been input in the Lir simulation, it does not require any further checking. However, for the FloWave OERF simulation, there were not available mooring line tension readings. Therefore, Figure 18 presents the fitting between the underwater markers position records with the static results computed by OrcaFlex. The results suggest that an appropriate equilibrium position has been simulated. On the other hand, the quasi-static test simulation presents discrepancies with the simulated data. However, given that the greater discrepancies are within a range of tensions away from the testing tensions, i.e. 0 to 20 N, is assumed that the modelled axial stiffness is acceptable.

Once the static and quasi-static checks are done, drag coefficients and linear and quadratic wave frequency damping coefficients were set up. The radiation and viscous damping coefficients were calculated during the experimental campaign as explained in Section 5.10.1. Drag coefficients, on the other hand, were specified by using the trial and error method until the value produces a response matching the model test results. The normal drag coefficients providing the better fit to the experimental results were 0.78 and 0.74 in Lir NOTF and FloWave OERF respectively, while values of 0.008 and 0.01 were applied in the axial direction.

The results of the stiffness decay simulations present a high level of agreement when compared with the experimental results. The simulated stiffness decay time series correlate with the experiments conducted in Lir NOTF up to 0.9501, 0.9153, 0.9975, 0.8937, 0.9543, and 0.9737 in surge, sway, heave, pitch, roll, and yaw respectively. The correlation increases until 0.9972, 0.9838, 0.9881, 0.9992, 0.9942, and 0.9825 for surge, sway, heave, pitch, roll, and yaw modes of motion when compared with FloWave OERF experimental

results.

Regardless of the agreement shown between simulated and experimental stiffness decay results, it is worth mentioning the abnormal response shown in the experimental record for the surge mode of motion (Figure 6.6.2a) during the experiments conducted in Lir NOTF. After being hit by the wave, the model moves in the positive surge direction, i.e. dragged by the wave, until the mooring line tensions counter the inertia induced in the model by the wave. Then the model stops, and the restoring tensions induced by the mooring line in the model force the model to come back to the still position. After that, the model is supposed to repeat this behaviour in the negative surge direction, i.e. oscillates, as shown in Figure 6.6.10a during the experiments conducted in FloWave OERF. However, before reaching equilibrium between the inertia induced by the waves and the mooring tensions, i.e. the stop point mentioned before, and come back to the still position again, the model stops and moves back for approximately five seconds, and then continues the cycle normally. After reviewing, the tension records and the videos of the testing, it was concluded that the abnormal response was due to the mooring lines intercepting the model path during its negative surge direction excursion. It is also important to notice, how this event induces anomalous responses in sway, pitch, and roll responses, although, it does not affect excessively the resonance properties of the floating system.

Stiffness decay tests served as justification for the mooring configuration choice. Since no improvement regarding natural periods of oscillation was achieved by increasing the number of mooring lines nor by including the delta connection, the three mooring lines configuration was selected. No further investigation regarding the other mooring line configuration was conducted for the tests performed in Lir NOTF, and the testing conducted in FloWave OERF only included the selected mooring line configuration.

Regarding the wave quality, the simulated wave periods were adequately reproduced, but the amplitudes were adjusted to produce a wave as similar as possible to the tested

one. However, the experiments conducted in FloWave OERF at high frequencies, e.g. Figure 6.6.14, present discrepancies which can lead to inaccuracies on the simulated responses.

The simulated RAO values match adequately with those from experiments. Figure 6.6.3 presents the computed transfer functions compared with the experimental points produced while testing in Lir NOTF. Only the moored condition with the three mooring lines configuration in heading seas, i.e. a wave heading of zero degrees, was further analysed. Shapes and trends match satisfactorily. However, the testing capabilities were not able to produce waves with the relevant periods to validate the resonant properties, i.e. from four seconds on. Since the experiment in FloWave OERF only focused on the three mooring lines configuration, extensive results were produced. Figures 6.6.11a and 6.6.12 present the simulated RAOs against the experimental ones for the free-floating and moored conditions in heading seas. Figures 6.6.11a and 6.6.12a show the heave resonant peak at 0.24 Hz whereas other modes of motion resonant peaks remain outside of the tested range. Figures 6.6.11c and 6.6.12c deserve special mention due to the existence of a resonant peak, i.e. 0.678 Hz, away from the natural frequency of oscillation in the pitch mode of motion.

RAOs validation implies that the numerical model performs well from an overall point of view under monochromatic regular wave excitation. Therefore, it is expected that the simulated response time series under regular wave loading match the testing records. Hitherto, the correlation concept, i.e. how strongly pairs of variables are related, has been used to compare different time series. However, for the regular and irregular wave cases, the root mean square error (RMSE), is the measure of agreement adopted. For the experiment conducted in Lir NOTF the RMSEs between the simulated time series and the testing responses are 0.0067, 0.0601, and 0.0588 for the wave elevation, the surge, and the pitch records respectively. The RMSE values computed for the experiment performed in FloWave OERF are 0.0037, 0.0122, 0.0245, and 0.0098 for the wave height, the heave,

the pitch, and the surge responses respectively.

Fitting the numerical model to testing responses under random wave loading is a complex task. Irregular waves, containing several different frequencies, make arise non-linearities in the responses and they are difficult or impossible to replicate. Moreover, for the simulation of the Lir NOTF results the numerical simulation was not forced to produce the same wave profile. Therefore, the simulated time-series do not match the experimental responses although the frequency of the numerical response fits well with the experimental one. However, the simulated and experimental wave height, surge, and pitch spectral density graphs (Figure 6.6.6) show good agreement between the experimental results and numerical simulations. Moreover, Figure 6.6.6 depicts the wave resonant peak at 0.89s in all the subplots, and subplot b and c show surge and pitch peaks in 0.04 and 0.13 Hz respectively.

For the simulation of the FloWave OERF results, the numerical simulation was forced to replicate the random wave profiles used while testing. By using this approach, a better fit with testing results can be obtained, and the use of the RMSE as a measure of goodness of fit is consistent again. The RMSEs between the simulated time series and the testing responses for the FloWave OERF experiments are 0.0013, 0.0496, 0.0572, and 0.0334 for the wave height, the heave, the pitch, and the surge modes of motion. The simulated and experimental wave height, heave, pitch, and surge spectral density plots (Figure 6.6.16) present a high level of agreement and complete match regarding resonance peak location. Moreover, the RAO values computed using irregular wave time series from both experiments and OrcaFlex simulation are shown in Figure 6.6.17 for a sea state with significant wave height of 4.5 m and a peak frequency of 8.5 s showing a good match in terms of frequency peak location. However, there is a mismatch between the signals due to the noise associated with the measurements.

6.8. Conclusions

Numerical simulations of the testing campaigns presented in the previous Chapters have been performed showing a high degree of matching with the experimental results.

ANSYS AQWA has been employed to perform a diffraction analysis of the scaled DTI-F system since it lays in between the 'all inertia' and 'diffraction' regimens. ANSYS AQWA was also used to simulate the two sets of free decay testing performed in Lir NOTF and FloWave OERF respectively. The initial model was slightly calibrated to match the experimental time series. The results of the free decay simulation present good agreement with experimental data and reproduce accurately natural frequencies of excitation and damping ratios.

OrcaFlex was used to perform further hydrodynamic calculations. The ANSYS AQWA diffraction outputs were successfully imported within the OrcaFlex environment. The initial OrcaFlex model was calibrated in terms of drag coefficients and linear and quadratic wave frequency damping coefficients to better match the experimental time series. OrcaFlex matches satisfactorily the pretensions, shapes, and stiffness of the mooring lines when compared with testing results. The results of a chain axial stiffness test were fed into the model. After completing the set up the numerical model, free and stiffness decay essays and regular and irregular wave experiments were simulated presenting very good fit with experimental results.

The stiffness decay simulated responses fit better with experimental results obtained in FloWave OERF since developing a numerical model of a straight cylinder is easier than for a trimmed structure as the one considered in Lir NOTF.

The simulated RAO values match well with the responses recorded during the experimental campaigns regardless of their origin, i.e. regular or random wave computed RAOs.

The RAO values computed from irregular waves help to validate the simulated RAOs

in the frequency ranges falling out the performance of the basin. The dynamic responses are acceptable even tough further design iterations are needed to optimise the dynamic behaviour of the FOWT. Given the overall results presented before, it must be concluded that the two different three-mooring lines configurations tested, i.e. asymmetric lines with trim and symmetric lines without trim, does not change the results noticeably.

In summary, the numerical models developed matched accurately the experimental results. Therefore, it must be concluded that the numerical models are acceptable to continue the research by coupling them with the aeroelastic model developed in Chapter 3.

Part III.

Closure

7. Conclusions

Floating offshore wind has made considerable progress towards commercialisation since the first floating wind farm started to produce power to the electrical grid in 2018. However, since floating offshore wind turbines (FOWT) are a relatively new technology, there are still many fields where further research is required. Therefore, FOWTs are still subject to research and development activities, including investigations from feasibility studies of new concepts, such as the one presented in this thesis, to the optimisation of a specific sub-system of a FOWT among many other research topics.

The present study is a step forward in the development of FOWTs since it presents parts of the early design loop of a new floating structure belonging to the spar buoy type but with a wider diameter compared to existing spar buoy designs.

This work aims to advance the development of the DTI-F concept, a floating substructure able to raise and lower the tower and nacelle set for effective cost reduction during construction, installation, maintenance and decommissioning. The main objective is to increase the TRL level of the DTI-F concept from 1 to 3.

Therefore, an aeroelastic numerical model of the Levenmouth wind turbine (WT) has been developed to calculate the required inputs for the subsequent stability and structural analysis. As a result, the functional load-matrix of the Levenmouth WT has been released. The initial design of the floater has been carried out using a series of numerical and experimental methods. The experiments were also used to validate the numerical model developed in this thesis. In summary, the DTI-F concept has evolved from

TRL 1 to 3 delivering valuable information regarding the Levenmouth WT aeroelastic phenomena and the hydrodynamic responses of a wide spar buoy type FOWT.

7.1. Numerical methods for aeroelastic analysis of wind turbines

To understand the behaviour of a large-scale WT, a stable and reliable aeroelastic numerical model of the Levenmouth WT was developed using the open-source NREL FAST code. The results of the numerical simulations were compared with the commissioning results simulated with another commercial code. As a result of the development of the NREL FAST simulation of the Levenmouth WT and the analysis of the simulation results, the following research contributions were found:

- The thrust at rated wind speed calculated with the aeroelastic numerical model is 18.5% larger than the estimates obtained using a simpler approach. The accurate estimation of the thrust value is crucial for the initial stability calculations because underestimating this value will lead to undesirable major problems in later stages, e.g. underestimation of mean trim, inaccurate input data for the subsequent hydrodynamic database, which may lead to platform instability.

- The functional load matrix of the Levenmouth WT has been calculated and released. The load-matrix is needed to perform the structural analysis of the floater and will influence the total mass of the floater allowing for a realistic floater sizing based on the use of the Levenmouth 7MW WT.

- Discrepancies were found between the results of the aeroelastic model developed within this research and the commissioning results of the Levenmouth WT. The differences arose due to (i) the different approaches used by the different codes to perform a particular calculation, e.g. different structural analysis approach,

different aeroelastic theories, different discretisation of the aeroelastic loads, (ii) the differences existing in the structure studied, e.g. different substructure, and (iii) the use of a different controller.

- Given the above-mentioned differences, further work should validate the results of the simulations against the Supervisory Control And Data Acquisition (SCADA) measurements.

It is worth noting that no fine-tuning has been performed in the aeroelastic numerical model developed in this work to match the commissioning results since the commissioning results are not validated. Moreover, the aeroelastic model developed in this work represents the as-built system of the Levenmouth WT in Fife, whereas the commissioning model considered a generic deployment site.

7.2. Baseline design

Using the results produced during the aeroelastic simulations, the baseline design of the DTI-F concept was developed using a parametric approach. The parametric design tool developed allows meeting the objectives in terms of draft reduction while fulfilling the special requirements of the DTI-F concept, i.e. enough floatability of the floating cylinder to lift the tower and nacelle set and enough ballast water to float the floating cylinder within the spar buoy, and satisfying all the initial stability requirements. As a result of several iterations, a suitable baseline design has been proposed and the following results have been obtained:

- An original spar-type floater design with a reduced draft and a wider diameter than the current spar buoy designs in the market. The new design will allow studying the behaviour of wider spar buoy floaters to be used in FOWTs. The draft of the spar was reduced from 80 to 62 m achieving the initial objective. The final spar diameter was set at 15 metres.

- A novel floater design has been developed meeting the requirements regarding the GM position but minimising the value to improve the dynamic behaviour of the FOWT system. The floater also fulfils an internal requirement stating that the righting moment of the system shall be equal or greater than 130% of the area under the wind heeling moment previously calculated.

- A heave plate was designed to provide the required additional added mass to the floating system helping to shift forward the heave natural period. The design natural periods of the floater are far away from the linear wave excitation for all the DoFs.

- Using the results from external structural analysis, a wall thickness of 350 mm was selected. The structural analysis considered bending, shear, and torsion loads throughout the floater.

- The design maximum angle of inclination of the floating system has been kept under 4.5 degrees leading to a high stiffness structure. The maximum accelerations recorded in the nacelle were 2.4 m/s2 meeting the guidelines imposed in the design basis.

- Three different mooring line configurations were designed and optimised to reduce the surge, sway and yaw responses avoiding excessive stress on the export cable. Two designs including three lines and one using four lines were considered. Each mooring line has three different types of chains.

- A suitable anchor system was designed to keep the system in place. Thirteen tonnes of nominal weight drag anchors were selected.

- Construction and deployment methods have been outlined and the required drafts for each construction stage have been calculated showing a floating system with the potential of being built in relatively shallow sites.

7.3. Experimental methods and analysis techniques for FOWT

Following the baseline design developed using a parametric approach, a 1:45 Froude scale model was designed, constructed, and subsequently tested in two experimental campaigns. The following contributions to knowledge were made:

- As a result of the free decay testing performed in Lir NOFT, the natural periods of oscillation of the free floater were calculated and scaled up to full-scale. The results at full-scale were 28 seconds in heave and 54 seconds in roll and pitch meaning that the initial floater design presented natural periods of oscillation far away from the linear wave excitation range. Therefore, the initial design met the constraints specified in the relevant standards.

- The damping ratio of the floating system was also calculated showing up to a 4.4% damping in heave due to the heave plate. The damping calculated ratio was in line with other dampings reported for similar configurations and highlighted the benefits of using a heave plate to increase the heave damping and therefore reduce the heave responses.

- The free decay test performed in FloWave presented the same results shown during the tests performed in Lir NOFT except for the natural periods in roll and pitch that were 50 seconds, meaning a 92.6% of agreement between both tests. The high level of agreement between the two testing campaigns validated the experimental results even tough slightly different setups were tested.

- As a result of the stiffness decay testing performed in Lir NOFT, the natural periods of oscillation of the moored floater at full-scale were calculated for three different mooring configurations. The three mooring lines without delta connection configuration was selected among the other two options proposed, i.e. 'three mooring

lines with delta connection' and 'four mooring lines configuration', due to a lack of improvement in terms of the natural period of oscillations. The selected mooring configuration, shown the same heave natural period of oscillation calculated in the free decay test, i.e. 28 seconds, whereas the pitch and roll natural periods decreased until 50 seconds. Surge, sway, and yaw natural periods were 169, 102, and 121 seconds, respectively.

- After applying the stated modifications in the original three mooring line configuration, the moored system was tested (stiffness decay test) again in FloWave OERF presenting 28, 51, 51, 207, 253, 137 seconds of natural period in heave, pitch, roll, surge, sway, and yaw, respectively. A considerable improvement was achieved in the surge and sway DoFs in terms of natural period, whereas only a sensible increase was accomplished in the yaw DoF. As stated before for the free decay testing, the natural periods of oscillation of the moored floater were far away from the linear wave excitation range, meaning that the moored floater is not likely to suffer from resonance due to the most energetic waves.

- The DTI-F floater was characterised by using the RAOs computed from regular waves, and these RAOs were used to forecast the maximum responses for different wave conditions. All the responses obtained met the requirements stated in the design basis and relevant standards.

- The analysis of the irregular sea states revealed dynamic responses within the requirements stated in the design basis, giving confidence on the floating system feasibility.

7.4. Numerical methods for hydrodynamic analysis of FOWT

An OrcaFlex Finite Elements Method (FEM)-based hydrodynamic model of the DTI-F was developed to further study the responses of the moored floating system.

A novel hybrid buoy-vessel model was developed to calculate the dynamic responses of the DTI-F. This solution was adopted to account for the fact that the DTI-F floater is mainly influenced by diffraction in certain wave conditions and mainly by inertia in other conditions given its large spar diameter, e.g. for the three smaller wave periods tested during the regular testing, the floater was mainly influenced by diffraction and for the other waves tested the floater was mainly influenced by inertia. The OrcaFlex model needed the results from a diffraction analysis as an input. Therefore, a diffraction analysis was performed using the panel model ANSYS AQWA. The results of both simulations, i.e. diffraction and dynamic analysis of moorings, were validated against the results obtained from the relevant experimental tests.

The following findings were inferred during the numerical model development and validation stages:

- The numerical models were validated against a wide range of static, quasi-static, and dynamic conditions including two realistic sea states using the JONSWAP spectrum.
- ANSYS AQWA potential flow solver was not able to capture the large-scale vortex shedding created by the heave plate during the heave motion of the floating system. The presence of the heave plate creates a recirculation zone in the boundary layer at the floater surface. This ultimately leads to flow detachment from the heave plate which is a phenomenon dominated by viscous forces and characterised by high vorticity. As the linear potential flow solver neglects viscous effects and considers the flow as being irrotational, it cannot capture the phenomenon. However,

the simulation of heave free decay time-series provided an excellent matching with the experimental results due to the low influence of drag within the hydrodynamic regime studied. Simulated free decay natural periods match perfectly testing results, whereas damping ratios match up to 95% in the worse cases, i.e. roll mode of motion. The overall matching of the simulated time series presented correlation values of 0.9975 for the free decay tests performed in Lir NOTF and 0.9960 for the experiments conducted in FloWave OERF. The high degree of matching between testing responses and simulation results indicated that the diffraction analysis results were adequate input for the following hydrodynamic model developed in OrcaFlex.

- The FEM-based hydrodynamic model of the moored spar buoy FWT in OrcaFlex captured the non-linearities as well as contributions to damping from mooring lines. The overall correlation between stiffness decay test and simulations was 0.9474 and 0.9908 in Lir NOTF and FloWave OERF respectively, whereas the overall RMSE between regular and irregular tests and simulations was 0.0418 and 0.0125 respectively. A close agreement with the experimental results gave the confidence to rely on the FEM based approach to carry out further investigations and optimisation loops of the DTI-F concept. And having both, near to one correlation values and near to zero RMSE values between numerical simulation and experimental results ensured this close agreement.

- As results of the irregular wave simulations, preliminary results of the global performance were obtained. The maximum responses of the floating system were investigated for a range of operational cases. At full scale, the maximum responses recorded were 4.1, 4.5, and 3.9 metres in surge, sway, and heave, and 2.2, 0.8, and 2.3 degrees in pitch, roll, and yaw respectively. These results ensured an optimal response behaviour of the system in realistic sea states.

- The overall agreement between experimental and numerical developments suggested that the numerical model was accurate enough to conduct further optimisation of the DTI-F concept using it in fully coupled simulations along with the aeroelastic model of the Levenmouth WT previously developed.

7.5. Transversal aspects

- Since the size of the new models of WTs become increasingly larger, new reference WTs are needed to design and model their foundations. Three main reference WTs are of public domain namely 5MW NREL, DTU 10MW, and recently was released the 15MW NREL. Regarding that, the aeroelastic development presented in this thesis will fill the gap between the 5MW NREL and the DTU 10MW reference WTs as soon as ORE Catapult makes the numerical model open source.

- The large diameter spar buoy floater presented in this thesis represents and hybrid design. The high degree of feasibility shown by the DTI-F concept highlights the potential for other hybrid concepts. Regarding that, hybrid concepts are a contemporary topic subjected to research with flagship developments like the Tetra-Spar concept combining a tension leg platform with barges.

7.6. Recommendations for future work

The completion of the present research allows to carry out further investigations regarding the coupled responses of the DTI-F concept under wave and wind loading. Once the aeroelastic model of the Levenmouth WT and the hydrodynamic model of the DTI-F substructure provide reliable results, next both models can be coupled. The coupling of the aforementioned models will lead to fully-coupled aero-hydro-servo-elastic simulations of the DTI-F concept. After investigating the effects of the wind on the DTI-F concept,

a new iteration design stage will lead to an increase of TRL from 3 to 5-6 allowing to move from development to deployment phases.

Further investigation regarding specific topics is needed as explained below:

- To validate the aeroelastic model, comparison with SCADA data is needed. Once the aeroelastic model is properly validated, simulation of all the design load cases mentioned in international standards must be run and further load-matrixes calculated.

- To evaluate the advantages provided by the unique capabilities of the DTI-F concept, a modified aeroelastic model accounting for a two-bladed WT should be developed.

- The coupled simulations using both, the Levenmouth WT and the modified two-bladed WT, must be validated against experimental records. To validate fully-coupled simulations, a software-in-the-loop (SiL) hydrodynamic testing will be required. SiL is a hybrid testing technique where the loads from the rotor are calculated by an aeroelastic model fed with the platform position recorded in real-time during the tank measurements. The calculated loads are then communicated to a calibrated ducted-fun that has been calibrated to produce the desired loading. SiL testing allows replicating the wind-rotor interaction loads without building a detailed scale-model of the blades. Therefore, the same hardware, i.e. ducted-fan, can be used to simulate the Levenmouth WT and the modified two-bladed WT only by changing the aerodynamic model during the experiment.

- Further optimisation of the catenary mooring and the seakeeping system is required. Detailed research on the responses of the DTI-F concept for different levels of pretension in the mooring line is recommended.

- Further optimisation regarding the influence of the heave plate on the responses is

needed. The development of a computational fluid dynamics (CFD) model of the DTI-F floater could shed some light on the vortex shedding phenomena occurring in the surroundings of the heave plate when the structure is heaving.

- In order to validate the results of the CFD model, it is recommended to look for a facility providing laser doppler velocimetry (LDV) or particle image velocimetry (PIV) measurement techniques. LVD and PIV can provide with flow visualisation, i.e. 2D or even 3D vector fields, using a laser to track particles.

8. Appendix I Technology Readiness Levels

The next Figure gives insight on the Technology Readiness Levels (TRL) as defined by NASA.

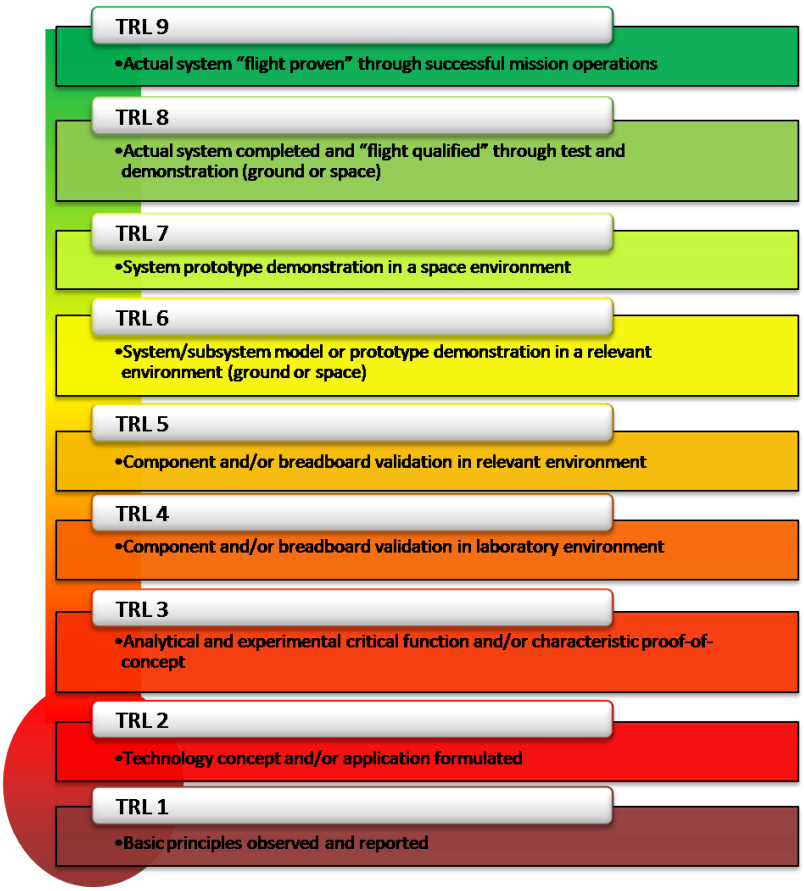

Figure 8.0.1.: Technology Readiness Level.

9. Appendix II WT Operating Regions

The next Figure gives insight on the WT Operating Regions as defined by NREL.

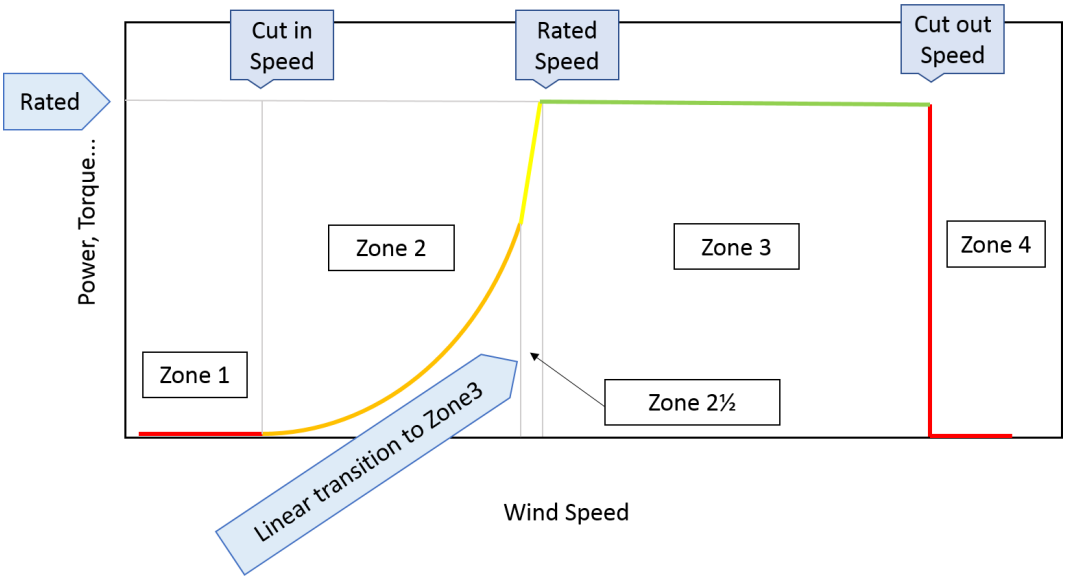

Figure 9.0.1.: Steady-state operating regions.

Bibliography

[1] Eia.gov. (2019). TODAY IN ENERGY. [online] Available at: https://www.eia.gov/todayinenergy/detail.php?id=12251 [Accessed 2 May 2019].

[2] Worldenergy.org. (2019). World Energy Trilemma. [online] Available at: https://www.worldenergy.org/work-programme/strategic-insight/assessment-of-energy-climate-change-policy/ [Accessed 2 May 2019].

[3] Rhubarbgreen, V. (2019). The core of energy policy in 2017. [online] Rose Galloway Green. Available at: https://galloway.green/2017/08/01/the-core-of-energy-policy-in-2017/ [Accessed 2 May 2019].

[4] Ec.europa.eu. (2019). Renewable energy statistics - Statistics Explained. [online] Available at: https://ec.europa.eu/eurostat/statistics-explained/index.php/Renewable_energy_statistics [Accessed 1 Oct. 2019].

[5] Carter, R. (2006). Boat remains and maritime trade in the Persian Gulf during the sixth and fifth millennia BC. Antiquity, 80(307), pp.52-63.

[6] Price, T. (2005). James Blyth — Britain's First Modern Wind Power Pioneer. Wind Engineering, 29(3), pp.191-200.

[7] WindEurope. (2019). Wind energy in Europe, Scenarios for 2030 | WindEurope.

[online] Available at: https://windeurope.org/about-wind/reports/wind-energy-in-europe-scenarios-for-2030/ [Accessed 3 May 2019].

[8] WindEurope. (2019). German offshore wind auction strengthens case for accelerated build-out | WindEurope. [online] Available at: https://windeurope.org/newsroom/press-releases/german-offshore-wind-auction-strengthens-case-for-accelerated-build-out/ [Accessed 3 May 2019].

[9] WindEurope (2019). Offshore Wind in Europe: Key trends and statistics 2018. [online] Brussels. Available at: https://windeurope.org/wp-content/uploads/files/about-wind/statistics/WindEurope-Annual-Offshore-Statistics-2018.pdf [Accessed 3 May 2019].

[10] Equinor.com. (2018). Our offshore wind projects - Our offshore wind projects - equinor.com. [online] Available at: https://www.equinor.com/en/what-we-do/new-energy-solutions/our-offshore-wind-projects.html [Accessed 20 May 2018].

[11] Equinor.com. (2018). World's first floating wind farm has started production - World's first floating wind farm has started production - equinor.com. [online] Available at: https://www.equinor.com/en/news/worlds-first-floating-wind-farm-started-production.html [Accessed 4 Sep. 2018].

[12] NASA. (2019). Technology Readiness Level. [online] Available at: https://www.nasa.gov/directorates/heo/scan/engineering/technology/txt_accordion1.html [Accessed 9 Oct. 2019].

[13] The Carbon Trust (2015). Market and Technology Review. Floating Offshore Wind. [online] Available at: https://www.carbontrust.com/media/670664/floating-offshore-wind-market-technology-review.pdf [Accessed 20 May 2018].

[14] European Wind Energy Association (2013). Deep Water. The next step for offshore wind energy. [online] Available at:

http://www.ewea.org/fileadmin/files/library/publications/reports/Deep_Water.pdf [Accessed 20 May 2018].

[15] Paulsen, U., Vita, L., Madsen, H., Hattel, J., Ritchie, E., Leban, K., Berthelsen, P. and Carstensen, S. (2012). 1st DeepWind 5 MW Baseline design. Energy Procedia, 24, pp.27-35.

[16] Lefebvre, S. and Collu, M. (2012). Preliminary design of a floating support structure for a 5MW offshore wind turbine. Ocean Engineering, 40, pp.15-26.

[17] Borisade, F., Choisnet, T. and Cheng, P. (2016). Design study and full scale MBS-CFD simulation of the IDEOL floating offshore wind turbine foundation. Journal of Physics: Conference Series, 753, p.092002

[18] Oguz, E., Clelland, D., Day, A., Incecik, A., López, J., Sánchez, G. and Almeria, G. (2018). Experimental and numerical analysis of a TLP floating offshore wind turbine. Ocean Engineering, 147, pp.591-605.

[19] Adam, F., Myland, T., Dahlhaus, F. and Großmann, J. (2015). GICON®-TLP for wind turbines – the path of development. Renewable Energies Offshore, pp.651-656.

[20] Driscoll, F., Jonkman, J., Robertson, A., Sirnivas, S., Skaare, B. and Nielsen, F. (2016). Validation of a FAST Model of the Statoil-hywind Demo Floating Wind Turbine. Energy Procedia, 94, pp.3-19.

[21] Questfwe.com. (2019). Moorings – Quest Floating Wind Energy. [online] Available at: https://questfwe.com/documentation-center/moorings/ [Accessed 3 May 2019].

[22] Borg, M., Collu, M. (2015). A comparison between the dynamics of horizontal and vertical axis offshore floating wind turbines. Phil. Trans. R. Soc. A373:20140076

[23] Concretemarinesolutions.com. (2019). DTI-50. [online] Available at: http://www.concretemarinesolutions.com/index.html [Accessed 12 Aug. 2019].

[24] Windpoweroffshore.com. (2019). Statoil launches Hywind challenge. [online] Available at: https://www.windpoweroffshore.com/article/1305595/statoil-launches-hywind-challenge [Accessed 12 Aug. 2019].

[25] YouTube. (2019). THE HYWIND® INSTALLATION CHALLENGE. [online] Available at: https://www.youtube.com/watch?v=M6w5OiRMS0o [Accessed 12 Aug. 2019].

[26] Taylor, R. (2009). Tower structure and method of raising and lowering said structure. WO2009147449A1.

[27] Questfwe.com. (2019). [online] Available at: https://questfwe.com/wp-content/uploads/2018/07/Hywind-Scotland.pdf [Accessed 9 May 2019].

[28] Fraunhofer Institute For Solar Energy Systems (2018). Levelized Cost of Electricity Renewable Energy Technologies. [online] Freiburg. Available at: https://www.ise.fraunhofer.de/content/dam/ise/en/documents/publications/studies/EN2018_Fraunhofer-ISE_LCOE_Renewable_Energy_Technologies.pdf [Accessed 9 May 2019].

[29] Navigant Consulting, (2013). Offshore Wind Market and Economic Analysis. [online] Burlington. Available at: https://www1.eere.energy.gov/wind/pdfs/offshore_wind_market_and_economic_analysis.pdf [Accessed 30 Jun. 2016].

[30] Manwell, J., McGowan, J. and Rogers, A. (2002). Wind energy explained. Chichester: Wiley.

[31] Cruz, J. and Atcheson, M. (2016). Floating Offshore Wind Energy. Basel, Switzerland: Springer.

[32] Hau, E. (2013). Wind Turbines. Berlin, Heidelberg: Springer Berlin Heidelberg.

[33] JHA, A. (2017). Wind Turbine Technology. Miami, CRC Press.

[34] avind (2012). Strategy for wind turbine components and subsystems. [online] Available at: https://ens.dk/sites/ens.dk/files/Forskning_og_udvikling/strategy_for_wind_turbine_components_and_subsystems.2012.pdf [Accessed 27 May 2019].

[35] Rivkin, D. and Silk, L. (2013). Wind turbine control systems. Burlington, MA: Jones & Bartlett Learning.

[36] Cordle, A. and Jonkman, J. (2011). State of the Art in Floating Wind Turbine Design Tools. Proceedings of the 21st International Offshore and Polar Engineering Conference. [online] Available at: https://www.nrel.gov/docs/fy12osti/50543.pdf [Accessed 20 Nov. 2018].

[37] DTU Wind Energy (2015). Overview of the numerical models used in the consortium and their qualification. LIFES50+. [online] Available at: http://lifes50plus.eu/wp-content/uploads/2015/12/GA_640741_LIFES50-_D4.4.pdf [Accessed 20 Nov. 2018].

[38] Goupee, A., Kimball, R., Ridder, E., Helder, J., Robertson, A. and Jonkman, J. (2018). A Calibrated BladeElement/Momentum Theory Aerodynamic Model of the MARIN Stock Wind Turbine. Proceedings of the 25th International Offshore and Polar Engineering Conference. [online] Available at: https://www.nrel.gov/docs/fy15osti/63568.pdf [Accessed 20 Nov. 2018].

[39] Le Cunff, C., Heurtier, J., Piriou, L., Berhault, C., Perdrizet, T., Teixeira, D., Ferrer, G. and Gilloteaux, J. (2013). Fully Coupled Floating Wind Turbine Simulator Based on Nonlinear Finite Element Method: Part I — Methodology. Volume 8: Ocean Renewable Energy

[40] Qi, Q., Barltrop, N. (2015). Unsteady aerodynamics of offshore floating wind turbines using free vortex wake model. Proceedings of the 25th International Offshore and Polar Engineering Conference. [online] Available at: https://strathprints.strath.ac.uk/54960/7/Qi_Barltrop_IOPEC_2015_Offshore_floating_wind_turbines_using_free_vortex_wake_model.pdf [Accessed 20 Nov. 2018].

[41] Ingram, G. (2011). Wind Turbine Blade Analysis using the Blade Element Momentum Method. Durham: Durham University.

[42] Sedaghatizadeh, N., Arjomandi, M., Cazzolato, B. and Kelso, R. (2017). Wind farm noises: Mechanisms and evidence for their dependency on wind direction. Renewable Energy, 109, pp.311-322.

[43] University of Notre Dame (2014). Aerodynamic Performance. University of Notre Dame.

[44] National Research Council. (2007). Environmental Impacts of Wind-Energy Projects. Washington, DC: The National Academies Press. https://doi.org/10.17226/120191935

[45] Tony Burton, Nick Jenkins, David Sharpe, and Ervin Bossanyi. Wind Energy Handbook. Wiley. (2011).

[46] Rosti, M., Omidyeganeh, M. and Pinelli, A. (2016). Video: Dynamic stall of an aerofoil in ramp-up motion. 69th Annual Meeting of the APS Division of Fluid Dynamics - Gallery of Fluid Motion. [online] Available at: https://gfm.aps.org/meetings/dfd-2016/57d02d43b8ac3117910004d8 [Accessed 20 Nov. 2018].

[47] Zahle, F., Aagaard Madsen, H., & Sørensen, N. N. (2009). Evaluation of tower shadow effects on various wind turbine concepts. Research in Aeroelasticity.

Danmarks Tekniske Universitet, Risø. Roskilde, Denmark. [online] Available at: http://orbit.dtu.dk/files/3550506/ris-r-1698.pdf [Accessed 27 May 2019].

[48] Suzuki, A. (2000). Application of Dynamic Inflow Theory to Wind Turbine Rotors. Salt Lake City: Department of Mechanical Engineering, University of Utah.

[49] ORE Catapult. (2017). Catapult gives CLOWT to its Levenmouth turbine - Catapult. [online] Available at: https://ore.catapult.org.uk/press-release/catapult-gives-clowt-levenmouth-turbine/ [Accessed 14 Nov. 2017].

[50] Jonkman, J. and Buhl, M. (2005). FAST user's guide. 1st ed. Golden, Colo.: National Renewable Energy Laboratory.

[51] Bir, G. (2005). User's guide to BModes (software for computing rotating beam coupled modes). 1st ed. Golden, CO: National Renewable Energy Laboratory.

[52] NWTC Information Portal (IECWind). [online] Available at: https://nwtc.nrel.gov/IECWind. [Accessed 10 March 2017].

[53] Jonkman, B. and Buhl, M. (2006). TurbSim user's guide. 1st ed. Golden, CO: National Renewable Energy Laboratory.

[54] Wang, Q., Jonkman, J., Sprage, M. and Jonkman, B. (2016). BeamDyn. 1st ed. Golden, CO: National Renewable Energy Laboratory.

[55] Jonkman, J., Hayman, G., Jonkman, B. and Damiani, R. (2015). AeroDyn v15 User's Guide and Theory Manual. 1st ed. Golden, CO: National Renewable Energy Laboratory.

[56] Jonkman, J. (2013). Overview of the ServoDyn Control & Electrical-Drive Module.

[57] NWTC Information Portal (FAST-OrcaFlex Interface). [online] Available at: https://nwtc.nrel.gov/OrcaFlexInterface. [Accessed 10 March 2017].

[58] NWTC Information Portal (SubDyn). [online] Available at: https://nwtc.nrel.gov/SubDyn. [Accessed 10 March 2017].

[59] Offshore Renewable Energy Catapult, (2016). Levenmouth 7MW demonstration offshore wind turbine. [online] Fife, Scotland, UK: ORE Catapult. Available at: https://ore.catapult.org.uk/wp-content/uploads/2016/04/Levenmouth-7MW-demonstration-offshore-wind-turbine.pdf [Accessed 10 Mar. 2017].

[60] Haid, L., Matha, D., Stewart, G., Lackner, M., Jonkman, J. and Robertson, A. (2013). Simulation-Length Requirements in the Loads Analysis of Offshore Floating Wind Turbines. [online] Available at: https://www.nrel.gov/docs/fy13osti/58153.pdf [Accessed 31 May 2019].

[61] Wind turbines - Design requirements (2005). IEC 61400-1 1st ed. Geneva: International Electrotechnical Commission.

[62] Wind turbines - Design requirements for offshore wind turbines (2009). IEC 61400-3 1st ed. Geneva: International Electrotechnical Commission.

[63] Bush, E. (2008). ModeShapePolyFitting.

[64] Dtuwindenergy.github.io. (2015). Source Documentation — Basic DTU Wind Energy Controller. [online] Available at: http://dtuwindenergy.github.io/BasicDTUController/srcdocs.html#f/turbine_controller_mod/turbine_controller [Accessed 20 Mar. 2017].

[65] Jonkman, J. and Musial, W. (2010). Offshore Code Comparison Collaboration (OC3) for IEA Task 23 Offshore Wind Technology and Deployment. [online] Golden, Colorado. Available at: https://www.nrel.gov/docs/fy11osti/48191.pdf [Accessed 5 Feb. 2018].

[66] Vorpahl, F., Strobel, M., Jonkman, J., Larsen, T., Passon, P. and Nichols, J. (2013). Verification of aero-elastic offshore wind turbine design codes under IEA Wind Task XXIII. Wind Energy, 17(4), pp.519-547.

[67] Robertson, A., Jonkman, JM., Vorpahl, F., Popko, W., Qvist, J., Frøyd, L., Chen, X., Azcona, J., Uzunoglu, E., Guedes Soares, C., Luan, C., Yutong, H., Pengcheng, F., Yde, A., Larsen, T.J., Nichols, J., Builds, R., Lei, L., Nygaard, T.A., Manolas, D., Heege, A., Ringdalen Vatne, S., Duarte, T., Godreau, C., Hansen, H.F., Nielsen, A.W., Riber, H., Le Cunff, C., Beyer, F., Yamaguchi, A., Jung, K.J., Shin, H., Shi, W., Park, H. & Alves, M. (2014), Offshore code comparison collaboration continuation within IEA Wind Task 30: Phase II results regarding a floating semisubmersible wind system. in Proceedings of the ASME 2014 33rd International Conference on Ocean, Offshore and Arctic Engineering. vol. 9B, OMAE2014-24040, American Society of Mechanical Engineers.

[68] Det Norske Veritas-Germanischer Lloyd (2010). Recommended Practice DNV-RP-F205, Global Performance Analysis of Deepwater Floating Structures.

[69] Lopez-Pavon, C. and Souto-Iglesias, A. (2015). Hydrodynamic coefficients and pressure loads on heave plates for semi-submersible floating offshore wind turbines: A comparative analysis using large scale models. Renewable Energy, 81, pp.864-881.

[70] Tao, L. and Cai, S. (2004). Heave motion suppression of a Spar with a heave plate. Ocean Engineering, 31(5-6), pp.669-692.

[71] Fassardi, C. (2002). Tank testing and data analysis techniques for the assessment of sailboat hydrodynamic characteristics. [online] Available at: http://vm2330.sgvps.net/~syrftest/images/library/20150702141832.pdf [Accessed 20 Nov. 2018].

[72] Serret, J., Tezdogan, T., Stratford, T., Thies, P.R. and Venugopal, V. (2018).

Model test of the DTI-Floating wind concept. Proceedings of the 3rd International Conference on Offshore Renewable Energy. [online] Available at: https://strathprints.strath.ac.uk/65393/1/Serret_etal_CORE2018_Model_test_of_the_DTI_Floating_wind_concept.pdf [Accessed 15 Oct. 2018].

[73] International Towing Tank Conference (2019). Lir-NOTF. [online] Available at: https://ittc.info/media/8356/lir-facilities.pdf [Accessed 11 Jun. 2019].

[74] Sutherland, D., Noble, D., Steynor, J., Davey, T. and Bruce, T. (2017). Characterisation of current and turbulence in the FloWave Ocean Energy Research Facility. Ocean Engineering, 139, pp.103-115.

[75] INNWIND.EU (2017). D4.22: Methods for performing scale-tests for method and model validation of floating wind turbines.

[76] Serret, J. (2018). Code comparison of a NREL-FAST model of the Levenmouth wind turbine with the GH Bladed commissioning results. Proceedings of the ASME 2018 37th International Conference on Ocean, Offshore and Arctic Engineering. [online] Available at: http://proceedings.asmedigitalcollection.asme.org/proceeding.aspx?articleid=2704882 [Accessed 20 Nov. 2018].

[77] www4.edesign.co.uk. (2019). Wave Gauges | Edinburgh Designs. [online] Available at: http://www4.edesign.co.uk/product/wavegauges/ [Accessed 20 Jun. 2019].

[78] Det Norske Veritas-Germanischer Lloyd. Rules and standards. (2019). Lightweight determination - Ships (inclining test and lightweight survey). [online] Available at: https://rules.dnvgl.com/docs/pdf/DNV/cn/1990-02/99-V850.pdf [Accessed 11 Jun. 2019].

[79] Kotikalpudi, A., Taylor, B., Moreno, C., Pfifer, H. and Balas, G. (2019). Swing Tests for Estimation of Moments of Inertia. University

of Minnesota-Aerospace Engineering and Mechanics. [online] Available at: https://conservancy.umn.edu/bitstream/handle/11299/167676/BFF%20Moment%20of%20Inertia%20Testing.pdf?sequence=1&isAllowed=y [Accessed 11 Jan. 2019].

[80] Brown.edu. (2018). Dynamics and Vibrations: Notes: Free Damped Vibrations. [online] Available at: https://www.brown.edu/Departments/Engineering/Courses/En4/Notes/vibrations_free_damped/vibrations_free_damped.htm

[81] Faltinsen, O. (1990). Sea Loads on Ships and Offshore Sturctures. Cambridge University Press.

[82] Harnois, V., Weller, S.D., Johanning, L., et al., 2015. Numerical model validation for mooring systems: method and application for wave energy converters. Renew. Energy 75, 869–887.

[83] Yang, C., Weller, S., Wang, Y., Ning, D. and Johanning, L. (2017). Hydrodynamic response of a submerged tunnel element suspended from a twin-barge under random waves. Ocean Engineering, 135, pp.63-75.

[84] Sethuraman, L. and Venugopal, V. (2013). Hydrodynamic response of a stepped-spar floating wind turbine: Numerical modelling and tank testing. Renewable Energy, 52, pp.160-174.

[85] Ahn, H. and Shin, H. (2019). Model test and numerical simulation of OC3 spar type floating offshore wind turbine. International Journal of Naval Architecture and Ocean Engineering, 11(1), pp.1-10.

[86] Matha, D., Sandner, F., Molins, C., Campos, A. and Cheng, P. (2015). Efficient preliminary floating offshore wind turbine design and testing methodologies and application to a concrete spar design. Philosophical Transactions of the Royal Society A: Mathematical, Physical and Engineering Sciences, 373(2035), p.20140350.

[87] Det Norske Veritas-Germanischer Lloyd (2013). Design of Floating Wind Turbine Structures. Offshore Standard DNV-OS-J103. [online] Available at: https://rules.dnvgl.com/docs/pdf/DNV/codes/docs/2013-06/OS-J103.pdf [Accessed 17 Aug. 2019].

[88] Benitz, M., Schmidt, D., Lackner, M., Stewart, G., Jonkman, J. and Robertson, A. (2014). Comparison of Hydrodynamic Load Predictions Between Reduced Order Engineering Models and Computational Fluid Dynamics for the OC4-DeepCwind Semi-Submersible. Volume 9B: Ocean Renewable Energy.

[89] Tran, T. and Kim, D. (2017). A CFD study of coupled aerodynamic-hydrodynamic loads on a semisubmersible floating offshore wind turbine. Wind Energy, 21(1), pp.70-85.

[90] Chakrabarti, S. (1987). Hydrodynamics of offshore structures. Southampton: Computational Mechanics.

[91] Le Méhauté, B. (1976). An introduction to hydrodynamics and water waves. New York: Springer-Verlag.

[92] Cheetham, P., S. Du and R. May, 2007. Hydrodynamic analysis of ships side by side. Proceeding of 1st International Aerospace CFD Conference. Paris, France.

[93] Colby, M.K., M.E. Nasroullahi and K. Tumer, 2011. Optimizing ballast design of wave energy converters using evolutionary algorithms. Proceeding of 13th Annual Genetic and Evolutionary Computation Conference (GECCO 2011). Dublin, Ireland.

[94] Ansyshelp.ansys.com. (2019). ANSYS AQWA 19.1 - Aqwa Theory Manual. [online] Available at: https://ansyshelp.ansys.com/account/secured?returnurl=/Views/Secured/corp/v191/aqwa_thy/aqwa_thy.html [Accessed 20 Aug. 2019].

[95] ANSYS (2016). Aqwa-Librium. ANSYS Aqwa Suite.

[96] Ansyshelp.ansys.com. (2019). ANSYS AQWA - User Manual. [online] Available at: https://ansyshelp.ansys.com/account/secured?returnurl=/Views/Secured/corp/v191/wb_aqwa/wb_aqwa.html [Accessed 20 Aug. 2019].

[97] Ansyshelp.ansys.com. (2019). ANSYS AQWA 19.1 - Aqwa Reference Manual. [online] Available at: https://ansyshelp.ansys.com/account/secured?returnurl=/Views/Secured/corp/v191/aqwa_ref/aqwa_ref.html [Accessed 20 Aug. 2019].

[98] Orcina (n.d.). Orcaflex for offshore wind. Technical Notes. [online] Ulverston: Orcina. Available at: https://www.orcina.com/wp-content/uploads/OrcaFlex-for-offshore-wind.pdf [Accessed 26 Aug. 2019].

[99] Orcina.com. (n.d.). Importing hydrodynamic data. [online] Available at: https://www.orcina.com/webhelp/OrcaFlex/Content/html/Importinghydrodynamicdata.htm [Accessed 26 Aug. 2019].

[100] Orcina (n.d.). Equation of Motion for Spar Buoys in OrcaFlex. Knowledge Base Article. [online] Ulverston: Orcina. Available at: https://www.orcina.com/wp-content/uploads/Spar-Buoy-Equation-of-Motion.pdf [Accessed 26 Aug. 2019].

[101] Orcina (n.d.). Hybrid Buoy-Vessel Modelling. Knowledge Base Article. [online] Ulverston: Orcina. Available at: https://www.orcina.com/wp-content/uploads/Buoy-Vessel-Modelling.pdf [Accessed 26 Aug. 2019].

[102] Orcina.com. (n.d.). WebHelp: Lines. [online] Available at: https://www.orcina.com/webhelp/OrcaFlex/Default.htm [Accessed 26 Aug. 2019].

[103] Orcina (n.d.). Statics Convergence Guide. Knowledge Base Article. [online] Ulverston: Orcina. Available at: https://www.orcina.com/wp-content/uploads/Statics-Convergence-Guide.pdf [Accessed 26 Aug. 2019].